Identification of Blade-root Joint Dynamics in Turbine Disks

Doctoral Dissertation
Doctoral Program in Mechanical Engineering (33^{rd}cycle)

Identification of Blade-root Joint Dynamics in Turbine Disks

By

Zeeshan Saeed

******

Supervisor(s):
Prof. Teresa M. Berruti
Prof. Christian M. Firrone

Doctoral Examination Committee:
Prof. Annalisa Fregolent, Sapienza Università di Roma, Rome, Italy
Prof. Ender Cigeroglu, Middle East Technical University, Ankara, Turkey

Politecnico di Torino
2021

Declaration

I hereby declare that, the contents and organization of this dissertation constitute my own original work and does not compromise in any way the rights of third parties, including those relating to the security of personal data.

Zeeshan Saeed
2021

* This dissertation is presented in partial fulfillment of the requirements for **Ph.D. degree** in the Graduate School of Politecnico di Torino (ScuDo).

Acknowledgements

This PhD has been an exciting journey of learning and personal development; it certainly involves interaction and support of many without whom it would have been impossible to arrive at this point.

First of all, I can't ever say or do enough to thank my parents for their unconditional love, prayers, blessings and support at every step of my life. Alongside my parents, my siblings have been pivotal in providing me with the strength and support in my education and development. I am here because they truly brought me here.

My wife, Sara, despite knowing the sacrifices she would have to make by leaving behind the perks of life and her friends, has been extremely supportive of my decisions. I thank you Sara for all this and taking such good care of me. My twin daughters, Manfa and Minha, who grew up whilst learning many firsts of the life during these years, have undoubtedly been the real reason and motivation behind this.

I would like to thank my supervisors Prof. Teresa Berruti and Prof. Christian Firrone who entrusted me for this role and directed me from the very beginning to follow the course. They have been extremely patient and supportive in my difficult phases. Their scientific acumen, enthusiasm in testing new ideas, analysis of methods and results and providing new insights have been greatly helpful in my own personal development.

Since the project was funded by the EU's project EXPERTISE (721865), the coordination boards and bodies involved therein are thankfully acknowledged. Most importantly, on the budgetary as well as on the personal front, Prof. Stefano Zucca has been highly accommodating and friendly. I thank him for his professional and ever-smiling support.

I would especially thank Prof. Daniel Rixen for his worthy contribution in my work. I admire his teaching, writing and especially his critique style which brings one's best to the fore. He has been a great inspirational source for me.

Many of my colleagues have helped me by going an extra mile whilst other have done so by their time and useful insights. In this regard, many thanks to Umer, Rizwan, Peyman, Reddy, Mehrdad, Steven, Guilherme and Siva. Efforts of my Master's student, Meysam Kazeminasab, are also acknowledged for conducting parts of the experimental campaigns.

In the end, I would thank the Almighty for providing countless blessings, for bringing the people and opportunities in my life, and for knitting us in the very fabric of existence.

Zeeshan Saeed

Torino, June 2021

Abstract

Bladed-disks are fundamental bricks of the rotating parts of a turbomachine. They are operated in harsh operating conditions of elevated temperatures and pressures at high speeds. This can lead to high structural vibration and high cycle fatigue failures. Thus, it is strongly desired to dampen the vibration and also to predict the vibratory response accurately. The connections at blade-root and shroud, among other sources, can be utilized to dampen the vibration. However, predicting the connection or joint dynamics is extremely challenging, mainly due to complex vibratory characteristics of the blades and disk, their small and unreachable interface Degrees-of-Freedom (DoF), and uncertainty of the contact conditions.

This work aims to identify dynamics of blade-root connections through experimental measurements in the dynamic substructuring framework. The inability to acquire an adequate set of the interface DoF measurements compels one to use hybrid modelling and expansion techniques in order to describe the substructure dynamic behaviour. Thereafter, the joint in the assembled blade-disk system is identified through the inverse approach or substructure decoupling methods. The inherent sensitivity of the inverse methods to small errors are also investigated and they are reduced by introducing a new correlation approach in the original expansion method. The joint identification applications, in practice, have been limited to most simple test cases and configurations. In this work, these methods have been reviewed mathematically to better understand their limitations and to provide links with the general dynamic substructuring framework. A substructure decoupling based on the expansion strategy is demonstrated on a bladed-disk system with a dove-tail type connection. The test-case is academic yet the joint is realistic and more complex compared to other test-cases in the literature. The research findings may enable to better predict the response of built-up bladed-disk systems at the design and testing stages.

Contents

List of Figures

List of Tables

Nomenclature

Abbreviations

COMAC	Co-Ordinate Modal Assurance Criterion
DoF	Degree(s) of Freedom
EMPC	Equivalent Multi-Point Connection
FAAC	Frequency Amplitude Assurance Criterion
FBS	Frequency Based Substructuring
FDAC	Frequency Domain Assurance Criterion
FRAC	Frequency Response Assurance Criterion
FRF	Frequency Response Function
GAC	Global Amplitude Criterion
GSC	Global Shape Criterion
IDM	Interface Displacement Mode
IRC	Inverse Receptance Coupling
IS	Inverse Substructuring
LAC	Local Amplitude Criterion
LMFBS	Lagrange Multiplier Frequency Based Substructuring
MAC	Modal Assurance Criterion

MIMO	Multiple Inputs Multiple Outputs
POC	Pseudo Orthoginality Check
SD	Substructure Decoupling
SEMM	System Equivalent Model Mixing
SEREP	System Equivalent Reduction Expansion Process
SIMO	Single Input Multiple Outputs
SISO	Single Input Single Output
VP	Vitual Point

Latin Symbols

$\mathbf{B}$	Signed Boolean matrix
$\mathbf{C}$	Damping matrix
$\mathbf{f}, \tilde{\mathbf{f}}$	External force vector
$\bar{\mathbf{f}}$	Vector of primally assembled external forces
$\mathbf{g}$	Interface force vector
$\mathbf{I}$	Identity Matrix
$\mathbf{K}$	Stiffness matrix
$\mathbf{L}$	Localisation matrix
$\mathbf{M}$	Mass matrix
m	Number of responses or number of rows
N	Number or count
n	Number of modes or number of columns
$\mathbf{q}$	Vector of unique displacements in primal assembly or a vector of virtual coordinates

$\mathbf{R}$	Interface Displacement Modes matrix
$\mathbf{S}$	Matrix of singular values on the diagonal
$\mathbf{T}$	Transformation matrix
t	Time
$\mathbf{U}$	Unitary matrix of left singular vectors
$\mathbf{u}, \tilde{\mathbf{u}}$	Displacement vector
$\mathbf{V}$	Unitary matrix of right singular vectors
$\mathbf{W}$	Weighting matrix
X, Y, Z	Global coordinates
x, y, z	Local coordinates
$\mathbf{Y}$	Dynamic flexibility or FRF matrix
$\bar{\mathbf{Y}}$	Primally assembled FRF matrix
$\mathbf{Z}$	Dynamic stiffness matrix
$\bar{\mathbf{Z}}$	Primally assembled dynamic stiffness matrix

Greek Symbols

δ	Relaxation term for compatibility
η	Vector of modal amplitudes
θ	Angular coordinates
λ	Interface or reaction force intensity
μ	Residual
ρ	Residual term
Φ	Matrix of mode shapes or eigen modes
ϕ	Short symbol for FRAC

χ	Expansion term
Ψ	SEREP expansion matrix
ψ	An arbitrary mode shape vector
ω	Frequency in rad/s

Superscripts

$(\bullet)^*$	Complex conjugate
$(\bullet)^+$	Generalized or pseudo inverse
A, B	Substructure identifiers for dummy substructures as well as for the blade and the disk, respectively
AB	Identifier of an assembly of two substructures
AJB	Identifier of an assembly with explicit joint dynamics
Δ	Delta model
E	Experimental
exp	Experimental model
J	Joint
ov	Overlay model
v	Translational node
R	Removed model
S	Expanded or hybrid model obtained by SEMM
N	Numerical model
v	Virtual node

Subscripts

b	Set of physical boundary DoF

C	Compatibility
c	Subset of x where responses are measured
E	Equilibrium
e	Subset of x where excitations are applied
ϕ	Corresponds to modal transformation
g	Set of all (global) DoF on a substructure
i	Set of internal DoF
int	interface
j	Set of boundary DoF on substructure A
k	Set of boundary DoF on substructure B
n	Iteration count
o	Set of other useful and measurable internal DoF but used only for validation
p, q	Dummy indices for matrix elements
r	Set of internal DoF on substructure A
s	Set of internal DoF on substructure B
v	Same as c but used for validation
w	Same as e but used for validation
x	Set of measurable internal DoF on a substructure

Chapter 1

Introduction

1.1 Overview

Many mechanical systems often experience high amplitudes of oscillation during their service life. This may ultimately lead to their premature failure caused by the high cycle fatigue (HCF) phenomenon [1]. Therefore, it becomes very important to accurately predict the dynamic characteristics of a mechanical system under a dynamic load. One of the biggest hurdles in the prediction methods is the presence of joints in the system. On the one hand, these joints are connection elements that hold together several structural components, but on the other hand, they introduce uncertainties and make the dynamic response prediction extremely challenging. The effect of the uncertainty of the joints is so significant on the assembly that a lot of interest has been devoted to the their modelling over the last four decades including non-linear effects. However, when it comes to experimental validation of the models, only simple geometries and contact interfaces are considered.

In simple words, a joint can be seen as a difference between an assembly and its associated substructures. When this difference is added back to the substructures, it should produce the assembly. However, in experimental joint identification, it is mostly not the case. From a structural engineer's perspective, this process consists in modelling the joint as a structural entity between two structures and then to identify it by system identification (inverse approach) from experimental measurements. In this regard, numerous experimental and hybrid (numerical and experimental) attempts

have been made to identify the joint between two structures of relatively simple geometric characteristics.

However, for complex mechanical systems, it will not be an overstatement that the experimental joint identification hasn't progressed much. To support this, one can refer to two 27 years apart studies by Tsai and Chou (1988) [2] and Tol and Özgüven (2015) [3]. The identified joints therein are of a minimalistic size on the simplest of test-cases (academic bolted beams) and cannot be used for a slightly complex structural system such as a blade-disk connection (a key structural assembly in aero-engines and gas turbines), even after so many years of research.

1.2 Joints in turbines

Joints can be of many types, namely lap, flanged, weld, interference-fit, dove-tail, fir-tree joints. Some of these joints are common in many industrial applications. The dove-tail and fir-tree joints are specifically found in turbo-machines (aero-engines, power turbines and compressors).

There can be thousands of joints in an aero-engine or a turbine. Bladed-disks, being rotating parts mounted on a shaft(s) are composed of a disk with many blades connected by a dove-tail or a fir-tree arrangement (Fig. 1.1) called here as blade-root joints. In these bladed-disks, there can be additional joints such as shrouds – blade-to-blade connections – or under-platform dampers. These assemblies should be able to withstand the loads that are caused by the surrounding fluid and high rotational speeds. The joint interfaces, under a dynamic load, can experience some relative motion. This creates an avenue of energy dissipation due to frictional forces generated by the relative motion. For the joints near the root, it is desirable to have no relative motion thereby minimizing the dissipation [4]. On the contrary, the joints away from the root (blade platform, mid-span damper or shrouds) are designed to mitigate any unwanted vibration i.e. to dampen the vibration amplitudes. The problem at hand is well-described by Brake [4]:

"The uncertainty regarding all of these joints has led researchers to the conclusion that the single greatest opportunity for improving models of aeroturbines and reducing weight (in order to improve efficiency) is the development of an improved model of jointed systems."

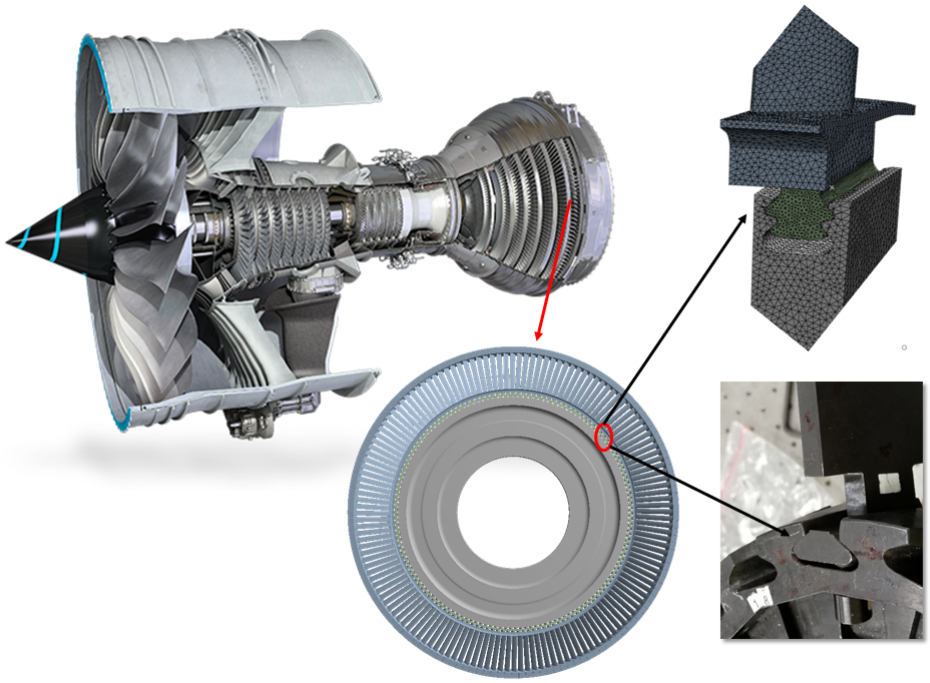

Fig. 1.1 An aero-engine (courtesy: Rolls Royce) with many bladed-disks. On the top right is a fir-tree and on the bottom right is a dove-tail connection between the blade and disk.

As opposed to the jointed systems, blades and disk can also be made as a single unit with the blade integral to the disk hub, known as *blisks*. Their use originates from the need to improve efficiency by making lighter components among other economic factors. However, these single-piece blisks rely only on internal (structural) damping or aerodynamic damping which can sometimes become negative. This may lead to overall negative damping or aerodynamic instability called flutter [5]. This further emphasizes the above argument that if the jointed systems are indeed unavoidable, their models must be improved.

1.3 Problem statement

Joints have well-developed design guidelines with respect to static loads and can be found in many machine design texts, see for example [6]. From dynamics point of view, historically, they have been seen as a limitation which introduce uncertainty in the assembled system's response. As a result, a designer may overcompensate this uncertainty in the factor of safety resulting in heavier components.

With the advent of new substructuring methods, now-a-days, one can measure components and assemble them to generate rather accurate models (for instance, in automotive applications) [7–9]. In these applications with the discrete and resilient interface, joint identification has also been successful [10, 11].

The type of interfaces in a blade-root joint pose two main challenges, namely

1. measurement inaccessibility at the interface locations, and
2. continuous interfaces (the contact points are not discrete, as opposed to bolted or lap joints).

For the first challenge, measuring dynamics at the interfaces, in dynamic substructuring, is a pre-requisite to couple or decouple substructures which is certainly not possible for blade-root joints due to lack of space for mounting sensors or exciting the structure. The second challenge is associated with one or more pairs of contacting surfaces. Consequently, it may not be known a priori where the actual contact takes place and how much surface area of each side comes into contact. Additionally, under realistic tightening conditions, these joints are highly stiff, unlike the resilient joints. For these reasons, such interfaces have not been attempted in the experimental dynamic substructuring, especially for joint identification, as it was discussed above. There is a strong need to understand the interface dynamics of blade-roots (or continuous and inaccessible interfaces) and their influence on the overall assembly.

1.4 Objectives of the thesis

The main goal of this thesis is to investigate dynamic substructuring methods suitable for the blade-root interfaces in order to experimentally identify the dynamics of the joint (or coupling) between a realistic blade and disk. Considering the challenges laid out in the problem statement, the goal can be achieved by completing the following objectives:

1. To explore expansion methods in order to predict interface dynamics of the inaccessible Degrees-of-freedom (DoF).

2. To analyse and review substructuring methods suitable for joint identification including the classical methods.
3. To select a suitable academic bladed-disk test-case (or design if not available) which must have a dove-tail or fir-tree arrangement at the root.
4. To conduct experimental campaigns suitable for expansion of the dynamics.
5. To define interface appropriately (rotations) to identify the joint.
6. To improve further the limitations of the expansion methods, if encountered.
7. To identify the root-joint dynamics in a broad frequency band-width.

Since this thesis deals with experimental work on a realistic geometry representative of an actual dove-tail joint, the work assumes that the excitation forces are not high enough to induce high relative motion. As a result, the theory of linear system dynamics can be applied. If the excitations were to be high, non-linearity would have to be considered which might make the identification even more challenging.

1.5 Organization of the dissertation

Following the introductory discussion in this chapter, the remainder of this thesis will be structured as follows:

Chapter 2 presents the theoretical foundation of the dynamic substructuring methods. Frequency based substructuring (FBS) has been discussed in detail for coupling and decoupling of a substructure. Some examples are also presented of the dummy substructures discussed in the text to provide the reader with more elaborate mathematical and matrix representations. The challenges associated with experimental substructuring are discussed.

Chapter 3 describes the most common dynamic expansion approaches. Two most popular expansion methods, SEREP[1] and SEMM[2], are mathematically compared. Their pros and cons are discussed. The SEMM method is then applied on the academic bladed-disk.

[1] System Equivalent Reduction Expansion Process – a modal expansion method
[2] System Equivalent Model Mixing – a frequency based expansion method

Chapter 4 addresses some limitations of SEMM by introducing correlations in it. The method is described in detail mathematically and schematically. Later, its effectiveness is demonstrated on the same blade-disk measurements by filtering out bad or uncorrelated measurements.

Chapter 5 presents a review of most of the frequency-based joint identification strategies. It compares mathematically, using a unified notation, several methods to provide important links to the literature. The thesis also categorises these methods in three broad identification classes, namely inverse receptance coupling, inverse substructuring and substructure decoupling. The method appropriate for a blade-root joint identification is also presented in this chapter.

Chapter 6 briefly describes the importance of interface definition. It attends to the fact that prior to identification, it is of utmost importance to have an appropriate interface definition. It covers different strategies to include rotational effect by the measured translations. Various sensitivity studies are performed to show the effectiveness as compared to the validation.

Chapter 7 presents finally the results of joint identification in this research. Different realizations of constraints, substructure models and joint are employed for this purpose. Efforts are made to improve the joint as much as possible.

Chapter 8 as a final part of this thesis presents the conclusions arising from the current research along with recommendations for further development of this research topic.

Chapter 2

Dynamic Substructuring

A usual human approach to solving a complex system is to divide it into several bits or parts and then analyse those parts separately. Likewise, Dynamic Substructuring (DS) is an approach in which a large and complex mechanical system is broken down into smaller substructures for better understanding of their dynamic behaviour. It provides a systematic framework to model and synthesize components and the system built-up by those components.

In dynamic substructuring methods, the most well-known methods are in the class of component mode synthesis (CMS). They were perceived as model reduction methods due to high computational effort required for full finite element models. They usually define a component's nodal coordinates as a function of the most dominant motion or *modes* – also called as generalized coordinates – which are usually smaller in number compared to the total number of coordinates. Consequently, the so-called reduced order models can be used for further analysis or assembled with other components leading to a reduced set of coordinates in the assembly. In this regard, the first development can be attributed to Hurty [12] and Craig and Bampton [13]. Due to limited computational power available at that time, the CMS methods received great attention and led to multiple reduction methods by Gladwell [14], Guyan [15], MacNeal [16] and Rubin [17].

The methods based on fixed interface modes by Guyan and Craig-Bampton and free interface modes by MacNeal and Rubin are quite popular and commonly available in commercial finite element softwares. The key success factors of a reduction method are: the accuracy, the time taken to compute the reduction basis,

the shape or sparsity of the reduced matrices and the assembling procedure (before or after reduction). Another method called the dual Craig-Bampton method [18, 19] uses the same ingredients as MacNeal's and Rubin's method, but assembles the substructures in a dual way using interface forces. The development of reduction methods is still continuing to date since one method does not fit all sizes. For example, reduced order models specific to turbomachinery bladed-disks for mistuning were developed in [20–25]. Comparative studies on several of these reduction methods have been presented in [26, 27]. Sometimes, a reduced system can still contain too many coordinates and may require secondary reduction by employing the so-called characteristic constraint modes [28].

Another class of dynamic substructuring is Frequency based substructuring (FBS) which provides a framework to dynamically couple or decouple two or more substructures in frequency domain. The methods developed in this class are more suitable for measurements. Substructuring in frequency domain dates back to 1941 by Duncan [29] and 1946 by Sofrin [30]. It has evolved in the methodology over the years by Jetmundsen et al. [31] who used the graph theory to couple multiple systems. The method had improved computational efficiency due to one inverse operation of the interface receptance (or admittance) instead of three, as done classically in the impedance coupling method [32]. This also resulted in better accuracy whilst coupling the measured frequency response functions (FRFs) of substructures. The original formulation of Jetmundsen et al. [31] was generalized later by Gordis et al. [33].

A more systematic approach was then proposed by De Klerk et al. [34] in which they reformulated the frequency based coupling to a dual formulation, also known as Lagrange Multiplier Frequency Based Substructuring (LMFBS). The method is powerful in the sense that it systematically introduced Boolean matrices that help maintain book-keeping of all the degrees-of-freedom in the assembly procedure. This generalization now makes it convenient to perform coupling or even decoupling [32, 35–37] of substrucutures.

The dynamic substructuring can prove to be of great advantage in the following cases [38–40]:

- For larger systems, for example, automotive or spacecraft design, where different working groups can collaborate so that each group can work on individual components.

- By working on smaller parts, the local dynamic behaviour is easy to understand compared to the entire system.
- In non-linear structural dynamics, the non-linearity is often confined locally on a smaller portion. Solving such non-linearity using the full system may be highly costly. Instead it is feasible to apply dynamic substructuring to break it into the linear and non-linear parts and speed-up the solution.
- During design optimization studies, only a part of the structure may need to be updated or changed instead of modifying the entire structure. The substructuring approach can be beneficial in saving a lot of computational effort.
- In the experimental world, it is often not possible to measure the full system (due to lack of space or lack of required force for a large system). Measuring only the parts of it and coupling on those points can help achieve an assembled system.
- It allows substitute coupling for the parts which are not manufactured yet. By combining its numerical model with an already manufactured and tested substructures, one can make predictions of the total system.

2.1 Representing the dynamics of a system

A structural system can be modelled in different ways depending upon the conditions (operating conditions, computational capacity for a numerical model or initial conditions) and the user needs. For example, from a testing perspective, a structural health diagnostician might be interested in the time histories of the measured signals on a running machine during the start-up or shut-down phases. He / she might also need to inspect the spectral content during a continuous run (steady-state) thus necessitating a transformation to the frequency domain. An experimentalist might be interested in viewing the test system as mode shapes extracted from measured FRFs (see Fig. 2.1 bottom right).

From a pure modelling perspective, given that a structure can be discretized using finite elements known as physical domain (stiffness matrix $\mathbf{K}$, mass matrix $\mathbf{M}$ and

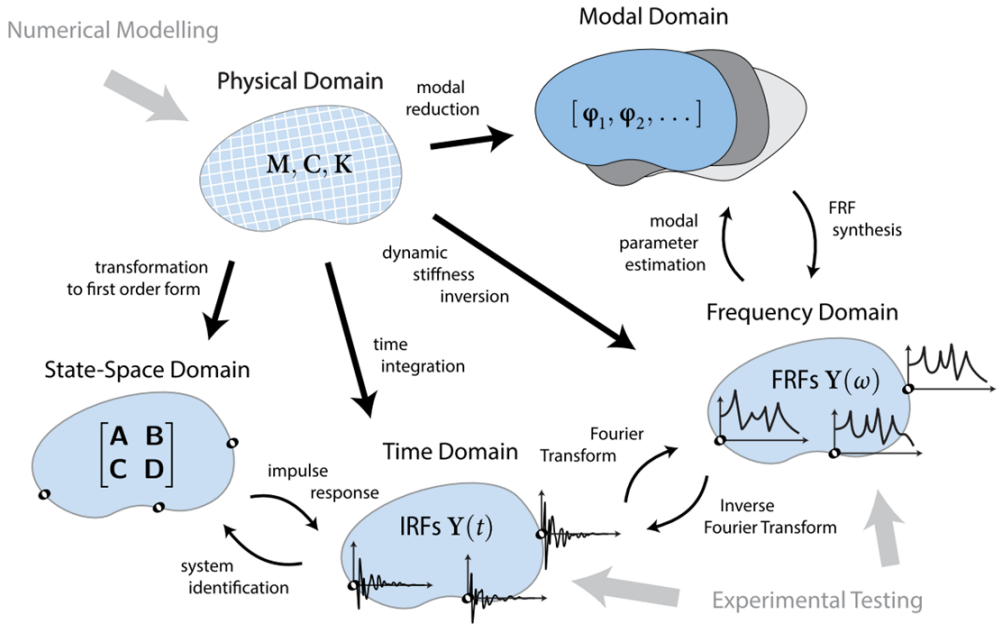

Fig. 2.1 An overview of various domains of a mechanical system [8]

damping matrix **C**), its solution can be expressed in either of these domains: modal, frequency and time (Fig. 2.1 top left).

As depicted in Fig. 2.1, if the dynamics are represented in one domain, it is possible to transform to another. A mathematical overview on these domains and their transformations is covered by van der Seijs [8]. For details on each domain with respect to substructuring, interested readers can refer to [41, 42] for impulse based substructuring, [43–45] for state-space identification and substructuring, and [46, 47] for modal domain substructuring. In this thesis, the emphasis is made on the frequency domain representation whereby the dynamics of the structures are measured from actual tests directly as the frequency response function or calculated by inverting the dynamic stiffness from the physical domain or synthesized from the modal domain.

2.2 Frequency based substructuring

Frequency based substructuring (FBS) provides a framework to dynamically couple or decouple two or more substructures. This class of methods is quite popular amongst the experimentalists or test-analysts. It owes its popularity to the fact

that the measured quantities (FRFs) can be used directly for substructuring instead of extracting the parameters first, for instance, modal properties. However, there are certain challenges in the experimental FBS methods related to sensitivity of measurement errors [40, 48–50]. Despite these challenges, as discussed in the introduction to this chapter that, these methods have improved greatly in their approach over the years.

The following subsections present in detail the different formulations of FBS using the primal and dual assembly procedure along with some examples to provide insight into the coupling and decoupling of substructures.

2.2.1 Equation of motion

Let us take a mechanical structure described as a linear time invariant system of equations of motion (EQM) under the action of an external force $\mathbf{f}(t)$.

$$\mathbf{M}\ddot{\mathbf{u}}(t) + \mathbf{C}\dot{\mathbf{u}}(t) + \mathbf{K}\mathbf{u}(t) = \mathbf{f}(t) \tag{2.1}$$

where $\mathbf{u}$ is a vector of displacements, and $\dot{\mathbf{u}}$ and $\ddot{\mathbf{u}}$ are its first (velocity) and second (acceleration) time derivatives, respectively. $\mathbf{M}, \mathbf{K}$ and $\mathbf{C}$ are mass, stiffness and proportional damping matrices, respectively. These matrices are typically obtained from a finite element analysis using in-house codes or many commercial softwares.

Assuming that the applied force $\mathbf{f}(t)$ is periodic with amplitude $\tilde{\mathbf{f}}$ and circular frequency ω in rad/s such that

$$\mathbf{f}(t) = \Re(\tilde{\mathbf{f}} e^{i\omega t}). \tag{2.2}$$

The system response to the force $\mathbf{f}(t)$ is also periodic of the form $\mathbf{u}(t) = \Re(\tilde{\mathbf{u}} e^{i\omega t})$, so the EQM becomes:

$$(-\omega^2\mathbf{M} + i\omega\mathbf{C} + \mathbf{K})\,\tilde{\mathbf{u}}(\omega) = \tilde{\mathbf{f}}(\omega) \tag{2.3}$$

$$\mathbf{Z}(\omega)\,\tilde{\mathbf{u}}(\omega) = \tilde{\mathbf{f}}(\omega) \tag{2.4}$$

where

$$\mathbf{Z}(\omega) \triangleq -\omega^2\mathbf{M} + i\omega\mathbf{C} + \mathbf{K} \tag{2.5}$$

is the dynamic stiffness. This quantity can be calculated from the matrices $\mathbf{M}, \mathbf{K}$ and $\mathbf{C}$, if available (from FE models, for example) for each excitation frequency ω. However, elements of $\mathbf{Z}(\omega)$ can be interpreted to be obtained by calculating (or measuring) a force at p DoF and applying a unit displacement at q DoF whilst grounding all the remaining DoF i.e. constraining every DoF $r \neq q$ to have zero displacement. It can be written mathematically as:

$$Z_{pq} \triangleq \left.\frac{f_p}{u_q}\right|_{u_{r\neq q}=0} \tag{2.6}$$

The explicit frequency dependence is omitted in the above equation and will be done so from here onwards, for the sake of clarity. When it comes to experimental measurements, a more intuitive quantity is the response over force or inverse of the dynamic stiffness called Frequency Response Function (FRF).

$$\mathbf{Y} \triangleq \mathbf{Z}^{-1} \tag{2.7}$$

Equivalent to Eq. (2.6), the definition of elements of $\mathbf{Y}$ is

$$Y_{pq} \triangleq \left.\frac{u_p}{f_q}\right|_{f_{r\neq q}=0} \tag{2.8}$$

It can be seen from the above expression that one does not need to constrain the whole structure in order to obtain an output-input relationship between DoF p and q, in contrast to Eq. (2.6), because it requires that all the DoF $r \neq q$ are left unforced. The only DoF to be excited is the q^{th}. This makes FRFs easier and more intuitive from an experimental point-of-view.

The FRFs can be collected by measuring responses in the form of displacement, velocity or acceleration at DoF p whilst exciting at DoF q and repeating for the whole set of DoF. Depending upon the type of measured responses, the FRFs $\mathbf{Y}(\omega)$ can have different names which are listed in Table 2.1 along with the corresponding nomenclature of $\mathbf{Z}(\omega)$ [51]. For more information on the characteristics of these different FRFs based on translational DoF, the readers are referred to Ewins [51]. The rotational counterparts of the response and force (torque) are also possible [52], however, they have not gained much attention to acquire separate names.

Table 2.1 Names of FRFs based on the response quantity type

Response Quantity	$\mathbf{Y}(\omega)$	$\mathbf{Z}(\omega)$
Displacement u	Receptance or admittance	Dynamic stiffness
Velocity $\dot{u}$	Mobility	Mechanical impedance
Acceleration $\ddot{u}$	Accelerance	Apparent mass

The common approaches to measure FRFs are by SISO (single input, single output), SIMO (single input, multi outputs) or MIMO (multi inputs, multi outputs) methods. The first two approaches are straightforward as their names imply; however, MIMO requires special arrangements and processing [53, 54]. For our analysis purpose, SISO or SIMO approaches are utilized in acquiring the FRF matrices. Each FRF is a result of a Fourier transform of the time domain response divided by the Fourier transform of the time domain excitation. There are several books that provide guidelines on the quantities (auto- and cross-spectral densities, coherence), windowing and other signal processing techniques. Two excellent book references on measuring correct FRFs and performing the modal analysis from practical point of view are Ewins [51] and Avitabile [55].

2.2.2 Coupling of substructures

Frequency based substructuring (FBS) provides a framework to dynamically couple two or more substructures. It requires frequency domain representation of the substructures such as Frequency Response Functions (FRFs) or dynamic stiffness or similar quantities of Table 2.1. Let us consider two substructure A and B of Fig. 2.2 with their indicated set of internal and boundary DoF. Let us first write the EQMs of the first substructure A:

$$\mathbf{Z}^A\mathbf{u}^A = \mathbf{f}^A + \mathbf{g}^A \quad \text{or} \quad \begin{bmatrix} \mathbf{Z}^A_{ii} & \mathbf{Z}^A_{ib} \\ \mathbf{Z}^A_{bi} & \mathbf{Z}^A_{bb} \end{bmatrix} \begin{Bmatrix} \mathbf{u}^A_i \\ \mathbf{u}^A_b \end{Bmatrix} = \begin{Bmatrix} \mathbf{f}^A_i \\ \mathbf{f}^A_b \end{Bmatrix} + \begin{Bmatrix} \mathbf{g}^A_i \\ \mathbf{g}^A_b \end{Bmatrix} \tag{2.9}$$

Note that the tilde sign is dropped over $\mathbf{u}$ and $\mathbf{f}$ to avoid loaded notations. However, they still correspond to the harmonic amplitudes. The vector $\mathbf{g}^A$ contains the reaction forces at the boundary b DoF with no reaction forces on the internal DoF i.e. $\mathbf{g}^A_i = \mathbf{0}$. Expressing substructure B in the same way:

$$\mathbf{Z}^B\mathbf{u}^B = \mathbf{f}^B + \mathbf{g}^B \quad \text{or} \quad \begin{bmatrix} \mathbf{Z}^B_{ii} & \mathbf{Z}^B_{ib} \\ \mathbf{Z}^A_{bi} & \mathbf{Z}^B_{bb} \end{bmatrix} \begin{Bmatrix} \mathbf{u}^B_i \\ \mathbf{u}^B_b \end{Bmatrix} = \begin{Bmatrix} \mathbf{f}^B_i \\ \mathbf{f}^B_b \end{Bmatrix} + \begin{Bmatrix} \mathbf{g}^B_i \\ \mathbf{g}^B_b \end{Bmatrix} \tag{2.10}$$

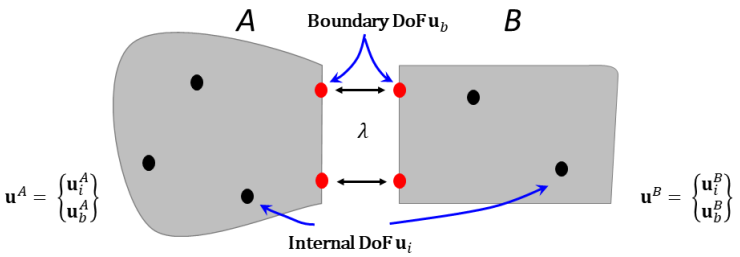

Fig. 2.2 Two uncoupled subsructures A and B.

The dynamic stiffnesses $\mathbf{Z}^A$ and $\mathbf{Z}^B$ can be arranged in a block diagonal matrix and the associated displacement and force vectors can be concatenated to express the uncoupled equation of motion.

$$\mathbf{Z}\,\mathbf{u} = \mathbf{f} + \mathbf{g} \tag{2.11}$$

where

$$\mathbf{Z} = \begin{bmatrix}\mathbf{Z}^A & \\ & \mathbf{Z}^B\end{bmatrix} \quad \mathbf{u} = \begin{Bmatrix}\mathbf{u}^A \\ \mathbf{u}^B\end{Bmatrix}, \quad \mathbf{f} = \begin{Bmatrix}\mathbf{f}^A \\ \mathbf{f}^B\end{Bmatrix}, \quad \mathbf{g} = \begin{Bmatrix}\mathbf{g}^A \\ \mathbf{g}^B\end{Bmatrix} \tag{2.12}$$

Since the two substructures are to be joined together, the displacements at the boundary DoF should be equal or compatible. By doing so, the substructures would feel reaction forces through the interface (shown as λ to be equal in magnitude but opposite in direction in Fig. 2.2). These two constraints, namely compatibility and equilibrium, can be supplemented with the uncoupled equations (2.11) by expressing the compatibility as $\mathbf{B}\mathbf{u} = \mathbf{0}$ and the equilibrium as $\mathbf{L}^T\mathbf{g} = \mathbf{0}$. The whole set of equations and constraints is called three-field formulation [40, 56] and is expressed as:

$$\begin{cases}\mathbf{Z}\,\mathbf{u} = \mathbf{f} + \mathbf{g}, \\ \mathbf{B}\,\mathbf{u} = \mathbf{0}, \\ \mathbf{L}^T\mathbf{g} = \mathbf{0}\end{cases} \tag{2.13}$$

where $\mathbf{L}$ and $\mathbf{B}$ are Boolean matrices used in the assembling process to be discussed next. This three-field formulation can be coupled in a *primal* way or *dual* way. These two coupling methods and their inter-relations are discussed in detail below.

2.2.2.1 Primal coupling

The primal type of coupling is quite common in finite element assembling procedures. The primal coupling consists in localizing all the redundant DoF of the associated substructures. This means that any repeated DoF at the boundary of either of the two substructures are expressed as a unique set of DoF. As a result, the displacements are made compatible *a priori* at the boundary DoF. In order to assemble the substructures, a localization matrix $\mathbf{L}$ is defined such that

$$\mathbf{u} = \mathbf{L}\mathbf{q} \tag{2.14}$$

where $\mathbf{u}$ contains all the DoF of the substructures and $\mathbf{q}$ contains only the unique set of DoF. In other words, the two sets of *boundary DoF* on A and B are considered as one. Substituting $\mathbf{u} = \mathbf{L}\mathbf{q}$ in the first of Eq. (2.13) and pre-multiplying both sides by $\mathbf{L}^T$ leads to:

$$\mathbf{L}^T\mathbf{Z}\mathbf{L}\mathbf{q} = \mathbf{L}^T\mathbf{f} + \mathbf{L}^T\mathbf{g} \tag{2.15}$$

It can be easily noticed that $\mathbf{L}^T\mathbf{g} = \mathbf{0}$ since $\mathbf{L}$ simply picks and sums the interface forces $\mathbf{g}_b^A$ and $\mathbf{g}_b^B$. Thus, the equilibrium at the interface is satisfied. Eq. (2.15) so becomes:

$$\bar{\mathbf{Z}}\,\mathbf{q} = \bar{\mathbf{f}} \tag{2.16}$$

where

$$\bar{\mathbf{Z}} \triangleq \mathbf{L}^T\mathbf{Z}\,\mathbf{L}, \qquad \bar{\mathbf{f}} \triangleq \mathbf{L}^T\mathbf{f} \tag{2.17}$$

are the primally assembled dynamic stiffness of the system and the force vector, respectively. The set of primal DoF $\mathbf{q}^{AB} = \mathbf{q}$ of the assembly is shown on the left side of Fig. 2.3.

The equivalent form for the FRFs is then obtained by:

$$\mathbf{q} = \bar{\mathbf{Z}}^{-1}\,\bar{\mathbf{f}} = \left(\mathbf{L}^T\mathbf{Y}^{-1}\,\mathbf{L}\right)^{-1}\bar{\mathbf{f}} \tag{2.18}$$

It can be seen clearly that this assembly approach requires an inversion of $\mathbf{Y}$ which means that two inversions of $\mathbf{Y}^A$ and $\mathbf{Y}^B$ separately and then another inversion of $\mathbf{L}^T\mathbf{Y}^{-1}\,\mathbf{L}$ i.e. a total of three inversions. This has been the traditional method in FBS using the primal approach, commonly known as impedance coupling since impedance or dynamic stiffness matrices are used in the assembly process. Inverting

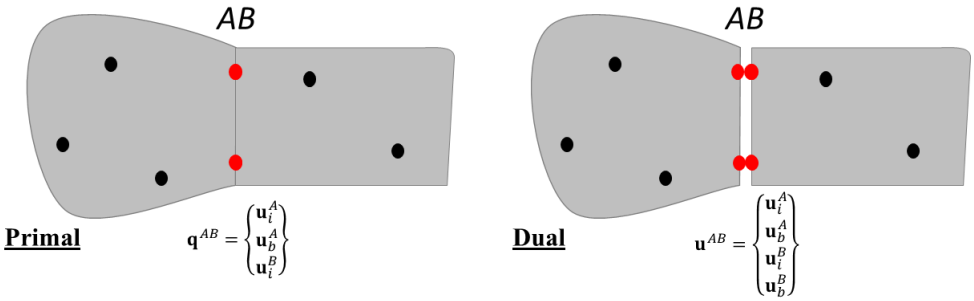

Fig. 2.3 The FBS coupling: A and B are to be coupled at their boundary DoF. On the left is primal coupling with a unique set of DoF $\mathbf{q}^{AB}$ of the coupled system. On the right is dual coupling including the boundary DoF $\mathbf{u}^{AB}$ of both A and B.

the measured FRFs to obtain the impedance matrix is problematic due to the fact that the noise and errors cause ill-conditioning. The method was improved by Jetmundsen et al. [31] by introducing only one inversion and later generalized by Gordis et al. [33]. The method was later reformulated by De Klerk et al. [34] in dual formulation and is commonly being practised now-a-days.

Example 1: Primal Coupling

Consider the dummy substructures A and B of Fig. 2.2 with the indicated DoF

$$\mathbf{u} = \begin{Bmatrix} \mathbf{u}_i^A \\ \mathbf{u}_b^A \\ \mathbf{u}_i^B \\ \mathbf{u}_b^B \end{Bmatrix} \quad \text{and a unique set} \quad \mathbf{q} = \begin{Bmatrix} \mathbf{u}_i^A \\ \mathbf{u}_b^A \\ \mathbf{u}_i^B \end{Bmatrix}.$$

This leads to the localization matrix of this form:

$$\mathbf{L} = \begin{bmatrix} \mathbf{I} & \mathbf{0} & \mathbf{0} \\ \mathbf{0} & \mathbf{I} & \mathbf{0} \\ \mathbf{0} & \mathbf{0} & \mathbf{I} \\ \mathbf{0} & \mathbf{I} & \mathbf{0} \end{bmatrix}$$

It can be easily verified that

$$\mathbf{L}^T\mathbf{g} = \begin{bmatrix} \mathbf{I} & \mathbf{0} & \mathbf{0} & \mathbf{0} \\ \mathbf{0} & \mathbf{I} & \mathbf{0} & \mathbf{I} \\ \mathbf{0} & \mathbf{0} & \mathbf{I} & \mathbf{0} \end{bmatrix} \begin{Bmatrix} \mathbf{g}_i^A \\ \mathbf{g}_b^A \\ \mathbf{g}_i^B \\ \mathbf{g}_b^B \end{Bmatrix} = \begin{Bmatrix} \mathbf{g}_i^A \\ \mathbf{g}_b^A + \mathbf{g}_b^B \\ \mathbf{g}_i^B \end{Bmatrix} = \begin{Bmatrix} \mathbf{0} \\ \mathbf{0} \\ \mathbf{0} \end{Bmatrix}$$

because on the internal DoF $\mathbf{g}_i^A = \mathbf{g}_i^B = \mathbf{0}$ and on the boundary DoF equilibrium is satisfied when $\mathbf{g}_b^A + \mathbf{g}_b^B = -\lambda + \lambda = \mathbf{0}$. Also

$$\bar{\mathbf{Z}} = \mathbf{L}^T\mathbf{Z}\mathbf{L} = \mathbf{L}^T \begin{bmatrix} \mathbf{Z}_{ii}^A & \mathbf{Z}_{ib}^A & \mathbf{0} & \mathbf{0} \\ \mathbf{Z}_{bi}^A & \mathbf{Z}_{bb}^A & \mathbf{0} & \mathbf{0} \\ \mathbf{0} & \mathbf{0} & \mathbf{Z}_{ii}^B & \mathbf{Z}_{ib}^B \\ \mathbf{0} & \mathbf{0} & \mathbf{Z}_{bi}^B & \mathbf{Z}_{bb}^B \end{bmatrix} \mathbf{L} = \begin{bmatrix} \mathbf{Z}_{ii}^A & \mathbf{Z}_{ib}^A & \mathbf{0} \\ \mathbf{Z}_{bi}^A & \mathbf{Z}_{bb}^A + \mathbf{Z}_{bb}^B & \mathbf{Z}_{bi}^B \\ \mathbf{0} & \mathbf{Z}_{ib}^B & \mathbf{Z}_{ii}^B \end{bmatrix}$$

The dynamics stiffness associated with the boundary DoF of A and B are simply summed, as seen above. This assembly produced the same coupled dynamic stiffness as would be obtained by assembling the stiffness or mass matrices in Finite Element methods. In order to get the coupled FRF matrix $\mathbf{Y}_{primal}^{AB}$, one inverts the assembled dynamic stiffness $\bar{\mathbf{Z}}$.

2.2.2.2 Dual coupling

The dual coupling of substructures relies on enforcing equilibrium *a priori*, as opposed to the primal coupling wherein the compatibility was enforced first. The dual coupling process begins by expressing the interface forces $\mathbf{g}$ as Lagrange multipliers λ or interface force intensities:

$$\mathbf{g} = -\mathbf{B}^T\lambda \tag{2.19}$$

The matrix $\mathbf{B}$ is a signed Boolean matrix. In this form, the interface forces act in opposite directions for a pair of interface DoF, because of the way $\mathbf{B}$ is constructed (to be explained later). Inserting Eq. (2.19) in Eq.(2.11) and supplementing it with

the compatibility equation leads to

$$\begin{cases} \mathbf{Z}\,\mathbf{u} + \mathbf{B}^T\lambda = \mathbf{f}, \\ \mathbf{B}\,\mathbf{u} = \mathbf{0} \end{cases} \tag{2.20}$$

or in the matrix form

$$\begin{bmatrix} \mathbf{Z} & \mathbf{B}^T \\ \mathbf{B} & \mathbf{0} \end{bmatrix} \begin{Bmatrix} \mathbf{u} \\ \lambda \end{Bmatrix} = \begin{Bmatrix} \mathbf{f} \\ \mathbf{0} \end{Bmatrix} \tag{2.21}$$

The duality is clear in Eq. (2.21) from the solution vector containing two quantities together i.e. displacements $\mathbf{u}$ and (interface) forces λ. However, one may not need to determine λ except in some special cases, so one can proceed to eliminate them and solve for $\mathbf{u}$. Keeping only $\mathbf{u}$ on the left side in the first of Eq. (2.20)

$$\mathbf{u} = \mathbf{Z}^{-1}(\mathbf{f} - \mathbf{B}^T\lambda) \tag{2.22}$$

and putting in the second of Eq. (2.20)

$$\mathbf{B}\,\mathbf{u} = \mathbf{B}\mathbf{Z}^{-1}(\mathbf{f} - \mathbf{B}^T\lambda) = \mathbf{0} \tag{2.23}$$

gives the expression for

$$\lambda = (\mathbf{B}\mathbf{Z}^{-1}\mathbf{B}^T)^{-1}\mathbf{B}\mathbf{Z}^{-1}\mathbf{f}\,. \tag{2.24}$$

When λ is substituted back in Eq. (2.22), the dually assembled displacement vector is calculated as follows:

$$\mathbf{u} = \mathbf{Z}^{-1}\left(\mathbf{f} - \mathbf{B}^T(\mathbf{B}\mathbf{Z}^{-1}\mathbf{B}^T)^{-1}\mathbf{B}\mathbf{Z}^{-1}\mathbf{f}\right) \tag{2.25}$$

or

$$\mathbf{u} = \left(\mathbf{Z}^{-1} - \mathbf{Z}^{-1}\mathbf{B}^T(\mathbf{B}\mathbf{Z}^{-1}\mathbf{B}^T)^{-1}\mathbf{B}\mathbf{Z}^{-1}\right)\mathbf{f} \tag{2.26}$$

Finally, knowing that $\mathbf{Z}^{-1} = \mathbf{Y}$

$$\boxed{\mathbf{u} = \left(\mathbf{Y} - \mathbf{Y}\mathbf{B}^T(\mathbf{B}\mathbf{Y}\mathbf{B}^T)^{-1}\mathbf{B}\mathbf{Y}\right)\mathbf{f}} \tag{2.27}$$

is the famous single-line Lagrange-Multiplier FBS or LMFBS expression in order to couple the substructures. This form is quite suitable from experimental point of view since only a part of the measured FRFs, namely interface FRFs, have to be inverted. Note that the interface DoF appear twice in the $\mathbf{u}$ vector, as indicated in Fig. 2.3 right. Eq. (2.27) can be written in a compact form as:

$$\mathbf{u} = \mathbf{Y}^{AB}\mathbf{f}\,; \tag{2.28}$$

Due to its usage in the thesis multiple times, a handy function-type notation is adopted for the dually coupled FRF matrix $\mathbf{Y}^{AB}$ to denote coupling (or decoupling) of multiple substructures as follows, for example, for A and B:

$$\mathbf{Y}^{AB} = fbs(\mathbf{Y},\mathbf{B}) \quad \text{where} \quad \mathbf{Y} = \begin{bmatrix} \mathbf{Y}^{A} & \\ & \mathbf{Y}^{B} \end{bmatrix} \tag{2.29}$$

with an appropriate definition of the Boolean matrix $\mathbf{B}$ to satisfy the compatibility conditions.

2.2.2.3 Interpretation of LMFBS

In order to physically interpret the LM-FBS equation, let us express Eq. (2.27) as

$$\begin{aligned} \mathbf{u} &= \mathbf{Y}\mathbf{f} - \mathbf{Y}\mathbf{B}^{T}\left(\mathbf{B}\mathbf{Y}\mathbf{B}^{T}\right)^{-1}\mathbf{B}\mathbf{Y}\mathbf{f} \\ \mathbf{u} &= \mathbf{Y}\mathbf{f} - \mathbf{Y}\mathbf{B}^{T}\left(\mathbf{B}\mathbf{Y}\mathbf{B}^{T}\right)^{-1}\mathbf{u}_{int} \\ \mathbf{u} &= \mathbf{Y}\mathbf{f} - \mathbf{Y}\mathbf{B}^{T}\mathbf{Z}_{int}\mathbf{u}_{int} \\ \mathbf{u} &= \mathbf{Y}\mathbf{f} - \mathbf{Y}\mathbf{B}^{T}\lambda \end{aligned} \tag{2.30}$$

Note that the relevant terms in the top equation are renamed successively in the following equations. These terms are illustrated graphically in Fig. 2.4 through the example substructures A and B. Consider that B is subjected to an external force $\mathbf{f}_B$ in one direction only whilst no force is applied on A as indicated in Fig. 2.4(a). Due to this force $\mathbf{f} = \{\mathbf{0}^T \quad \mathbf{f}^{B^T}\}^T$ on the uncoupled A and B, a gap is formed by the term $\mathbf{Y}\mathbf{f}$ i.e. the uncoupled response. Since $\mathbf{Y}$ is a measure of flexibility, the substructure B deforms due to the external force whilst A is unaffected. The amount of the gap is calculated by $\mathbf{u}_{int} = \mathbf{B}\mathbf{Y}\mathbf{f}$, as shown in Fig. 2.4(b). In order to close this gap $\mathbf{u}_{int}$,

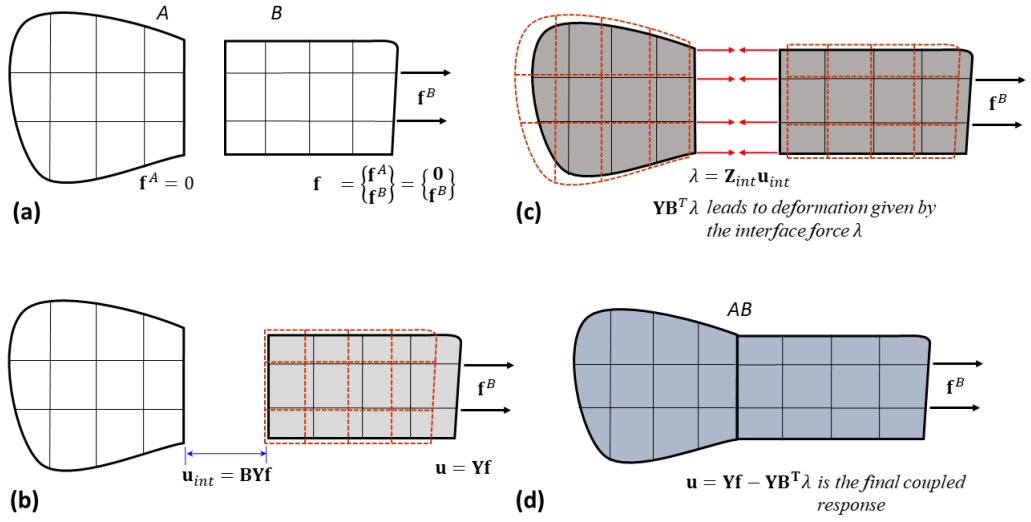

Fig. 2.4 Illustration of the LM-FBS coupling at an arbitrary frequency. The deformation are only indicative.

the interface should have stiffness $\mathbf{Z}_{int} = (\mathbf{BYB}^T)^{-1}$ to produce the interface force $\lambda = \mathbf{Z}_{int}\mathbf{u}_{int}$. The substructures feel this force λ when it is pre-multiplied by $\mathbf{YB}^T$, as illustrated in Fig. 2.4(c). As a result, both the substructures deform. The final step is to combine the uncoupled response $\mathbf{Yf}$ and the response $\mathbf{YB}^T\lambda$ due to λ in Fig. 2.4(d) to obtain the response of the coupled system.

Example 2: Dual Coupling

Consider again substructures A and B of Fig. 2.2 with the indicated DoF $\mathbf{u}$. The $\mathbf{B}$ matrix for this problem should be written in the following form to result in the correct displacement compatibility

$$\mathbf{B}\,\mathbf{u} = \begin{bmatrix}\mathbf{0} & -\mathbf{I} & \mathbf{0} & \mathbf{I}\end{bmatrix}\begin{Bmatrix}\mathbf{u}_i^A\\ \mathbf{u}_b^A\\ \mathbf{u}_i^B\\ \mathbf{u}_b^B\end{Bmatrix} = \mathbf{u}_b^B - \mathbf{u}_b^A = \mathbf{0}\,.$$

Now let us look at the dually coupled FRF matrix $\mathbf{Y}^{AB}$

$$\begin{aligned}\mathbf{Y}^{AB} &= \mathbf{Y} - \mathbf{Y}\mathbf{B}^T(\mathbf{B}\mathbf{Y}\mathbf{B}^T)^{-1}\mathbf{B}\mathbf{Y} \\ &= \begin{bmatrix} \mathbf{Y}^A_{ii} & \mathbf{Y}^A_{ib} & \mathbf{0} & \mathbf{0} \\ \mathbf{Y}^A_{bi} & \mathbf{Y}^A_{bb} & \mathbf{0} & \mathbf{0} \\ \mathbf{0} & \mathbf{0} & \mathbf{Y}^B_{ii} & \mathbf{Y}^B_{ib} \\ \mathbf{0} & \mathbf{0} & \mathbf{Y}^B_{bi} & \mathbf{Y}^B_{bb} \end{bmatrix} - \begin{bmatrix} -\mathbf{Y}^A_{ib} \\ -\mathbf{Y}^A_{bb} \\ \mathbf{Y}^B_{ib} \\ \mathbf{Y}^B_{bb} \end{bmatrix} \left[\mathbf{Y}^A_{bb} + \mathbf{Y}^B_{bb}\right]^{-1} \begin{bmatrix} -\mathbf{Y}^A_{bi} & -\mathbf{Y}^A_{bb} & \mathbf{Y}^B_{bi} & \mathbf{Y}^B_{bb} \end{bmatrix}\end{aligned}$$

By performing the algebraic steps and gathering terms for the first column of the coupled matrix, we get

$$\mathbf{Y}^{AB} = \begin{bmatrix} \mathbf{Y}^A_{ii} - \mathbf{Y}^A_{ib}[\mathbf{Y}^A_{bb} + \mathbf{Y}^B_{bb}]^{-1}\mathbf{Y}^A_{bi} & \dots & \dots & \dots \\ \mathbf{Y}^A_{bi} - \mathbf{Y}^A_{bb}[\mathbf{Y}^A_{bb} + \mathbf{Y}^B_{bb}]^{-1}\mathbf{Y}^A_{bi} & \dots & \dots & \dots \\ \mathbf{Y}^B_{ib}[\mathbf{Y}^A_{bb} + \mathbf{Y}^B_{bb}]^{-1}\mathbf{Y}^A_{bi} & \dots & \dots & \dots \\ \mathbf{Y}^B_{bb}[\mathbf{Y}^A_{bb} + \mathbf{Y}^B_{bb}]^{-1}\mathbf{Y}^A_{bi} & \dots & \dots & \dots \end{bmatrix} \tag{2.31}$$

In this form, one can see how each DoF in the coupled system AB is influenced by the corresponding interface DoF on substructures A and B. The first term, for instance, indicates the coupled receptance which would result in a displacement of the coupled system (internal DoF corresponding to substructure A) under an applied force on the same DoF.

2.2.2.4 From dual to primal

In the dually couple admittance $\mathbf{Y}^{AB}$, the interface DoF are repeated. In particular to Example 2, the second and fourth rows and columns of the so-obtained assembled admittance are identical. One could delete one of the redundant rows and columns and so the external forces acting on interface DoF of the individual substructures can also be summed up

$$\mathbf{q} = \begin{Bmatrix} \mathbf{u}^A_i \\ \mathbf{u}^A_b = \mathbf{u}^B_b \\ \mathbf{u}^B_i \end{Bmatrix} = \bar{\mathbf{Y}}^{AB} \begin{Bmatrix} \mathbf{f}^A_i \\ \mathbf{f}^A_b + \mathbf{f}^B_b \\ \mathbf{u}^B_i \end{Bmatrix}$$

where $\bar{\mathbf{Y}}^{AB}$ contains only the independent rows and columns. Alternatively, $\bar{\mathbf{Y}}^{AB}$ can be obtained systematically by the use of the localisation matrix $\mathbf{L}$ defined earlier during the three-field formulation. However, starting from the dual assembly, $\mathbf{B}$

matrix is used instead of $\mathbf{L}$. The matrix $\mathbf{L}$ can be derived from the third of Eq. (2.13) that

$$\mathbf{L}^T\mathbf{g} = -\mathbf{L}^T\mathbf{B}^T\lambda \tag{2.32}$$

This implies that $\mathbf{B}^T$ lies in the null-space of $\mathbf{L}^T$ and similarly one can deduce for $\mathbf{L}$, namely

$$\begin{cases} \mathbf{B}^T = null(\mathbf{L}^T), \\ \mathbf{L} = null(\mathbf{B}) \end{cases} \tag{2.33}$$

Using $\mathbf{L}$ either given by $\mathbf{u} = \mathbf{L}\mathbf{q}$ or by Eq. (2.33), one can retrieve the primal variables $\mathbf{q}$, $\bar{\mathbf{f}}$ and the corresponding primally coupled FRF matrix $\bar{\mathbf{Y}}^{AB}$.

$$\begin{cases} \mathbf{q} = \mathbf{L}^+\mathbf{u}, \\ \bar{\mathbf{f}} = (\mathbf{L}^T)^+\mathbf{f}, \\ \bar{\mathbf{Y}}^{AB} = \mathbf{L}^+\mathbf{Y}^{AB}(\mathbf{L}^T)^+ \end{cases} \tag{2.34}$$

The pseudo-inverse effectively takes the average over the entries in the non-unique rows and columns, creating the new primal admittance matrix $\bar{\mathbf{Y}}^{AB}$. This is same as manually selecting the unique rows and columns from the FRF matrix. Irrespective of the primal or dual assembly method, the result of the coupled system should, theoretically, be identical.

2.2.3 Decoupling of substructures

Whilst the coupling of substructures is intended to know the overall dynamic behaviour of the entire system, it may be desired, sometimes, to understand the local dynamics of a sub-component. This can be achieved by decoupling a known substructure from the known assembly to identify an unknown substructure, also called substructure identification. In substructure identification methods, the popular ones are based on structural modification [57, 32], direct decoupling (or substructure decoupling) [35, 50, 37], receptance coupling [2, 58, 3] or inverse substructuring [59, 10, 11].

The details of the latter three approaches will be discussed in Chapter 5 in the context of joint identification. We use here the direct or substructure decoupling method based on the dual approach in order to identify a substructure or a component.

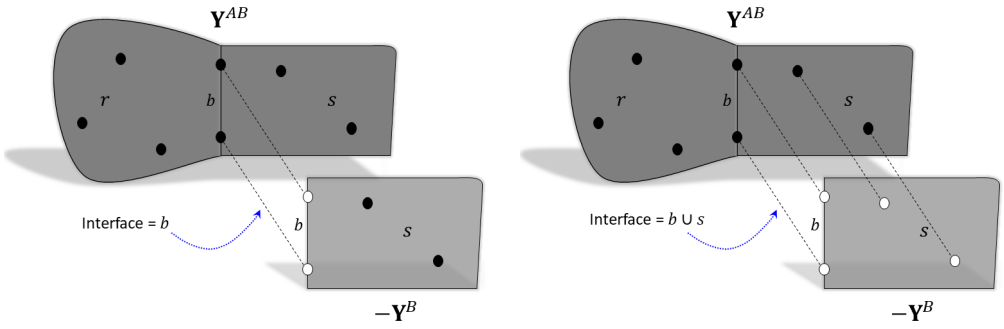

(a) standard interface (b) extended interface

Fig. 2.5 Two instances of interface definitions. In the standard interface, only the boundary or coupling DoF are considered. In the extended interface, some internal DoF are also included. The depicted interface in (b) is the limiting case in which all of the internal DoF are included.

The substructure decoupling consists in removing dynamics of one substructure, say B, from an assembly AB to obtain A, as shown in Fig. 2.5a. Let us begin with a dynamic stiffness matrix assembled primally for substructure A and B.

$$\mathbf{Z}^{AB} = \begin{bmatrix} \mathbf{Z}^{A}_{ii} & \mathbf{Z}^{A}_{ib} & \mathbf{0} \\ \mathbf{Z}^{A}_{bi} & \mathbf{Z}^{A}_{bb} + \mathbf{Z}^{B}_{bb} & \mathbf{Z}^{B}_{bi} \\ \mathbf{0} & \mathbf{Z}^{B}_{ib} & \mathbf{Z}^{B}_{ii} \end{bmatrix} \tag{2.35}$$

In $\mathbf{Z}^{AB}$, one can clearly see contribution of each substructure whilst being coupled at the boundary DoF. Upon inverting $\mathbf{Z}^{AB}$, one gets the FRF matrix $\mathbf{Y}^{AB}$ in which this distinction is lost because $\mathbf{Y}^{AB}$ represents that each DoF has a coupling with every other DoF (output-input relationship exists for every DoF). Hence, different subscripts r and s are used to denote the internal DoF of substructure A and B, respectively. The resulting coupled FRF matrix[1] looks like this:

$$\mathbf{Y}^{AB} = \begin{bmatrix} \mathbf{Y}^{AB}_{rr} & \mathbf{Y}^{AB}_{rb} & \mathbf{Y}^{AB}_{rs} \\ \mathbf{Y}^{AB}_{br} & \mathbf{Y}^{AB}_{bb} & \mathbf{Y}^{AB}_{bs} \\ \mathbf{Y}^{AB}_{sr} & \mathbf{Y}^{AB}_{sb} & \mathbf{Y}^{AB}_{ss} \end{bmatrix} \tag{2.36}$$

[1] In the assembled form, it is always a great deal to measure FRFs between internal to boundary DoF or vice versa. As a result, most of the substructure or joint identification methods usually use only the FRF sets from internal to internal DoF. This aspect is covered in detail in Chapter 5

In order to decouple B from AB, the FRF matrix of B,

$$\mathbf{Y}^B = \begin{bmatrix} \mathbf{Y}^B_{ss} & \mathbf{Y}^B_{sb} \\ \mathbf{Y}^B_{bs} & \mathbf{Y}^B_{bb} \end{bmatrix} \tag{2.37}$$

is represented fictitiously (with a negative sign) in the uncoupled FRF matrix

$$\mathbf{Y} = \begin{bmatrix} \mathbf{Y}^{AB} & \mathbf{0} \\ \mathbf{0} & -\mathbf{Y}^B \end{bmatrix} \tag{2.38}$$

to proceed for the direct decoupling using first of the 3-field formulation Eq. (2.13).

$$\mathbf{u} = \mathbf{Y}(\mathbf{f}+\mathbf{g}) \tag{2.39}$$

where

$$\mathbf{u} = \begin{Bmatrix} \mathbf{u}^{AB} \\ \mathbf{u}^B \end{Bmatrix}, \quad \begin{Bmatrix} \mathbf{f}^{AB} \\ \mathbf{f}^B \end{Bmatrix} \quad \text{and} \quad \begin{Bmatrix} \mathbf{g}^{AB} \\ \mathbf{g}^B \end{Bmatrix}. \tag{2.40}$$

Also $\mathbf{u}^{AB}$ can be written as:

$$\mathbf{u}^{AB} = \begin{Bmatrix} \mathbf{u}_r \\ \mathbf{u}_b \\ \mathbf{u}_s \end{Bmatrix}, \tag{2.41}$$

and likewise for $\mathbf{f}^{AB}$ and $\mathbf{g}^{AB}$. One needs to define appropriate compatibility and equilibrium through the interface. Unlike substructure coupling, in decoupling, it is possible to define a set of DoF which may not be a physical boundary DoF on the associated (sub)structures. By boundary DoF, it is meant that the substructures are actually coupled or connected through them. Therefore, a distinction is made between a physical boundary DoF and an interface. The interface is defined by any set of DoF which is used in the decoupling process to cancel the dynamic effect of a substructure. It may very well contain also some or all of the internal DoF (see Fig. 2.5). Based on what DoF are included in the interface, the following definitions of the interface are relevant [37]:

- **standard interface:** including only the boundary DoF set b (Fig. 2.5a),
- **extended interface:** including boundary b as well as internal DoF of the substructure to be decoupled, denoted here by s for simplicity of subscripts

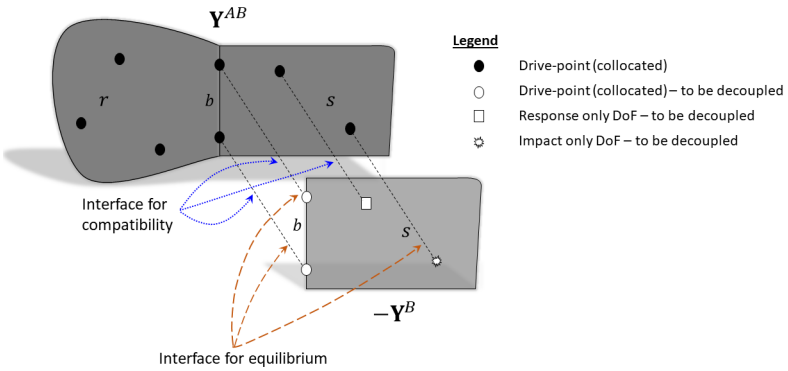

Fig. 2.6 Different interfaces for compatibility and equilibrium in a decoupling problem. In B alone, it is assumed that there are limited FRFs available on the internal DoF, for the demonstration purpose.

(Fig. 2.5b). A variant of extended interface is **mixed interface** [60] which includes subsets of boundary and internal DoF (Fig. 2.6).

Apart from the inclusion of internal DoF in the interface, it can also be different in terms of compatibility and equilibrium. This implies that the two conditions can be satisfied on different DoF sets. Fig. 2.6 depicts this situation by including in $\mathbf{Y}^B$ a non-collocated[2] set of FRFs.

In order to apply the compatibility to Eq. (2.39), the following should hold:

$$\mathbf{B}_C\,\mathbf{u} = \mathbf{0}, \quad \text{or} \quad \begin{bmatrix}\mathbf{B}_C^{AB} & \mathbf{B}_C^{B}\end{bmatrix} \begin{Bmatrix}\mathbf{u}^{AB} \\ \mathbf{u}^{B}\end{Bmatrix} = \mathbf{0} \tag{2.42}$$

where $\mathbf{B}_C = [\mathbf{B}_C^{AB} \quad \mathbf{B}_C^{B}]$ selects the interface DoF (based on whether it is standard or extended). Although separate Boolean matrices were not used for the coupling problem in Section 2.2.2.2, they are equally valid there. In the separate Boolean matrices, one must ensure that they have opposite signs on each pair of connected substructures. Similarly, the Localisation matrix $\mathbf{L}_E$ can be defined to satisfy equilibrium on the

[2]By collocated, we mean that every DoF is an output as well as an input so as to have a square FRF matrix. It includes also the drive-point FRFs. All the matrices discussed so far were considered to be of this form. A non-collocated matrix needs not have the drive-point FRFs. In the decoupling problem, the compatibility and equilibrium DoF can be different, thus leading to a non-collocated interface DoF set.

interface DoF, such that

$$\mathbf{L}_E^T\mathbf{g}=\mathbf{0} \quad \text{or} \quad \begin{bmatrix}\mathbf{L}_E^{AB}\\ \mathbf{L}_E^{A}\end{bmatrix}^T \begin{Bmatrix}\mathbf{g}^{AB}\\ \mathbf{g}^{B}\end{Bmatrix}=\mathbf{0} \tag{2.43}$$

The 3-field formulation for the decoupling problem becomes:

$$\begin{cases}\mathbf{u}=\mathbf{Y}(\mathbf{f}+\mathbf{g}),\\ \mathbf{B}_C\,\mathbf{u}=\mathbf{0},\\ \mathbf{L}_E^T\mathbf{g}=\mathbf{0}\,.\end{cases} \tag{2.44}$$

Let us assemble the uncoupled system of Eq. (2.44) in the dual way. The equilibrium $\mathbf{g}_b^{AB}+\mathbf{g}_b^{B}=\mathbf{0}$ is ensured a priori by setting $\mathbf{g}_b^{AB}=-\mathbf{g}_b^{B}=\boldsymbol{\lambda}$ with $\boldsymbol{\lambda}$ being the interface force intensities. If a Boolean matrix $\mathbf{B}_E$ is defined similar to $\mathbf{B}_C$, but related to interface equilibrium DoF, then

$$\mathbf{g}=-\mathbf{B}_E^T\boldsymbol{\lambda} \tag{2.45}$$

leads to the condition

$$\mathbf{L}_E^T\mathbf{g}=-\mathbf{L}_E^T\mathbf{B}_E^T\boldsymbol{\lambda}=\mathbf{0}. \tag{2.46}$$

It can be deduced that $\mathbf{B}_E^T$ lies in the nullspace of $\mathbf{L}_E^T$ and vice versa.

$$\begin{cases}\mathbf{L}_E^T\mathbf{B}_E^T=\mathbf{0}\\ \mathbf{B}_E\mathbf{L}_E=\mathbf{0}\end{cases} \tag{2.47}$$

Substituting Eq. (2.45) in the first of Eq. (2.44) gives:

$$\begin{cases}\mathbf{u}=\mathbf{Y}(\mathbf{f}-\mathbf{B}_E^T\boldsymbol{\lambda}),\\ \mathbf{B}_C\,\mathbf{u}=\mathbf{0},\end{cases} \tag{2.48}$$

Following the same procedure of Eq. (2.21) to (2.27) leads to the single-line expression:

$$\mathbf{u}=\left(\mathbf{Y}-\mathbf{Y}\,\mathbf{B}_E^T(\mathbf{B}_C\,\mathbf{Y}\,\mathbf{B}_E^T)^{+}\,\mathbf{B}_C\mathbf{Y}\right)\mathbf{f} \tag{2.49}$$

This is a general form of decoupling with all the DoF of both AB and B. There are some redundant and meaningless rows and columns which need to be eliminated. $(\bullet)^+$ denotes the generalized inverse due to the fact that the interface flexibility matrix can be non-square. In other words, $\mathbf{B}_C$ and $\mathbf{B}_E$ are not the same, in general.

Voormeeren and Rixen [50] derived the resulting decoupled system using only the DoF set $\mathbf{u}^{AB}$. This becomes possible when it is assumed that the substructure B has no external forces. Thus, what remains meaningful is only the substructure A DoF in $\mathbf{u}^{AB}$. The formulation is derived here by splitting the first of Eq. (2.44) and representing the interface force $\mathbf{g}$ as λ.

$$\mathbf{u}^{AB} = \mathbf{Y}^{AB}(\mathbf{f}^{AB} - \mathbf{B}_E^{AB^T}\lambda) \tag{2.50}$$

$$\mathbf{u}^{B} = -\mathbf{Y}^{B}(-\mathbf{f}^{B} - \mathbf{B}_E^{B^T}\lambda) = \mathbf{Y}^{B}\mathbf{B}_E^{B^T}\lambda \tag{2.51}$$

Note that we used $\mathbf{f}^B = \mathbf{0}$ in the last equation. Substituting the above two equations in the compatibility equation in the second of Eq. (2.44) and solving for λ:

$$\begin{aligned} &\mathbf{B}_C^{AB}\mathbf{Y}^{AB}(\mathbf{f}^{AB} - \mathbf{B}_E^{AB^T}\lambda) + \mathbf{B}_C^{B}\mathbf{Y}^{B}\mathbf{B}_E^{B^T}\lambda = \mathbf{0} \\ \Longrightarrow\ &\left(-\mathbf{B}_C^{AB}\mathbf{Y}^{AB}\mathbf{B}_E^{AB^T} + \mathbf{B}_C^{B}\mathbf{Y}^{B}\mathbf{B}_E^{B^T}\right)\lambda = -\mathbf{B}_C^{AB}\mathbf{Y}^{AB}\mathbf{f}^{AB} \\ \Longrightarrow\ &\lambda = \left(\mathbf{B}_C^{AB}\mathbf{Y}^{AB}\mathbf{B}_E^{AB^T} - \mathbf{B}_C^{B}\mathbf{Y}^{B}\mathbf{B}_E^{B^T}\right)^{+}\mathbf{B}_C^{AB}\mathbf{Y}^{AB}\mathbf{f}^{AB} \end{aligned} \tag{2.52}$$

and putting it back in Eq. (2.50) gives the final expression of the decoupled system:

$$\mathbf{u}^{AB} = \left(\mathbf{Y}^{AB} - \mathbf{Y}^{AB}\mathbf{B}_E^{AB^T}\left(\mathbf{B}_C^{AB}\mathbf{Y}^{AB}\mathbf{B}_E^{AB^T} - \mathbf{B}_C^{B}\mathbf{Y}^{B}\mathbf{B}_E^{B^T}\right)^{+}\mathbf{B}_C^{AB}\mathbf{Y}^{AB}\right)\mathbf{f}^{AB} \tag{2.53}$$

Recall that $\mathbf{u}^{AB}$ was defined in Eq. (2.41) which contains $\mathbf{u}_r$ (internal DoF of A) and $\mathbf{u}_s$ (internal DoF of B) and a unique set of boundary DoF $\mathbf{u}_b$. Only the rows and columns corresponding to the DoF of A are to be retained. Eq. (2.53) allows one to better inspect the equation. The substructure B is disconnected from AB via the interface, as seen in the interface flexibility (the expression to be inverted in the parentheses). It was discussed above that the interface in decoupling can contain internal DoF and the compatibility and equilibrium DoF do not have to be collocated. This gives rise to many variants of the interface. In order for it to be solvable, the interface flexibility needs to be determined or over-determined. This condition is

satisfied if one chooses the interface DoF such that

$$rank(\mathbf{B}_C) \geq rank(\mathbf{B}_E) \geq N_b \tag{2.54}$$

where N_b is the number of boundary or coupling DoF. It simply states that there should be more interface compatibility equations than equilibrium equations which should eventually be greater than the physical boundary DoF.

Example 3: Interfaces in Decoupling

Consider that substructure B needs to be decoupled from AB, as shown in Fig. 2.5. The assembly AB is describe as:

$$\mathbf{u}^{AB} = \begin{Bmatrix} \mathbf{u}_r \\ \mathbf{u}_b \\ \mathbf{u}_s \end{Bmatrix} = \mathbf{Y}^{AB}\mathbf{f}^{AB} = \begin{bmatrix} \mathbf{Y}^{AB}_{rr} & \mathbf{Y}^{AB}_{rb} & \mathbf{Y}^{AB}_{rs} \\ \mathbf{Y}^{AB}_{br} & \mathbf{Y}^{AB}_{bb} & \mathbf{Y}^{AB}_{bs} \\ \mathbf{Y}^{AB}_{sr} & \mathbf{Y}^{AB}_{sb} & \mathbf{Y}^{AB}_{ss} \end{bmatrix} \begin{Bmatrix} \mathbf{f}_r \\ \mathbf{f}_b \\ \mathbf{f}_s \end{Bmatrix}$$

Substructure B is decoupled using Eq. (2.53) in three ways by choosing different $\mathbf{B}_C$ and $\mathbf{B}_E$.

1. Standard interface, when only the boundary DoF are included in the interface

$$\mathbf{B}^{AB}_C = \mathbf{B}^{AB}_E = \begin{matrix} \mathbf{u}_r & \mathbf{u}_b & \mathbf{u}_s \end{matrix} \\ \begin{bmatrix} \mathbf{0} & -\mathbf{I} & \mathbf{0} \end{bmatrix}, \qquad \mathbf{B}^{B}_C = \mathbf{B}^{B}_E = \begin{matrix} \mathbf{u}^B_s & \mathbf{u}^B_b \end{matrix} \\ \begin{bmatrix} \mathbf{0} & \mathbf{I} \end{bmatrix}$$

The response of A is obtained as:

$$\begin{Bmatrix} \mathbf{u}_r \\ \mathbf{u}_b \\ \mathbf{u}_s \end{Bmatrix} = \mathbf{Y}^{AB} - \begin{bmatrix} \mathbf{Y}^{AB}_{rb} \\ \mathbf{Y}^{AB}_{bb} \\ \mathbf{Y}^{AB}_{sb} \end{bmatrix} \left[\mathbf{Y}^{AB}_{bb} - \mathbf{Y}^{B}_{bb} \right]^{-1} \begin{bmatrix} \mathbf{Y}^{AB}_{br} & \mathbf{Y}^{AB}_{bb} & \mathbf{Y}^{AB}_{bs} \end{bmatrix} \begin{Bmatrix} \mathbf{f}_r \\ \mathbf{f}_b \\ \mathbf{f}_s \end{Bmatrix} \tag{2.55}$$

2. Extended interface, when all the internal DoF along with the boundary DoF make the interface

$$\mathbf{B}^{AB}_C = \mathbf{B}^{AB}_E = \begin{matrix} \mathbf{u}_r & \mathbf{u}_b & \mathbf{u}_s \end{matrix} \\ \begin{bmatrix} \mathbf{0} & -\mathbf{I} & \mathbf{0} \\ \mathbf{0} & \mathbf{0} & -\mathbf{I} \end{bmatrix}, \qquad \mathbf{B}^{B}_C = \mathbf{B}^{B}_E = \begin{matrix} \mathbf{u}^B_s & \mathbf{u}^B_b \end{matrix} \\ \begin{bmatrix} \mathbf{0} & \mathbf{I} \\ \mathbf{I} & \mathbf{0} \end{bmatrix}$$

$$\begin{Bmatrix}\mathbf{u}_r\\ \mathbf{u}_b\\ \mathbf{u}_s\end{Bmatrix} = \mathbf{Y}^{AB} - \begin{bmatrix}\mathbf{Y}^{AB}_{rb} & \mathbf{Y}^{AB}_{rs}\\ \mathbf{Y}^{AB}_{bb} & \mathbf{Y}^{AB}_{bs}\\ \mathbf{Y}^{AB}_{sb} & \mathbf{Y}^{AB}_{ss}\end{bmatrix} \begin{bmatrix}\mathbf{Y}^{AB}_{bb}-\mathbf{Y}^{B}_{bb} & \mathbf{Y}^{AB}_{bs}-\mathbf{Y}^{B}_{bs}\\ \mathbf{Y}^{AB}_{sb}-\mathbf{Y}^{B}_{sb} & \mathbf{Y}^{AB}_{ss}-\mathbf{Y}^{B}_{ss}\end{bmatrix}^{-1} \begin{bmatrix}\mathbf{Y}^{AB}_{br} & \mathbf{Y}^{AB}_{bb} & \mathbf{Y}^{AB}_{bs}\\ \mathbf{Y}^{AB}_{sr} & \mathbf{Y}^{AB}_{sb} & \mathbf{Y}^{AB}_{ss}\end{bmatrix} \begin{Bmatrix}\mathbf{f}_r\\ \mathbf{f}_b\\ \mathbf{f}_s\end{Bmatrix} \tag{2.56}$$

3. Mixed interface, all the internal and boundary DoF for compatibility whilst only the boundary for equilibrium (note that one could choose other variants).

$$\mathbf{B}^{AB}_C = \begin{matrix}\mathbf{u}_r & \mathbf{u}_b & \mathbf{u}_s\end{matrix}\\ \begin{bmatrix}\mathbf{0} & -\mathbf{I} & \mathbf{0}\\ \mathbf{0} & \mathbf{0} & -\mathbf{I}\end{bmatrix}, \qquad \mathbf{B}^{B}_C = \begin{matrix}\mathbf{u}^B_s & \mathbf{u}^B_b\end{matrix}\\ \begin{bmatrix}\mathbf{0} & \mathbf{I}\\ \mathbf{I} & \mathbf{0}\end{bmatrix}$$

$$\mathbf{B}^{AB}_E = \begin{matrix}\mathbf{f}_r & \mathbf{f}_b & \mathbf{f}_s\end{matrix}\\ \begin{bmatrix}\mathbf{0} & -\mathbf{I} & \mathbf{0}\end{bmatrix}, \qquad \mathbf{B}^{B}_E = \begin{matrix}\mathbf{f}^B_s & \mathbf{f}^B_b\end{matrix}\\ \begin{bmatrix}\mathbf{0} & \mathbf{I}\end{bmatrix}$$

$$\begin{Bmatrix}\mathbf{u}_r\\ \mathbf{u}_b\\ \mathbf{u}_s\end{Bmatrix} = \mathbf{Y}^{AB} - \begin{bmatrix}\mathbf{Y}^{AB}_{rb}\\ \mathbf{Y}^{AB}_{bb}\\ \mathbf{Y}^{AB}_{sb}\end{bmatrix} \begin{bmatrix}\mathbf{Y}^{AB}_{bb}-\mathbf{Y}^{B}_{bb}\\ \mathbf{Y}^{AB}_{sb}-\mathbf{Y}^{B}_{sb}\end{bmatrix}^{+} \begin{bmatrix}\mathbf{Y}^{AB}_{br} & \mathbf{Y}^{AB}_{bb} & \mathbf{Y}^{AB}_{bs}\\ \mathbf{Y}^{AB}_{sr} & \mathbf{Y}^{AB}_{sb} & \mathbf{Y}^{AB}_{ss}\end{bmatrix} \begin{Bmatrix}\mathbf{f}_r\\ \mathbf{f}_b\\ \mathbf{f}_s\end{Bmatrix} \tag{2.57}$$

4. Pseudo interface, if only the internal DoF are considered (no boundary DoF) in the interface.

$$\mathbf{B}^{AB}_C = \begin{matrix}\mathbf{u}_r & \mathbf{u}_b & \mathbf{u}_s\end{matrix}\\ \begin{bmatrix}\mathbf{0} & \mathbf{0} & -\mathbf{I}\end{bmatrix}, \qquad \mathbf{B}^{B}_C = \begin{matrix}\mathbf{u}^B_s & \mathbf{u}^B_b\end{matrix}\\ \begin{bmatrix}\mathbf{I} & \mathbf{0}\end{bmatrix}$$

$$\mathbf{B}^{AB}_E = \begin{matrix}\mathbf{f}_r & \mathbf{f}_b & \mathbf{f}_s\end{matrix}\\ \begin{bmatrix}\mathbf{0} & \mathbf{0} & -\mathbf{I}\end{bmatrix}, \qquad \mathbf{B}^{B}_E = \begin{matrix}\mathbf{f}^B_s & \mathbf{f}^B_b\end{matrix}\\ \begin{bmatrix}\mathbf{I} & \mathbf{0}\end{bmatrix}$$

$$\begin{Bmatrix}\mathbf{u}_r\\ \mathbf{u}_b\\ \mathbf{u}_s\end{Bmatrix} = \mathbf{Y}^{AB} - \begin{bmatrix}\mathbf{Y}^{AB}_{rs}\\ \mathbf{Y}^{AB}_{bs}\\ \mathbf{Y}^{AB}_{ss}\end{bmatrix} \left[\mathbf{Y}^{AB}_{ss}-\mathbf{Y}^{B}_{ss}\right]^{-1} \begin{bmatrix}\mathbf{Y}^{AB}_{sr} & \mathbf{Y}^{AB}_{sb} & \mathbf{Y}^{AB}_{ss}\end{bmatrix} \begin{Bmatrix}\mathbf{f}_r\\ \mathbf{f}_b\\ \mathbf{f}_s\end{Bmatrix} \tag{2.58}$$

In the last two examples, we used all the internal DoF. However, from a practical point of view, the full set of the internal DoF is not required to be considered as long as the number of interface DoF are not less than the number of coupling (boundary) DoF.

The above four forms in Eqs. (2.55), (2.56), (2.57) and (2.58) allow us to see clearly the respective interfaces simply by virtue of different definitions of $\mathbf{B}_C$ and $\mathbf{B}_E$.

A Special Case: As seen in the first two cases of standard and extended interface when $\mathbf{B}_C = \mathbf{B}_E$, the final LMFBS equation (2.53) can be written in a compact and simple form. First, let g be a set of all the DoF such that $g = \{i, b\} = \{r, s, b\}$, then the equation becomes:

$$\mathbf{u}^{AB} = \left(\mathbf{Y}^{AB}_{gg} - \mathbf{Y}^{AB}_{gb} (\mathbf{Y}^{AB}_{bb} - \mathbf{Y}^{B}_{bb})^{+} \mathbf{Y}^{AB}_{bg} \right) \mathbf{f}^{AB} \tag{2.59}$$

This form will be used in the frequency based expansion method in Chapter 3.

The need for various interfaces for substructure identification perhaps arises due to the reason that there is some compliance at the interface i.e. the DoF are not coupled rigidly in reality. Since the interface surfaces can be of continuous nature, there also exits some uncertainty of the contact. Consequently, the rigid coupling $\mathbf{Bu} = \mathbf{0}$ is weakened by choosing different sets of DoF by changing $\mathbf{B}$. Thus, using different interface definitions is, in essence, an attempt to find a solution (coupling paths) through the realm of uncertain coupling points.

2.3 Challenges in experimental substructuring

Even though FBS is quite popular, it presents numerous problems if applied in its elementary form [40, 61, 62, 39]. The assembly procedures outlines above do not account for errors arising from measurement or modelling errors, nor do they consider practical difficulties encountered during an experiment. In the following subsections, some of the challenges in experimental substructuring are discussed.

1. Experimental Errors: In any measurement campaign, errors are unavoidable. The measured FRFs as the main ingredient in the LMFBS equation (2.27) are usually polluted with noise and other errors such as sensor mounting and excitation errors, errors due to signal leakage, or improper use of windowing. The level of these errors may be more prominent in a single FRF (where signal to noise ratio is low, especially at or near anti-resonances), or FRFs at other locations (for example, drive

point FRFs or rotational FRFs). The interface FRF matrix, despite being a smaller submatrix compared to the entire matrix, has still to be inverted. This might lead to amplification of those small errors. In the coupled FRFs, these amplifications can cause spurious peaks [48] and erroneous results.

2. Collocated DoF: The LMFBS equation (2.27) assumes that the measured FRF matrices are square. It implies that each DoF is collocated (both output and input) and so the drive point FRFs are also present for every interface or internal DoF. whilst in reality, these FRFs are difficult to measure in practice and are prone to errors [51, 39].

3. Rotational DoF: It is customary to measure only the translational FRFs on a structure. This information is often not sufficient to completely constrain the interface i.e. the interface remains too soft. Therefore, the importance of rotations cannot be undermined in a dynamic substructuring problem [63]. However, measuring rotations directly is not feasible as yet for light structures, even though some research is being conducted on directly measuring rotations [61, 64]. To this end, one is left with approximating the rotational effect by different means presented in the literature [65–67]. More discussion on this to follow in Chapter 5 and 6.

4. Interface surfaces: The interface between connecting substructures can be of different types, e.g. lap joints connected by bolts, dove-tail joints, pin-joints. Often these joints form continuous interface surfaces, whereas the measurements can only be performed at discrete points. In this case, a sufficient number of FRFs have to be measured. For bolted joints, the measuring point on the substructures is a hole and thus one has to measure near the bolt holes. In other events, measurements at the interface may not be possible at all due to constricted space for either response measurement or exciting the interface DoF. All these limitations may introduce errors in the measured or otherwise approximated (by expansion) FRFs.

5. Singularity of interface in a decoupling problem: Related to the decoupling, there is an additional problem of singularity of the interface FRF matrix. Since a decoupling interface can be of extended type, it was shown in [56] that if an extended interface is collocated, the interface FRF matrix is singular at all frequencies. Due to the small errors in the FRFs, the singularity may be avoided but it may still be ill-conditioned.

2.3.1 Some remedial actions

Some of the errors outlined above can be avoided by accounting for them from the very beginning of a test campaign. Alternatively, their effect can be reduced by using several techniques suggested in the literature. However, one must bear in mind that those techniques help avoid a part of the error whilst introducing other limitations or errors caused by the technique itself. A classic example of this is to estimate modal parameters from the measured FRFs and then synthesize the FRFs from the estimated parameters. The so-called modal filter may reduce the undesired effect of noise and errors; however, it poses many other limitations such as modal truncation, inaccuracy of parameters in cases of high modal density or high damping or inaccurate rigid body modes estimation. The remedial actions are briefed as follows:

Modal filter: As discussed, by applying the modal filter, the errors in the FRF can be reduced to produce clean and smooth FRFs. One also does not need to approximate the rotations since now it is the modes of the interface which are coupled rather than the physical DoF. The result is weakening of the interface which may serve to be useful in some cases [46]. Nevertheless, rotational effect by finite difference method can be used even for modal substructuring [65].

Expansion for inaccessible interface DoF: In the event of no access to the interface DoF, one may use expansion methods such as SEREP, SEMM or model updating techniques. These dynamic expansion methods are discussed in this thesis in Chapter 3.

Rotations by virtual point interface: A virtual point type interface description is possible by assuming the rigid behaviour of the measured points around the interface. This formation leads to an error minimization by over-determined least squared interface which includes also the rotational effects [67].

Smart techniques: In some instances, it has been shown that by truncating the lowest singular values (possibly related to errors), the coupling results can be improved [68, 69]. It has also proved useful in the case of singularity of the interface FRF matrix in the substructure decoupling problems [56].

2.4 Summary

This chapter covers the basic concepts of dynamic substructuring (DS). It starts with a quick review of literature on two major classes of DS: component mode synthesis and frequency based substructuring. The latter being the most relevant from an experimental point of view, is discussed in detail. In order to couple two or more substructures, primal and dual assembly procedures are presented mathematically. The dual method, also known as Lagrange Multiplier Frequency Based Substructuring (LMFBS), is a method suitable for coupling experimental substructures. Graphical interpretations and examples are provided for insights into the methods.

FBS framework can easily be extended to decouple a substructure from its assembly. In this case, different realizations of interface can be utilized in order to better predict the unknown substructure.

Since errors can affect the quality of measured FRFs, the assembled system can have some non-physical spurious effects. The possible error sources and their remedial actions are discussed at the end of the chapter.

Chapter 3

Dynamic Expansion

Part of the work described in this chapter was previously published in [70–72].

A mechanical component in any system should have a certain reliability that can be predicted by its different descriptions, called models. Each model can describe some of its aspects but lacks in the other. Therefore, it needs to be validated against another model. From the dynamics viewpoint, for example, a numerical model can provide a larger description of the system dynamics based on the nominal or ideal properties (geometry, material, constraints), but it may lack the characteristics of the actual component. On the other hand, an experimental model of the same may provide richer and compact information to be used for validation purposes but the testing may have been performed out of its usual service environment [51]. Besides, the measurements can only be performed on a limited set of the degrees-of-freedom (DoF) and can be prone to random noise and errors. This implies that one cannot absolutely say that one model describes the actual system in its entirety. Therefore, the two model descriptions of the same component should complement each other in order to make accurate predictions.

3.1 General Description of an FRF Model

Whilst measuring mechanical systems' dynamic response, response based methods in frequency domain are undoubtedly very popular and convenient. For linear systems, transfer functions amongst different DoF can provide an adequate set for

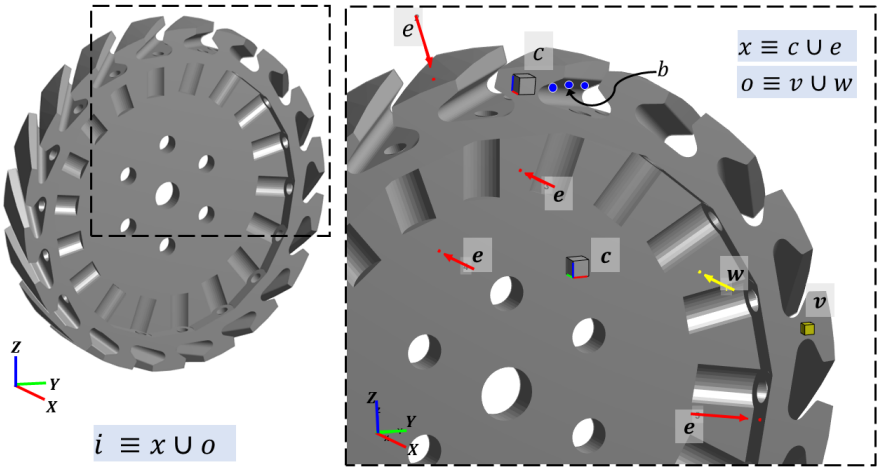

Fig. 3.1 An academic disk on which the different DoF sets are indicated. For demonstration, boundary DoF b are displayed only for one disk-slot. The lack of space in the slot inhibits any direct measurement there. On the internal DoF i, there are two tri-axial accelerometers labelled c, and one uni-axial accelerometer labelled v for validation. Among five e and w impacts, w is designated as a validation impact. All of them form a set of internal DoF $i \equiv x \cup o$ where x and o are indicated in the top right corner.

model updating, modal parameters estimation, state-space or other types of system identification methods. In fact, the first step is usually to measure the FRFs. Consider a general FRF model of a component which consists of internal $\mathbf{u}_i$ and boundary $\mathbf{u}_b$ displacements. On the same degrees of freedom, a set of input forces can also be defined i.e. forces $\mathbf{f}_i$ acting on the internal and $\mathbf{f}_b$ on the boundary DoF. The corresponding FRF matrix $\mathbf{Y}$ consists of all the FRFs between output and input DoF.

$$\mathbf{Y} = \begin{bmatrix} \mathbf{Y}_{ii} & \mathbf{Y}_{ib} \\ \mathbf{Y}_{bi} & \mathbf{Y}_{bb} \end{bmatrix}, \quad \mathbf{u} = \begin{Bmatrix} \mathbf{u}_i \\ \mathbf{u}_b \end{Bmatrix}, \quad \text{and} \quad \mathbf{f} = \begin{Bmatrix} \mathbf{f}_i \\ \mathbf{f}_b \end{Bmatrix} \tag{3.1}$$

Since Eq. (3.1) contains the point and transfer functions among all the input and output DoF, it is called a collocated DoF set. Such DoF set is essential for computing the coupled admittance in Eq. (2.27). This could easily be obtained from an analytical or numerical model. In order to check the reliability of the numerical model, an experimental validation is always desired. However, the number of measurements in the experiment is limited due to inaccessibility of some DoF for either response measurement or excitation or even due to limited number of measuring equipment. For bladed-disk interfaces such as dove-tail (Fig. 3.1) and fir-

tree type joints, the boundary DoF b are clearly neither measurable nor excitable and hence $\mathbf{Y}_{bb}$, $\mathbf{Y}_{ib}$ and $\mathbf{Y}_{bi}$ can not be obtained experimentally. Only the internal FRF $\mathbf{Y}_{ii}$ are accessible from measurement point-of-view. However, not all the internal FRFs can be measured accurately. Especially, accurate measurement of the drive-point FRFs is very challenging in practice [51, 73]. Besides these, other DoF belonging to internal system could also be retained in an onward analysis. Therefore, the set of internal DoF i is divided into two sets:

$$\mathbf{u}_i = \begin{Bmatrix} \mathbf{u}_x^T & \mathbf{u}_o^T \end{Bmatrix}^T \quad \text{and} \quad \mathbf{f}_i = \begin{Bmatrix} \mathbf{f}_x^T & \mathbf{f}_o^T \end{Bmatrix}^T \tag{3.2}$$

The different subscripts represent:

- x: a set of DoF where measurements are possible,
- o: a set of other useful internal DoF.

From the limited measurable set of FRFs on x, a key question arises: how to predict the unmeasurable boundary DoF b or o?

3.2 Methods for predicting unmeasured dynamics

The common methods for prediction of unmeasured substructure dynamics (FRFs) are discussed in the next subsections with more emphasis on the technique, SEMM, selected as a working method in this thesis, in order to provide a good theoretical basis.

3.2.1 Model updating methods

In structural dynamics, it is quite common that the numerical predictions and experimental results disagree. Thus updated models are required to produce the dynamic behaviour of the actual structure. In this respect, Finite Element (FE) model updating of mechanical systems [74–78] has been very popular for over the last four decades. The main principle is to minimize a residual vector of measured and predicted quantities by differentiating sensitivity matrices with respect to the design parameters [77, 79]. In this way, the predicted quantities (in the numerical model)

are regarded as an updated model and can thus be used as a valid representation of the unmeasured quantities. Typically, a first order Taylor series approximation is used for the unknown updating parameters θ.

$$\rho = \mathbf{S}\,\Delta\theta \tag{3.3}$$

where ρ is the residual vector of the difference between the measured and predicted parameters, $\mathbf{S}$ is the sensitivity matrix containing the first order derivatives of the dynamic parameters with respect to the design parameters, and $\Delta\theta$ is the unknown vector representing the changes in design parameters. By solving Eq. (3.3) for $\Delta\theta$, the system matrices can be updated. The residual vector ρ can be defined with respect to modal parameters in the class of modal methods [80] or with respect to FRFs in the class of response-based methods [81].

The modal methods certainly require accurate modal parameters extraction. Experimental modal analysis can introduce errors especially when the structure exhibits close modes or regions of high modal density [82]. Another issue is that non-unique solutions emerge when the sensitivity matrix $\mathbf{S}$ is under-determined or ill-conditioned [83]. Furthermore, discrepancies arising from constraints (boundary conditions) make the task even more difficult. Besides, incorporating damping into models by either modal or response-based requires special attention and methods [84]. With ever-increasing applications, more model-updating methods are being developed. An in-situ transmissibility based model updating of constrained structures is recently proposed in [85].

3.2.2 CMS methods

The classical CMS based reduction methods, if inverted, can also be seen as expansion methods. These methods were reviewed in Chapter 2. Since most of the CMS methods use some combination of physical coordinates (master) and modal coordinates, it is generally quite difficult to measure these generalized coordinates directly. In fact, one has to measure the FRFs first and then extract modal parameters. In addition to these, the other physical coordinates need also to be measured. For example, in Guyan's [15] or Craig-Bampton's [13] method, constraint modes cannot be measured easily due to the reason that realizing an ideal constraint is very challenging in practice. For the same basis, measuring fixed interface modes is yet

another endeavouring task. The free interface modes CMS reduction methods, on the other hand, have also been attempted by experimentalists [86–88] but they did not gain popularity.

3.2.3 Expansion methods

Expansion methods in the literature are commonly used to predict the dynamic behaviour to the unmeasured DoF. Some of the expansion methods are based on polynomials that provide an analytical basis to obtain the unmeasured dynamics. They are usually very specific to applications. To name a few, a rotor-bearing system in [89], a beam [90] and cylindrical shells [91]. A method called the round trip theory [92] can be seen as an expansion of the FRFs measured at limited locations. The method produces a collocated FRF matrix by measuring responses at all the DoF whilst exciting one or few, or vice versa. This is essentially an expansion of the measured FRFs whereby responses are measured on the interface DoF by avoiding the excitations on the interface. It is very useful when there is not sufficient space to excite the interface DoF, but just a little bit to mount the sensors to measure the responses. This type of expansion is suitable for automotive applications with resilient joint elements. These methods might prove useful in their target application, but they cannot be generalized.

In the modal domain, System Equivalent Reduction Expansion Process (SEREP) expands the measured modes to the unmeasured modes by means of a numerical modal basis [93]. The method is simple and cheap since it uses the invariant modal basis. The expanded modes can be used to transform the full system matrices (stiffness, mass) or to synthesize FRFs directly. Since the measured modes have to be estimated from modal estimation methods, there is always some unaccounted residual and so the number of modes have to be equal to or less than the measured DoF. This results in deficiency of the rank. Later, this aspect will be treated more in detail.

In the response based measurements, a recent expansion technique called System Equivalent Model Mixing (SEMM) exploits different equivalent models of the same component [94]. It is based on Frequency Based Substructuring framework [34]. A set of FRFs over a limited DoF in a physical component is overlaid on a larger DoF in its parent numerical model. The resulting hybrid or the expanded model of the

SEMM mimics the measurements and the remaining DoF are the expansion. The SEMM can be thought as the frequency domain counter-part of the SEREP. It has certain advantages over the SEREP such as: 1) modal parameters estimation is not required and hence no limitation on the closely spaced modes nor on the damping, 2) mode shapes need not to be measured, 3) the hybrid model is full rank. But it comes at the cost of frequency dependent response function matrices which is not significant with the modern day computing resources and the development of reduced order models.

SEREP and SEMM are more general and can be extended to application where structure's measured modes [1] and FRFs, respectively, are available. The two methods will be discussed in the following sections.

3.3 SEREP

System Equivalent Reduction Expansion Process or SEREP can be used as a method of reduction as well as expansion of modes of two equivalent systems [93]. It utilizes the basic principle of modal superposition that describes the solution as a sum of individual modal contributions. Let us consider the disk of Fig. 3.1 in which the modes have been measured on x DoF. The set of DoF o and b cannot be measured and thus need to be expanded. The solution can be transformed to modal domain as:

$$\mathbf{u} = \Phi\eta \quad \Longrightarrow \quad \begin{Bmatrix} \mathbf{u}_x \\ \mathbf{u}_o \\ \mathbf{u}_b \end{Bmatrix} = \begin{bmatrix} \Phi_x \\ \Phi_o \\ \Phi_b \end{bmatrix} \eta \tag{3.4}$$

where Φ is an $m \times n$ mode shape matrix and the subscripts x, o, b denote the respective partitions of Φ. From Eq. (3.4),

$$\mathbf{u}_x = \Phi_x\eta \tag{3.5}$$

or

$$\eta = (\Phi_x^T\Phi_x)^{-1}\Phi_x^T\mathbf{u}_x = \Phi_x^+\mathbf{u}_x\,. \tag{3.6}$$

[1] Even though measured modes are extracted from measured FRFs, here a distinction is made in terms of the basis, used in SEREP and SEMM, respectively.

where Φ_x^+ is the Moore-Penrose pseudo inverse of the partitioned mode shape matrix. Putting it back in Eq. (3.4) results in

$$\begin{Bmatrix} \mathbf{u}_x \\ \mathbf{u}_o \\ \mathbf{u}_b \end{Bmatrix} = \begin{bmatrix} \Phi_x \\ \Phi_o \\ \Phi_b \end{bmatrix} \Phi_x^+ \mathbf{u}_x = \underbrace{\Phi \Phi_x^+}_{\mathbf{T}_\phi} \mathbf{u}_x \tag{3.7}$$

Considering that the modes Φ in Eq. (3.6) are the numerical modes, then using $\mathbf{T}_\phi$ one can expand the measured modes Φ_x^E (corresponding to measurements on the DoF set x) onto Φ as follows:

$$\Psi = \mathbf{T}_\phi \, \Phi_x^E = \Phi \, \Phi_x^+ \, \Phi_x^E = \Phi (\Phi_x^T \Phi_x)^{-1} \Phi_x^T \, \Phi_x^E \tag{3.8}$$

$\mathbf{T}_\phi$ is the SEREP transformation matrix. SEREP needs a finite element model (FEM) whose eigenvectors are well-tuned to the experimental mode shapes. If the measured DoF m_x are greater than modes $n_\phi < n$, then the measured modes Φ_x^E are expanded in a least square sense on the numerical modes Φ. This also means that a smoothing (or filtering) is applied.

Using the expanded modes Ψ, one can synthesize an expanded FRF matrix [95, 96] or use the transformation $\mathbf{T}_\phi$ matrix to obtain the mass and stiffness matrices. The SEREP method has been quite popular and has been used in numerous applications [97–100].

3.3.1 Limitations

The quality of the SEREP expansion depends on the selection of measured DoF – here denoted by x – since the generalized inverse is based on the partition of x DoF as well as on the selected numerical modes. Johansson and Abrahamsson [101] proposed an optimization strategy to find an optimal numerical basis to improve the quality of the SEREP expansion. It can be noticed that SEREP is inherently rank deficient. When $m_x = n$, then the pseudo-inverse is a simple inverse and the transformation is referred to as SEREPa. However, its rank is still limited because no matter how many DoF one can measure, the rank will be determined by the modes present in the frequency range of interest.

In addition to the above, there may exist some discrepancy between measured and numerical coordinates leading to non-smoothness of the expanded mode shapes. A correlation based smoothness was suggested in the SEREP method called Variability Improvement of Key Inaccurate Node Groups [95, 102]. The work made use of statistical correlations such as Modal Assurance Criteria (MAC) and Pseudo Orthogonality Check (POC) to retain only the correlated DoF or modes.

3.4 SEMM

The System Equivalent Model Mixing or SEMM [94] is an expansion technique that mixes (couples) in frequency domain different equivalent models of the same structure. In substructure coupling sense, when two substructures are coupled, the result is a mathematically assembled system. In SEMM, the coupling happens between two equivalent models of the same (sub-)system. This would imply an assembly of two models, for example, numerical and experimental whilst desiring a good equivalence between the two. However, the assembly effect is eliminated by decoupling another equivalent numerical model. The net result is a hybrid model that behaves exactly like the experiments on the coupling points (DoF) whilst the other points are expanded. The SEMM method has gained popularity very quickly and is being applied in multiple applications [103–108].

SEMM relies on three models, namely, a parent, an overlay and a removed model. In Klaassen et al. [94], its different interface formulations are presented. A recap of the models used in SEMM and the corresponding coupling/decoupling interface formulations is presented below.

3.4.1 Parent model

The parent model provides a larger spatial description of the system since it can contain all the DoF in terms of numerical or FE representation. The unmeasured DoF, as discussed in Section 3.1, are thus available in the numerical model – similar to the numerical modes used in SEREP. The parent model needs to be expressed in the admittance or FRF form which can be obtained from a full finite element model (FEM) or a reduced form of it.

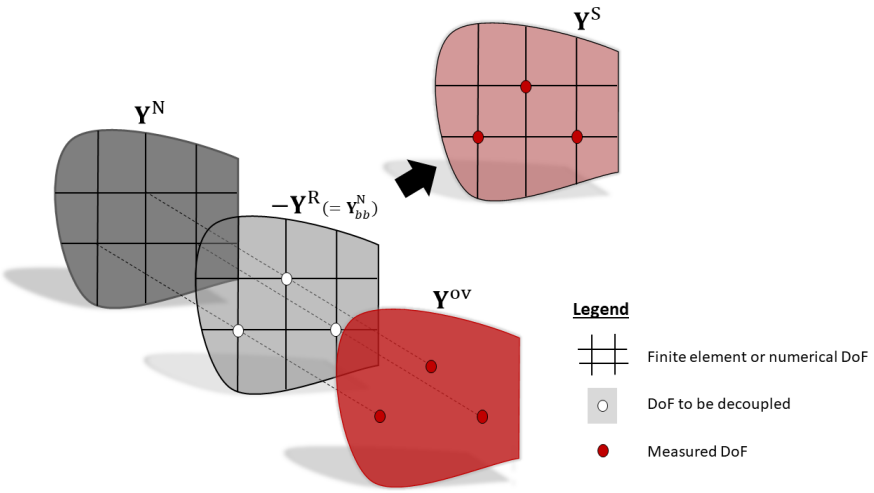

Fig. 3.2 Equivalent models of the substructure A. The parent numerical model $\mathbf{Y}^{\mathrm{N}}$ has all the essential DoF required for the analysis. A limited set of measured FRFs in $\mathbf{Y}^{\mathrm{ov}}$ are coupled to $\mathbf{Y}^{\mathrm{N}}$. The parent dynamics are decoupled by the removed model $\mathbf{Y}^{\mathrm{R}}$ and coupled by $\mathbf{Y}^{\mathrm{ov}}$. The resulting hybrid or expanded model $\mathbf{Y}^{\mathrm{S}}$ is exact at the corresponding overlay model's DoF.

Since generating an FRF model from a full FEM [2] can be very costly, one can use one of the many reduction methods in the literature. After the reduction, according to the DoF partition in Eq. (3.1) and (3.2), parent model's DoF set, referred to as global DoF $\mathbf{u}_g$, can be written as follows:

$$\mathbf{u}_g^{\mathrm{N}} = \mathbf{Y}_{gg}^{\mathrm{N}}\,\mathbf{f}_g^{\mathrm{N}} \quad \Longrightarrow \quad \begin{Bmatrix}\mathbf{u}_x\\ \mathbf{u}_o\\ \mathbf{u}_b\end{Bmatrix}^{\mathrm{N}} = \underbrace{\begin{bmatrix}\mathbf{Y}_{xx} & \mathbf{Y}_{xo} & \mathbf{Y}_{xb}\\ \mathbf{Y}_{ox} & \mathbf{Y}_{oo} & \mathbf{Y}_{ob}\\ \mathbf{Y}_{bx} & \mathbf{Y}_{bo} & \mathbf{Y}_{bb}\end{bmatrix}^{\mathrm{N}}}_{\mathbf{Y}^{\mathrm{N}}} \begin{Bmatrix}\mathbf{f}_x\\ \mathbf{f}_o\\ \mathbf{f}_b\end{Bmatrix}^{\mathrm{N}} \tag{3.9}$$

where $g = i \cup b = x \cup o \cup b$. The parent model is depicted in dark grey colour in Fig. 3.2 with a grid.

[2] Alternative to direct FRF matrix computation from direct inversion of FE model is the frequency response calculation under a known excitation vector: 1) The methods based on Krylov subspace are iterative and approximate the solution vector up to a set tolerance, see for example, [109, 110]. 2) Another very common approach is to use a truncated set of modal or eigenvectors and approximate the solution by the modal superposition principle [111]. 3) Methods based on interpolatory model order reduction use several Krylov sequence vectors of dynamic stiffness to form a reduction basis to find the harmonic response. This approach is called "Moment Matching" or "Padé approximation" [112, 27]. In order to further reduce the computational cost, new fast preconditioners are being developed [113] along with their recycling [114, 115]. Since this work deals with FRF matrices, only direct matrix inversion is used [116].

3.4.2 Overlay model

In order to describe a structure's response experimentally, only a few points are available for measurements (coloured DoF in Fig. 3.2). As discussed in Section 3.1, measuring FRFs is not practically possible on the boundary DoF (also some parts of internal DoF). Then it is possible to describe the experimental FRF model from Eq. (3.2) in the following:

$$\mathbf{u}_x^{\mathrm{ov}} = \mathbf{Y}_{xx}^{\mathrm{ov}} \mathbf{f}_x^{\mathrm{ov}} \tag{3.10}$$

In the SEMM terminology, $\mathbf{Y}^{\mathrm{ov}}$ is a model whose dynamics are important and need to be imposed on the numerical parent model. In a practical application of SEMM, this overlay model collects experimental results. This can include FRFs where the response and the force are along the same DoF (drive-point) and FRFs where the response and the force are along different DoF (transfer). It is well-known that accurately measuring drive-point FRFs can become very challenging. Obviously, Eq. (3.10) contains both the point and transfer functions. It will be seen later in the chapter how to avoid point FRFs and still construct a hybrid model which includes them.

3.4.3 Removed model

Using the FBS framework, the parent and overlay models can be coupled. However, it would still contain the dynamics of the numerical model. These dynamics could be conflicting and undesired because a numerical model always needs to be tuned or updated to the experimental data. The dynamics of the numerical model are removed by decoupling: on the one end, a reduced form of the numerical model; or on the other end, the entire numerical model. The decoupling interface due to the removed model $\mathbf{Y}^{\mathrm{R}}$ can so be standard or extended (see Section 2.2.3 for details).

3.4.4 Hybrid model

The hybrid model $\mathbf{Y}^{\mathrm{S}}$ is obtained by coupling the overlay model with the parent model and decoupling at the same time the removed model. Mathematically, using

the aforementioned equivalent models, the uncoupled admittance matrix

$$\mathbf{Y} = \begin{bmatrix} \mathbf{Y}^{\mathrm{N}} & & \\ & -\mathbf{Y}^{\mathrm{R}} & \\ & & \mathbf{Y}^{\mathrm{ov}} \end{bmatrix}, \tag{3.11}$$

the appropriate signed Boolean matrices

$$\mathbf{B}_C = \begin{array}{c} \begin{matrix} \mathbf{u}_x^{\mathrm{N}} & \mathbf{u}_o^{\mathrm{N}} & \mathbf{u}_b^{\mathrm{N}} & \mathbf{u}_x^{\mathrm{R}} & \mathbf{u}_o^{\mathrm{R}} & \mathbf{u}_b^{\mathrm{R}} & \mathbf{u}_x^{\mathrm{ov}} \end{matrix} \\ \left[\begin{array}{ccc|ccc|c} -\mathbf{I} & \mathbf{0} & \mathbf{0} & \mathbf{I} & \mathbf{0} & \mathbf{0} & \mathbf{0} \\ \mathbf{0} & -\mathbf{I} & \mathbf{0} & \mathbf{0} & \mathbf{I} & \mathbf{0} & \mathbf{0} \\ \mathbf{0} & \mathbf{0} & -\mathbf{I} & \mathbf{0} & \mathbf{0} & \mathbf{I} & \mathbf{0} \\ \mathbf{0} & \mathbf{0} & \mathbf{0} & -\mathbf{I} & \mathbf{0} & \mathbf{0} & \mathbf{I} \end{array}\right] \end{array}, \tag{3.12}$$

and

$$\mathbf{B}_E = \begin{array}{c} \begin{matrix} \mathbf{f}_x^{\mathrm{N}} & \mathbf{f}_o^{\mathrm{N}} & \mathbf{f}_b^{\mathrm{N}} & \mathbf{f}_x^{\mathrm{R}} & \mathbf{f}_o^{\mathrm{R}} & \mathbf{f}_b^{\mathrm{R}} & \mathbf{f}_x^{\mathrm{ov}} \end{matrix} \\ \left[\begin{array}{ccc|ccc|c} -\mathbf{I} & \mathbf{0} & \mathbf{0} & \mathbf{I} & \mathbf{0} & \mathbf{0} & \mathbf{0} \\ \mathbf{0} & -\mathbf{I} & \mathbf{0} & \mathbf{0} & \mathbf{I} & \mathbf{0} & \mathbf{0} \\ \mathbf{0} & \mathbf{0} & -\mathbf{I} & \mathbf{0} & \mathbf{0} & \mathbf{I} & \mathbf{0} \\ \mathbf{0} & \mathbf{0} & \mathbf{0} & -\mathbf{I} & \mathbf{0} & \mathbf{0} & \mathbf{I} \end{array}\right] \end{array} \tag{3.13}$$

are substitued in Eq. (2.45) to get dually coupled admittance $\tilde{\mathbf{Y}}$ which is then reduced to the primal DoF by the following transformation:

$$\mathbf{Y}^{\mathrm{S}} = (\mathbf{L}_C)^{+}\, \tilde{\mathbf{Y}}\, (\mathbf{L}_E^T)^{+} \tag{3.14}$$

The localisation matrices $\mathbf{L}_C$ and $\mathbf{L}_E$ can be obtained by calculating the nullspace of respective $\mathbf{B}_C$ and $\mathbf{B}_E$. The hybrid model can be expressed in a single-line expression in the same manner as it was derived in Section 2.2.3. In particular, in decoupling, one can express the dually assembled system in the DoF of the assembled system. In the case of SEMM, this corresponds to the numerical parent model's $\mathbf{Y}^{\mathrm{N}}$ DoF set. The three models to be assembled in Eq. 3.11 can then be assembled in two steps:

1. decouple overlay $\mathbf{Y}^{\mathrm{ov}}$ from the removed model $\mathbf{Y}^{\mathrm{R}}$ – called the delta model $\mathbf{Y}^{\Delta}$

2. decouple $\mathbf{Y}^{\Delta}$ from $\mathbf{Y}^{\mathrm{N}}$

Using this two step process and with the removed model's two definitions, the corresponding formulations for the hybrid models are derived in the following subsections.

3.4.4.1 Hybrid model with standard interface

One of the limiting cases in SEMM is obtained if one sets the removed model as a reduced form of the parent model, as shown in Fig. 3.2 and defined as:

$$\mathbf{Y}^{\mathrm{R}} \triangleq \mathbf{Y}^{\mathrm{N}}_{xx} \tag{3.15}$$

The delta model $\mathbf{Y}^{\Delta}$ is a decoupling of $\mathbf{Y}^{\mathrm{ov}}$ from $\mathbf{Y}^{\mathrm{R}} = \mathbf{Y}^{\mathrm{N}}_{xx}$ on the same x DoF. The LMFBS equation (2.53) in Section 2.2.3 is used to decouple the models here:

$$\mathbf{Y}^{\Delta} = \mathbf{Y}^{\mathrm{R}} - \mathbf{Y}^{\mathrm{R}}(\mathbf{Y}^{\mathrm{R}} - \mathbf{Y}^{\mathrm{ov}})^{-1}\mathbf{Y}^{\mathrm{R}} \tag{3.16}$$

Recall that the Boolean matrices pick the elements belonging to the interface DoF. Replacing $\mathbf{Y}^{\mathrm{R}}$ with its definition in Eq. (3.15)

$$\mathbf{Y}^{\Delta} = \mathbf{Y}^{\mathrm{N}}_{xx} - \mathbf{Y}^{\mathrm{N}}_{xx}(\mathbf{Y}^{\mathrm{N}}_{xx} - \mathbf{Y}^{\mathrm{ov}})^{-1}\mathbf{Y}^{\mathrm{N}}_{xx} \tag{3.17}$$

The hybrid model $\mathbf{Y}^{\mathrm{S}}$ is then the decoupling of $\mathbf{Y}^{\Delta}$ from $\mathbf{Y}^{\mathrm{N}}$:

$$\mathbf{Y}^{S} = \mathbf{Y}^{\mathrm{N}}_{gg} - \mathbf{Y}^{\mathrm{N}}_{gx}(\mathbf{Y}^{\mathrm{N}}_{xx} - \mathbf{Y}^{\Delta})^{-1}\mathbf{Y}^{\mathrm{N}}_{xg} \tag{3.18}$$

Inserting in the above equation, the expression of $\mathbf{Y}^{\Delta}$ and simplifying

$$\begin{aligned}\mathbf{Y}^{\mathrm{S}} =& \mathbf{Y}^{\mathrm{N}}_{gg} - \mathbf{Y}^{\mathrm{N}}_{gx}\left(\mathbf{Y}^{\mathrm{N}}_{xx} - \left(\mathbf{Y}^{\mathrm{N}}_{xx} - \mathbf{Y}^{\mathrm{N}}_{xx}(\mathbf{Y}^{\mathrm{N}}_{xx} - \mathbf{Y}^{\mathrm{ov}})^{-1}\mathbf{Y}^{\mathrm{N}}_{xx}\right)\right)^{-1}\mathbf{Y}^{\mathrm{N}}_{xg} \\ =& \mathbf{Y}^{\mathrm{N}}_{gg} - \mathbf{Y}^{\mathrm{N}}_{gx}\left(\mathbf{Y}^{\mathrm{N}}_{xx}(\mathbf{Y}^{\mathrm{N}}_{xx} - \mathbf{Y}^{\mathrm{ov}})^{-1}\mathbf{Y}^{\mathrm{N}}_{xx}\right)^{-1}\mathbf{Y}^{\mathrm{N}}_{xg}\end{aligned} \tag{3.19}$$

The final expression becomes

$$\mathbf{Y}^{\mathrm{S}} = \mathbf{Y}^{\mathrm{N}}_{gg} - \mathbf{Y}^{\mathrm{N}}_{gx}(\mathbf{Y}^{\mathrm{N}}_{xx})^{-1}(\mathbf{Y}^{\mathrm{N}}_{xx} - \mathbf{Y}^{\mathrm{ov}})(\mathbf{Y}^{\mathrm{N}}_{xx})^{-1}\mathbf{Y}^{\mathrm{N}}_{xg} \tag{3.20}$$

In this form, the hybrid model has some effect of the internal system of the numerical model. This becomes evident when Eq. (3.20) is split in two parts as below:

$$\mathbf{Y}^{\mathrm{S}} = \underbrace{\mathbf{Y}^{\mathrm{N}}_{gg} - \mathbf{Y}^{\mathrm{N}}_{gx}(\mathbf{Y}^{\mathrm{N}}_{xx})^{-1}\mathbf{Y}^{\mathrm{N}}_{xg}}_{\rho^{\mathrm{N}}} + \underbrace{\mathbf{Y}^{\mathrm{N}}_{gx}(\mathbf{Y}^{\mathrm{N}}_{xx})^{-1}\mathbf{Y}^{\mathrm{ov}}(\mathbf{Y}^{\mathrm{N}}_{xx})^{-1}\mathbf{Y}^{\mathrm{N}}_{xg}}_{\chi} \tag{3.21}$$

The residual ρ^{N} is purely numerical. This term resembles the inverse of the dynamic stiffness of the internal DoF [8, 94, 60] of the parent model[3] and arises from the fact that only a part of the parent model $\mathbf{Y}^{\mathrm{N}}_{xx}$ was removed. In Appendix A, it has been shown how the dynamic stiffness of the internal DoF is a condensed form of the FRF matrix when the boundary DoF are fixed. The residual term may appear to affect the overall predicted dynamics of the hybrid model; however, its presence makes the hybrid model full rank which was absent in SEREP. In fact, the form of the residual can be changed by selecting a larger part of the parent model to make it more robust. This variant of SEMM is discussed in the next subsection.

3.4.4.2 Hybrid model with extended interface

The other limiting case of SEMM is when the removed model is the entire parent model (Fig. 3.3), namely

$$\mathbf{Y}^{\mathrm{R}} \triangleq \mathbf{Y}^{\mathrm{N}} = \mathbf{Y}^{\mathrm{N}}_{gg} \tag{3.22}$$

The delta model $\mathbf{Y}^{\Delta}$ now is written in the same way as before.

$$\mathbf{Y}^{\Delta} = \mathbf{Y}^{\mathrm{N}}_{gg} - \mathbf{Y}^{\mathrm{N}}_{gx}(\mathbf{Y}^{\mathrm{N}}_{xx} - \mathbf{Y}^{\mathrm{ov}})^{-1}\mathbf{Y}^{\mathrm{N}}_{xg} \tag{3.23}$$

The hybrid model $\mathbf{Y}^{\mathrm{S}}$ is then decoupling of $\mathbf{Y}^{\Delta}$ from $\mathbf{Y}^{\mathrm{N}}$:

$$\mathbf{Y}^{\mathrm{S}} = \mathbf{Y}^{\mathrm{N}}_{gg} - \mathbf{Y}^{\mathrm{N}}_{gg}(\mathbf{Y}^{\mathrm{N}}_{gg} - \mathbf{Y}^{\Delta})^{-1}\mathbf{Y}^{\mathrm{N}}_{gg} \tag{3.24}$$

Following the same derivation steps, the final expression for the extended interface is:

$$\mathbf{Y}^{\mathrm{S}} = \mathbf{Y}^{\mathrm{N}}_{gg} - \mathbf{Y}^{\mathrm{N}}_{gg}(\mathbf{Y}^{\mathrm{N}}_{xg})^{+}(\mathbf{Y}^{\mathrm{N}}_{xx} - \mathbf{Y}^{\mathrm{ov}})(\mathbf{Y}^{\mathrm{N}}_{gx})^{+}\mathbf{Y}^{\mathrm{N}}_{gg} \tag{3.25}$$

[3] Here, by internal DoF it is meant the DoF other than x which are not measured.

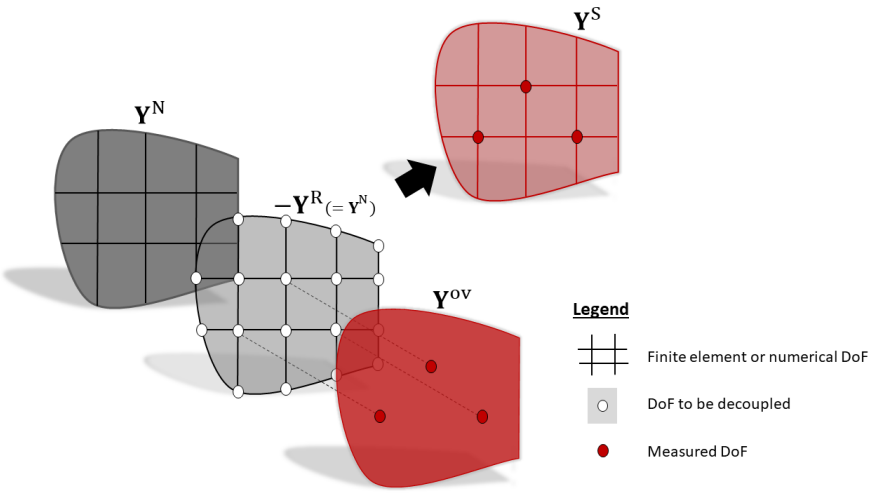

Fig. 3.3 Equivalent models of the substructure A. The parent numerical model $\mathbf{Y}^{\mathrm{N}}$ has the essential DoF. Its own dynamics are decoupled by the removed model $\mathbf{Y}^{\mathrm{R}}$ and coupled by $\mathbf{Y}^{\mathrm{ov}}$. The resulting hybrid or expanded model $\mathbf{Y}^{\mathrm{S}}$ mimics at the corresponding overlay model's DoF.

where the inverse is replaced with the pseudo inverse since the matrices $\mathbf{Y}^{\mathrm{N}}_{xg}$ and $\mathbf{Y}^{\mathrm{N}}_{gx}$ are not square. The terms of this version of SEMM can be separated in the same way as for Eq. (3.21).

$$\mathbf{Y}^{\mathrm{S}} = \underbrace{\mathbf{Y}^{\mathrm{N}}_{gg} - \mathbf{Y}^{\mathrm{N}}_{gg}(\mathbf{Y}^{\mathrm{N}}_{xg})^{+}\mathbf{Y}^{\mathrm{N}}_{xx}(\mathbf{Y}^{\mathrm{N}}_{gx})^{+}\mathbf{Y}^{\mathrm{N}}_{gg}}_{\rho^{\mathrm{N}}} + \underbrace{\mathbf{Y}^{\mathrm{N}}_{gg}(\mathbf{Y}^{\mathrm{N}}_{xg})^{+}\mathbf{Y}^{\mathrm{ov}}(\mathbf{Y}^{\mathrm{N}}_{gx})^{+}\mathbf{Y}^{\mathrm{N}}_{gg}}_{\chi} \tag{3.26}$$

The residual term ρ^{N} in this case is not the inverse of the dynamic stiffness, as with the standard decoupling interface. As a result, the expansion has lesser effect of the internal dynamics of $\mathbf{Y}^{\mathrm{N}}$, also illustrated in Fig. 3.3 by the change in colour of the hybrid model $\mathbf{Y}^{\mathrm{S}}$. This form of SEMM is more useful. It also enables the use of filtering by virtue of pseudo-inverses which can be computed by singular value decomposition [117, 69]. Note that we discussed only the limiting cases. Whereas, different conditions on the decoupling interface can be applied to get variants of the extended interface formulation of SEMM.

3.4.4.3 Hybrid model with extended interface: Non-collocated overlay model

Up until now, it was the removed model which was changed whilst the overlay model was kept of the form $\mathbf{Y}^{\mathrm{ov}}_{xx}$ which is a square and collocated FRF matrix. From practical

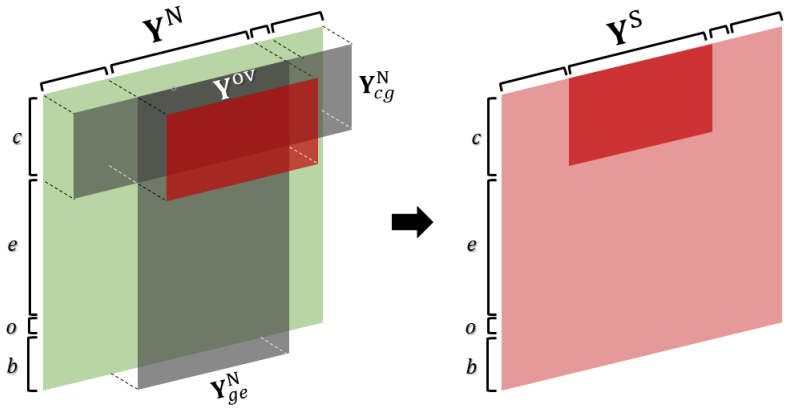

Fig. 3.4 A pictorial illustration of the extended interface formulation of SEMM when the overlay model is non-collocated. The interface is so indicated by the blocks of $\mathbf{Y}^{\mathrm{N}}$ used as pseudo-inverses in Eq. 3.29.

point-of-view, drive point FRFs are very challenging to acquire [118, 51, 47, 73]. When triaxial accelerometers are mounted on a point, all three directions of the point cannot be excited. SEMM makes it viable to measure a non-collocated FRF matrix and then use it in the expansion. A further division of the x DoF into c and e

$$\mathbf{u}_x = \begin{Bmatrix} \mathbf{u}_c \\ \mathbf{u}_e \end{Bmatrix} \quad \text{and} \quad \mathbf{f}_x = \begin{Bmatrix} \mathbf{f}_c \\ \mathbf{f}_e \end{Bmatrix} \tag{3.27}$$

and defining an experimental FRF that contains

$$\mathbf{u}_c^{\mathrm{ov}} = \mathbf{Y}^{\mathrm{ov}} \mathbf{f}_e^{\mathrm{ov}} \tag{3.28}$$

where the subscripts represent:

- c: set of DoF where responses are measured by triaxial accelerometers (or by other sensor types),
- e: set of DoF where excitations are applied by a modal impact hammer

Using the new overlay model and the extended interface form of SEMM, the appropriate expansion in the hybrid model looks as follows:

$$\mathbf{Y}^{\mathrm{S}} = \mathbf{Y}^{\mathrm{N}}_{gg} - \mathbf{Y}^{\mathrm{N}}_{gg} \left(\mathbf{Y}^{\mathrm{N}}_{cg}\right)^{+} \left(\mathbf{Y}^{\mathrm{N}}_{ce} - \mathbf{Y}^{\mathrm{ov}}_{ce}\right) \left(\mathbf{Y}^{\mathrm{N}}_{ge}\right)^{+} \mathbf{Y}^{\mathrm{N}}_{gg} \tag{3.29}$$

Note that this form is achieved by using different $\mathbf{B}_C$ and $\mathbf{B}_E$. It allows one to measure as many FRFs as possible, provided they are independent, to include in the expansion. The different models interacting in the expansion process form an interface that looks as depicted in Fig. 3.4. In this work, the formulation of Eq. (3.29) is preferred for all of the experimental results. For the sake of convenience, a function notation is employed for this equation as,

$$\mathbf{Y}^{\mathrm{S}} = semm(\,\mathbf{Y}^{\mathrm{N}},\,\mathbf{Y}^{\mathrm{ov}}\,) \tag{3.30}$$

to be used later in the thesis. Of course, another input to the function can be the DoF set according to which the partitions in Eq. (3.29) are done. This is left to the context of the discussion.

3.4.5 Singular value filtering in SEMM

In this subsection, the effect of singular values (SV) truncation (called SV filtering) whilst computing the pseudo-inverses is investigated. In SEMM, the first use of SV filtering was made in [117] and applied to a numerical benchmark structure i.e. only a single uncoupled structure was considered. Let $\mathbf{P}$ denote one of the pseudo-inverses in Eq. (3.25) or (3.29). It can be decomposed into:

$$\mathbf{P} = \mathbf{U}\mathbf{S}\mathbf{V}^H \tag{3.31}$$

where $\mathbf{S}$ is a matrix containing singular values σ_j on its diagonal such that $\sigma_1 > \sigma_2 > \ldots > \sigma_N$, with N being the smallest dimension of $\mathbf{P}$. The matrices $\mathbf{U}$ and $\mathbf{V}$ are unitary matrices containing left and right singular vectors, $\mathbf{u}_j$ and $\mathbf{v}_j$, respectively. $(\bullet)^H$ denotes complex conjugate transpose. Eq. (3.31) can be expressed in the summation form for all N singular values and vectors in the following form:

$$\mathbf{P} = \sum_{j}^{N} \mathbf{u}_j \sigma_j \mathbf{v}_j^H . \tag{3.32}$$

In this form, the contribution of each jth singular value can be clearly seen. The pseudo inverse can be computed from Eq. (3.31)

$$\mathbf{P}^{+} = \mathbf{V}\mathbf{S}^{-1}\mathbf{U}^H . \tag{3.33}$$

Note that the use has been made of the unitary matrix property, $\mathbf{U}\mathbf{U}^H = \mathbf{U}^H\mathbf{U} = \mathbf{I}$ and $\mathbf{V}\mathbf{V}^H = \mathbf{V}^H\mathbf{V} = \mathbf{I}$. Thus, $\mathbf{P}^+$ according to the form in Eq. (3.32) becomes

$$\mathbf{P}^+ = \sum_j^N \mathbf{v}_j {\sigma_j}^{-1} \mathbf{u}_j^H. \tag{3.34}$$

The singular values in $\mathbf{S}^{-1}$ appear as ${\sigma_j}^{-1}$. By retaining only $k < N$ singular values, one can approximate the inverse as follows:

$$\mathbf{P}^+ \approx \sum_j^{k<N} \mathbf{v}_j {\sigma_j}^{-1} \mathbf{u}_j^H. \tag{3.35}$$

Thus, it becomes clearer that the smallest $(N-k)$ singular values, those more affected by errors, in the inverse problem give the largest contribution to the solution and for this reason they are discarded. Since $\mathbf{P}$, in general, is a frequency dependent matrix, the decomposition needs to be done at every frequency.

3.4.5.1 Advantages and limitations of SEMM

The different formulations so far can be summarized to have the following advantages and limitations:

1. The hybrid model $\mathbf{Y}^{\mathrm{S}}$ has the same DoF structure as the parent numerical model $\mathbf{Y}^{\mathrm{N}}$.
2. The dynamics of $\mathbf{Y}^{\mathrm{ov}}$ are exactly imposed on the corresponding DoF of $\mathbf{Y}^{\mathrm{N}}$.
3. For the remaining blocks of $\mathbf{Y}^{\mathrm{S}}$, the FRFs are expansions on the unmeasurable DoF.
4. $\mathbf{Y}^{\mathrm{S}}$ is full rank in standard as well as extended formulation due to the presence of the numerical residual ρ^{N}. In the latter, this residual does not affect the expansion adversely.
5. The experimental FRFs in $\mathbf{Y}_{ce}^{\mathrm{ov}}$ have not been inverted during the process; yet any noise in the experimental model is transmitted to the hybrid model.
6. The pseudo inverses enable filtering by discarding the lowest singular values, as discussed in Section 3.4.5 to reduce the effect of noise and errors.

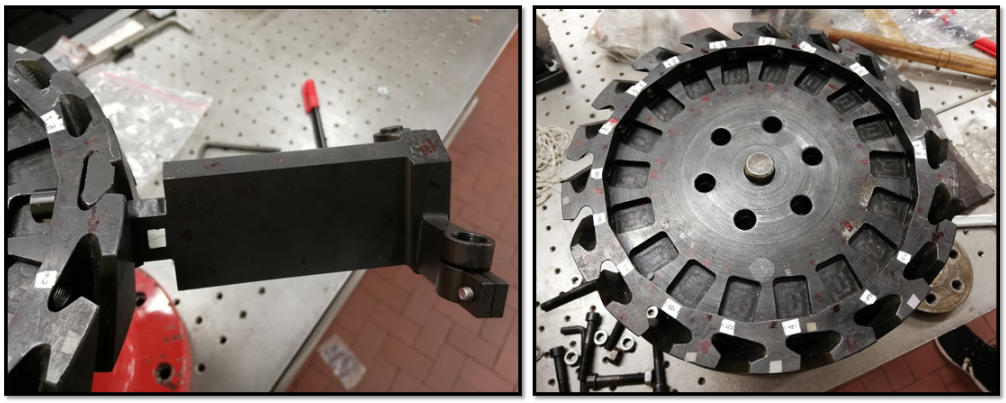

(a) (b)

Fig. 3.5 The actual blade and disk (a) The blade shown as connected in a disk slot (b) The disk

7. The modelling or expansion error is the norm of the difference $|\mathbf{Y}^{\mathrm{N}}_{xx} - \mathbf{Y}^{\mathrm{ov}}|$. Of course, it depends on the closeness between the two models.

8. By using a non-collocated DoF in the overlay model, one may avoid measuring the drive-point FRFs. However, it may lead to non-symmetric or non-reciprocal hybrid model matrix.

3.5 Experimental test-cases

The test-geometries for application of the SEMM method are a disk and a blade, to be tested as single components here in this chapter and chapter 4. The disk has 18 slots to host as many blades (Fig. 3.5). Their nominal characteristics are listed in Table 3.1. The blade and disk connection is characterised by a dove-tail joint – typically found in turbine or compressor disks. Their geometric and finite element models are illustrated in Fig. 3.6. The two components will be assembled and tested in chapters 6 and 7 for the joint identification.

3.5.1 Test campaigns and experiment design

There are two test campaigns whose results will be presented in this chapter and the thesis from here on. In each campaign, the blade is tested in a constraint-free

Table 3.1 Nominal characteristics of the blade and disk

Characteristics	Blade	Disk
Material	Steel	Steel
Nominal length	120 mm (max. length)	100 mm (diameter)
Nominal weight	0.250 kg	2.480 kg

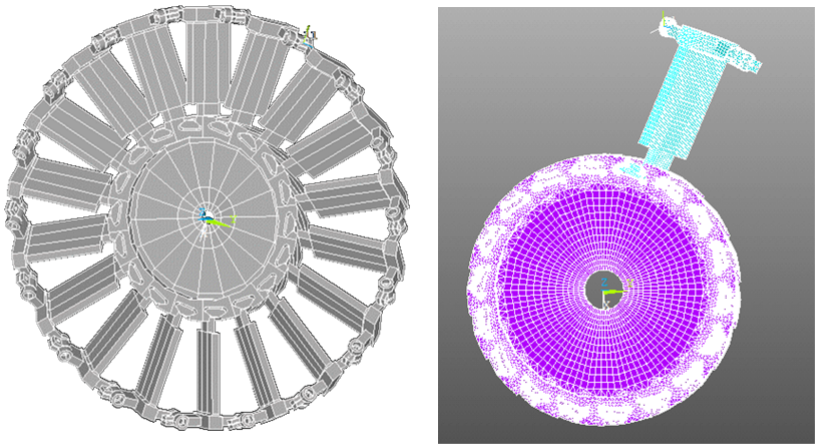

Fig. 3.6 Models of the blade disk: (a) geometric model of the full disk with all blades (b) finite element model of one blade and disk

condition. The disk has been tested constrained in the first campaign. In the second campaign, the constraint is removed and hence the disk is tested as a free component. The constraints are realized as follows in each test campaign:

1. Campaign 1: The blade suspended on flexible wires (Fig. 3.7a).
2. Campaign 1: The disk rigidly connected by six bolts to a cylindrical attachment (Fig. 3.7b).
3. Campaign 2: The same disk suspended on flexible wires (Fig. 3.7c)

Five tri-axial accelerometers are positioned on the blade and five on the disk. During each FRF measurement campaign, an instrumented hammer is used for the excitation on the locations indicated in Fig. 3.8. These number of measured DoF are deemed essential in order to observe and control the desired (interface DoF). For practical

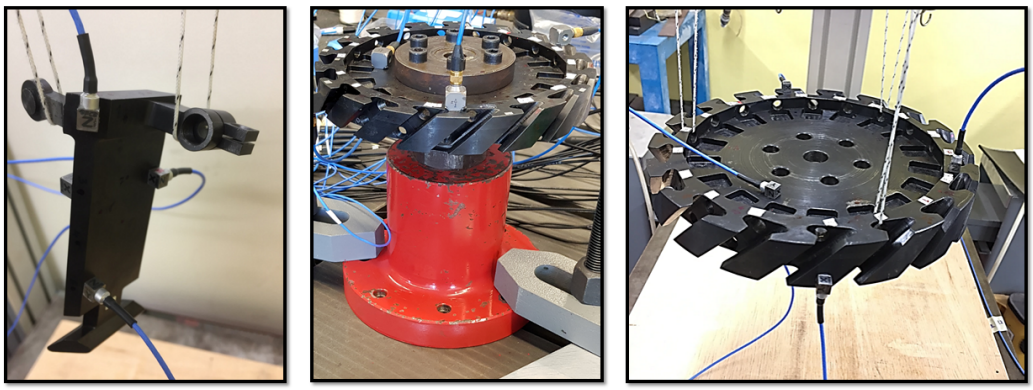

Fig. 3.7 The realized boundary conditions along with the mounted triaxial sensors (15 response channels for each component). (a) and (b) form campaign-1. (c) campaign-2: the sensor positions on the disk in campaign-1 are retained but with different sensor make and type.

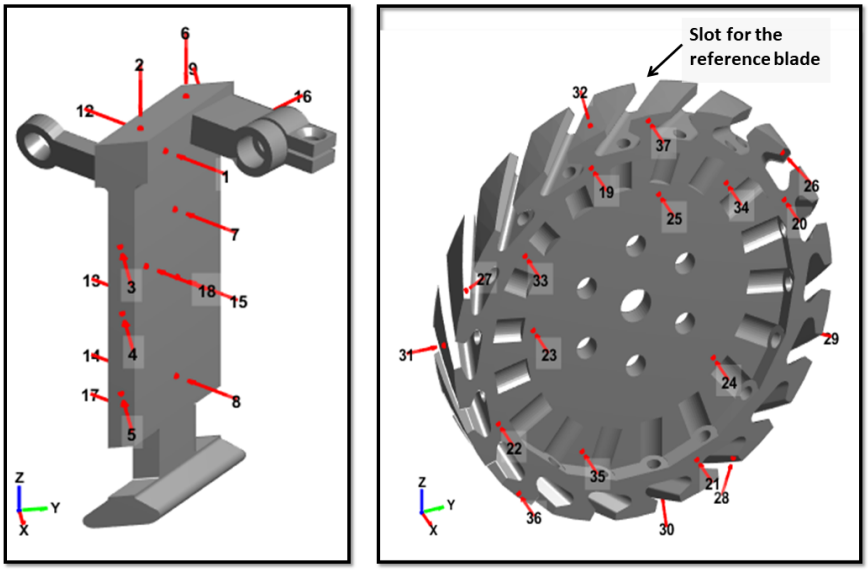

Fig. 3.8 The impact positions on the blade and the disk. 18 impacts on the blade and 19 on the disk. The impact positions do not change in the two campaigns.

experimental reasons, the impact points are never coincident with the measurement points where the accelerometers are positioned.

Recalling that SEMM needs a parent (numerical) model of each substructure, therefore, finite element (FE) models in ANSYS were created for both the blade

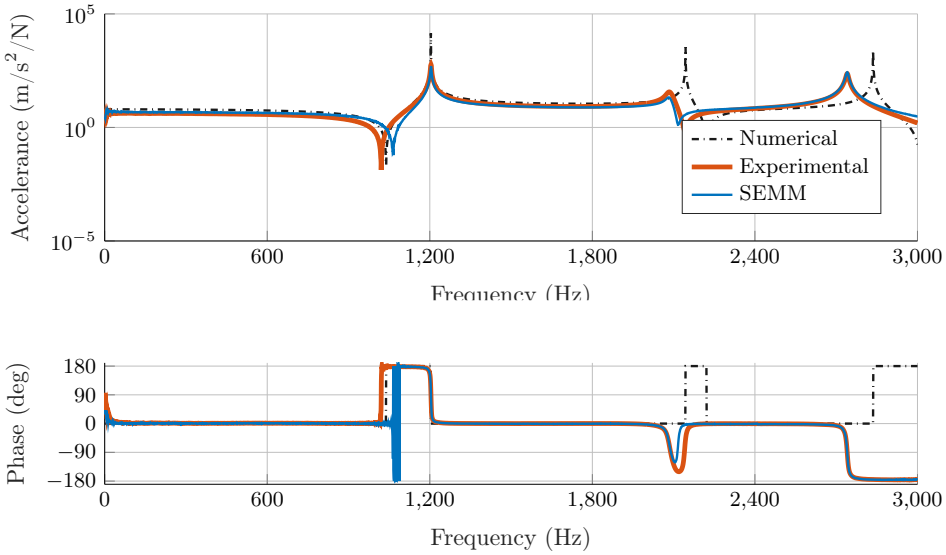

Fig. 3.9 Comparison of FRFs on the blade in campaign-1

and the disk. These FE models were then reduced by Hurty-Craig-Bampton (HCB) transformation to retain only the physical master DoF together with 200 fixed-interface eigen modes. The retained master DoF include all the internal DoF in Fig. 3.7 and Fig. 3.8 as well as the boundary DoF on the joint surfaces (as were indicated in Fig. 3.1. The parent models according to the SEMM terminology, are then obtained by computing the accelerance FRFs.

3.6 Results

This section presents the validation of the SEMM method on each substructure i.e. the blade and disk in the two campaigns. In the SEMM method, the overlay model is a set of experimental FRFs that provides the dynamics at some DoF to the parent model. Since SEMM is exact on those measured DoF, an FRF comparison on such DoF will be trivial. Therefore, for validation purpose, a group of some experimental FRFs was kept out of the overlay model as reference measurements, designated as $\mathbf{u}_o$.

3.6.1 FRF prediction by SEMM

Fig. 3.9 shows the validation of the SEMM method for the single blade by comparing numerical, experimental and the hybrid FRF generated by the SEMM method. The FRFs predicted by the SEMM model are overlapping well with the experimental ones. The numerical FRFs do not have any damping but the SEMM model captures the damping fairly well. There is one small discrepancy in the first anti-resonance which happens to be due to unavoidable human errors whilst mounting the sensors or exciting the structure.

The FRFs for the disk in the constrained condition is shown in Fig. 3.10. The FRFs predicted by the SEMM model do not match so well for the disk in the presence of many modes. This discrepancy between the numerical and experimental results can be attributed to the reasons listed below.

1. The numerical model of the disk does not take into account the masses of the accelerometers. They alter the cyclic symmetry of the disk. Furthermore, the mass of these accelerometers is greater than those mounted on the blade.
2. Most importantly, the constraints applied to the disk's FE model to fix its centre do not correspond exactly to the actual constraint condition of the disk. Actually, the disk centre is connected to a flanged type fixture which is attached rigidly to a bench, see Fig. 3.7b. The fixture introduces some of its own dynamics in the frequency band. whilst modelling the same fixture (along with the disk) in ANSYS, the displacement boundary condition is not ideally matched with the actual setup.

Remark 1. *From the modal content in Fig. 3.9, it is evident that there are only three modes in the 3000 Hz range. By using a modal parameter extraction, one can only extract three flexible modes in this range. In order to have more modes, the bandwidth would have to be increased. It was, however, tested with the available hardware that there were only two more modes before 5000 Hz, making the total of five modes whilst the power spectral density of the input signal and coherence degraded significantly. The SEREP method then would have provided an expanded model of rank 5. It would be noted in Chapter 6 (and already reported in [62]) that for the joint identification of the blade-root here required a system of more than 12 independent DoF. Thus, SEREP is not suitable in this case.*

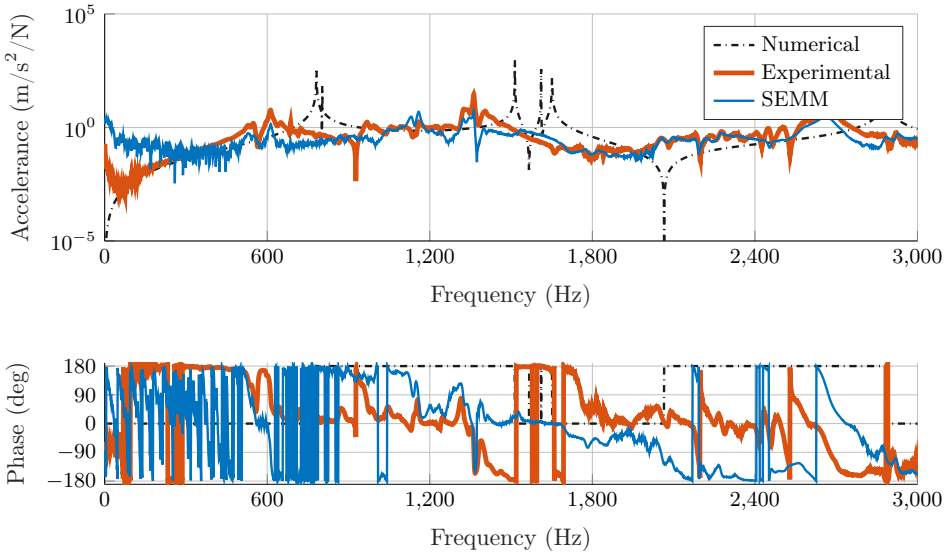

Fig. 3.10 Comparison of FRFs on the disk in campaign-1

On the disk's modal content Fig. 3.10, even though there are more modes but clearly the modal estimation would not be very accurate due to high modal content and high damping. Therefore, the SEMM expansion method is appropriate for this test-case.

The disk is then remeasured in campaign-2, as discussed above, with the constraint in the disk centre removed. The resulting FRFs are plotted in Fig. 3.11. The numerical (black dotted) FRF agrees well with the the experimental FRF already. The modelling errors caused by the constraint have been removed. The hybrid FRF obtained by SEMM predicts the resonance peaks exactly. Some differences in the anti-resonances are attributed to the unavoidable human errors in the experimentation. This expansion in the unconstrained disk FRFs is certainly more reliable than that in Fig. 3.10.

3.6.2 Condition number and singular value filtering

In the previous subsection, the FRFs predicted by SEMM were in agreement with the measured ones, justifying the use of SEMM method. Although the hybrid models are full rank, they can be ill-conditioned sometimes. Therefore, it is a good practice to

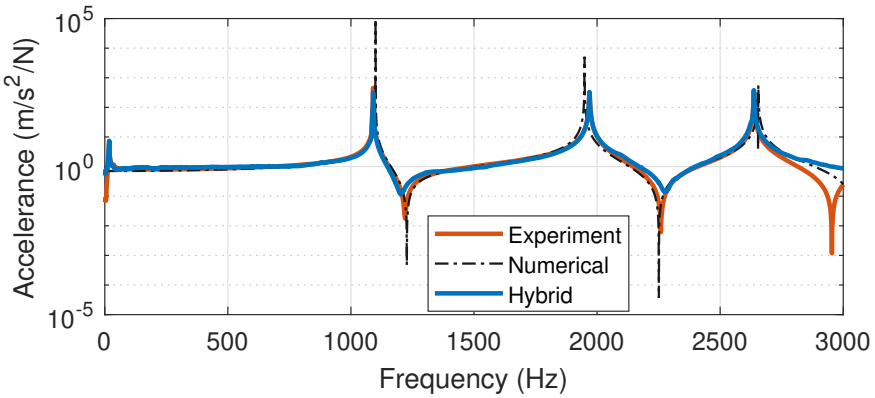

Fig. 3.11 Comparison of FRFs on the disk in campaign-2

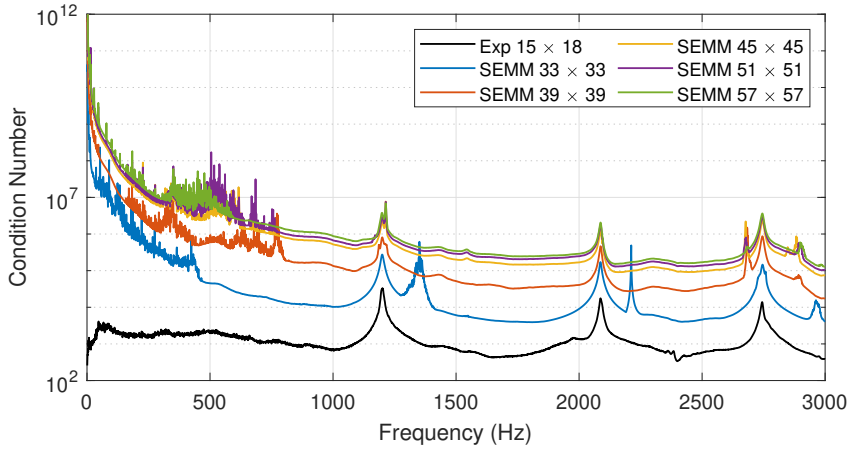

Fig. 3.12 Condition number of the blade hybrid models and the effect of number of interface DoF.

inspect those hybrid models more in detail, so that any limitations can be understood beforehand.

In this regard, we inspect the condition number of the blade's hybrid models on the frequency axis as the number of expansion DoF are increased in Fig. 3.12. Condition number is defined as the ratio of the largest to the lowest singular value. In the figure, the peaks in the experimental plot (black line) refer to the resonances where the condition number is on the order of 10^4. Note that the experimental model size is 15×18. Then the hybrid models are generated successively from the numerical models of different sizes. The first model size is 33×33. The number 33 comes from the sum of 15 response channels from five triaxial sensors and 18 excitation channels i.e. all the measured DoF are included in the numerical model

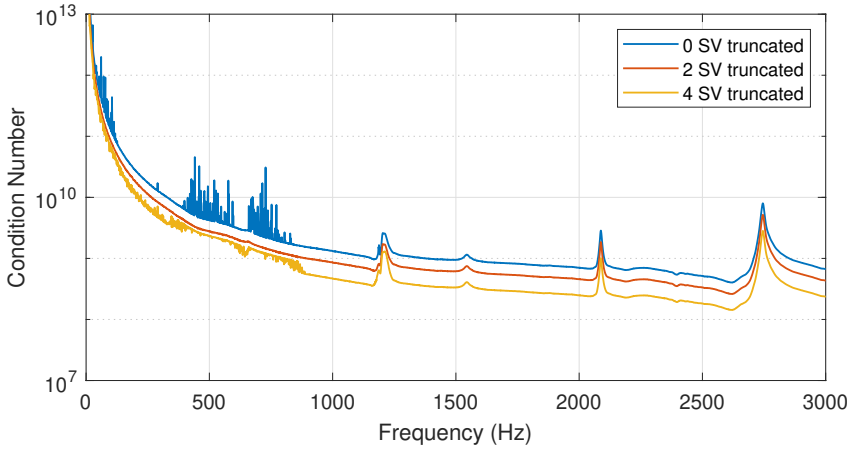

Fig. 3.13 Condition number by truncating 2 singular values successively in the blade hybrid models of size 57×57.

and expansion is performed only on these. This is nothing but an expansion of the unexcited DoF or unmeasured responses in order to have a square FRF matrix. It is seen that the condition number of this model size is higher than the experimental matrix. Then 6 interface DoF are included to make the model size 39, and so on. The result is a gradual increase of the condition number. The higher condition number implies that one may experience difficulties when the interface FRF matrix is inverted in the dynamic substructuring. Moreover, the condition number from 0–750 Hz seems to have high fluctuations which can be attributed to the lowest singular values becoming even smaller by the increased model order.

The singular value (SV) filtering can be employed in this case. By removing the smallest 2 SVs successively in Fig. 3.13, the new condition number is lower and shows that the noise was attributed to the filtered SVs. Whilst removing 02 SVs eliminates high fluctuation in 0-750 Hz band, removing 2 additional SVs introduces more fluctuations. Similarly, the disk hybrid model's condition number can also be inspected by truncating singular values in Fig. 3.14. Here, only 1 SV is truncated first which shows improvement in the 0–250 Hz band. The spurious peaks near 1800 and 2350 Hz also disappear. Note that these are not the modes. In fact, the modes are the small peaks near 1100, 1950 and 2650 Hz.

The SV truncation can serve beneficial in large models but it should be done with caution by not over filtering the meaningful dynamic content.

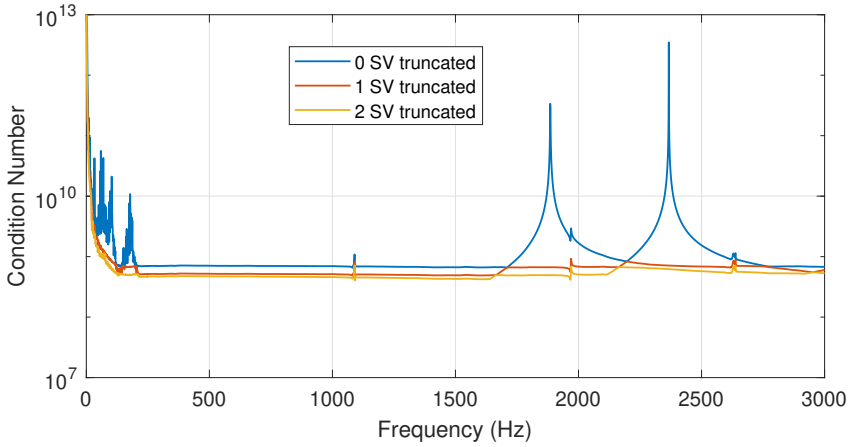

Fig. 3.14 Condition number by truncating 1 singular value successively in the disk hybrid models of size 58×58.

3.7 Summary

This chapter presents the dynamic expansion methods for those components on which only a limited number of measurements are possible, for example, the blade-root joint – the object under investigation. The techniques for reliable prediction of dynamics are discussed including model updating, CMS reduction inverse view, special purpose polynomial expansion, and round trip theory for FRFs. More popular methods SEREP and SEMM are covered in more detail with their different formulations.

The SEMM formulations are derived using the LMFBS notation. The advantages of SEMM over SEREP are also highlighted in general and in the context of the blade-root joint. The experimental setups and campaigns are introduced which will be used throughout the thesis. The results of SEMM hybrid or expanded models are presented which show promising prediction on the blade as well as the disk. The modelling errors in the disk due to constraint are isolated and it is shown that SEMM produced good agreement of FRFs throughout the frequency bandwidth without the need to calculate damping.

Other than the FRFs, the condition number of the hybrid models is also inspected. By increasing the size of the numerical model, the condition number increases which warrants the use of singular value truncation.

Chapter 4

Introducing Correlations in SEMM

Part of the work described in this chapter was previously published in [71, 119, 72].

In test-based analysis, measured and predicted quantities often need to be compared over a certain domain (modal, time, frequency). Their one-to-one visual comparison is practical only when the quantities are scalars or the system degrees-of-freedom (DoF) are small in number. Since mechanical systems can have many test or analysis DoF, it becomes difficult to draw quantitative inferences on all of them. It is, therefore, a natural human desire to make a qualitative (good or bad) as well quantitative assessment (number or percentage). For this purpose, statistical correlations are deployed to provide a quantitative measure usually between 0 and 1 describing how good or bad are the measured and predicted quantities for various DoF. Depending on the type of quantities to be assessed, one correlation metric is not enough. As a result, several correlation techniques have been (and are being) developed suitable for specific needs. Especially their use is very common in model updating [120, 79] as well as in expansion methods.

4.1 Overview of correlation methods

Due to the popularity of the modal methods, the first application of correlating measured and numerical mode shapes was by Allemang and Brown [121]. The so-called Modal Assurance Criteria (MAC) is used as a key correlation since 1982.

It return a value between 1 and 0 for j^{th} and k^{th} mode by:

$$MAC_{jk} = \frac{|\psi_j^{\mathrm{E}^*}\ \psi_k^{\mathrm{N}}|^2}{\psi_j^{\mathrm{E}^*}\ \psi_j^{\mathrm{E}}\ \ \psi_k^{\mathrm{N}^*}\ \psi_k^{\mathrm{N}}} \tag{4.1}$$

where ψ^{E} and ψ^{N} are experimental and numerical mode shapes and $(\star)^*$ represents complex conjugate transpose if the modes are complex. The unity values indicate a good similarity between the two mode shapes. *MAC* is usually biased towards those coordinates which have higher values and thus the contribution of small valued coordinates is not properly accounted. Therefore, another metric known as Co-Ordinate MAC (COMAC) was introduced by Lievens and Ewins [122] to find similarity among the DoF. COMAC for the i^{th} DoF is defined as:

$$COMAC_i = \frac{\left[\sum_{j=1}^{n} |\psi_{ij}^{\mathrm{E}}\ \psi_{ij}^{\mathrm{N}}|\right]^2}{\sum_{j=1}^{n}(\psi_{ij}^{\mathrm{E}})^2\ \ \sum_{j=1}^{n}(\psi_{ij}^{\mathrm{N}})^2} \tag{4.2}$$

where ψ_{ij} is a modal coefficient corresponding to DoF i and modal coordinate j with $j = 1, \ldots, n$ modes. Since normal modes also have a property of orthogonality (mass-orthogonality), it is good to make this check between measured ψ^{E} and numerical ψ^{N} modes or modal matrices. Based on the orthogonality, Pseudo Orthogonality Check (POC) is quite common among various other correlations [123]. POC is simply:

$$POC = \psi^{\mathrm{E}}\,\mathbf{M}\,\psi^{\mathrm{N}} \tag{4.3}$$

where $\mathbf{M}$ is the mass matrix. The result should be a matrix with ones on the diagonal and zeros elsewhere to indicate the mass orthogonality. Similarly, stiffness matrix $\mathbf{K}$ can be used to check whether or not it reduces to natural frequencies on the diagonal. One can list many modal correlation metrics. The reader may refer to Ewins [124] for their detailed review.

Another class of correlations exists for frequency response functions. In contrast to the modal correlations, there is another dimension of the problem i.e. frequency. Therefore, correlations in frequency domain can be divided in two categories: i) those which correlate each FRF belonging to DoF i, j over a given frequency range [125, 126] and ii) those which correlate overall shape of the FRF matrix (or a row or column) at each frequency line [120, 124, 127].

In the first category are Frequency Response Assurance Criterion *FRAC* defined by:

$$FRAC_{ij} = \frac{|\mathbf{Y}^{\mathrm{S}}_{ij}(\omega)\ \mathbf{Y}^{\mathrm{exp}^*}_{ij}(\omega)|^2}{\mathbf{Y}^{\mathrm{S}}_{ij}(\omega)\ \mathbf{Y}^{\mathrm{S}*}_{ij}(\omega).\ \mathbf{Y}^{\mathrm{exp}}_{ij}(\omega)\ \mathbf{Y}^{\mathrm{exp}*}_{ij}(\omega)} \tag{4.4}$$

where $\mathbf{Y}^{\mathrm{S}}_{ij}(\omega)$ and $\mathbf{Y}^{\mathrm{exp}}_{ij}(\omega) \in \mathbb{C}^{n_\omega \times 1}$ are predicted (by SEMM, see Chapter 3) and experimental FRF measured over DoF i and excited at DoF j. n_ω is number of spectral points and $(\star)^*$ represents the complex conjugate transpose. A strong correlation is indicated by 1 whilst a no correlation is indicated by 0. $FRAC_{ij}$ is a COMAC-like correlation [122] since it takes into account the coordinate information. For differently scaled FRFs, *FRAC* can be similar. Therefore, a variant of the above Frequency Amplitude Assurance Criterion *FAAC* to correlate amplitudes.

$$FAAC_{ij} = \frac{2|\mathbf{Y}^{\mathrm{S}}_{ij}(\omega)\ \mathbf{Y}^{\mathrm{exp}^*}_{ij}(\omega)|}{\mathbf{Y}^{\mathrm{S}}_{ij}(\omega)\ \mathbf{Y}^{\mathrm{S}*}_{ij}(\omega) + \mathbf{Y}^{\mathrm{exp}}_{ij}(\omega)\ \mathbf{Y}^{\mathrm{exp}*}_{ij}(\omega)} \tag{4.5}$$

In the second category are Frequency Domain Assurance Criterion *FDAC* [128], Global Shape Criterion *GSC* and Global Amplitude Criterion *GAC* [120]. *FDAC* takes into account the frequency shift between predicted and measured FRFs normally encountered in model updating. It is defined as:

$$FDAC(\omega_s, \omega_e) = \frac{|\mathbf{y}^{\mathrm{S}^*}_j(\omega_s)\ \mathbf{y}^{\mathrm{exp}}_j(\omega_e)|^*\ |\mathbf{y}^{\mathrm{S}^*}_j(\omega_s)\ \mathbf{y}^{\mathrm{exp}}_j(\omega_e)|}{\mathbf{y}^{\mathrm{S}^*}_j(\omega_s)\mathbf{y}^{\mathrm{S}}_j(\omega_s)\ \mathbf{y}^{\mathrm{exp}*}_j(\omega_e)\mathbf{y}^{\mathrm{exp}}_j(\omega_e)} \tag{4.6}$$

where $\mathbf{y}^{\mathrm{S}}_j \in \mathbb{C}^{m\times 1}$ is a vector of predicted responses excited at j^{th} DoF with the fixed frequency ω_s and $\mathbf{y}^{\mathrm{exp}}_j \in \mathbb{C}^{m\times 1}$ is a vector of measured responses excited at the same DoF j with the fixed frequency of ω_e, and m are the number of responses. This allows to compare FRFs at two different frequencies assuming that they are shifted. In this way, one correlates the shapes of two distinct frequencies. With a slight modification in the numerator of Eq. (4.6) and using the same frequency $\omega = \omega_s = \omega_e$, one calculates *GSC* and *GAC*.

$$GSC = \frac{|\mathbf{y}^{\mathrm{S}^*}_j(\omega)\ \mathbf{y}^{\mathrm{exp}}_j(\omega)|^2}{\mathbf{y}^{\mathrm{S}^*}_j(\omega)\mathbf{y}^{\mathrm{S}}_j(\omega)\ \mathbf{y}^{\mathrm{exp}*}_j(\omega)\mathbf{y}^{\mathrm{exp}}_j(\omega)} \tag{4.7}$$

$$GAC = \frac{2|\mathbf{y}_j^{S*}(\omega)\ \mathbf{y}_j^{exp}(\omega)|}{\mathbf{y}_j^{S*}(\omega)\mathbf{y}_j^{S}(\omega) + \mathbf{y}_j^{exp*}(\omega)\mathbf{y}_j^{exp}(\omega)} \tag{4.8}$$

These two measures allow one to correlate shape and amplitudes of FRFs excited at DoF j and visualize them at all the frequencies ω.

In the decade of 1990, correlations development was on boom. Since then, numerous applications have used them to update their models or test the truthfulness of the prediction methods. Of course, there are more variations than the listed correlations for which one can refer to [120, 127, 129, 79] for more insights. Still some developments on correlations are in progress. More important is that how one obtains the vectors or matrices that need to be correlated. Two very recent papers are by Chen et al. [130] and Kodric et al. [105] which propose similar strategies to find out inconsistent data or measurements. These two studies also have similarities with the method developed herein and called *Correlated SEMM*. This is discussed next by introducing correlations in the SEMM method in order to filter out bad or poor quality measurements.

4.2 Correlations in SEMM

In the previous chapter, a structure's hybrid model by the SEMM methodology was obtained which essentially is a coupling of its overlay (experimental) and numerical models. The hybrid model can be significantly affected by the discrepancies between the measurements and numerical model. For instance, the location of sensors on the actual structure and the corresponding DoF in its numerical model may not be exactly coincident, thereby, introducing some variations in the respective FRFs. The same holds for the impact positions and directions. In addition to this, unavoidable noise in the measured FRFs also transmits to the hybrid model. Moreover, the numerical model due to its discretization type, material properties and boundary conditions will always have some differences from its experimental counterpart. It is, therefore, of paramount importance to identify the best set of measurements that represent the overall system dynamics while filtering out the ones that do not correlate well with the system.

We introduced a technique of checking the correlation between the FRFs in a systematic way in the SEMM procedure. This new approach, called *correlated*

SEMM, is a-posteriori (offline) analysis i.e. after doing an experimental campaign and making necessary checks of the data quality by coherence or visual or other means provided in the data acquisition system. Since the online checks are limited, some measurements can be more corrupted or uncorrelated than others. When all these measurements are used to generate a hybrid model, the expansion may be erroneous. By the new correlated approach, the aim is to improve the quality of the substructure hybrid models as much as possible before a subsequent coupled structure model is created (see Chapter 5 to 7). In this work, we used *FRAC* to quantify the discrepancies between the FRFs of the two models in a convenient way. In particular, the correlation of FRFs is computed between hybrid model (instead of the numerical model) and the FRFs from measurements kept only for validation and not included in the hybrid model. The FRAC from Eq. (4.6) is redefined in a function notation:

$$\phi_{ij} \triangleq FRAC\big(\mathbf{Y}^{\mathrm{S}}_{ij}(\omega), \mathbf{Y}^{\mathrm{exp}}_{ij}(\omega)\big) = \frac{|\mathbf{Y}^{\mathrm{S}}_{ij}(\omega)\ \mathbf{Y}^{\mathrm{exp}*}_{ij}(\omega)|^2}{\mathbf{Y}^{\mathrm{S}}_{ij}(\omega)\ \mathbf{Y}^{\mathrm{S}*}_{ij}(\omega).\ \mathbf{Y}^{\mathrm{exp}}_{ij}(\omega)\ \mathbf{Y}^{\mathrm{exp}*}_{ij}(\omega)} \tag{4.9}$$

Before embarking on the correlation strategy, let us elaborate the experimental model that contains transfer functions on all the measurable DoF $\mathbf{u}^{\mathrm{exp}}$ and $\mathbf{f}^{\mathrm{exp}}$ as follows:

$$\mathbf{u}^{\mathrm{exp}} = \mathbf{Y}^{\mathrm{exp}}\mathbf{f}^{\mathrm{exp}} \quad \Longrightarrow \quad \begin{Bmatrix}\mathbf{u}_c\\ \mathbf{u}_e\end{Bmatrix}^{\mathrm{exp}} = \begin{bmatrix}\mathbf{Y}_{ce} & \mathbf{Y}_{cw}\\ \mathbf{Y}_{ve} & \mathbf{Y}_{vw}\end{bmatrix}^{\mathrm{exp}} \begin{Bmatrix}\mathbf{f}_e\\ \mathbf{f}_w\end{Bmatrix}^{\mathrm{exp}} \tag{4.10}$$

The different subscripts were shown in Fig. 3.1 and explained in the following:

- c: set of DoF where responses are measured by triaxial accelerometers (or by other sensor types)
- e: set of DoF where excitations are applied by a modal impact hammer
- v: set of DoF where responses are measured as $\mathbf{u}_c$ but reserved for validation.
- w: set of DoF where excitations are applied as $\mathbf{f}_e$ but reserved for validation.

$\mathbf{Y}^{\mathrm{exp}}$ may, in general, contain point or transfer FRFs. For more practical reasons, the point FRFs are not measured and so $\mathbf{Y}^{\mathrm{exp}}$ is rectangular of size $m \times n$. From

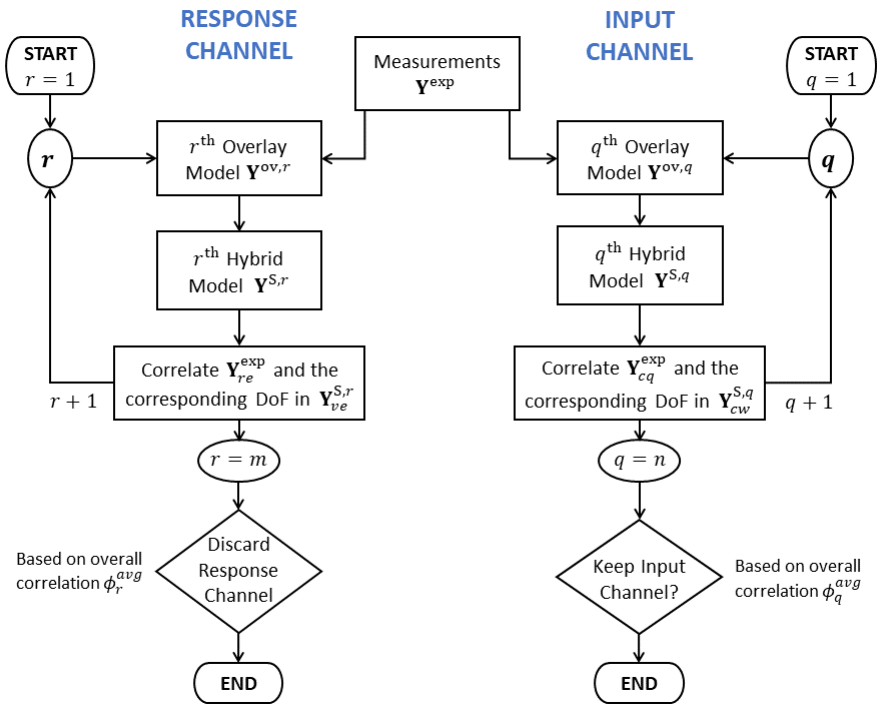

Fig. 4.1 The process flow of the method to identify the uncorrelated response and input channels.

$\mathbf{Y}^{exp}$, different subsets called overlay models $\mathbf{Y}^{ov}$, are created to generate the hybrid models by the SEMM method. The process is explained in detail below and shown in Fig. 4.1:

1. Define an overlay model such that one response channel (a row $\mathbf{Y}_{re}^{exp}$) from $\mathbf{Y}^{exp}$ is excluded in the overlay model to be kept for validation, i.e.

$$\mathbf{Y}^{ov,r} \subset \mathbf{Y}^{exp} : \mathbf{Y}_{re}^{exp} \notin \mathbf{Y}^{ov,r} \tag{4.11}$$

   where $r = 1, 2, ..., m$. Since one channel has been excluded, the size of $\mathbf{Y}^{ov,r}$ is $(m-1) \times n$. The channel $\mathbf{Y}_{re}^{exp}$ is now considered as the moving validation channel (MVC) and is graphically shown in the upper left part of Fig. 4.2a.

2. Perform expansion by the SEMM method with $\mathbf{Y}^{ov,r}$ as per Eq. (3.29) to get $\mathbf{Y}^{S,r}$, i.e. $\mathbf{Y}^{S,r} = semm(\mathbf{Y}^{N}, \mathbf{Y}^{ov,r})$.

3. The corresponding r^{th} expanded channel $\mathbf{Y}_{ve}^{S,r}$ is correlated with $\mathbf{Y}_{re}^{exp}$ (see Fig. 4.2a) by computing FRAC, as per Eq. (4.9). FRAC is computed over a

Table 4.1 Summarized action steps to generate overlay and hybrid models in order to find correlations among all DoF or channels (both response and input). The dimension of the overlay matrix is different for response or input channels correlations. Note that $size(\mathbf{Y}^{\text{exp}}) = m \times n$.

Action	**Response Channel**	**Input Channel**
Define overlay models	$\mathbf{Y}^{\text{ov},r} \subset \mathbf{Y}^{\text{exp}} : \mathbf{Y}^{\text{exp}}_{re} \notin \mathbf{Y}^{\text{ov},r}$ for $r = 1,2,\ldots,m$ $size(\mathbf{Y}^{\text{ov},r}) = (m-1) \times n$	$\mathbf{Y}^{\text{ov},q} \subset \mathbf{Y}^{\text{exp}} : \mathbf{Y}^{\text{exp}}_{cq} \notin \mathbf{Y}^{\text{ov},q}$ for $q = 1,2,\ldots,n$ $size(\mathbf{Y}^{\text{ov},q}) = m \times (n-1)$
Generate hybrid models	$\mathbf{Y}^{\text{S},r} = semm(\mathbf{Y}^{\text{N}}, \mathbf{Y}^{\text{ov},r})$	$\mathbf{Y}^{\text{S},q} = semm(\mathbf{Y}^{\text{N}}, \mathbf{Y}^{\text{ov},q})$
Compute correlations	$\phi_{re} = FRAC(\mathbf{Y}^{\text{S},r}_{ve}, \mathbf{Y}^{\text{exp}}_{re})$ $\phi^{avg}_r = \frac{1}{n}\sum_{j=1}^{n} \phi_{rj}$	$\phi_{cq} = FRAC(\mathbf{Y}^{\text{S},q}_{cw}, \mathbf{Y}^{\text{exp}}_{cq})$ $\phi^{avg}_q = \frac{1}{m}\sum_{i=1}^{m} \phi_{iq}$
Plot and decide	$r = \{1,\ldots m\}$ vs ϕ^{avg}_r	$q = \{1,\ldots n\}$ vs ϕ^{avg}_q

fixed frequency band in Eq. (4.9) for two given FRFs. However, the explicit dependence of the FRFs on frequency ω is not shown for the sake of clarity in the above expressions. The FRAC, thus computed for the pairs of FRFs in $\mathbf{Y}^{S,r}_{ve}$ and $\mathbf{Y}^{\text{exp}}_{re}$ are denoted by ϕ_{re} and used for calculating ϕ^{avg}_r as follows:

$$\phi^{\text{avg}}_r = \frac{1}{n}\sum_{j=1}^{n} \phi_{rj} \tag{4.12}$$

The parameter in Eq. (4.12) can be considered an indication of an overall correlation level of the response channel r.

4. The process is repeated for all the remaining channels up to $r = m$, i.e. each time one channel r in $\mathbf{Y}^{\text{exp}}$ is excluded from the r^{th} overlay model.

5. The low correlated *response channels* are identified based on the average correlation in Eq. (4.12).

In a similar way, by successively excluding the columns from the overlay model, the respective correlations can be computed for the input channels. Fig. 4.2b illustrates the procedure by excluding q^{th} column from $\mathbf{Y}^{\text{exp}}$. The two schemes of computing correlations are listed side by side in Table 4.1 and depicted in Fig. 4.1 for further clarity.

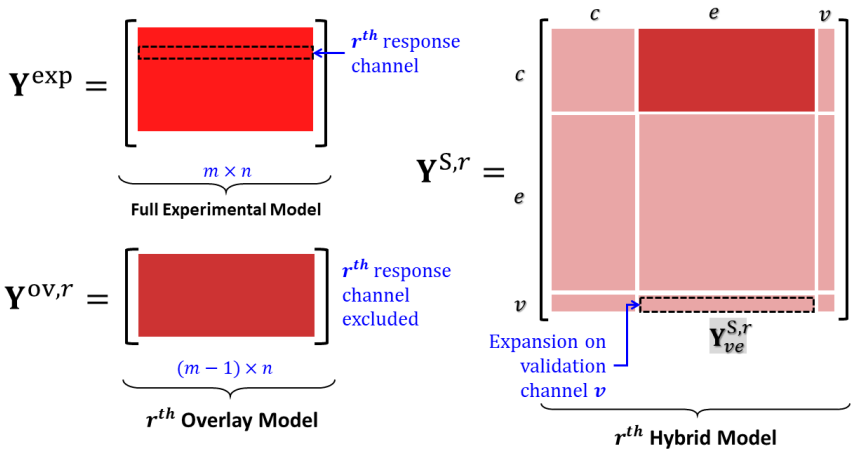

(a) The overlay model $\mathbf{Y}^{\text{ov},r}$ is short of the r^{th} response channel (row) in experimental model $\mathbf{Y}^{\text{exp}}$. In the respective r^{th} hybrid model $\mathbf{Y}^{\text{S},r}$, the correlation is calculated between $\mathbf{Y}^{\text{S},r}_{ve}, \mathbf{Y}^{\text{exp}}_{re}$. For simplicity, the DoF set in $\mathbf{Y}^{\text{S},r}$ consists of only $g = \{c, e, v\}$.

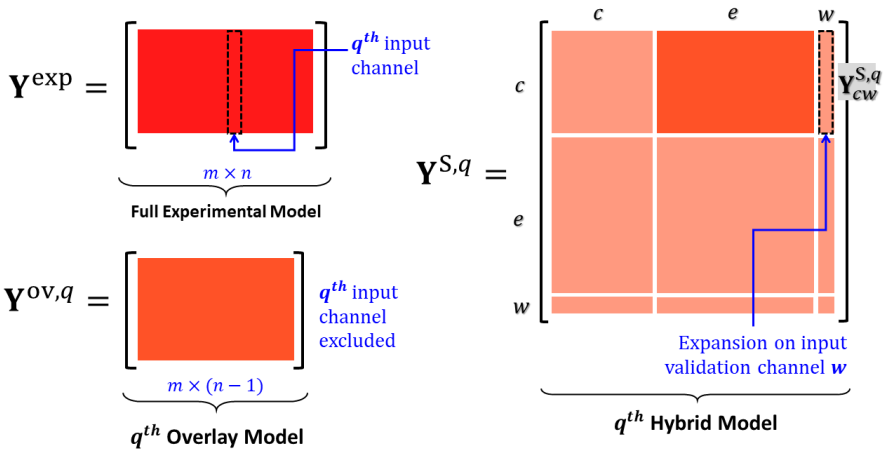

(b) The overlay model $\mathbf{Y}^{\text{ov},q}$ is short of the q^{th} input channel (column) in experimental model $\mathbf{Y}^{\text{exp}}$. In the respective q^{th} hybrid model $\mathbf{Y}^{\text{S},q}$, the correlation is calculated between $\mathbf{Y}^{\text{S},q}_{cw}, \mathbf{Y}^{\text{exp}}_{cq}$. For simplicity, the DoF set in $\mathbf{Y}^{\text{S},r}$ consists of only $g = \{c, e, w\}$.

Fig. 4.2 Illustration of the different models used to find correlated or uncorrelated response channels and input channels. The DoF set in the hybrid models $\mathbf{Y}^{\text{S}}$ are shown only for the internal DoF. Note the difference in the DoF structure in the top and bottom figure. The colour of $\mathbf{Y}^{\text{exp}}$ is the same in both figures to signify that $\mathbf{Y}^{\text{ov},r}$ and $\mathbf{Y}^{\text{ov},q}$ are its subsets. The same colour appearance of the overlay model in the respective hybrid model shows the mimicking behaviour of those DoF.

4.2.1 Physical interpretation

The correlation analysis can be interpreted physically from the observability and controllability perspective. At the step r, when r^{th} channel is excluded from the construction of the hybrid model, there are $m-1$ response channels which try to observe the r^{th} channel through the SEMM expansion. FRAC as a correlation provides a measure or degree of observability. By repeating the process until $r = m$, each response channel has undergone an observability check (performance review) by the rest of the channels in terms of FRAC. Computing the overall performance, for example, by averaged FRAC values in Eq. (4.12), the best or least observed channels can be identified. A similar interpretation holds also for the input channels from the controllability perspective. In short, excluding the input channel q, how well $n-1$ input channels could control the q^{th} input channel.

4.2.2 Criteria for channel filtering

If one or more channels have low correlation at the end of the process, the following could be the probable reasons:

1. the DoF associated with the channel(s) did not have significant dynamic contribution in the selected frequency band. Thus, they could not be fully observed or controlled by the other measured channels.

2. the location of sensors or impacts and the corresponding DoF in the numerical model were not coincident.

Different criteria can be assumed to select the channels to keep after the FRAC analysis. A minimum threshold value criterion would imply that all the channels with a correlation level below the threshold will be disregarded. This could lead to missing the sufficient number of independent measurement channels necessary for an onward analysis. For this reason, it was chosen to define a minimum number z required for the joint identification Chapter 7. In this way, only the z channels with the highest correlation levels are kept, all the other channels are discarded.

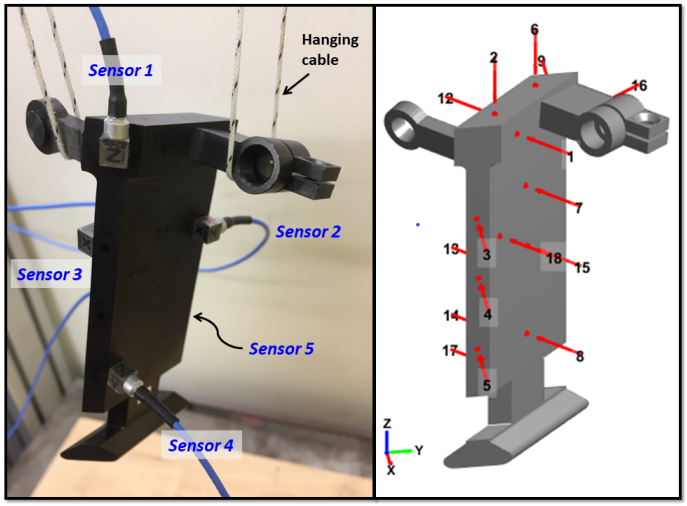

Fig. 4.3 Experimental setup for impact testing of the blade. Reproduced from chapter 3.

4.2.3 Method's applicability

The method *correlated SEMM* may appear to be restricted to applications relating to expansion by the SEMM method only. However, the framework outlined above can be used to filter out bad measurements in any linear FRF measurement campaign which can be encountered often times. The SEMM then provides only a means to calculate the FRF correlations assuming that a viable numerical model of the component is available.

4.3 Results

In order to find the correlations of hybrid models by the above-mentioned method, two structural components are considered: i) blade and ii) disk. The blade tests are conducted in a constraint-free condition. The disk tests are conducted in two configurations: constraint-free and constrained configuration for a detailed analysis on the method's sensitivity to numerical model, experimental FRFs as well as to the sensor intrusiveness effect.

Table 4.2 Details of numerical and experimental parameters of the blade and disk tested in constraint free conditions. Note a missing channel in the response channel labels. This channel had unusual high noise floor and was not included in the correlation analysis. The channels with the lowest average FRAC levels are also listed after the correlation analysis.

Type	**Description**	**Blade** A	**Free disk** B
Experimental Setup	Number of accelerometers	5	5
	Number of available response channels	15	15
	Number of useful response channels (m)	14	14
	Labels for response channels	{1-8, 10-15}	{16-23, 25-30}
	Number of input channels (n)	18	19
	Labels for input channels	{1–18}	{19–37}
Numerical Modelling	Young's Modulus (GPa)	190	178
	Density (kg/m^3)	7800	7800
	Fixed interface modes	200	200
Correlation Analysis	Poorly correlated response channels	ch # 4	ch # 27
	Poorly correlated input channels	ch # 4, 17	ch # 30, 31

4.3.1 Correlation analysis of the blade

The sensors as per the actual mounting on the blade and the impacts as per the experiment design are as shown in Fig. 4.3. The sensors are triaxial accelerometers and the excitations are made with a modal impact hammer. The details about the sensors and channels are given in Table 4.2. The free constraint is realized by suspending the blade on flexible wires with their modes far below the first mode of the blade. From these measurements, the accelerance FRFs of the blade A are collected in $\mathbf{Y}^{\text{exp},A}$.

Numerical modelling consisted in creating corresponding FE models from the solid geometries. The discretization was done with Solid elements in ANSYS and with the material properties listed in Table 4.2. The FE models were then reduced by Hurty-Craig-Bampton [13] method by retaining only the essential nodes and fixed interface modal amplitudes. The retained DoF corresponded to the nodes of sensors, impacts and the interface. From the reduced systems, accelerance FRFs are computed and stored in $\mathbf{Y}^{\text{N},A}$.

The blade's overlay models are generated from the measured FRFs $\mathbf{Y}^{\text{exp},A}$ of size 14×18 (Table 4.2). In order to compute correlations for the response channels, 14 overlay models are taken as subsets where each model corresponds to the exclusion of r^{th} response channel. The expansion in each hybrid model is checked by computing the FRAC. Since FRAC is computed between two FRFs over the frequency range of

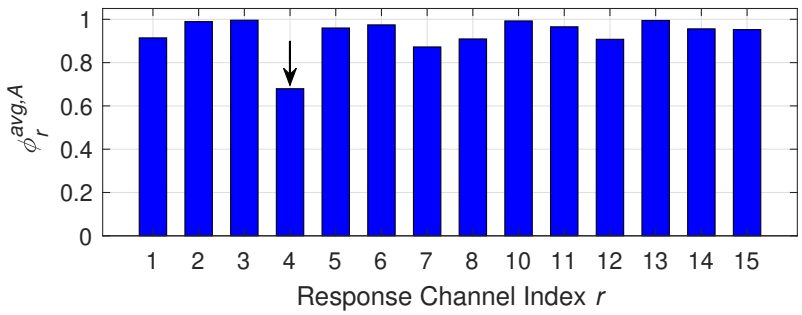

(a)

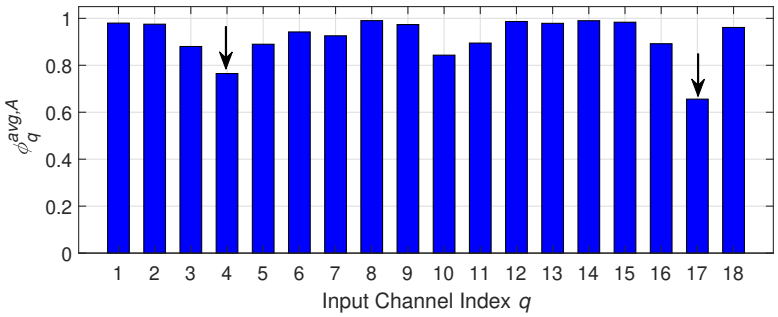

(b)

Fig. 4.4 Average FRAC of the blade A against response channels and (b) input channels. The channels which are removed from measurements based on the lowest FRAC are indicated with arrows.

1 – 3000 Hz, the average FRAC is then plotted against all the 14 response channels in Fig. 4.4a. It can be seen that overall correlation levels are higher than 0.80 except for $r = 4$. This means that this channel or DoF could not be *well-observed* by the other channels, when this was removed from $\mathbf{Y}^{\mathrm{ov},A}$. Following the same method for the input channels by skipping the q^{th} column in $\mathbf{Y}^{\mathrm{exp},A}$ to generate q^{th} overlay and hybrid models, the average FRAC values are plotted as bars in Fig. 4.4b versus the input channels. The correlations are again good for many input channels with the exception of $q = 4$ and $q = 17$ marked with two arrows.

If the channels or DoF with low correlations are retained in the measurements and the standard SEMM method is applied, some of the resulting FRFs may have some inconsistencies. In the standard SEMM, all the measured FRFs (except the validation) are included in the overlay model such that $\mathbf{Y}^{\mathrm{ov},A} = \mathbf{Y}_{ce}^{\mathrm{exp},A}$. In Fig. 4.5, for the sake of validation, an FRF by standard SEMM (thin solid line) is compared with a corresponding experimental FRF (called Reference) and for this reason not included in the construction of $\mathbf{Y}^{\mathrm{S},A}$.

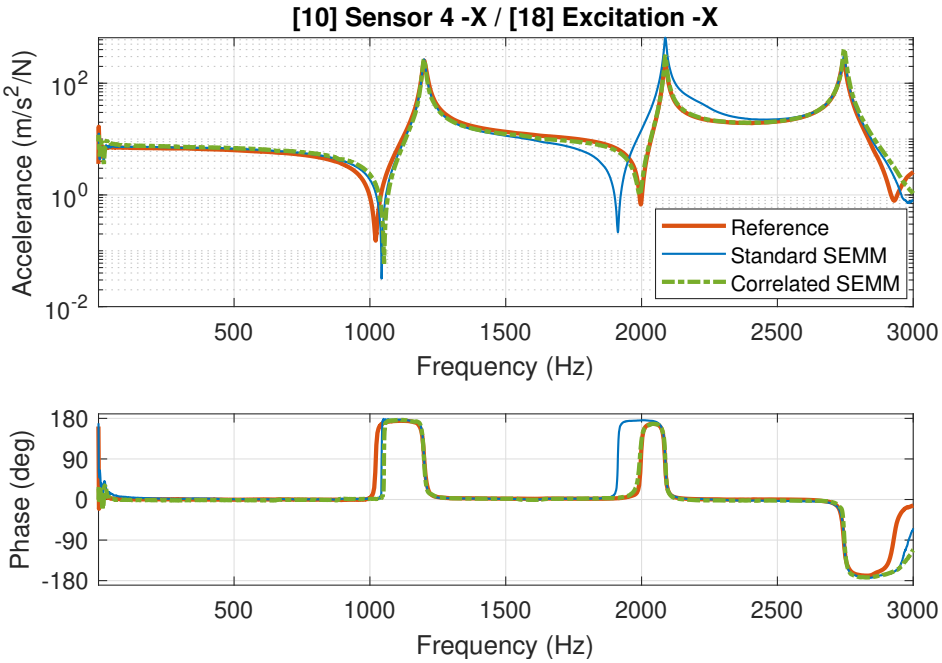

Fig. 4.5 FRFs of the blade with standard SEMM and correlation based SEMM when the lowest correlated channels marked with arrows in Fig. 4.4 are removed from the measurements. The reference FRF is $\mathbf{Y}^{\text{exp},A}_{10,18}$ with description shown at the top of the FRF.

At the first glance, the standard SEMM method $\mathbf{Y}^{\text{S},A}$ expands the dynamics really well in most of the frequency band. This is because experimental and numerical FRF models are quite close. However, comparing the standard SEMM and reference curves, some inconsistencies are visible especially around $1700-2200$ Hz. In the same figure, it is plotted as dash-dotted line the FRF (labelled: 'Correlated SEMM') obtained from SEMM after filtering out the lowest correlated channels $r=4$, $q=4$ and $q=17$. These channels have been filtered according to the criterion adopted in Section 4.2.1. It can be noticed that this FRF obtained by new correlated hybrid model $\hat{\mathbf{Y}}^{\text{S},A}$ agrees extremely well with the reference FRF both in amplitude and phase (Fig. 4.5). From an a-posteriori check on the measurements of each channel, it came out that the channels discarded by FRAC were not good for different reasons. In detail:

- channel $r=4$ had very low response levels in the shown frequency bandwidth and was, therefore, prone to be easily polluted with noise
- input channels $q=4$ and $q=17$ did not produce good FRF due to human errors in the impact direction or location.

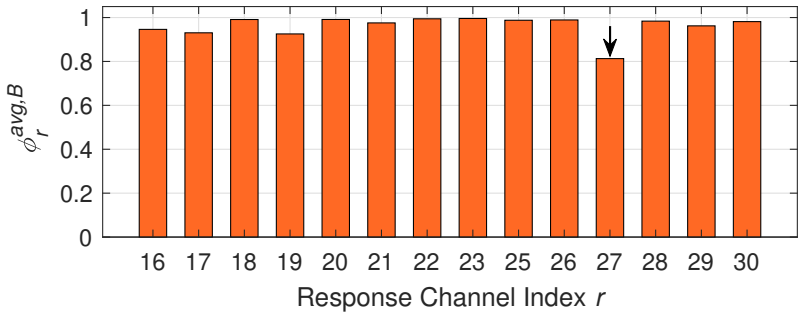

(a)

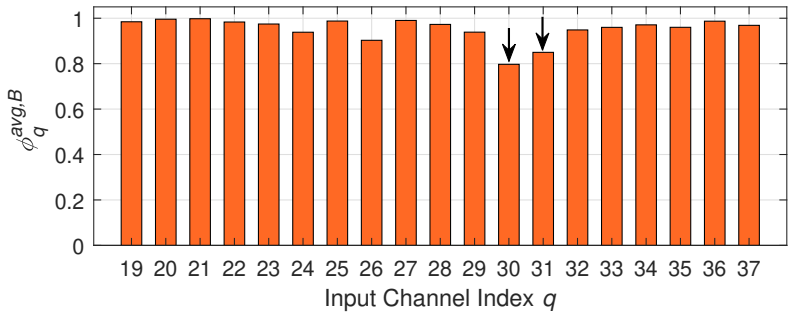

(b)

Fig. 4.6 Average FRAC of the disk B against response channels and (b) input channels. The channels which are removed from measurements based on the lowest FRAC are indicated with arrows.

4.3.2 Correlation analysis of the free disk

After the blade's analysis, the free disk's correlations are calculated. Note this configuration of the disk was discussed as campaign-2 in Section 3.5 and depicted in Fig. 3.7. Its specific modelling and channel details for the correlation analysis are listed in Table 4.2 alongside the blade.

The disk's FRAC bar graphs similar to that of the blade are shown in Fig. 4.6 both for the response channels and input channels. One response channel with label $r = 27$ and two input channels with label $q = 30$ and $q = 31$ are found to be the least correlated. By filtering these channels from the experimental (and the overlay) model and regenerating the hybrid model of the disk, the filtering effect is seen in Fig. 4.7. From the figure, it is evident that the standard SEMM using all the measurements produce an FRF that does not overlap with the reference FRF around the first antiresonance from 1200 to 1800 Hz. On the contrary, a remarkably

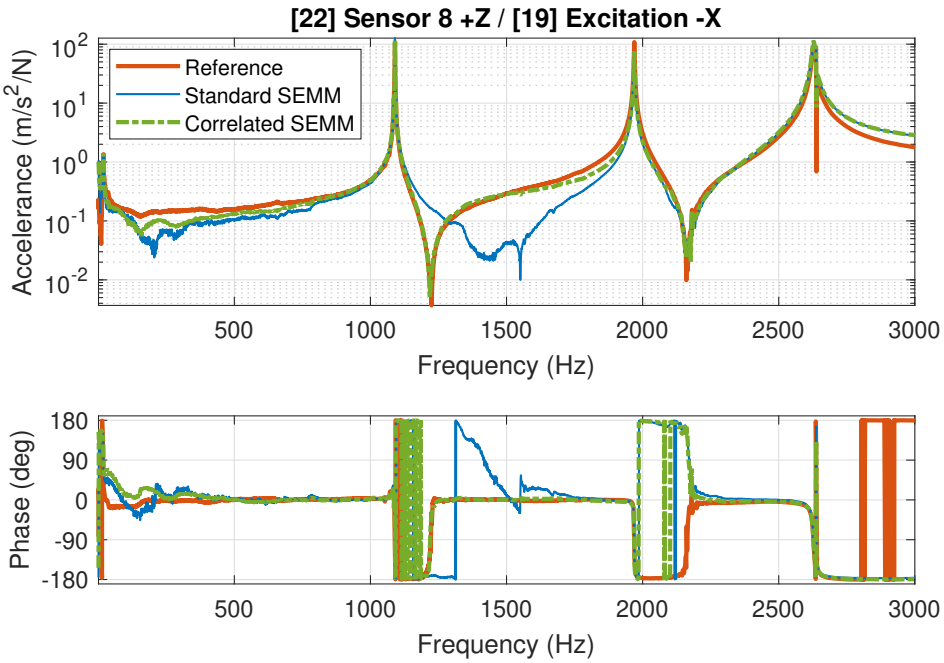

Fig. 4.7 FRFs of the disk with standard SEMM and correlation based SEMM when the lowest correlated channels marked with arrows in Fig. 4.6 are removed from the measurements. The reference FRF is $\mathbf{Y}^{\text{exp},A}_{22,19}$ with description shown at the top of the FRF.

improved FRF is obtained with the correlated SEMM in both the amplitude and phase. It can also be noticed that prediction also improves slightly in 0–700 Hz.

4.3.3 Correlation analysis of the fixed disk

In this subsection, the same correlated SEMM method is applied to the fixed disk component shown in Fig. 4.8. The aim of this investigation is to apply the correlated SEMM method to a more complicated test structure whose numerical modelling is often difficult. The disk is constrained to the test-bench in the centre by means of a bolted joint. The primary reason for choosing the constrained disk is that it is always difficult to model the boundary conditions correctly and this will be illustrated by a great difference between purely numerical FRFs and the measured FRF.

A typical experimental response is shown in Fig. 4.9 (orange curve). It is possible to see how the response is definitively more complex than the one obtained for the blade since the level of modal density is high for a wide frequency bandwidth. Moreover, the support in the middle of the disk is greatly affecting the overall

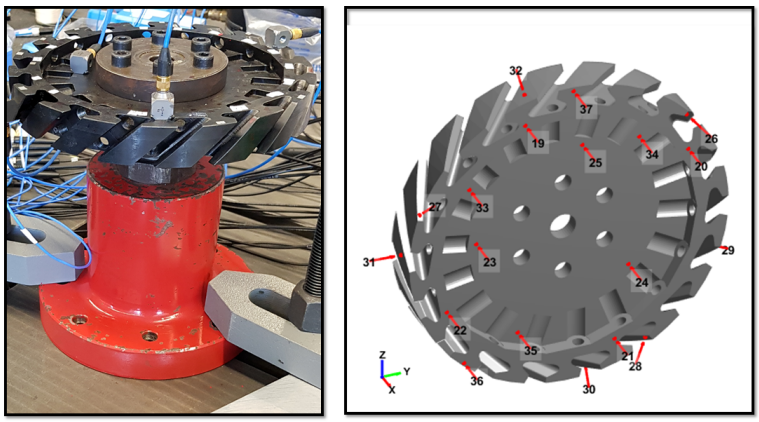

Fig. 4.8 Experimental setup for impact testing of the disk.

Table 4.3 Details of numerical and experimental parameters of the disk *B*.

Type	**Description**	**Disk Model 1**	**Disk Model 2**
Numerical Modelling	Young's Modulus (GPa)	190	150
	Density (kg/m^3)	7850	7850
	Fixed interface modes	200	200
Experimental Setup	Number of accelerometers	5	
	Number of used response channels (m)	14	
	Labels for response channels	{2–15}	
	Number of input channels (n)	19	
	Labels for input channels	{1–19}	

dynamics. In the same figure (Fig. 4.9(a)), the calculated forced response of the corresponding FE model is shown for two different Young's moduli (see Table 4.8): the blue curve is obtained with a nominal value of the Young modulus while the green curve is obtained by changing the Young modulus in order to have some resonance peaks closer to the experimental resonance peaks.

However, for both the numerical FRFs, it is possible to see that the numerical models are far from the one of the overlay model. The main reason is to be associated to the lack of cyclic symmetry for the actual disk and the constraint, while in the FE models the cyclic symmetry property is nominally guaranteed by a cyclic geometry and constraints. The FRFs are expanded by SEMM method of both the numerical models and an example of the final response after expansion is shown in Fig. 4.9(b) corresponding to $\mathbf{Y}^{\text{exp}}_{4,10}$. Note that the measured FRF on these DoF (response channel 4 and input channel 10) was not used to generate the expanded models. In the figure, it is possible to see that the Expanded model 2 FRF matches better than that of the

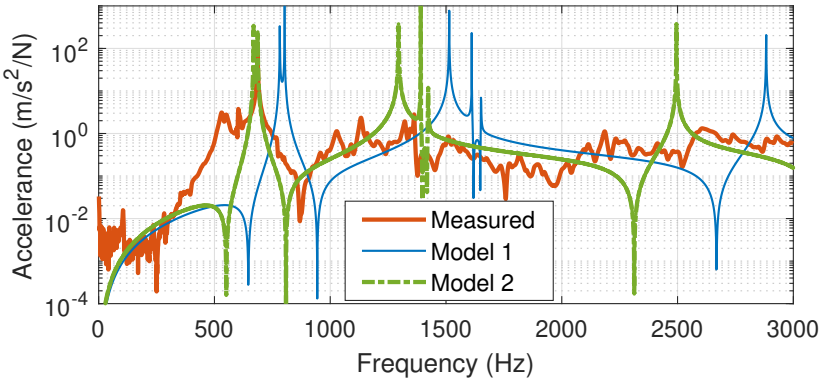

(a) Numerical or parent FRFs compared with the reference FRF

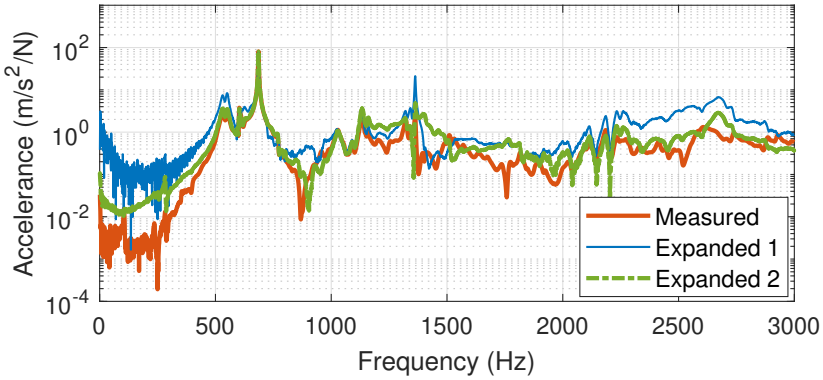

(b) Hybrid FRFs compared with the reference FRF

Fig. 4.9 Comparing FRFs of two different numerical models. Disk FRF at channel 4 (sensor 2) excited at the input channel 10 i.e. $\mathbf{Y}^{\text{exp}}_{4,10}$. The corresponding hybrid models (bottom) are also shown. The FRF of the model 2 has higher correlation with the measurement.

Expanded model 1 with the measured response. Hence, it can be concluded that the numerical model plays a significant role in the expansion and one can expect different results in a subsequent correlation analysis.

By using the correlation approach, the average FRAC values are depicted in the bar plot of Fig. 4.10. for the two expanded models. Each bar represents how well the validation channel is reconstructed by all the other response channels. The bar values are further averaged and shown in Table 4.4 (With all channels) in order to give a global index of the expansion goodness. It is clear from the table and Fig. 4.10 that Model 2 gives better global correlation (and a better hybrid model). According to the correlations, the least correlated channels are different for each model (channel

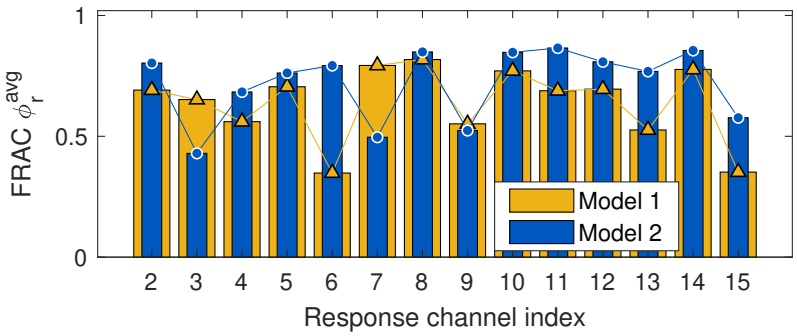

Fig. 4.10 FRAC bar plot for the disk vs Response Channels. Two different numerical models are used to generate the respective hybrid models and the corresponding correlation levels.

6 for Model 1 and channel 3 for Model 2). Consequently, one may want to discard these channels from the measurement set to generate new hybrid models.

In order to improve the result of the correlation calculated for Model 2, Response Channel 3 is removed from the experimental model since this channel gives the worst correlation. Similarly, Response Channel 6 can be done away with for Model 1. The result is an improvement of the global FRAC index of Table 4.4 for the respective models for which these actions were made and vice versa the global FRAC index decreases when a response channel associated to a good correlated channel is removed.

4.3.4 Effect of sensor mass loading

As previously mentioned, the sensors used for response measurement are triaxial accelerometers. They were preferred over more sophisticated non-intrusive measurement equipment, such as laser doppler vibrometry (LDV) [131, 132] for the different reasons listed below.

1. It is very difficult to obtain accurate measurements by LDV on unconstrained structures (such as the hung blade) due to the presence of rigid body modes.

2. The signal-to-noise ratio in LDV is higher and requires additional processing [133, 132].

3. For a multi-response measurement (SIMO – single input, multi output) with a manual hammer, the FRF measurement by LDV introduces additional uncer-

Table 4.4 Overall Mean FRAC Values for the Disk

	Model 1	**Model 2**	**Model 2 with Sensor Mass**
With All Channels	0.638	0.719	0.720
Without Channel 3	0.637	0.741	0.742
Without Channel 6	0.660	0.713	0.714

tainty of exciting again and again the same point to measure all the responses leading to more human error.

4. In the substucturing context, the accelerometer sensor mass loading effect can be taken into account in the process with a good degree of accuracy [51, 134].

In order to find out a possible influence of the accelerometers masses on the results of the hybrid model, the case of the constrained disk (Model 2) was reprocessed by keeping into account the accelerometers masses. Assuming that the mounted accelerometers only add inertia on the disk, their mass can either be 1) coupled to the numerical model or 2) decoupled from the experimental FRFs [51]. In the first case, the accelerometers' masses are added to the numerical model of the disk. In the second case, the numerical model does not have the added masses, but the effect must be decoupled from the measurements [134–136]. Theoretically, this last choice is possible but practically it needs inversion of the measured FRFs [40, 50], and hence, not preferred.

The first solution was then selected for the present case. There are five accelerometers, as shown in Fig. 4.8 at five different locations; each of them has a nominal mass of 6.5 grams. Therefore, we added a point mass in the numerical Model 2 of the disk at the accelerometers' positions. New expanded models were then generated to compute the updated FRAC values. The resulting overall mean FRAC values are listed in the last column of Table 4.4. By comparing the last two columns of the table, it can be noticed that the mean FRAC values are almost unchanged between 'Model 2' and 'Model 2 with Sensor Mass'. Thus, it can be concluded that the sensor loading has little or no effect on the expanded dynamics of the disk.

4.4 Discussion

In the global FRAC values, the improvement may seem marginal (about 2 percent points) but it should not be considered so. Even if there was no overall FRAC improvement (after discarding the uncorrelated channels), it would mean that the lesser number of channels could have the same observability or controllability. Most importantly, the correlation levels should not drop after an uncorrelated channel was removed.

The correlated SEMM method on the blade showed that, when the experimental and numerical models are close, the correlation indices are higher. The same was also demonstrated for the free disk case. In constraint-free systems, good numerical models are easy to produce.

In the application of the method to the fixed constrained disk – a more complicated test structure – the use of different numerical models demonstrates that even though the overall correlation levels are low, one could still point out the uncorrelated channels depending upon the modal directions of the numerical model. Nonetheless, the closer the numerical model is to the measured model, the better would be the correlation based channels' filtering and the hybrid models.

The FRAC as a correlation index used herein concerns more to the shape of the FRF. The other formulation is the FRF amplitude $FRAC^a$ correlation, also called Local Amplitude Correlation [127] defined as:

$$LAC_{ij} = \frac{2|\mathbf{Y}_{ij}^{\mathrm{S}}(\omega)\ \mathbf{Y}_{ij}^{\mathrm{exp}*}(\omega)|}{\mathbf{Y}_{ij}^{\mathrm{S}}(\omega)\ \mathbf{Y}_{ij}^{\mathrm{S}*}(\omega) + \mathbf{Y}_{ij}^{\mathrm{exp}}(\omega)\ \mathbf{Y}_{ij}^{\mathrm{exp}*}(\omega)} \tag{4.13}$$

In our analysis, the *LAC* values demonstrated the same pattern as the FRAC shape ϕ and thus were not shown here for clarity. In fact, one could show more correlation metrics as well as perform numerous tests on the method by tweaking some measurements, for example, by: i) adding noise in some measurement channels, ii) wrongly labelling the impacts or responses, iii) changing the direction of an impact, and so on. The method can be shown to work easily. In fact, a very recent rather parallel to the present work is the development of the same method independently by Kodric et al. [105]. In their work, the authors made use of local amplitude criterion and coherence like function to calculate correlation levels. Each correlation metric produced the same results. Some of the above-mentioned tests of introducing errors

deliberately were also performed in their work and revealed the robustness of the method. However, their test-case was a simple beam test-case while ours are rather realistic and light-weight structures like blade and disk. In our work, the method is tested on different numerical models of the disk through a commonly experienced problem of boundary constraint. In addition to this, the sensor intrusiveness is also taken into account.

4.5 Summary

This chapter introduces a new method to identify uncorrelated or bad measurement channels in an FRF measurement campaign. Since the SEMM method in its original formulation can include effects of measurement errors, the effect is reduced by using correlations in frequency domain. The chapter begins with a review of various correlation methods originally used in modal methods (MAC, POC) and then extended to frequency response methods (FRAC). The new method of correlations is elaborated by the help of mathematical expressions, process charts and matrix illustration, followed by the physical interpretation from the observability and controllability perspective.

The new correlation approach is then applied to the blade and disk as stand-alone components wherein the bad response and input channels are identified. The resulting hybrid FRFs show remarkable improvement. The effect of different numerical models is also investigated by using the constrained disk measurement campaign along with the sensor mass-loading effect. It is shown that the correlation approach is robust even for different numerical models and is insensitive to the mass-loading effect.

In the end, attention is drawn towards a similar and parallel developments to this work to emphasize the need for filtering of inconsistent measurements.

Chapter 5

Joint Identification Methods

Most engineering structures are assembled by holding together different components with various joining techniques. Among those, the non-permanent joints such as bolted, riveted, pinned, dove-tail, affect greatly the dynamic response prediction. It is well-known that, when subjected to dynamic loads, the added flexibility introduced by the joint to the structure heavily affects its behaviour. This effect may manifest as a change in the stiffness or the natural frequencies of the system or the amount of damping. Due to these factors, joints require different modelling and parameter estimation techniques to accurately predict the structural response. Broadly, the effect of joints can be modelled into the system as a forward problem or as an inverse problem [4, 137], like in many other fields [138].

The classical forward problem finds the effect of a given cause by using the appropriate law or model. The solution of these problems is generally unique, and it is insensitive to small changes in the problem. Such problems are called well-posed and they typically arise from the so-called direct problems of natural sciences [138]. In the joint modelling context, this means, for example, calculating the displacement (effect) of a jointed system under an applied load (cause). Even though the joint may introduce non-linearity in the system, whose solution may be difficult to find, the solution is still unique[1]. On the effect of joints, numerous publications attempt to predict the dynamic response by different methods for various joints and their configurations [19, 139–145]. With the advancements in computational resources,

[1]Multiple solutions of non-linear systems in a forward problem are the result of different initial conditions which can be uniquely found when the same initial condition is used.

more sophisticated methods are being developed for non-linear back-bone curves or response envelopes [146–149].

On the other side are the problems inverse to the classical forward problems which may be interpreted as finding the cause of a given effect. The problems of estimating parameters from transfer functions (modal parameter extraction), determining internal characteristics from measurements on the system boundary, calculating a force from a displacement field etc. fall in this category. The inverse problems are often ill-posed because distinct causes can produce the same effect or small changes in the effect can correspond to large changes in a given cause.

The joint identification is an inverse-problem which consists in determining a set of joint parameters from the dynamics of the assembled system to account for the difference that exists between the assembled system and the substructures. Such differences are typical in the presence of joints which not only may introduce non-linearity but also uncertainty of the contact (even when considered as a linear system). Although in practice, the properties of some joints are non-linear, many joints' characteristics can be regarded as approximately linear [58].

The identification of joint or difference between the assembly and the substructures has been of great interest in various areas of structural dynamics. The most noteworthy applications have been in the machine tooling industry [150–152, 3] and the automotive industry for Noise Vibration and Harshness (NVH) problems [59, 10, 7, 11]. In the machine tools, the interest has been in predicting the dynamic response when tool tips of different types are used. In the NVH problems, the vibration and noise has to be minimized in the passive substrucutures. This implies that all those structural or airborne paths should then be designed in such a way that the passive component receives minimum vibration or sound [153–155, 103]. In this regard, it is crucial to identify the dynamic characteristics of the resilient joint elements to be installed between the active (a source that actively generates vibration) and passive (a receiver that usually vibrates due to the presence of the source) subsystems.

The substructure identification problems can be ill-posed even when the system under consideration are numerical, as highlighted by D'Ambrogio and Fregolent [35, 36, 56] and Voormeeren and Rixen [50]. However, the identification problems are rooted in the observation of a system, usually observed in reality from a physical phenomenon or realized in the laboratory as an experiment. Due to the errors

associated with measurements, the ill-posed problems and the sensitivity of the methods to these errors, the identification problems lead to incoherent or spurious results. Therefore, the actual systems researched for joint identification in practice have been quite simple. Furthermore, various assumptions are made during the identification process which renders the methods specific only to those particular applications. Besides, it is a human tendency to represent a complex phenomenon as a single parameter or a set of parameters. For example, representing kinematics of an entire contact by a tangential stiffness, a normal stiffness and a friction coefficient [156–158] or representing a tractor with a few lumped masses and springs and model them as dynamic substructures [159]. The results of such simplified systems may be good enough for the cited applications but not others. Thus, a higher fidelity modelling or identification is deemed necessary, as will be shown in Chapter 6 and 7.

In this chapter, we review the popular joint identification methods based on dynamic substructuring. Since various methods exist with different names, they can be classified into three broad categories:

I. Inverse Receptance Coupling (IRC),

II. Inverse Substructuring (IS),

III. Substructure Decoupling (SD).

Each method is presented in a unified notation of the FBS methodology which should make it easy to correlate with one another.

5.1 General joint identification approach

There have been numerous strategies proposed in the literature to identify the joint characteristics from the assembly. Irrespective of their classification, each method needs a set of essential elements which are depicted in Fig. 5.1 and listed below:

1. substructure dynamics,
2. assembly dynamics observing the joint behaviour,
3. a joint model,
4. a mathematical framework that provides a set of equations to identify the joint,

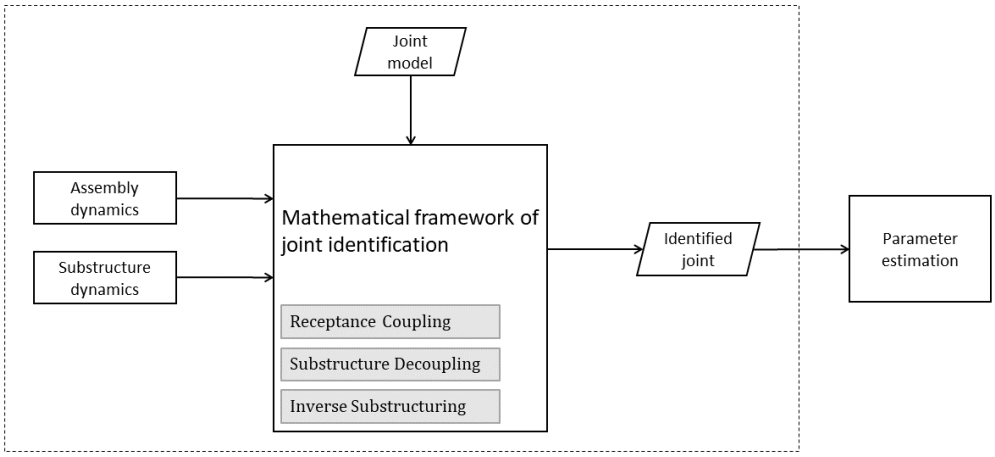

Fig. 5.1 General depiction of joint identification approaches – their framework and constituents.

5. the identified joint, and
6. an equivalent estimate of the joint parameters.

In the following subsections, an overview of each element is provided whilst referring to the related literature. The different methods will then be discussed in detail in the sections named as the methods themselves.

5.1.1 Substructure dynamics

Since the effect of substructure has to be removed from the assembly, an important input to the joint identification is the substructure dynamics. All the connected substructures must have their dynamics (measured, analytical or numerical) on the internal DoF and on the interface DoF (coupling DoF). Due to numerous difficulties in acquiring accurate FRFs in a measurement setup, many times the substructure models are only numerical or analytical. For components with the fixed boundary conditions, the numerical modelling may pose yet another challenge [160]. In fact, this thesis has covered so far the aspects related to substructures and how to predict by expansion the interface dynamics in Chapter 3 and 4. The interface so obtained by translational FRFs is not complete in spatial sense [63]. The need for a complete interface description is discussed in Section 5.1.1.1.

Before that, it is good to clarify in this chapter and onwards that the notion of a joint is generally associated with an assembly of substructures. One may also regard the interface as a joint. However, we distinguish between the two terms by the following definitions:

A **joint** is an entity that exists only in an assembly. It does not exist if substructures are not connected.

An **interface** is a part of the structure whose dynamics represent those DoF through which a connection is established with another substructure. These DoF always exist on the substructures even if they are not connected together.

5.1.1.1 Interface dynamics

In order to feed the substructures into a joint identification method, they must be described with sufficient spatial dynamic content i.e. enough DoF have to be measured or predicted. Whilst this may be easy to do on the internal DoF which are more accessible, it is difficult to do so on the interface DoF. Even on the internal DoF, mostly translational FRFs are easy to measure. Therefore, more DoF are needed to properly constrain the interface. This gives rise to using rotations as an additional set of constraints which are certainly hard to measure. Therefore, they have to be calculated from the translational FRFs.

Duarte and Ewins [65] reviewed the rotational DoF and traced it back to as far as 1969 where the problem of spatial incompleteness is studied due to limited measuring capacity on the interface. In their paper of year 2000 [65], they referred to many works classifying various methods of including rotational coordinates.

One possibility is to measure the rotations directly [61, 98, 64] by rotational accelerometers. However, these sensors are usually heavy and may only be suitable for bulky structures. Sensor loading becomes too significant for small-sized structural components. Therefore, one has to derive rotational effect indirectly. The finite difference approach by Duarte and Ewins [65] has been one of the popular methods for this purpose which uses finite differences of closely spaced translational DoF and approximates the rotational FRFs.

An implicit method of incorporating the rotations is an Equivalent Multi-point Connection (EMPC) [66] with an interface consisting of a non-collinear DoF set. This is similar to a finite element model in which an element with only translations

is considered. Based on the EMPC approach, the virtual point transformation (VPT) [153] was proposed as an upgradation of EMPC. In this approach, the measured translations are projected on the interface displacement modes which then describe the interface as a virtual point. Each virtual point interface then consists of both the translation and rotations – all collocated and suitable for FBS. In this work, the virtual point interface is used for our blade-root joint. Its mathematical details are presented in Section 6.2.

5.1.1.2 Internal dynamics

In addition to the interface dynamics, the internal dynamics must also be predicted in a joint identification process. Their role is pivotal for two reasons:

- A set amongst the internal DoF is used to remove their effect and produce a joint. In other words, the joint effect can only be obtained after any internal effects have been isolated from the assembly and substructures. This will be seen in detail in Sections 5.2, 5.3 and 5.4.
- Validation of the method i.e. to verify whether the identified joint produced a response on a set of key internal DoF (for example, on the blade-tip in a turbine, the wing-tip in an aeroplane).

5.1.2 Assembly dynamics

Since the joint is the delta between the assembly and the associated substructures, it is imperative that the assembly dynamics are known (measured). In the assembled state, however, the joint or coupling DoF are not accessible because the fastening leads to closing of the gap. Therefore, measurements on the coupling DoF is mostly not possible, as depicted in Fig. 5.2(a). In some applications related to vibration isolation in the vehicles (as discussed in the introduction to this chapter), the resilient rubber elements may provide some access to or near the coupling DoF (Fig. 5.2(b)). The methods used therein are usually referred to in-situ substructuring or inverse substructuring (see Section 5.4). Irrespective of the access to the joint DoF, the joint dynamics must be observable. That is, when the internal DoF are measured on the assembly, the effect of joint must be observable in the internal DoF.

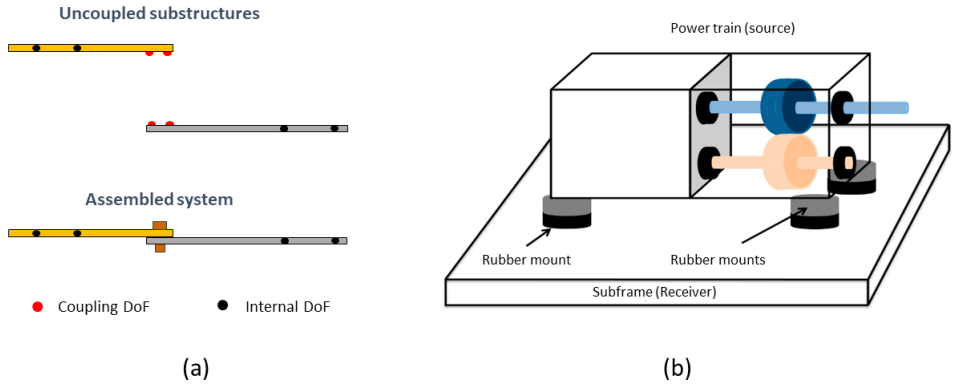

Fig. 5.2 (a) A simple bolted joint connection: the indicated coupling DoF can be measured in the uncoupled substructures but cannot be measured when they are assembled. In this case, it is only possible to measure on the internal DoF. (b) A source and a receiver assembled with the rubber mounts, adapted from [155]. There is some space for measurements in the assembly.

It is worth mentioning that the explicitly measured coupling DoF are often necessary for some methods such as IS (as discussed above) or SD. Even though some measurements can be performed in-situ in Fig. 5.2(b), but sometimes it is not possible to measure the complete FRF matrix. For example, exciting some DoF may not be realized on the so-called passive DoF. Moorhouse and Elliott [92] developed the round trip theory in which an FRF matrix (Green's function) can be constructed for a set of passive DoF, thus providing an expanded set of FRFs. In the SD methods, the coupling DoF dynamics in the assembled system can be obtained by the iterative scheme by Ren and Beards [161]. This method was further improved by Batista and Maia [162] by a demonstration on a numerical case-study. It is yet to be applied to a real life application. A SEMM based expansion strategy by Klaassen and Rixen [163] has been shown to expand the coupling DoF dynamics in the assembly. The method will be explained in detail in Section 5.5 and used for the joint identification purpose.

5.1.3 Joint model

When modelling a joint in dynamic substructuring, it can mean different types or formulations. The selection of the right joint identification method can then be based on the modelling assumptions. The joint system can be treated as quasi-static – a set

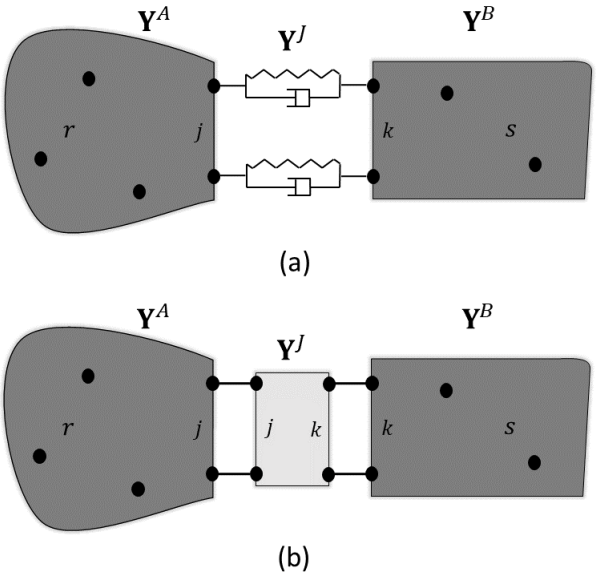

Fig. 5.3 Joint models: (a) In a quasi-static joint, no inertia is considered. The damper shown is a dash-pot. The choice is arbitrary. (b) An inertial or dynamic joint.

of springs and dampers, as shown in Fig. 5.3(a). From a mathematical point of view, this is a relaxation of the compatibility condition in the frequency based formulation [164] such as inverse receptance coupling, since no inertia is assumed from the joint. The inverse substructuring methods also neglect the inertial effect of the joint due to negligible mass of the rubber elements (bushings) compared to the connected substructures.

When the joint is considered to have also the inertial effect, it has to be treated as a substructure [42, 163] and the equilibrium on each coupling DoF has to be satisfied. This type of joint model is depicted in Fig. 5.3(b) whereby the black dots on the box indicate degree-of-freedom on the joint (modelled as a substructure). Although by fraction, the fasteners (bolts, rivets) can contribute to the inertial effects in the joint. Note that the fasteners appear only when talking about the assembly and not the substructures. Other than identifying their inertial effect in the joint, they can be included in the substructures during testing or modelling.

Another consideration in the joint model is whether the connection is flexible or highly stiff. The IS methods again consider the flexible or resilient joints. The highly stiff joints pose a great risk of being prone to noise [141].

5.1.4 A mathematical framework

The purpose of a method is to provide a set of equations to define relationships amongst its different variables. The mathematical formulation in most joint identification methods is based on assembling (or disassembling) of substructures. The principle steps in each method are to assemble the substructures by:

(i) writing equations of motion of the uncoupled substructures,

(ii) satisfying interface equilibrium and

(iii) ensuring interface displacement compatibility.

Depending on how the substructures and the assembled system are expressed and joint model type, the methods of identification can be mathematically exploited to produce a joint. The methods for joint identification discussed herein are based on frequency domain (as are common identification strategies). Each method's mathematical framework will be presented using symbols coherent with the previous chapters.

5.1.5 Identified joint

The output of the joint identification should clearly be the joint itself. Ideally, the joint should be a set of parameters that would produce the desired coupled system. It should not have identified any errors associated with measurements or modelling. However, in all practical applications, the identified joint contains lots of spurious effects which can also be non-physical.

Whether an identification is a physical or a non-physical joint (cause), can be verified by the following tests:

(i) By recoupling the identification to the substructures and by comparing it with a set of measured responses which were not used in the identification. This means that the identification produced a response (frequency response) of another set of internal DoF.

(ii) By estimating parameters from the identification. The parameters should then be physical. For example, real or imaginary parts are in accordance with

the FRF type (receptance or accelerance); or the coefficients of stiffness or damping are positive on the diagonal; or the identified matrices are symmetric or reciprocal.

5.1.6 Parameter estimation of the joint

Many IRC works use curve-fitting to experimental data as a way to extract joint parameters. Starting from a calculated quantity (say, receptance), parameters (associate with dynamic stiffness) are to be identified. Since the search region for joint parameters is usually very wide, the fitting is generally not very successful [165]. The formulations usually attempted in the literature are based on least squares solutions [2] or other application-specific optimization schemes [151, 166, 3].

In the following sections, the three methods of joint identification are presented mathematically derived using the FBS notation and reviewed from different presentations by several authors.

5.2 Inverse Receptance Coupling

Inverse Receptance coupling (IRC) is one of the most popular method of identifying the joints. This approach consists in coupling the FRFs or receptances (or mobility, accelerance) of substructures to give a mathematically coupled system. Then the corresponding blocks in this coupled system and in the actual measured assembly can be compared to give a set of equations from which the joint can be identified as depicted in Fig. 5.4. It can be seen from the figure that it allows to choose at convenience appropriate blocks from which the joint equations can be derived. The receptance coupling can take into account both of the joint types (quasi-static or inertial), as discussed above. Due to this, the mathematical treatment becomes different. Its details in relation to the two joint types, as described in the literature, are discussed separately in Subsections 5.2.1 and 5.2.2.

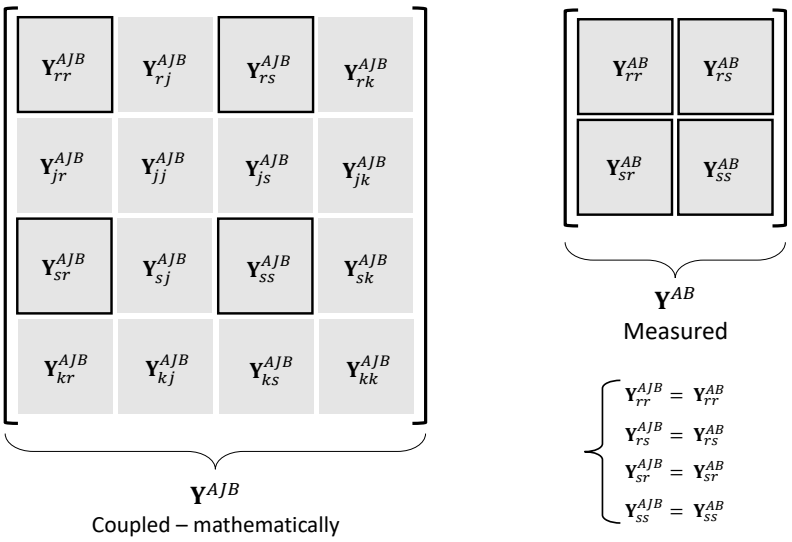

Fig. 5.4 The receptance coupling is equating the measured FRF blocks on the assembly and the mathematically coupled FRFs.

5.2.1 IRC for quasi-static joints

Depending on the specific type of application, one may consider a quasi-static (spring and damper) joint model or an inertial (spring, damper and mass) joint model, as discussed in Section 5.1.3. Let us recall the dual formulation for two rigidly connected substructures:

$$\begin{cases} \mathbf{u} &= \mathbf{Y}(\mathbf{f} - \mathbf{B}^T\lambda) \\ \mathbf{Bu} &= \mathbf{0} \end{cases} \quad \text{where} \quad \mathbf{Y} = \begin{bmatrix} \mathbf{Y}^A & \\ & \mathbf{Y}^B \end{bmatrix} \tag{5.1}$$

Note that equilibrium is satisfied a-priori in the dual formulation by setting the interface forces $\mathbf{g} = -\mathbf{B}^T\lambda$ (see Section 2.2.2.2). The equation $\mathbf{Bu} = \mathbf{0}$ ensures exact displacement compatibility. By introducing the quasi-static joint model expressed as receptance[2] $\mathbf{Y}^J$ would cause some displacement incompatibility at the interface. This can be expressed as:

[2]It should be noted for this type of joint, the $\mathbf{Z}^J$ matrix is singular at all frequencies. Hence one cannot compute $\mathbf{Y}^J$ for a numerical system unless some mass is introduced. One such problem is also encountered in this thesis in Section 7.1. However, from an experimental point of view, one deals with the measured quantities i.e. FRFs which are susceptible to noise and so it is possible to use the joint admittance $\mathbf{Y}^J$ that would relax the interface compatibility when multiplied by the interface intensity λ.

$$\mathbf{Bu} = \mathbf{Y}^J \boldsymbol{\lambda} \tag{5.2}$$

to signify that the delta δ in displacement at the interface $\mathbf{u}_k^B - \mathbf{u}_j^A = \boldsymbol{\delta} = \mathbf{Y}^J \boldsymbol{\lambda}$ [49, 164]. Substituting the first of Eq. (5.1) in Eq. (5.2) and solving for $\boldsymbol{\lambda}$ gives:

$$\begin{aligned} \mathbf{BY}(\mathbf{f} - \mathbf{B}^T \boldsymbol{\lambda}) &= \mathbf{Y}^J \boldsymbol{\lambda} \\ \implies \boldsymbol{\lambda} &= (\mathbf{BYB}^T + \mathbf{Y}^J)^{-1} \mathbf{BYf}\,. \end{aligned} \tag{5.3}$$

$\boldsymbol{\lambda}$ can now be inserted back in the first of Eq. (5.1) to obtain the displacements

$$\mathbf{u} = \big(\mathbf{Y} - \mathbf{YB}^T (\mathbf{BYB}^T + \mathbf{Y}^J)^{-1} \mathbf{BY}\big)\mathbf{f} \tag{5.4}$$

and the coupled receptance (FRF)

$$\mathbf{Y}^{AJB} = \mathbf{Y} - \mathbf{YB}^T (\mathbf{BYB}^T + \mathbf{Y}^J)^{-1} \mathbf{BY} \tag{5.5}$$

where the subscript J in $\mathbf{Y}^{AJB}$ denotes the explicit presence of joint dynamics whose effect is clearly included in the interface stiffness of Eq. (5.5).

Let us expand the above receptance matrix in terms of different blocks of substructures. Before that, we relabel the interface DoF. The substructure internal DoF in Section 2.2.3 were relabelled with subscripts r and s for substructure A and B, respectively. Likewise, the boundary DoF are also relabelled from here on as j and k for A and B, respectively (also indicated in Fig. 5.3). The notation is adopted from [3] to help tracking the DoF in the uncoupled substructures as well as the coupled structure. Thus, $\mathbf{Y}^A$ and $\mathbf{Y}^B$ are written as:

$$\mathbf{Y}^A = \begin{bmatrix} \mathbf{Y}_{rr}^A & \mathbf{Y}_{rj}^A \\ \mathbf{Y}_{jr}^A & \mathbf{Y}_{jj}^A \end{bmatrix}, \quad \mathbf{Y}^B = \begin{bmatrix} \mathbf{Y}_{ss}^B & \mathbf{Y}_{sk}^B \\ \mathbf{Y}_{ks}^B & \mathbf{Y}_{kk}^B \end{bmatrix} \tag{5.6}$$

As shown in Example 2 of Section 2.2.3, all the terms in Eq. (5.5) using the above relabelled partitions can be expanded as follows:

$$\mathbf{Y}^{AJB} = \begin{bmatrix} \mathbf{Y}_{rr}^A - \mathbf{Y}_{rj}^A \mathbf{Z}_{int} \mathbf{Y}_{jr}^A & \mathbf{Y}_{rj}^A - \mathbf{Y}_{rj}^A \mathbf{Z}_{int} \mathbf{Y}_{jj}^A & \mathbf{Y}_{rj}^A \mathbf{Z}_{int} \mathbf{Y}_{ks}^B & \mathbf{Y}_{rj}^A \mathbf{Z}_{int} \mathbf{Y}_{kk}^B \\ \mathbf{Y}_{jr}^A - \mathbf{Y}_{jj}^A \mathbf{Z}_{int} \mathbf{Y}_{jr}^A & \mathbf{Y}_{jj}^A - \mathbf{Y}_{jj}^A \mathbf{Z}_{int} \mathbf{Y}_{jj}^A & \mathbf{Y}_{jj}^A \mathbf{Z}_{int} \mathbf{Y}_{ks}^B & \mathbf{Y}_{jj}^A \mathbf{Z}_{int} \mathbf{Y}_{kk}^B \\ \mathbf{Y}_{sk}^B \mathbf{Z}_{int} \mathbf{Y}_{jr}^A & \mathbf{Y}_{sk}^B \mathbf{Z}_{int} \mathbf{Y}_{jj}^A & \mathbf{Y}_{ss}^B - \mathbf{Y}_{sk}^B \mathbf{Z}_{int} \mathbf{Y}_{ks}^B & \mathbf{Y}_{sk}^B - \mathbf{Y}_{sk}^B \mathbf{Z}_{int} \mathbf{Y}_{kk}^B \\ \mathbf{Y}_{kk}^B \mathbf{Z}_{int} \mathbf{Y}_{jr}^A & \mathbf{Y}_{kk}^B \mathbf{Z}_{int} \mathbf{Y}_{jj}^A & \mathbf{Y}_{ks}^B - \mathbf{Y}_{kk}^B \mathbf{Z}_{int} \mathbf{Y}_{ks}^B & \mathbf{Y}_{kk}^B - \mathbf{Y}_{kk}^B \mathbf{Z}_{int} \mathbf{Y}_{kk}^B \end{bmatrix} \tag{5.7}$$

where

$$\mathbf{Z}_{int} = \left(\mathbf{B}\mathbf{Y}\mathbf{B}^T + \mathbf{Y}^J\right)^{-1} = \left(\mathbf{Y}^A_{jj} + \mathbf{Y}^B_{kk} + \mathbf{Y}^J\right)^{-1} \tag{5.8}$$

is the interface stiffness.

Consider that the measured FRFs on the assembly are collected in $\mathbf{Y}^{AB}$ whilst measuring only on the internal DoF

$$\mathbf{Y}^{AB} = \begin{bmatrix} \mathbf{Y}^{AB}_{rr} & \mathbf{Y}^{AB}_{rs} \\ \mathbf{Y}^{AB}_{sr} & \mathbf{Y}^{AB}_{ss} \end{bmatrix} \tag{5.9}$$

then the receptance coupling is simply equating the blocks in $\mathbf{Y}^{AB}$ with those in $\mathbf{Y}^{AJB}$ in Eq. (5.7).

Clearly, four equations can be written now by comparing $\mathbf{Y}^{AB}$ and $\mathbf{Y}^{AJB}$ (depicted also graphically in Fig. 5.4).

$$\mathbf{Y}^{AB}_{rr} = \mathbf{Y}^A_{rr} - \mathbf{Y}^A_{rj}\left(\mathbf{Y}^A_{jj} + \mathbf{Y}^B_{kk} + \mathbf{Y}^J\right)^{-1}\mathbf{Y}^A_{jr} \tag{5.10a}$$

$$\mathbf{Y}^{AB}_{rs} = \mathbf{Y}^A_{rj}\left(\mathbf{Y}^A_{jj} + \mathbf{Y}^B_{kk} + \mathbf{Y}^J\right)^{-1}\mathbf{Y}^B_{ks} \tag{5.10b}$$

$$\mathbf{Y}^{AB}_{sr} = \mathbf{Y}^B_{sk}\left(\mathbf{Y}^A_{jj} + \mathbf{Y}^B_{kk} + \mathbf{Y}^J\right)^{-1}\mathbf{Y}^A_{jr} \tag{5.10c}$$

$$\mathbf{Y}^{AB}_{ss} = \mathbf{Y}^B_{ss} - \mathbf{Y}^B_{sk}\left(\mathbf{Y}^A_{jj} + \mathbf{Y}^B_{kk} + \mathbf{Y}^J\right)^{-1}\mathbf{Y}^B_{ks} \tag{5.10d}$$

If more sets of coupled measurements are available on the coupling DoF, one can derive more equations. Assuming that all the FRFs in Eqs. (5.10) can be measured or predicted, the only unknown is $\mathbf{Y}^J$ which can be found from any or all of the equations. Up until here, most RC methods use one or more of the above equations to derive the joint parameters with some application-specific simplifications and consideration of the rotational coordinates (to be discussed shortly). In fact, the IRC methods gained their popularity due to these simple expressions and avoidance of joint coordinates in the assembly. Any of the above equation should produce the same joint $\mathbf{Y}^J$, from the mathematical standpoint. Due to errors in experiments and modelling, the results can be different, as observed by Tol and Özgüven [3]. This difficulty gives rise to various conditioning, linear least squares or other non-linear optimization schemes implemented within the inverse receptance coupling approach.

The receptance coupling Eqs. (5.10), provide a mathematical basis for derivation of the joint. Depending upon the needs of an application, multiple approaches have

been devised. One of the very first approach has been that of Tsai and Chou [2] in which all four Eqs. (5.10) are put together in the matrix form to solve for the interface dynamic stiffness as follows:

$$\mathbf{Y}^{AB} = \begin{bmatrix} \mathbf{Y}^A_{rr} - \mathbf{Y}^A_{rj}\mathbf{Z}_{int}\mathbf{Y}^A_{jr} & \mathbf{Y}^A_{rj}\mathbf{Z}_{int}\mathbf{Y}^B_{ks} \\ \mathbf{Y}^B_{sk}\mathbf{Z}_{int}\mathbf{Y}^A_{jr} & \mathbf{Y}^B_{ss} - \mathbf{Y}^B_{sk}\mathbf{Z}_{int}\mathbf{Y}^B_{ks} \end{bmatrix}, \tag{5.11}$$

$$\mathbf{Y}^{AB} - \begin{bmatrix} \mathbf{Y}^A_{rr} & \\ & \mathbf{Y}^B_{ss} \end{bmatrix} = \begin{bmatrix} -\mathbf{Y}^A_{rj}\mathbf{Z}_{int}\mathbf{Y}^A_{jr} & \mathbf{Y}^A_{rj}\mathbf{Z}_{int}\mathbf{Y}^B_{ks} \\ \mathbf{Y}^B_{sk}\mathbf{Z}_{int}\mathbf{Y}^A_{jr} & -\mathbf{Y}^B_{sk}\mathbf{Z}_{int}\mathbf{Y}^B_{ks} \end{bmatrix}. \tag{5.12}$$

They can be written in a compact form

$$\mathbf{Y}^{\gamma} = \mathbf{Y}^{\alpha}\mathbf{Z}_{int}\mathbf{Y}^{\beta}\,. \tag{5.13}$$

$$\mathbf{Y}^{\gamma} = \mathbf{Y}^{\alpha}(\mathbf{Y}^A_{jj} + \mathbf{Y}^B_{kk} + \mathbf{Y}^J)\mathbf{Y}^{\beta} \tag{5.14}$$

where $\mathbf{Z}_{int}$ was defined in Eq. (5.8) along with the following definitions:

$$\mathbf{Y}^{\gamma} = \mathbf{Y}^{AB} - \begin{bmatrix} \mathbf{Y}^A_{rr} & \\ & \mathbf{Y}^B_{ss} \end{bmatrix}, \quad \mathbf{Y}^{\alpha} = \begin{bmatrix} -\mathbf{Y}^A_{rj} \\ \mathbf{Y}^B_{sk} \end{bmatrix} \quad \text{and} \quad \mathbf{Y}^{\beta} = \begin{bmatrix} \mathbf{Y}^A_{jr} & -\mathbf{Y}^B_{ks} \end{bmatrix}. \tag{5.15}$$

By inverting both sides of Eq. (5.14) and moving the terms to the left hand side, we get:

$$\left(\mathbf{Y}^{\gamma} - (\mathbf{Y}^{\beta})^{-1}(\mathbf{Y}^A_{jj} + \mathbf{Y}^B_{kk})(\mathbf{Y}^{\alpha})^{-1}\right)^{-1} = \mathbf{Y}^{\alpha}(\mathbf{Y}^J)^{-1}\mathbf{Y}^{\beta}. \tag{5.16}$$

Eq. (5.16) is then written as:

$$\mathbf{Y}^{\delta} = \mathbf{Y}^{\alpha}(\mathbf{K} + i\omega\mathbf{C})\mathbf{Y}^{\beta} \tag{5.17}$$

where $\mathbf{Y}^{\delta} = \left(\mathbf{Y}^{\gamma} - (\mathbf{Y}^{\beta})^{-1}(\mathbf{Y}^A_{jj} + \mathbf{Y}^B_{kk})(\mathbf{Y}^{\alpha})^{-1}\right)^{-1}$ and a quasi-static joint model is used which can be expressed as a frequency dependent dynamic stiffness as $\mathbf{Z}^J$ with stiffness $\mathbf{K}$ and damping $\mathbf{C}$:

$$\mathbf{Y}^J = (\mathbf{Z}^J)^{-1} = (\mathbf{K} + i\omega\mathbf{C})^{-1}\,. \tag{5.18}$$

Since the above set of equations are frequency dependent, Tsai and Chou [2] made use of n_ω frequency lines to express the above $2 \times n^2$ set of equations[3] and

[3] Due to complex FRFs having real and imaginary parts

transformed them to an overdetermined set of equations.

$$\mathbf{y}(\omega_z) = \mathbf{A}(\omega_z)\mathbf{x}(\omega_z) \tag{5.19}$$

where the i-th and j-th elements in $\mathbf{y}_i = \mathbf{A}_{ij}\mathbf{x}_j$ correspond to $\mathbf{Y}^{\delta}_{pq} = \mathbf{Y}^{\alpha}_{pl}(\mathbf{K}+i\omega\mathbf{C})_{lm}\mathbf{Y}^{\beta}_{mq}$ at frequency ω_z. By concatenating all the elements at other frequencies, an overdetermined system is obtained. The set of joint parameters in $\mathbf{x}$ is thus determined by taking the generalized inverse of $\mathbf{A}$.

$$\mathbf{x} = \mathbf{A}^{+}\mathbf{y} \tag{5.20}$$

The least-squared solution can provide different joint values depending on the chosen frequency band. For the same set of two beams coupled with a single bolt, Tsai and Chou calculated three different sets of stiffness and damping (2×2 joint system). Note that the substructures and assembly FRFs used in the identification were synthesized from modal parameters extracted from the directly measured FRFs.

On the other hand, Tol and Özgüven [3] used a slightly different strategy to find the joint parameters. They used each of the four Eqs. (5.10) to determine the joint parameters $\mathbf{Z}^J = (\mathbf{Y}^J)^{-1} = \mathbf{K}+i\omega\mathbf{C}$ and produced the following four expressions:

$$\mathbf{K}^* = \left(\mathbf{Y}^A_{jr}\left(\mathbf{Y}^A_{rr}-\mathbf{Y}^{AB}_{rr}\right)^{-1}\mathbf{Y}^A_{rj}-\mathbf{Y}^A_{jj}-\mathbf{Y}^B_{kk}\right)^{-1} \tag{5.21a}$$

$$\mathbf{K}^* = \left(\mathbf{Y}^B_{ks}\left(\mathbf{Y}^{AB}_{rs}\right)^{-1}\mathbf{Y}^A_{rj}-\mathbf{Y}^A_{jj}-\mathbf{Y}^B_{kk}\right)^{-1} \tag{5.21b}$$

$$\mathbf{K}^* = \left(\mathbf{Y}^A_{jr}\left(\mathbf{Y}^{AB}_{sr}\right)^{-1}\mathbf{Y}^B_{sk}-\mathbf{Y}^A_{jj}-\mathbf{Y}^B_{kk}\right)^{-1} \tag{5.21c}$$

$$\mathbf{K}^* = \left(\mathbf{Y}^B_{ks}\left(\mathbf{Y}^A_{ss}-\mathbf{Y}^{AB}_{ss}\right)^{-1}\mathbf{Y}^B_{sk}-\mathbf{Y}^A_{jj}-\mathbf{Y}^B_{kk}\right)^{-1}. \tag{5.21d}$$

Even though their approach falls under IRC, they called their method FRF decoupling. They also modelled rotations by second order central finite difference method on the bolted beams' interface from three translations. Their six-parameter joint system (translational, rotational and cross coupled terms of stiffness and damping) was used first on a numerical assembly of beams (simulated with noise) in which it was found that each equation produced different results. They used an unconstrained optimization scheme to find out the optimal set of parameters for which an accurate initial guess is required. In fact, they found the first Eq. (5.21a) to be more accurate than others which had the maximum error of 30%. They also tested their methodology on an experimental assembly of beams. For the experimental setup, one of their

beam was fixed which was measured, whilst the other beam was free-free (by FE model updating). In this case, they could only use the fourth equation Eq. (5.21d) for the joint identification. Through the identified joint parameters, they could show good agreement in their validation measurements.

Schmitz et al. [151] used Eq. (5.10a) or only $\mathbf{Y}_{rr}^{AJB}$ as their main receptance coupling equation and introduce the joint in terms of translational and rotational stiffness k_t, k_θ and damping c_t, c_θ, respectively. The final expression is then a function of translational and rotational FRFs with the joint parameters as unknowns $\mathbf{Y}_{rr}^{AJB} = f(k_t, k_\theta, c_t, c_\theta)$. The rotational FRFs are estimated analytically from substructure A, the tool, whilst neglecting this effect on substructure B, the holder/spindle; since it was not thought feasible to measure. Their problem can be represented mathematically as:

$$\begin{aligned} \underset{k_t,k_\theta,c_t,c_\theta}{\text{argmin}} \quad & \left|\left|\mathbf{Y}_{rr}^{AJB} - \mathbf{Y}_{rr}^{AB}\right|\right| = \left|\left|f(k_t,k_\theta,c_t,c_\theta) - \mathbf{Y}_{rr}^{AB}\right|\right| \\ \text{s.t.} \quad & k_\theta = \tau\, k_t \\ & c_\theta = \nu\, c_t \end{aligned} \tag{5.22}$$

where τ and ν are constants due to an assumption of proportionality of rotational stiffness and damping to their respective translational counterparts. In order to predict the coupled FRF, they vary the joint parameters manually to obtain a sufficient overlap with the measured FRF on the assembly. This can be regarded as a manual parameter search in optimization. They applied the method to three different sizes of tools having different slenderness ratios.

In a similar application is the work by Park et al. [150] in which instead of identifying a set of joint parameters, they estimate the interface FRFs on the holder/spindle $\mathbf{Y}^B$ in order to predict the coupled system's FRF. They also used Eq. (5.10a) or $\mathbf{Y}_{rr}^{AJB}$ and an additional coupled equation $\mathbf{Y}_{rj}^{AJB}$ expressed in Eq. (5.7). Using these two equations and neglecting the internal FRFs of B, they formulate the interface FRFs $\mathbf{Y}_{kk}^B$ as a non-linear function of rotational FRFs. If $\mathbf{Y}_{kk}^B$ can be expanded as below

$$\mathbf{Y}_{kk}^B = \begin{bmatrix} \mathbf{Y}_{tt}^B & \mathbf{Y}_{t\theta}^B \\ \mathbf{Y}_{\theta t}^B & \mathbf{Y}_{\theta\theta}^B \end{bmatrix}, \tag{5.23}$$

then $\mathbf{Y}_{tt}^B$ is easily measurable on B and the rotational counterparts $\mathbf{Y}_{\theta t}^B$ and $\mathbf{Y}_{\theta\theta}^B$ are the two unknowns. Using the two equations stated above, $\mathbf{Y}_{\theta t}^B$ and $\mathbf{Y}_{\theta\theta}^B$ are cast

as two non-linear variables for which two equations are available. The non-linear solution is determined using a symbolic toolbox at each frequency. Note that the rotational interface FRFs of the tool A are determined by finite element analysis.

In the above works, it can be noticed that the substructure B (spindle/holder assembly) is usually difficult to model because of the complex structural design and ground constraints. Ertürk et al. [167] developed an analytical framework to model spindle–holder sub-assembly and then coupling them with the tool to obtain the tool point FRFs. They introduced springs and dampers simulating the bearing effects and included them in the receptance coupling by means of structural modification method [57, 32, 168]. The joints between two connecting substructures were also added to model the discrepancies. Their study was more on developing an analytical framework for better modelling of such systems which laid foundation for future work on identification.

Özsahin et al. [169] is another work on joint parameters identification between the spindle-holder and tool. They again used $\mathbf{Y}_{rr}^{AJB}$ as the main element of the coupled matrix referring to the tool tip FRF. In the analytical study, they could exactly identify the joint parameters (stiffness and damping – linear and rotational including cross-coupling terms) which is typical in a noise-free, error-free case. When they added the noise, the parameters became frequency dependent, yet one could observe the variation about the actual values. On the experimental case, they used the Savitzky-Golay filtered FRFs to circumvent the sensitivity of the IRC method to the noise. The identified joint parameters were still frequency-dependent, however, with improved estimates.

5.2.2 IRC for joints with mass

When the model of the joint is inertial, the treatment of the receptance coupling equations becomes different. The joint has to be considered as a structural entity with masses on which additional equilibrium and compatibility conditions should be satisfied. In the FBS formulation, it means that additional compatibility and equilibrium equations have to be satisfied. This is in contrast to the relaxation of compatibility in the above section where the number of compatibility equations remained the same, as if for the rigid coupling. The main IRC strategies with this type of joint have been attempted by Ren and Beards [170, 171] and Mehrpouya

et al. [152] along with some RC substructure analysis based approaches Schmitz and Duncan [166]. The FBS formulation for such a joint begins with the following equations:

$$\begin{cases} \mathbf{u} & = \mathbf{Y}(\mathbf{f} - \mathbf{B}^T \lambda) \\ \mathbf{Bu} & = \mathbf{0} \end{cases} \quad \text{where} \quad \mathbf{Y} = \begin{bmatrix} \mathbf{Y}^A & & \\ & \mathbf{Y}^J & \\ & & \mathbf{Y}^B \end{bmatrix} \tag{5.24}$$

and

$$\mathbf{Y}^A = \begin{bmatrix} \mathbf{Y}^A_{rr} & \mathbf{Y}^A_{rj} \\ \mathbf{Y}^A_{jr} & \mathbf{Y}^A_{jj} \end{bmatrix}, \quad \mathbf{Y}^B = \begin{bmatrix} \mathbf{Y}^B_{ss} & \mathbf{Y}^B_{sk} \\ \mathbf{Y}^B_{ks} & \mathbf{Y}^B_{kk} \end{bmatrix}, \quad \mathbf{Y}^J = \begin{bmatrix} \mathbf{Y}^J_{jj} & \mathbf{Y}^J_{jk} \\ \mathbf{Y}^J_{kj} & \mathbf{Y}^J_{kk} \end{bmatrix}. \tag{5.25}$$

The interface compatibility is given by two equations now, namely

$$\begin{aligned} \mathbf{u}^J_j - \mathbf{u}^A_j &= \mathbf{0} \\ \mathbf{u}^J_k - \mathbf{u}^B_k &= \mathbf{0} \end{aligned} \tag{5.26}$$

which can be applied in Eq. (5.24) if we write the Boolean matrix $\mathbf{B}$ as:

$$\mathbf{B} = \begin{array}{c} \begin{matrix} \mathbf{u}^A_i & \mathbf{u}^A_j & \mathbf{u}^J_j & \mathbf{u}^J_k & \mathbf{u}^B_i & \mathbf{u}^B_k \end{matrix} \\ \left[\begin{array}{cc|cc|cc} \mathbf{0} & -\mathbf{I} & \mathbf{I} & \mathbf{0} & \mathbf{0} & \mathbf{0} \\ \mathbf{0} & \mathbf{0} & \mathbf{0} & \mathbf{I} & \mathbf{0} & -\mathbf{I} \end{array}\right] \end{array} \tag{5.27}$$

By following the same coupling procedure of Section 2.2.2.2, one obtains the general LMFBS dual coupling equation:

$$\mathbf{Y}^{AJB} = \mathbf{Y} - \mathbf{Y}\mathbf{B}^T(\mathbf{B}\mathbf{Y}\mathbf{B}^T)^{-1}\mathbf{B}\mathbf{Y}. \tag{5.28}$$

As it was done in Section 5.2 and Fig. 5.4 that the respective blocks are compared and equated. Then one proceeds to identify the joint dynamics from there. Eq. 5.28 can be expanded for all its terms. This dual system size is bigger than before and populating the full matrix may result in loss of legibility. Therefore, we would pick only the relevant blocks for the derivation of joint dynamics according to Ren and Beards' approach [170].

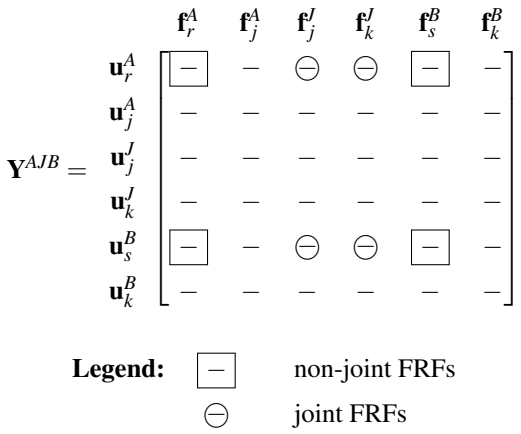

Fig. 5.5 A dually coupled system representing the relevant FRFs on non-joint and joint coordinates.

First, let us inspect the interface flexibility $\mathbf{Y}_{int}$ to find the joint dynamics.

$$\begin{aligned}\mathbf{Y}_{int} = \mathbf{B}\mathbf{Y}\mathbf{B}^T &= \begin{bmatrix} \mathbf{Y}_{jj}^A + \mathbf{Y}_{jj}^J & \mathbf{Y}_{jk}^J \\ \mathbf{Y}_{kj}^J & \mathbf{Y}_{kk}^J + \mathbf{Y}_{kk}^B \end{bmatrix} \\ &= \begin{bmatrix} \mathbf{Y}_{jj}^A & \\ & \mathbf{Y}_{kk}^B \end{bmatrix} + \begin{bmatrix} \mathbf{Y}_{jj}^J & \mathbf{Y}_{jk}^J \\ \mathbf{Y}_{kj}^J & \mathbf{Y}_{kk}^J \end{bmatrix}\end{aligned} \tag{5.29}$$

The interface is now the sum of boundary dynamics from the substructures, denoted here as $\mathbf{Y}_{bb}$, and the joint FRFs $\mathbf{Y}^J$. The above equation then becomes

$$\begin{aligned}\mathbf{Y}_{int} &= \mathbf{Y}_{bb} + \mathbf{Y}^J \\ &= \mathbf{Y}_{bb} + (\mathbf{Z}^J)^{-1} \\ &= (\mathbf{Z}^J)^{-1}(\mathbf{I} + \mathbf{Z}^J\mathbf{Y}_{bb})\end{aligned} \tag{5.30}$$

The combined stiffness of the interface $\mathbf{Z}_{int}$ can be written in the following form:

$$\mathbf{Z}_{int} = \mathbf{Y}_{int}^{-1} = (\mathbf{I} + \mathbf{Z}^J\mathbf{Y}_{bb})^{-1}\mathbf{Z}^J \,. \tag{5.31}$$

Ren and Beards [170] actually partitioned their coupled system into non-joint and joint coordinates, thus producing four blocks of FRFs. However, they used only the first block of non-joint FRFs for the application of their theoretical development. In order to derive their set of equations, consistent with the notation of this thesis, we use only the relevant blocks in the dually coupled system which is depicted in

Fig. 5.5. Redundant rows and columns can be noticed in the dually coupled system. The non-joint FRFs indicated with the squares can be collected in the following matrices:

$$\begin{aligned}\mathbf{Y}_{ii}^{AJB} &= \begin{bmatrix} \mathbf{Y}_{rr}^{A} - \mathbf{Y}_{rj}^{A}\mathbf{Z}_{11}\mathbf{Y}_{jr}^{A} & -\mathbf{Y}_{rj}^{A}\mathbf{Z}_{12}\mathbf{Y}_{jr}^{A} \\ -\mathbf{Y}_{sk}^{B}\mathbf{Z}_{21}\mathbf{Y}_{jr}^{A} & \mathbf{Y}_{ss}^{B} - \mathbf{Y}_{sk}^{B}\mathbf{Z}_{22}\mathbf{Y}_{ks}^{B} \end{bmatrix} \\ &= \begin{bmatrix} \mathbf{Y}_{rr}^{A} & \\ & \mathbf{Y}_{ss}^{B} \end{bmatrix} - \begin{bmatrix} \mathbf{Y}_{rj}^{A} & \\ & \mathbf{Y}_{sk}^{B} \end{bmatrix} \mathbf{Z}_{int} \begin{bmatrix} \mathbf{Y}_{rj}^{A} & \\ & \mathbf{Y}_{sk}^{B} \end{bmatrix}^{T}\end{aligned} \tag{5.32}$$

where $\mathbf{Y}_{ii}^{AJB}$ denotes the set of coupled FRFs on the non-joint coordinates and $\mathbf{Z}_{11}, \mathbf{Z}_{12}, \mathbf{Z}_{21}, \mathbf{Z}_{22}$ are partitions of the interface stiffness matrix of Eq. (5.31) defined as below:

$$\mathbf{Z}_{int} = \begin{bmatrix} \mathbf{Z}_{11} & \mathbf{Z}_{12} \\ \mathbf{Z}_{21} & \mathbf{Z}_{22} \end{bmatrix}. \tag{5.33}$$

Eq. (5.32) can also be written compactly

$$\mathbf{Y}_{ii}^{AJB} = \mathbf{Y}_{ii} - \mathbf{Y}_{ib}\mathbf{Z}_{int}\mathbf{Y}_{ib}^{T} \tag{5.34}$$

Each $\mathbf{Y}_{\star}$, without a superscript, represents an uncoupled block diagonal matrix in the order the matrices appeared in Eq. (5.32). Replacing $\mathbf{Z}_{int}$ from Eq. (5.31) gives

$$\mathbf{Y}_{ii}^{AJB} = \mathbf{Y}_{ii} - \mathbf{Y}_{ib}(\mathbf{I} + \mathbf{Z}^{J}\mathbf{Y}_{bb})^{-1}\mathbf{Z}^{J}\mathbf{Y}_{ib}^{T} \tag{5.35}$$

Similarly, the other set of FRFs relating non-joint coordinates to joint coordinates (shown as encircled blocks in Fig. 5.5) can be cast into the following matrices:

$$\begin{aligned}\mathbf{Y}_{ib}^{AJB} &= \begin{bmatrix} \mathbf{Y}_{rj}^{A}\mathbf{Z}_{11}\mathbf{Y}_{jj}^{J} + \mathbf{Y}_{rj}^{A}\mathbf{Z}_{12}\mathbf{Y}_{kj}^{J} & \mathbf{Y}_{rj}^{A}\mathbf{Z}_{11}\mathbf{Y}_{jk}^{J} + \mathbf{Y}_{rj}^{A}\mathbf{Z}_{12}\mathbf{Y}_{kk}^{J} \\ \mathbf{Y}_{sk}^{B}\mathbf{Z}_{21}\mathbf{Y}_{jj}^{J} + \mathbf{Y}_{sk}^{B}\mathbf{Z}_{22}\mathbf{Y}_{kj}^{J} & \mathbf{Y}_{sk}^{B}\mathbf{Z}_{21}\mathbf{Y}_{jk}^{J} + \mathbf{Y}_{sk}^{B}\mathbf{Z}_{22}\mathbf{Y}_{kk}^{J} \end{bmatrix} \\ &= \begin{bmatrix} \mathbf{Y}_{rj}^{A} & \\ & \mathbf{Y}_{sk}^{B} \end{bmatrix} \mathbf{Z}_{int} \begin{bmatrix} \mathbf{Y}_{jj}^{J} & \mathbf{Y}_{jk}^{J} \\ \mathbf{Y}_{kj}^{J} & \mathbf{Y}_{kk}^{J} \end{bmatrix}\end{aligned} \tag{5.36}$$

which can also be written compactly, like Eq. (5.32) and (5.34).

$$\mathbf{Y}_{ib}^{AJB} = \mathbf{Y}_{ib}\mathbf{Z}_{int}\mathbf{Y}^{J} \tag{5.37}$$

Note that the last matrix in the above equation is the joint flexibility $\mathbf{Y}^J$. Substituting $\mathbf{Z}_{int}$ from Eq. (5.31) in Eq. (5.36) and solving yields

$$\begin{aligned}\mathbf{Y}_{ib}^{AJB} &= \mathbf{Y}_{ib}(\mathbf{I}+\mathbf{Z}^J\mathbf{Y}_{bb})^{-1}\mathbf{Z}^J\mathbf{Y}^J \\ &= \mathbf{Y}_{ib}(\mathbf{I}+\mathbf{Z}^J\mathbf{Y}_{bb})^{-1}\end{aligned} \tag{5.38}$$

where $\mathbf{Z}^J\mathbf{Y}^J = \mathbf{I}$.

Generally, the receptance coupling approach would compare $\mathbf{Y}_{ii}^{AJB}$ with a corresponding set of measurements, say $\mathbf{Y}_{ii}^{AB}$, or comparing $\mathbf{Y}_{ib}^{AJB}$ with measured $\mathbf{Y}_{ib}^{AB}$, i.e.

$$\begin{cases}\mathbf{Y}_{ii}^{AB} = \mathbf{Y}_{ii} - \mathbf{Y}_{ib}(\mathbf{I}+\mathbf{Z}^J\mathbf{Y}_{bb})^{-1}\mathbf{Z}^J\mathbf{Y}_{ib}^T \\ \mathbf{Y}_{ib}^{AB} = \mathbf{Y}_{ib}(\mathbf{I}+\mathbf{Z}^J\mathbf{Y}_{bb})^{-1}\end{cases}. \tag{5.39}$$

In fact, Ren and Beards [170] went further and substituted the second of Eq. (5.39) in its first equation

$$\mathbf{Y}_{ii}^{AB} = \mathbf{Y}_{ii} - \mathbf{Y}_{ib}^{AB}\,\mathbf{Z}^J\,\mathbf{Y}_{ib}^T \tag{5.40}$$

$\mathbf{Z}^J$, as per IRC, can be solved easily from this equation,

$$\mathbf{Y}_{ib}^{AB}\,\mathbf{Z}^J\,\mathbf{Y}_{ib}^T = \mathbf{Y}_{ii} - \mathbf{Y}_{ii}^{AB} \tag{5.41}$$

In this formulation, it is necessary to measure the FRFs $\mathbf{Y}_{ib}^{AB}$ between non-joint and joint coordinates. Although Ren and Beards [170] devised an iterative strategy to obtain $\mathbf{Y}_{ib}^{AB}$ [161], their method's applicability thus becomes limited. Regardless of this, their approach on identifying the joint parameters used a constrained least squares solution by considering multiple response functions in a given frequency bandwidth, all concatenated together. First, the above equation is rearranged to this form:

$$\mathbf{z} = \mathbf{E}^+\,\mathbf{y}, \tag{5.42}$$

where $\mathbf{z}$ is the vector of unknown dynamic stiffness (for example, $z_{11}, z_{12}, z_{21}, z_{22}$ for a 2×2 system), $\mathbf{y}$ is calculated by the right hand side of Eq. (5.41) and $\mathbf{E}$ is the coefficient matrix obtained from the coefficients of $\mathbf{Y}_{ib}^{AB}$ and $\mathbf{Y}_{ib}^T$. The constraints can be introduced as follows:

$$\mathbf{z} = \mathbf{T}_\omega\,\mathbf{T}_s\,\mathbf{x} \tag{5.43}$$

The matrix $\mathbf{T}_s$ maintains the shape of the dynamic stiffness matrix of the joint (reciprocity or opposing effect of cross coupling terms etc.) and $\mathbf{T}_\omega$ is the matrix con-

taining multiples of $i\omega$ to make the vector $\mathbf{x}$ frequency independent. In Appendix B, one such constraint matrix is derived for a simple joint system. Ren and Beards also introduced various weighting functions to reduce the effect of large deviations in their constrained least-squared approach of parameter estimation. The test-object for their method were two rectangular beams joined by two aluminum pieces and a steel shell element cut from a nut. They used the element to introduce flexibility at the joint. They measured two DoF on each interface thereby making the joint system 4×4. Like others, their joint parameters were different based on the selected frequency bandwidth. The predicted response on the internal DoF was also quite satisfactory up to a 1000 Hz when compared with the validation measurement.

Schmitz and Duncan [166] introduced another substructure, the so-called extended holder[4] between the tool A and the spindle B. The presence of the extended holder, denoted here by J, is thus equivalent to adding an inertial joint model (J does not necessarily indicate a joint here but a substructure) which falls under the inertial joint based receptance coupling approach. The aim was to identify the interface FRF of the spindle B from the whole assembly measurements and the coupled receptances obtained by RC. In their previous paper, Schmitz et al. [151], the authors identified the joint parameters between the tool A and the holder/spindle B.

Their system can be depicted using our dummy substructures A and B in Fig. 5.6. The figure shows a simplified version of their tool A, extended holder J and spindle B assembly. In the first step, the coupled receptance $\mathbf{Y}_{rr}^{AJ}$ on the internal DoF r of A is calculated as:

$$\mathbf{Y}_{rr}^{AJ} = \mathbf{Y}_{rr}^{A} - \mathbf{Y}_{rj}^{A}\left(\mathbf{Y}_{jj}^{A} + \mathbf{Y}_{jj}^{J}\right)^{-1}\mathbf{Y}_{jr}^{A}\,. \tag{5.44}$$

Note that we used the first block of matrix in Eq. (5.32) whereof $\mathbf{Z}_{11} = \mathbf{Y}_{jj}^{A} + \mathbf{Y}_{jj}^{J}$. With the same strategy, $\mathbf{Y}_{rr}^{AJ}$ is coupled with $\mathbf{Y}_{kk}^{B}$ in the second step to give

$$\mathbf{Y}_{rr}^{AJB} = \mathbf{Y}_{rr}^{AJ} - \mathbf{Y}_{rk}^{AJ}\left(\mathbf{Y}_{kk}^{AJ} + \mathbf{Y}_{kk}^{B}\right)^{-1}\mathbf{Y}_{kr}^{AJ}\,. \tag{5.45}$$

Using measurements on $\mathbf{Y}_{rr}^{AJB} = \mathbf{Y}_{rr}^{AJB,meas}$, the spindle interface FRF $\mathbf{Y}_{kk}^{B}$ is thus calculated from the above equation:

$$\mathbf{Y}_{kk}^{B} = \mathbf{Y}_{kr}^{AJ}\left(\mathbf{Y}_{rr}^{AJ} - \mathbf{Y}_{rr}^{AJB,meas}\right)^{-1}\mathbf{Y}_{rk}^{AJ} - \mathbf{Y}_{kk}^{AJ}\,. \tag{5.46}$$

[4]Even though the extended holder is introduced as a sub-assembly, already composed of two substructures rigidly coupled together by receptance coupling, the method is easily extendable to multiple substructures, as shown in their paper.

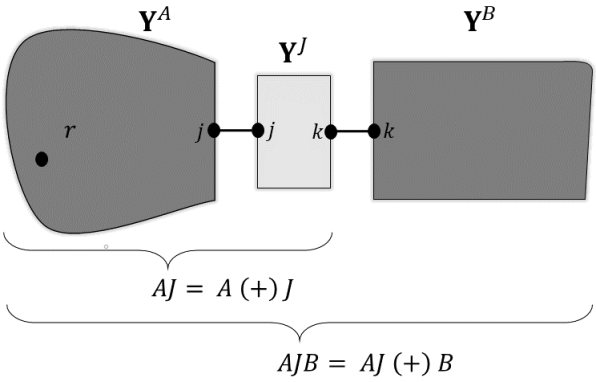

Fig. 5.6 Receptance coupling of three structures in two steps. In the first step, A and J are coupled forming the sub-assembly AJ. In the second step, AJ is coupled to B to form the final assembly AJB. Only a set of simplified DoF is indicated here. According to [166], A would be called the tool, J the extended holder, and B the spindle with no internal DoF.

The measurements are performed on the extendable tapered tool holder assembly whilst predicting analytically the individual receptances of the extended holder and the tool by the Euler-Bernoulli beam theory. It is remarked that the interface FRFs on J are obtained by the backward finite difference approach [65]. They showed the method worked fairly using Eq. (5.46). However, they needed to include some frequency and amplitude offset by introducing a joint model with damping and stiffness parameters, as per their previous approach [151]. Later, Kumar and Schmitz [172] used the same method but with the rotational FRFs calculated directly by the Euler-Bernoulli beam theory (instead of approximating by the finite difference formula) and showed improved prediction of the coupled system. The same method was also applied on a machine by Cheng et al. [173] by taking into account the rotational speed effect of the rotating tool head type machines.

Mehrpouya et al. [152] compared the two types of joint models using the IRC approach. They refer to the IRC approach when using the quasi-static joint whilst the inertial joint introduced in the IRC method is called the point mass model. The interface rotations on substructures were calculated analytically whilst using measured and predicted translations. Their experimental case-study was a modular tool assembly used in the milling process with the interchangeable cylinder as substructure A and the chuck as B. They measured three translational FRFs on the assembly, namely, $\mathbf{Y}_{rr}^{AJB}, \mathbf{Y}_{rj}^{AJB}$ and $\mathbf{Y}_{rk}^{AJB}$ since it was easily possible due to the simplicity of the geometries. The inertial joint model was modelled with no cross-coupling between translations and rotations, as follows:

$$\mathbf{Y}^J = \begin{bmatrix} k_t + i\omega c_t - m_t\omega^2 & \\ & k_\theta + i\omega c_\theta - m_\theta\omega^2 \end{bmatrix}^{-1} \tag{5.47}$$

where k_t, c_t, m_t are translational stiffness, damping and mass coefficients of the joint and likewise are the rotational counterparts for the subscript θ. Using the identified joint to recouple with A and B by both the joint types showed significant differences with each other as well as with the validation measurement near the resonances.

5.2.3 Concluding remarks on IRC

After reviewing the major IRC based methods, one can draw the process schematics as shown in Fig. 5.7. The mathematical treatment was seen to be different for the joint models. In this way, the approach becomes like a grey box in which a priori assumptions have to be made, as indicated in the figure. Due to the sensitivity of the methods to small unavoidable errors and noise, direct FRFs were seldom used. Instead the efforts were made to either apply modal or other filters, or update FE models, or use analytical models wherever possible. All the works tried to include interface rotations by computing them from explicit formulation, or by finite difference method, or implicitly included them by multi-point connection.

The assembly FRFs are always required to be measured for the experimental test-studies by using one or more elements of the coupled matrix. This provides a set of equations from which the joint can be obtained. The identification always comes out frequency dependent (noisy) which then requires some sort of parameter estimation by fitting based optimization schemes. In fact, the core difficulty lies in this aspect of the identification process in spite of simple test-geometries and very small joint systems – mostly 2×2 or 4×4 in the case of Ren and Beards [170].

In short, the general FBS framework provides an insight into the various IRC methods. It is almost impossible to go into details of each method, the mathematical links and major contributions of the research papers were outlined based on the six elements of general joint identification approaches (Section 5.1).

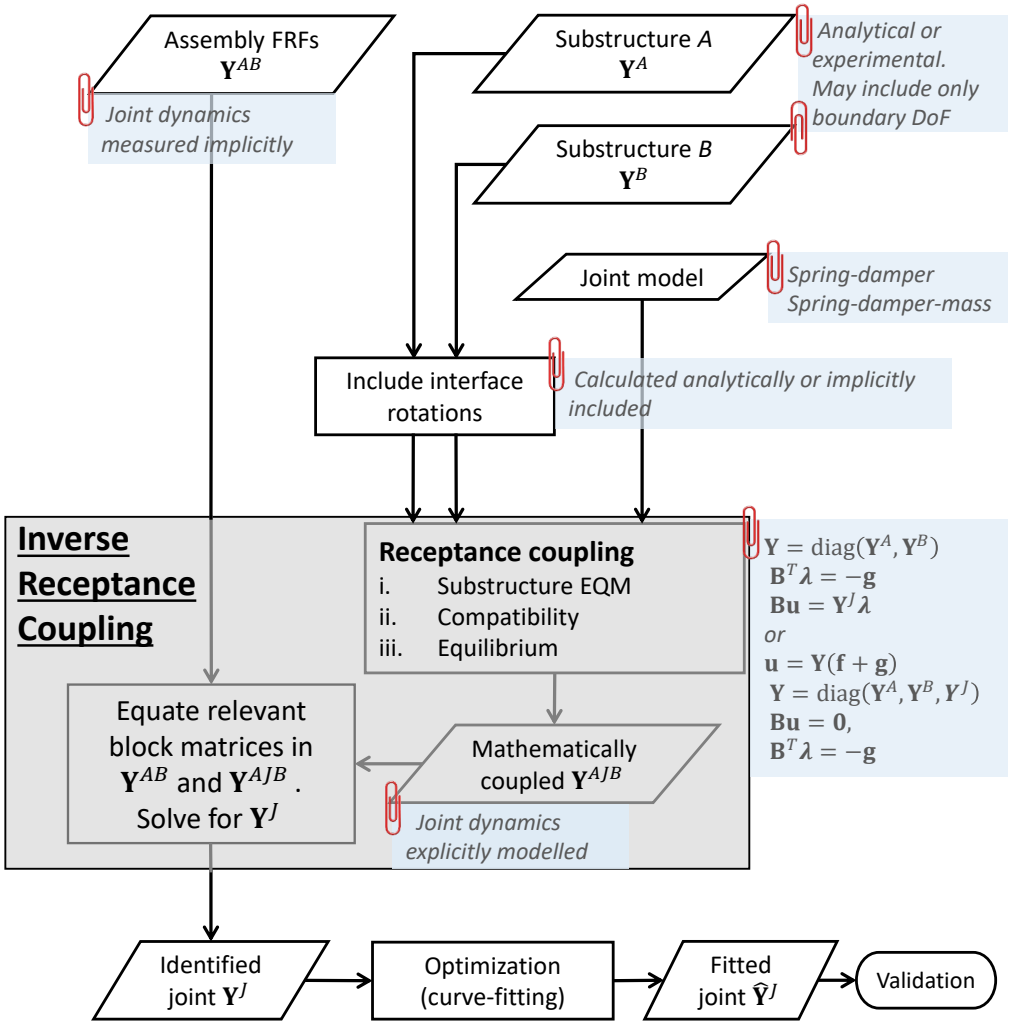

Fig. 5.7 Process flow of Inverse Receptance Coupling

5.3 Inverse Substructuring

Inverse substructuring (IS) is a class of methods suitable for dynamic identification of isolator properties connected between two substructures. These methods assume a certain form of the underlying mathematical quantities such as stiffness (refer to Section 5.1.3) to identify the joint element(s).

The vibration isolators or resilient elements are used to isolate the structure borne noise and vibration. They can be found in many engineering disciplines including auto-mobile engine mounts, resilient supports for buildings, flexible couplings for

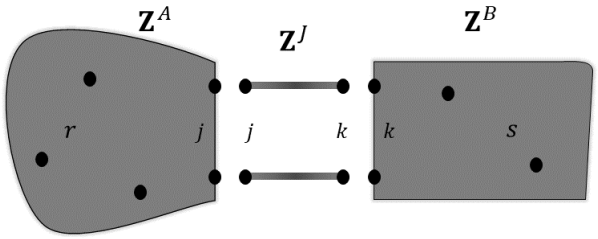

Fig. 5.8 Substructures A and B to be coupled through a resilient joint connection $\mathbf{Z}^J$

shipboard machinery and small isolators for domestic products [174]. Like other frequency based methods discussed herein, the preferred quantity, used for describing the resilient elements is also frequency dependent dynamic stiffness, denoted here by $\mathbf{Z}^J$ such that

$$\mathbf{Z}^J = \begin{bmatrix} \mathbf{Z}^J_{jj} & \mathbf{Z}^J_{jk} \\ \mathbf{Z}^J_{kj} & \mathbf{Z}^J_{kk} \end{bmatrix}. \tag{5.48}$$

Even though the IS methodology is based on the work by Zhen et al. [59, 175], the FBS framework presented in Chapter 2 is used, as done throughout this chapter. In order to mathematically identify $\mathbf{Z}^J$ from an assembly, let us create a coupled system by the primal coupling procedure presented in Example 1 of Section 2.2.2.1 for two substructures. In this case, three substructures or three dynamic stiffness matrices have to be considered, as shown in Fig. 5.8. The two connecting elements in the figure can be considered to be resilient. Let $\mathbf{Z}^A$ and $\mathbf{Z}^B$ be defined as:

$$\mathbf{Z}^A = \begin{bmatrix} \mathbf{Z}^A_{rr} & \mathbf{Z}^A_{rj} \\ \mathbf{Z}^A_{jr} & \mathbf{Z}^A_{jj} \end{bmatrix}, \quad \mathbf{Z}^B = \begin{bmatrix} \mathbf{Z}^B_{kk} & \mathbf{Z}^B_{ks} \\ \mathbf{Z}^B_{sk} & \mathbf{Z}^B_{ss} \end{bmatrix} \tag{5.49}$$

Note that the order of the internal s and interface k DoF in the partitioned matrix $\mathbf{Z}^B$ is reversed for didactic reasons. The three stiffnesses $\mathbf{Z}^A$, $\mathbf{Z}^J$ and $\mathbf{Z}^B$ are assembled by first putting them in a block diagonal matrix $\mathbf{Z} = diag(\mathbf{Z}^A, \mathbf{Z}^J, \mathbf{Z}^B)$ and the

localisation matrix $\mathbf{L}$, namely

$$\underbrace{\begin{Bmatrix} \mathbf{u}_r^A \\ \mathbf{u}_j^A \\ \mathbf{u}_j^J \\ \mathbf{u}_k^J \\ \mathbf{u}_k^B \\ \mathbf{u}_s^B \end{Bmatrix}}_{\mathbf{u}} = \underbrace{\begin{bmatrix} \mathbf{I} & \mathbf{0} & \mathbf{0} & \mathbf{0} \\ \mathbf{0} & \mathbf{I} & \mathbf{0} & \mathbf{0} \\ \mathbf{0} & \mathbf{I} & \mathbf{0} & \mathbf{0} \\ \mathbf{0} & \mathbf{0} & \mathbf{I} & \mathbf{0} \\ \mathbf{0} & \mathbf{0} & \mathbf{I} & \mathbf{0} \\ \mathbf{0} & \mathbf{0} & \mathbf{0} & \mathbf{I} \end{bmatrix}}_{\mathbf{L}} \underbrace{\begin{Bmatrix} \mathbf{q}_r \\ \mathbf{q}_j \\ \mathbf{q}_k \\ \mathbf{q}_s \end{Bmatrix}}_{\mathbf{q}} \tag{5.50}$$

with $\mathbf{q}$ as the primal DoF set. The assembled dynamic stiffness $\mathbf{Z}^{AJB}$ is then obtained by:

$$\begin{aligned} \mathbf{Z}^{AJB} &= \mathbf{L}^T \mathbf{Z} \mathbf{L}, \\ \mathbf{Z}^{AJB} &= \begin{bmatrix} \mathbf{Z}_{rr}^A & \mathbf{Z}_{rj}^A & \mathbf{0} & \mathbf{0} \\ \mathbf{Z}_{jr}^A & \mathbf{Z}_{jj}^A + \mathbf{Z}_{jj}^J & \mathbf{Z}_{jk}^J & \mathbf{0} \\ \mathbf{0} & \mathbf{Z}_{kj}^J & \mathbf{Z}_{kk}^J + \mathbf{Z}_{kk}^B & \mathbf{Z}_{ks}^B \\ \mathbf{0} & \mathbf{0} & \mathbf{Z}_{sk}^B & \mathbf{Z}_{ss}^B \end{bmatrix}. \end{aligned} \tag{5.51}$$

In the dynamic stiffness (or impedance) space, the coupling leads to summation of the dynamic stiffnesses corresponding to the boundary. The above equation can be written as a sum of three matrices

$$\mathbf{Z}^{AJB} = \begin{bmatrix} \mathbf{Z}_{rr}^A & \mathbf{Z}_{rj}^A & \mathbf{0} & \mathbf{0} \\ \mathbf{Z}_{jr}^A & \mathbf{Z}_{jj}^J & \mathbf{0} & \mathbf{0} \\ \mathbf{0} & \mathbf{0} & \mathbf{0} & \mathbf{0} \\ \mathbf{0} & \mathbf{0} & \mathbf{0} & \mathbf{0} \end{bmatrix} + \begin{bmatrix} \mathbf{0} & \mathbf{0} & \mathbf{0} & \mathbf{0} \\ \mathbf{0} & \mathbf{Z}_{jj}^J & \mathbf{Z}_{jk}^J & \mathbf{0} \\ \mathbf{0} & \mathbf{Z}_{kj}^J & \mathbf{Z}_{kk}^J & \mathbf{0} \\ \mathbf{0} & \mathbf{0} & \mathbf{0} & \mathbf{0} \end{bmatrix} + \begin{bmatrix} \mathbf{0} & \mathbf{0} & \mathbf{0} & \mathbf{0} \\ \mathbf{0} & \mathbf{0} & \mathbf{0} & \mathbf{0} \\ \mathbf{0} & \mathbf{0} & \mathbf{Z}_{kk}^B & \mathbf{Z}_{ks}^B \\ \mathbf{0} & \mathbf{0} & \mathbf{Z}_{sk}^B & \mathbf{Z}_{ss}^B \end{bmatrix} \tag{5.52}$$

or in a compact form

$$\mathbf{Z}^{AJB} = \bar{\mathbf{Z}}^A + \bar{\mathbf{Z}}^J + \bar{\mathbf{Z}}^B \tag{5.53}$$

where the overbars indicate the quantities with additional zero blocks. The isolator stiffness $\bar{\mathbf{Z}}^J$ can thus be found by subtracting $\bar{\mathbf{Z}}^A$ and $\bar{\mathbf{Z}}^B$ from $\bar{\mathbf{Z}}^{AJB}$, or

$$\bar{\mathbf{Z}}^J = \mathbf{Z}^{AJB} - \bar{\mathbf{Z}}^A - \bar{\mathbf{Z}}^B \tag{5.54}$$

If $\mathbf{Z}^A$, $\mathbf{Z}^B$ and $\mathbf{Z}^{AJB}$ are calculated by inverting their respective FRF matrices $\mathbf{Y}^A$, $\mathbf{Y}^B$ and $\mathbf{Y}^{AJB}$, respectively, then this approach would be similar to impedance modelling or the classical frequency based coupling methods (discussed in Chapter 2), since the inversions of the full FRF matrices lead to inaccuracies [40]. Furthermore, it requires measurement of the full assembly AJB and full substructure A and B. Since one needs to determine $\mathbf{Z}^J$, only connection DoF (j and k) can be sufficient. Let us assume that one has $\mathbf{Y}^{AB}_{jj}$ and $\mathbf{Y}^{AB}_{kk}$ from which the corresponding stiffness can be obtained, and likewise for substructures, then the following equation is sufficient for the identification:

$$\mathbf{Z}^J = \begin{bmatrix} \mathbf{Z}^A_{jj} + \mathbf{Z}^J_{jj} & \mathbf{Z}^J_{jk} \\ \mathbf{Z}^J_{kj} & \mathbf{Z}^J_{kk} + \mathbf{Z}^B_{kk} \end{bmatrix} - \begin{bmatrix} \mathbf{Z}^A_{jj} & \mathbf{0} \\ \mathbf{0} & \mathbf{Z}^B_{kk} \end{bmatrix}. \tag{5.55}$$

Even with this, the substructure stiffnesses are still needed. It is remarked that up until now, no assumption has been made about the resilient element. In fact, if the assumption about the resilient elements being massless compared to the substructures, are asserted, then the dynamic stiffness matrix of the element would have the off-diagonal terms equal to the diagonal terms in magnitude. This special property then provides a basis for the in-situ substructuring [176, 10, 174, 11]. The isolator dynamic stiffness then becomes

$$\mathbf{Z}^J = \begin{bmatrix} -\mathbf{Z}^J_{jk} & \mathbf{Z}^J_{jk} \\ \mathbf{Z}^J_{jk} & -\mathbf{Z}^J_{jk} \end{bmatrix}, \tag{5.56}$$

since $\mathbf{Z}^J_{jj} = -\mathbf{Z}^J_{jk} = -\mathbf{Z}^J_{kj} = \mathbf{Z}^J_{kk}$ and the reciprocity condition is applied. This property leads to the dynamic stiffness of the full system to become

$$\mathbf{Z}^{AJB} = \begin{bmatrix} \mathbf{Z}^A_{jj} - \mathbf{Z}^J_{jk} & \mathbf{Z}^J_{jk} \\ \mathbf{Z}^J_{jk} & -\mathbf{Z}^J_{jk} + \mathbf{Z}^B_{kk} \end{bmatrix} \tag{5.57}$$

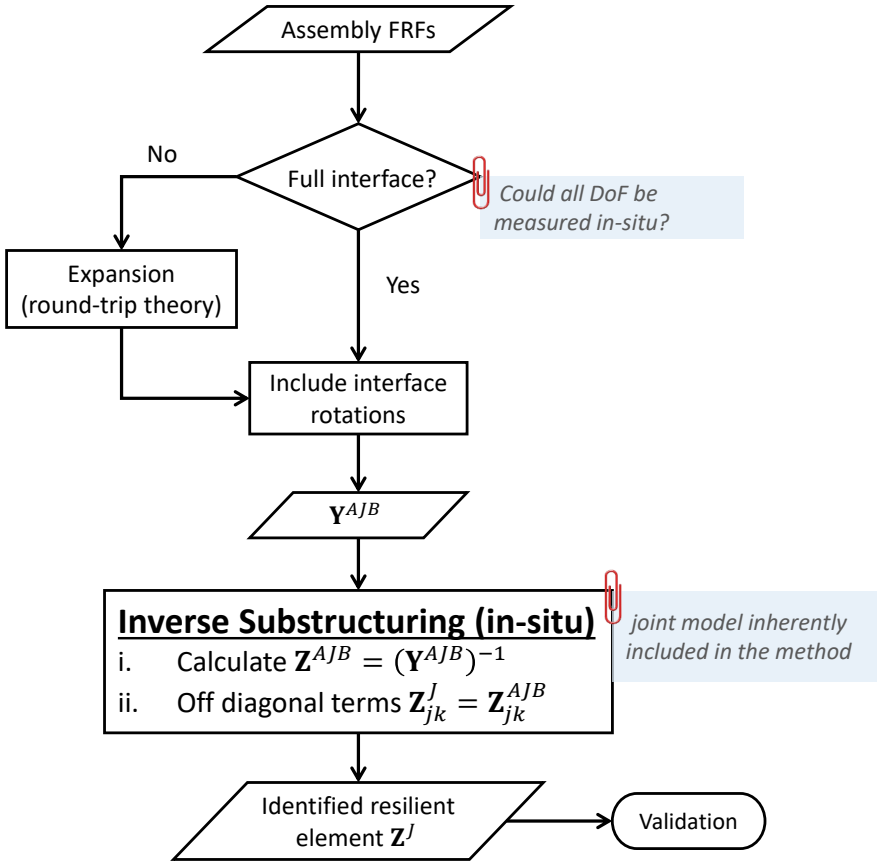

Fig. 5.9 General process flow for in-situ Inverse Substructuring

By using only the cross terms, the isolator's dynamic stiffness can be obtained. $\mathbf{Z}^{AJB}$ is calculated from the inverted measured FRFs and just by inspecting its off-diagonal terms, the isolator dynamics can be identified i.e. $\mathbf{Z}^{AJB}_{jk} = \mathbf{Z}^{J}_{jk}$. The in-situ identification does not require any substructure measurement. Its process flow is described schematically in Fig. 5.9. This type of identification becomes possible when the connection DoF in the assembly are accessible for measurement. Some expansion techniques can be used to obtain a full set of interface FRFs [92].

IS has, indeed, gained a lot of popularity and successful applications have been shown in the literature, see for example, [176, 10, 177]. In describing the interface dynamics, rotations have also to be considered in IS. Haeussler et al. [11] in their experimental study of the resilient joints used a virtual point type interface including translations and rotations. They have also investigated the negligible mass

assumption and the cross-coupling effect of different translational and rotational coordinates in their 12×12 system for the isolator. Other than identifying the isolator properties, FRFs of passive subsystem also need to be predicted or decoupled (see [7] on in-situ decoupling). An application to non-resilient joint systems has also been shown by Wang et al. [178]. In [179], linear inverse sub-structuring method is extended for non-linear systems, which can be applied to predict the FRFs of non-linear substructure only from the system-level FRFs of the coupled non-linear system.

5.4 Substructure Decoupling

Joint identification by Substructure Decoupling (SD) approach consists in removing (decoupling) the effect of substructures from their assembled system. SD is more general than IRC and IS, primarily due to the fact that it does not assume any a priori joint model. Thus, the identification methods in this class can be regarded as a black-box type identification.

Using the FRF matrices of the coupled system, the substructures' FRF are decoupled by their fictitious FRFs (preceded by negative signs). In Section 2.2.3, the decoupling process was demonstrated to identify one substructure from an assembly of two whilst neglecting any joint effects. It was seen there that the interface in this process may very well encompass the internal DoF set, the so-called extended interface. In fact, it can be argued that, other than the inherent ill-conditioning problem, the different formulations of the extended interface stem from the inability to account for compliance at the actual joint in substructure decoupling. Those interface formulations may improve substructure results in some applications but cannot be generalized [37]. By using SD, the joint between two jointed substructures can also be found in a similar way as done in Section 2.2.3.

In order to find the joint dynamics, we begin again by the three-filed formulation as below:

$$\begin{cases} \mathbf{u} = \mathbf{Y}(\mathbf{f}+\mathbf{g}) \\ \mathbf{B}\mathbf{u} = \mathbf{0} \\ \mathbf{B}^T\lambda = -\mathbf{g} \end{cases} \qquad \text{where} \quad \mathbf{Y} = diag(\mathbf{Y}^{AJB}, -\mathbf{Y}^{A}, -\mathbf{Y}^{B})\,. \tag{5.58}$$

The substructures receptances $\mathbf{Y}^A, \mathbf{Y}^B$ are decoupled by the negative signs. The equations can be (dis-)assembled by the LMFBS approach, as per Section 2.2.2.2 to yield the following joint equation

$$\bar{\mathbf{Y}}^J = \mathbf{Y} - \mathbf{Y}\mathbf{B}^T\left(\mathbf{B}\mathbf{Y}\mathbf{B}^T\right)^{-1}\mathbf{B}\mathbf{Y} \tag{5.59}$$

In this identification of joint $\bar{\mathbf{Y}}^J$, the following signed Boolean matrix can be used, assuming $\mathbf{Y}^{AJB}$ is primally coupled.

$$\mathbf{B} = \begin{array}{c} \begin{matrix} \mathbf{u}_r^{AJB} & \mathbf{u}_j^{AJB} & \mathbf{u}_s^{AJB} & \mathbf{u}_k^{AJB} & \mathbf{u}_r^{A} & \mathbf{u}_j^{A} & \mathbf{u}_s^{B} & \mathbf{u}_k^{B} \end{matrix} \\ \left[\begin{array}{cccc|cc|cc} -\mathbf{I} & \mathbf{0} & \mathbf{0} & \mathbf{0} & \mathbf{I} & \mathbf{0} & \mathbf{0} & \mathbf{0} \\ \mathbf{0} & \mathbf{0} & -\mathbf{I} & \mathbf{0} & \mathbf{0} & \mathbf{0} & \mathbf{I} & \mathbf{0} \end{array}\right] \end{array} \tag{5.60}$$

The compatibility is applied on the internal DoF in order to decouple their effect and obtain the joint dynamics. Since $\bar{\mathbf{Y}}^J$ is the result of a dual coupling, attention should be paid to the size of $\bar{\mathbf{Y}}^J$. In order to understand this, let N^A, N^B be the number of DoF (internal + boundary) in A and B, respectively, and N^J be the number of DoF on either side of the joint, then the total number of DoF for primally coupled AJB are $N^{AJB} = N^A + N^B$. From Eq. (5.59), the size of $\bar{N}^J = N^{AJB} + N^A + N^B = 2N^A + 2N^B$. In fact, one only needs to retain N^J rows and columns from $\bar{\mathbf{Y}}^J$ and so the final joint FRF matrix is denoted by $\mathbf{Y}^J$.

The SD process for a typical joint identification purpose is depicted in Fig. 5.10 indicating its generality as compared to IRC and IS. However, a great limitation in the joint identification by the SD method is that it assumes that the joint dynamics are explicitly present in the coupled system, represented here by $\mathbf{Y}^{AJB}$, unlike the inverse receptance coupling which exploits the implicit dynamics $\mathbf{Y}^{AB}$. If the interface DoF are not accessible in the assembly, SD based joint identification seems quite challenging. Several works by D'Ambrogio and Fregolent [35, 36, 56, 37, 180] and Voormeeren et al. [50] fall in the category of substructure decoupling or also called direct decoupling. However, these works targeted one of the two substructures as their main identification object instead of explicitly finding the joint. In terms of joint identification, the SD approach has only recently gained some attention including the work presented in this thesis. Expansion based strategies are needed to express the explicit joint effects, as shown in Fig. 5.10.

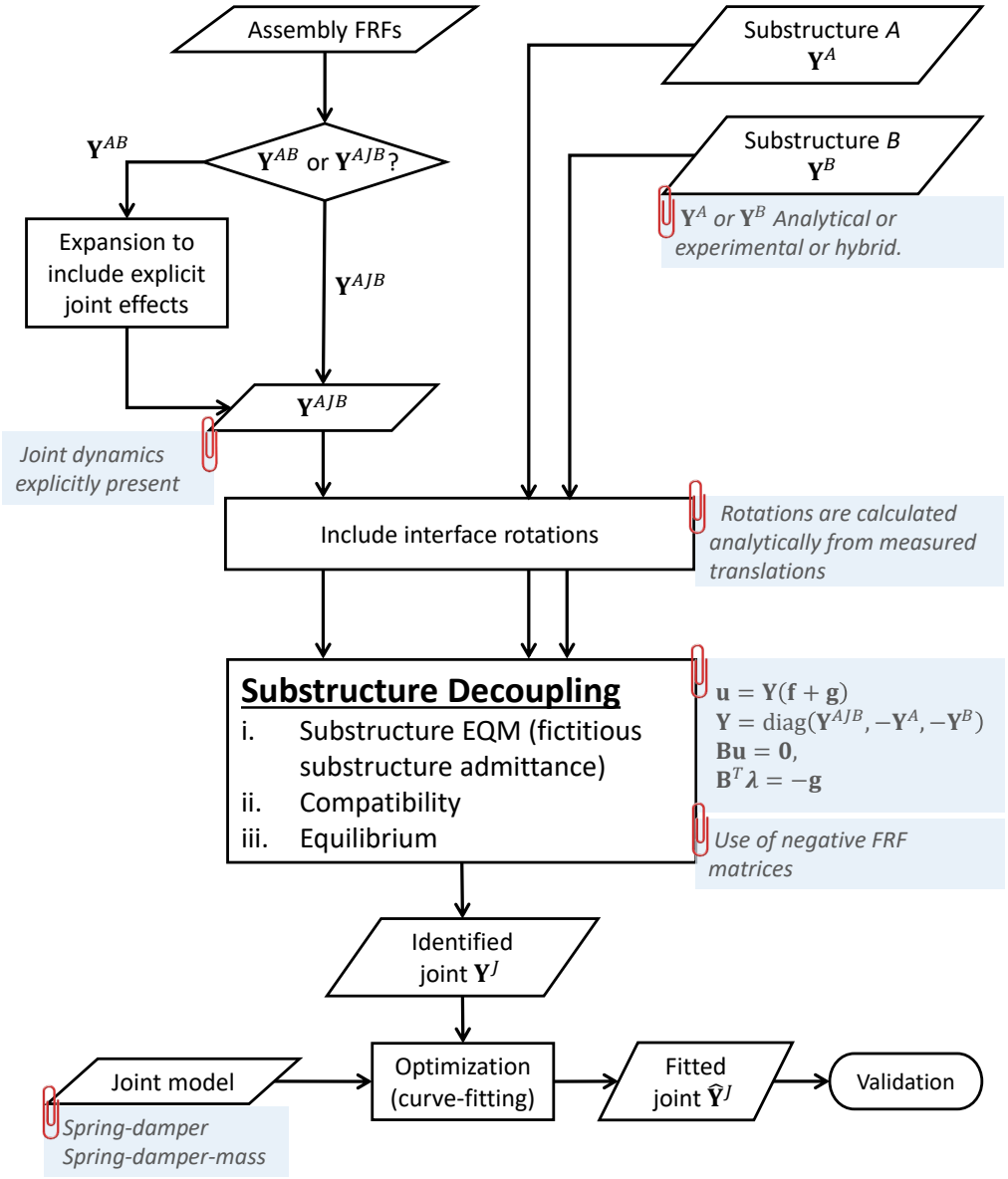

Fig. 5.10 General process flow for Substructure Decoupling

In fact, the very first numerical application of joint identification by SD can be attributed to Klaassen and Rixen [163]. However, they used the SEMM method to create a coupled system that consists of the explicit joint DoF. The experimental test-case joint of this thesis –the blade-root joint– has been investigated by this approach. The SEMM based substructure decoupling method will be explained in the next section and its results will be presented in Chapter 6 and 7. It will be seen that this approach enabled to identify a large joint system representative of the type of interfaces involved in this joint.

5.5 SEMM based Substructure Decoupling

In Chapter 3, the SEMM method was already explored to create an expanded substructure model. In the substructure decoupling of Section 5.4, it was pointed out that a coupled model $\mathbf{Y}^{AJB}$ with explicit joint dynamics is needed to enable a joint identification. Keeping this as our goal, this section presents how SEMM can be used on assembly level to predict an expanded assembly model $\mathbf{Y}^{\mathrm{S},AJB}$ from the expanded sub-models $\mathbf{Y}^{\mathrm{S},A}$ and $\mathbf{Y}^{\mathrm{S},B}$. The method is iterative in nature, since it requires successive coupling and decoupling procedures to determine the joint. The method was originally proposed by Klaassen and Rixen [163] on a numerical truss. Its first practical application on the blade-disk assembly was presented by Saeed et al. [70]. The following subsections stipulate the step-by-step approach.

5.5.1 Coupled numerical model

In order to create a numerical model of a single component, one could refer to a finite element software, as was done in Chapter 3. When one wants to create a numerical model of two connected substructures, it can be done by either coupling them rigidly or by adding some finite dynamic flexibility whose actual value is not known a priori. Since the expanded models of A and B ($\mathbf{Y}^{\mathrm{S},A}$ and $\mathbf{Y}^{\mathrm{S},B}$, respectively) were generated by SEMM, they shall be used as a basis for the coupled system's numerical model, denoted here by $\mathbf{Y}^{\mathrm{N},AJB}$. What remains to be done is adding the finite dynamic flexibility, called the guessed joint accelerance (or receptance, mobility) $\mathbf{Y}^{J}_{n}$. So, the coupled numerical accelerance $\mathbf{Y}^{\mathrm{N},AJB}$ can be written as:

$$\mathbf{Y}_n^{\mathrm{N},AJB} = fbs(\mathbf{Y},\mathbf{B}) \quad \text{with} \quad \begin{cases} \mathbf{Y} = diag(\mathbf{Y}^{\mathrm{S},A}, \mathbf{Y}_n^J, \mathbf{Y}^{\mathrm{S},B}) \\ \mathbf{B} = \left[\begin{array}{cc|cc|cc} \mathbf{u}_r^A & \mathbf{u}_j^A & \mathbf{u}_j^J & \mathbf{u}_k^J & \mathbf{u}_s^B & \mathbf{u}_k^B \\ \hline \mathbf{0} & -\mathbf{I} & \mathbf{I} & \mathbf{0} & \mathbf{0} & \mathbf{0} \\ \mathbf{0} & \mathbf{0} & \mathbf{0} & \mathbf{I} & \mathbf{0} & -\mathbf{I} \end{array}\right] \end{cases} \tag{5.61}$$

where the index $n = 1, 2, \ldots$ indicates the iteration number. The joint needs to be updated at every iteration and as a result, $\mathbf{Y}_k^{\mathrm{N},AJB}$ would also be updated.

5.5.2 Coupled experimental model

The measured FRFs on the coupled system $\mathbf{Y}^{\mathrm{exp},AB}$ contain joint dynamics implicitly. From this experimental model, an overlay model $\mathbf{Y}^{\mathrm{ov},AB}$ is taken as a subset and coupled with the numerical model $\mathbf{Y}_k^{\mathrm{N},AJB}$, according to Eq. (3.30). Note that this overlay model remains the same at each iteration. Obviously, the location of measurements on AB should be coherent with the DoF in the numerical model. The FRFs of the assembled system shall be coupled with $\mathbf{Y}^{\mathrm{N},AJB}$ which is a combination of two sub-models $\mathbf{Y}^{\mathrm{S},A}$ and $\mathbf{Y}^{\mathrm{S},B}$. Hence, the measurement locations on AB must correspond to the locations on A and B.

5.5.3 Coupled hybrid model

With the above coupled numerical and overlay models, the hybrid model is generated from Eq. (3.30) such that

$$\mathbf{Y}_n^{\mathrm{S},AJB} = semm(\mathbf{Y}_n^{\mathrm{N},AJB}, \mathbf{Y}^{\mathrm{ov},AB}) \,. \tag{5.62}$$

The hybrid model is also updated iteratively. Since $\mathbf{Y}_n^{\mathrm{N},AJB}$ has a guessed linear joint (or no joint can also be a tentative solution) at $n = 1$ which may be far from the actual one, so there may exist a high expansion error $|\mathbf{Y}_n^{\mathrm{N},AJB} - \mathbf{Y}^{\mathrm{ov},AB}|$.

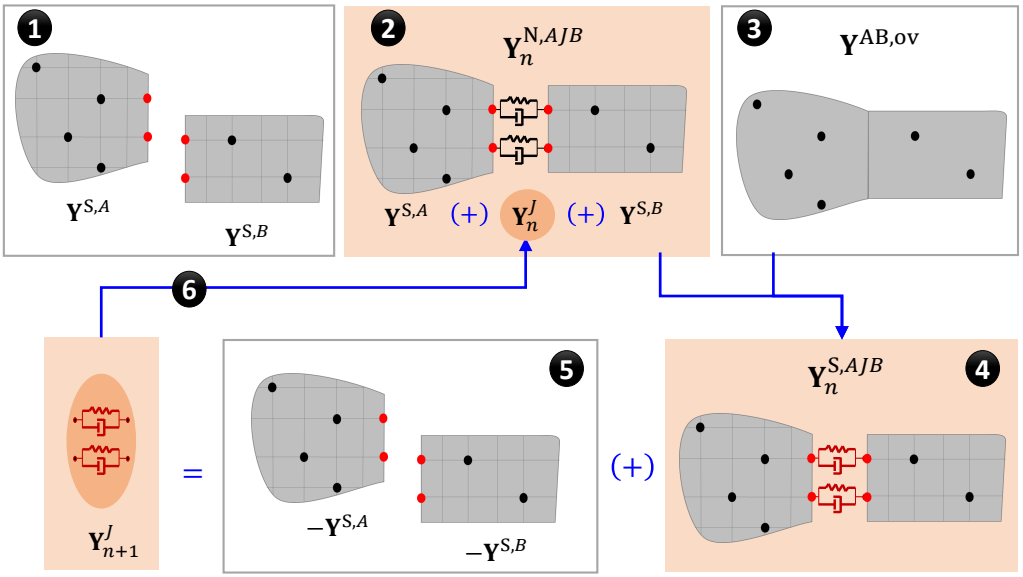

Fig. 5.11 The SEMM method at n-th iteration applied to an assembled system for joint identification. The quantities in the coloured blocks (2,4 and 6) are updated at each iteration k. The sign $(+)$ indicates coupling of substructures.

5.5.4 Identifying the joint

With the above models, it is now possible to decouple the joint dynamics by Eq. (5.63)

$$\mathbf{Y}_{n+1}^J = fbs(\mathbf{Y}, \mathbf{B}) \quad \text{with} \quad \mathbf{Y} = diag(\mathbf{Y}_n^{S,AJB}, -\mathbf{Y}^{S,A}, -\mathbf{Y}^{S,B}) \tag{5.63}$$

$\mathbf{Y}_{n+1}^J$ is then substituted in Eq. (5.61) to update the numerical model $\mathbf{Y}_{n+1}^{N,AJB}$, to subsequently generate an updated hybrid model $\mathbf{Y}_{n+1}^{S,AJB}$ in Eq. (5.62) and, thereafter, to decouple the joint $\mathbf{Y}_{n+2}^J$. The iterative process is graphically illustrated in Fig. 5.11. At each iteration, the updated joint improves because this is the only part that is updating the numerical model $\mathbf{Y}^{N,AJB}$. The process is repeated until the expansion error $\varepsilon = |\mathbf{Y}_k^{N,AJB} - \mathbf{Y}^{ov,AB}|$ between the numerical and the experimental model is reduced below a given threshold. It should be noted that:

1. The initial guess of $\mathbf{Y}_n^J$ at $n = 1$ can be a blank joint i.e. the substructures can be left uncoupled [163, 70].

2. $\mathbf{Y}_{n+1}^J$ obtained by LMFBS equation has all the rows and columns corresponding to the DoF of both the coupled and uncoupled models. It is necessary to retain only the independent entries [56].

3. The method converges faster by using weighted pseudo-inverses with higher weights assigned to the boundary DoF in Eq. (5.62). This aspect will be discussed in Section 5.5.6 and Chapter 7.

5.5.5 Interpretation

To identify the joint dynamics between two substructures A and B, we assume that we have trustworthy expanded models of the substructures, namely $\mathbf{Y}^{\mathrm{S},A}$ and $\mathbf{Y}^{\mathrm{S},B}$. To couple these sub-models, we make a first estimate of the interface dynamics $\mathbf{Y}_1^J$ to build a first estimate of the assembly $\mathbf{Y}_1^{\mathrm{N},AJB}$ which will be improved with measurements on the assembly $\mathbf{Y}^{\mathrm{ov},AB}$ by the SEMM procedure $\mathbf{Y}_1^{\mathrm{S},AJB}$. An improved estimate of the joint $\mathbf{Y}_2^J$ is then evaluated from this updated assembly model by decoupling substructures A and B. The new joint estimate $\mathbf{Y}_2^J$ is then used to create a new assembly model $\mathbf{Y}_2^{\mathrm{N},AJB}$ that is again updated $\mathbf{Y}_2^{\mathrm{S},AJB}$ with the same measurements $\mathbf{Y}^{\mathrm{ov},AB}$ and from which a further estimate of the joint dynamics $\mathbf{Y}_3^J$ is obtained by decoupling A and B. This iterative procedure can be repeated, assuming it converges to a joint for which the discrepancy between the model of the assembly and the measurements are minimized.

5.5.6 Weighted pseudo-inverses

It is interesting to point out that, when integrating the measured information in the parent model for the assembly, the inverses in Eq. (3.29) can be computed as weighted pseudo inverse. A diagonal weighting matrix $\mathbf{W}$ having different weights w for the DoF set is defined by

$$\mathbf{W} = diag(w_i, w_b) \tag{5.64}$$

where w_i and w_b correspond to the weights of internal and boundary DoF as before. Dropping the superscript of the coupled parent model's accelerance for clarity, the right-side pseudo inverse in Eq. (3.29) is then given by

$$\mathbf{Y}_{cg}^{+} = \mathbf{W}\,\mathbf{Y}_{cg}^{T}\,(\,\mathbf{Y}_{cg}\,\mathbf{W}\,\mathbf{Y}_{cg}^{T}\,)^{-1}, \tag{5.65}$$

and the left-side pseudo inverse

$$\mathbf{Y}_{ge}^{+} = (\mathbf{Y}_{ge}^{T} \mathbf{W} \mathbf{Y}_{ge})^{-1} \mathbf{Y}_{ge}^{T} \mathbf{W} . \tag{5.66}$$

Recall that $g = \{i, b\}$ is the global DoF set and $c, e \in i$ are the DoF set where measurements are performed. The above expressions hold if $\mathbf{Y}_{cg}$ has full row rank and $\mathbf{Y}_{ge}$ has full column rank. In case of rank deficiency or ill-conditioning, the inverses can be computed by singular value decomposition with the smallest singular values truncated.

The weighted pseudo inverses help expand the dynamics to the unmeasured DoF in a weighted least squares sense. Particularly, the physical boundary DoF $\mathbf{u}_b$ are assigned a higher weighting factor because these are the DoF to be identified in the process. This results in a decrease in the subsystem internal effects and an improvement of the convergence, as will be shown in Chapter 7.

5.6 Other identification classifications

In Sections 5.2, 5.3 and 5.4, many linear joint identification methods based on the proposed classification of IRC, IS and SD have been reviewed. It will be unfair to claim that other methods in literature also fall in these three classes. In fact, there may exist numerous other methods which use various other special techniques. They may not be put in these classes simply because they use a different formulation. One such method is by Hanss et el. [181] which uses fuzzy-valued parameters to model the uncertainty and variability of the model parameters identified from the measured data. It is also remarked that in almost all the the discussed identification methods, the uncertainty has not been accounted for obvious reasons of additional effort and absence of a robust and practical uncertainty framework suitable for inverse FRF problems. Some recent works for forward problems have been developed by Voormeeren et al. [49], Meggitt et al. [182] and Trainotti et al. [183].

Besides the jointed structures can easily become non-linear thus introducing yet another challenge in the identification process. For this purpose, parametric models are proposed to represent the non-linearity and energy dissipation due to slip in the joints [184]. Two review articles by Gaul and Nitsche [185] and Ibrahim and Pettit [141] provide a good primer on friction damping and non-linear identification in

bolted joints. For state-of-the-art in non-linear identification, one can refer to the recent review article by Noël and Kerschen [186].

5.7 Summary

This chapter is about the identification of a joint between two substructures. The joint identification being an inverse-problem consists in determining a set of joint parameters from the dynamics of the assembled system to account for the difference that exists between the assembled system and the substructures. The first section puts forth the basics of a general joint identification approach and introduces the essential elements including substructure and assembly dynamics, joint model and a mathematical framework. Based on the mathematical treatment and the approach, three classifications of joint identification are suggested, namely inverse receptance coupling (IRC), inverse substructuring (IS) and substructure decoupling (SD). These three classes of methods are reviewed from a mathematical point-of-view. The differences among all three are also presented in the form of their process flows.

The IRC methods, being the most popular in the tooling industry, have been extensively applied by many researchers. It has been demonstrated by the FBS approach that the different approaches stem from the same set of equations – usually one to two equations, and rarely three equations. The main differences in the approach are found in the treatment of rotational coordinates and fitting methods. The identified joint systems have been very small. The mathematical derivation for the joint also differs if the joint model is quasi-static or inertial.

The IS class of methods is more suitable to resilient elements where vibration isolation between a source subsystem and a receiver subsystem is the main objective. Using the FBS approach, it is shown that they use primal assembly of dynamic stiffnesses, instead of FRFs. They also employ a special topology of the dynamic stiffness by assuming massless isolators. Thus, the off-diagonal terms in the assembled stiffness matrix become a property of the isolator. Consequently, the isolator dynamic stiffness is found from in-situ assembly measurements whilst avoiding any substructure measurements.

A more broad and general class of joint identification is by SD which do not require any a priori joint model knowledge. These methods decouple the substruc-

ture's internal dynamics from the assembly model. However, due to the need of a full coupled matrix with explicit presence of the joint dynamics, they require expansion methods. Therefore, their applications have been limited.

Based on the SD method, the SEMM based decoupling is discussed in detail towards the end of this chapter. This method expands the measurements on a coupled system in order to obtain the explicit joint dynamics. This enables one to identify a joint by substructure decoupling which is more suitable to inaccessible interfaces and large joint systems. This method will be applied to the test-subject of this thesis in the following chapters.

Chapter 6

On the Interface Description of the Blade and the Disk

Part of the work described in this chapter was previously published in [62, 69, 71].

In Chapter 5, the joint identification method based on the SEMM expansion was presented. As with any joint identification method, the interface dynamics (measured or expanded) have to be adequately described. This implies that not only the translations but also the rotational DoF should be included in the interface. In the SEMM expansion, a numerical model that consists of only translations is usually generated by a Finite Element method (or its reduced form), as shown in Chapter 3 and 4. Alongside, an experimental model is also required that consists of the translational FRFs due to the reasons discussed in Chapter 5. The resulting expanded model by SEMM also consists of only the translational FRFs. Therefore, the rotational information at the interface is yet to be derived. The rotational dynamics can possibly be extracted from the limited expanded translational FRFs[1] in the expanded model.

Even if an interface consists of translations and rotations, their number and positions always have to be explored in an experimental setting due to uncertainty of the contacting DoF in the assembly. In order to understand and physically observe the variability at the interfaces, the static contact under a fixed pre-load was studied

[1]Despite being full rank, the condition number of a SEMM expanded model increases when extra numerical DoF (to be expanded on the interface) are included, as shown in Section 3.6.2. Therefore, the number of DoF to be expanded have to be limited. Whilst there are no hard guidelines on this number as yet, one is supposed to make a judgement call on this matter.

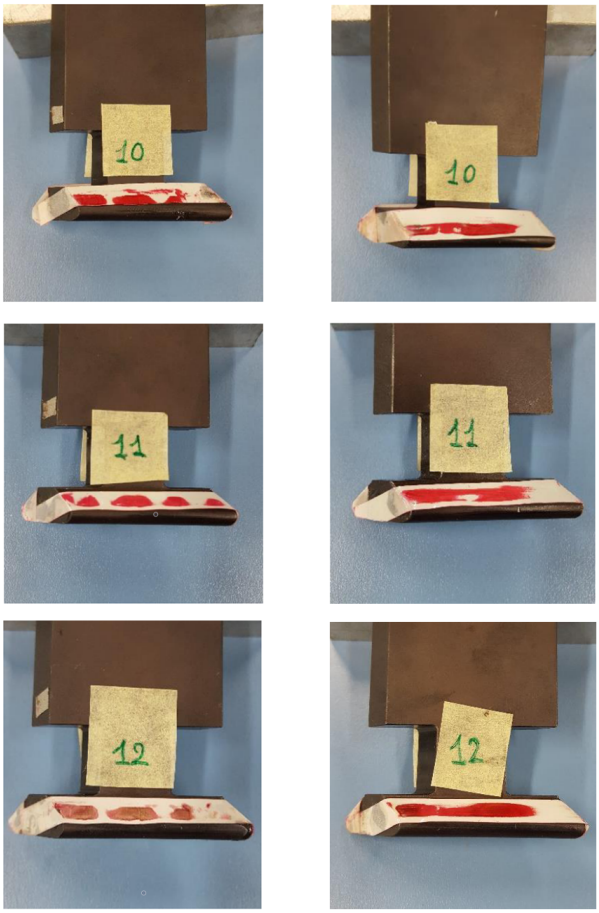

Fig. 6.1 Testing the static contact conditions on three different blades on the VITAL bladed-disk. The left and right pictures of each blade correspond to the two contacting sides [187].

on the VITAL bladed-disk [187]. Strips of changeable colour were installed on three blades (blade number 10, 11 and 12) when subjected to a certain pressure. The strips were carefully glued on these blades which were then assembled in their respective disk-slots by tightening the bolts. After carefully removing them, the variable and unpredictable patterns were observed on the blades, as depicted in Fig. 6.1. In all the three cases shown, a strong inhomogeneity of the blade attachment is clearly evident. Its effect on the structural dynamics of the whole assembly can then be considered to be more pronounced.

The above study indicates that it is of paramount importance that one determines in advance a certain number of interface DoF on more representative locations. This is usually achieved by performing sensitivity tests and knowing to what extent

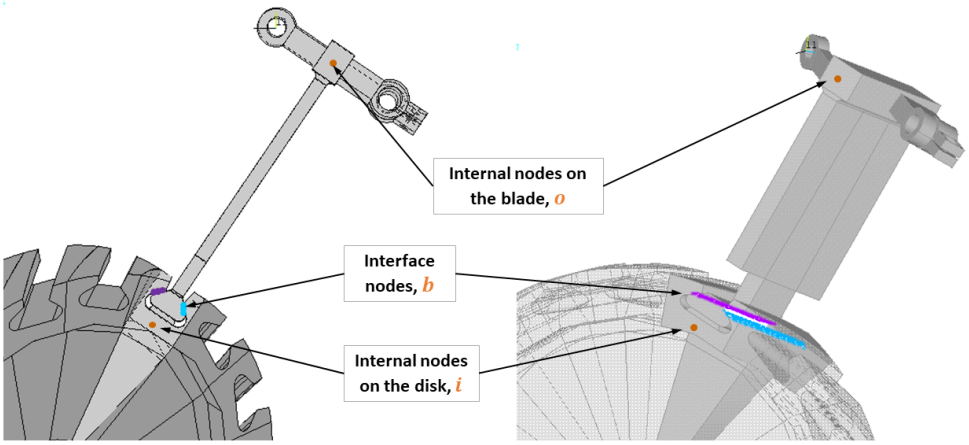

Fig. 6.2 A single blade and disk assembly showing the node locations. In this section, the indicated nodes o and i correspond to response (output) and force (input), respectively.

(frequency bandwidth), a reasonable prediction can be made. These aspects are mainly the objective of this chapter for the blade and the disk coupling interfaces. To characterize these interfaces, two sensitivity studies are performed in the following sections: a numerical translational DoF based analysis in Section 6.1 and a test-based mix of translational and rotational DoF analysis based on the virtual point methodology in Section 6.2.

6.1 A numerical investigation of the blade-disk interface

This section presents a numerical analysis on a single blade connected with the disk of Fig. 6.2 by perturbing the interface between the blade and the disk. The coupling of the two components is achieved by the LMFBS coupling method described in Section 2.2.2 without any joint effects. That is, a rigid coupling is realized by coupling different DoF to be shown later.

The disk as a stand-alone substructure is constrained at the centre whereas the blade is not constrained. Both the disk and the blade in this study are made of Steel with Young's modulus $E = 206$ GPa and density $\rho = 7800$ kg/m^3. The numerical models are generated in ANSYS using solid brick elements. All the DoF in this type of element are translational. A sufficient mesh refinement is performed to

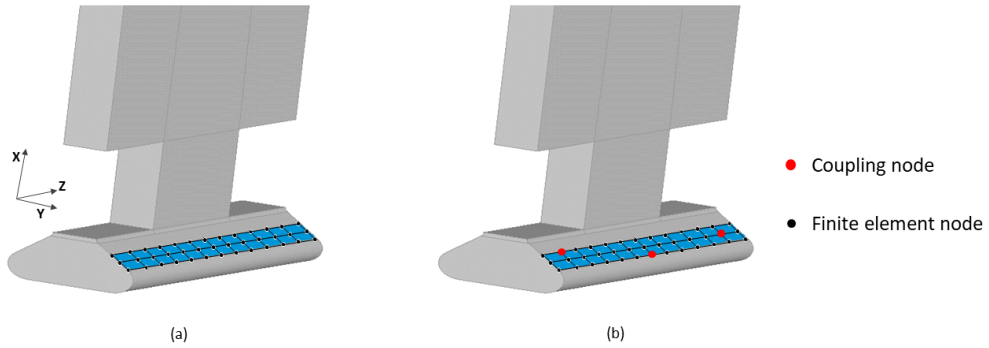

Fig. 6.3 An indicative set of nodes on the interface of the blade. The disk has the same set of nodes, generated from congruent meshing. Each node has three DoF. (a) All the finite element nodes on the interface are selected as master nodes for Craig-Bampton reduction. (b) An example of the nodes to be considered for coupling the blade and disk for the interface sensitivity analysis.

achieve convergence of the lower modes. Since a full disk computational model is required instead of a sector, a model order reduction was done according to the Craig-Bampton method [13] by selecting the whole interface ($490 \times 3 = 1470$ DoF) and an internal node ($1 \times 3 = 3$ DoF) as the master DoF and a set of fixed interface modal coordinates. The different node labels are indicated in Fig. 6.2. The blade finite element model was also reduced by selecting the same set of master DoF as on the disk. An indicative set of master DoF set is shown in Fig. 6.3. From the reduced system matrices, the FRF models are calculated by using the subsets of normal modes (SNM) [28, 111].

The FRFs obtained by keeping different number of normal modes in the modal superposition method revealed some interesting findings. Fig. 6.4 shows the drive-point FRF of the disk substructure (at i-th DoF in X-direction in Fig. 6.2) constructed by different normal modes. The solution required high number of modes at least up to 100 for the non-resonance response, as seen clearly in Fig. 6.4. If the disk FRFs are generated with 20 normal modes and subsequently coupled with the blade (having the same number of modes) according to the LMFBS method, then the reconstructed coupled response in Fig. 6.5 looks quite noisy. The response is captured well around the resonances but the remainder part has a lot of spurious peaks. Note that all the interface DoF are used in the coupling of FRFs; the only deficiency in the substructure FRFs comes from the lack of sufficient number of modes.

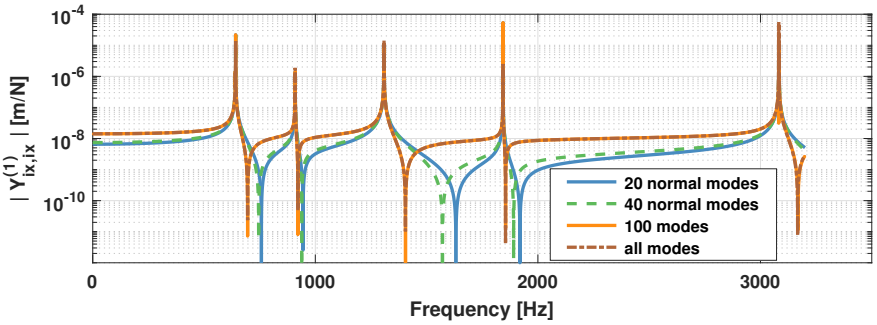

Fig. 6.4 Effect of normal modes on drive point FRF $\mathbf{Y}_{ix,ix}$ of the disk by considering different normal modes.

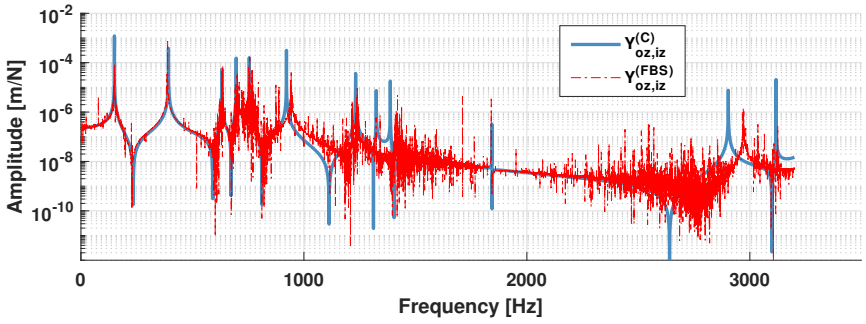

Fig. 6.5 Effect of low number of normal modes on the reconstructed FRF $\mathbf{Y}^{(FBS)}_{oz,iz}$ of the coupled structure compared with the reference solution $\mathbf{Y}^{(C)}_{oz,iz}$. Number of normal modes = 20.

In Rixen [48], the effect of measurement inaccuracies was investigated theoretically covering mainly three important factors: namely, pole-shifting, inconsistent modal content and measurement noise. These phenomena can cause spurious peaks in the coupled system which can be wrongly interpreted as modes of the coupled system. In the present case of the spuriousness in Fig. 6.5, we have investigated only one factor i.e. inconsistent modal content. By including a small number of modes to describe the disk substructure, the calculated FRFs are not true FRFs, as indicated by the moving anti-resonances. Since anti-resonances are local to each FRF, in contrast to the resonances as global properties, the modal content is perturbed in the disk for the selected set of 20 modes. Consequently, the spurious peaks are observed in the coupled blade-disk system in Fig. 6.5. This problem can be compared to an experimental substructure when the modal residuals (upper) are too significant to ignore. The resulting coupling will be detrimental, as shown here for the numerical

case. For more mathematical details on this subject, the readers should refer to Rixen [48].

In the discussion to follow, 100 modes are included to compute the blade and disk FRFs. From these FRF models, we select only a few nodes to couple the blade and the disk in order to predict the response of the reference system, as indicated in Fig 6.3. The intent is to simulate an experiment in which only a few DoF can be measured. So by doing this, it will be estimated which and how many translational DoF should at least be considered to define a proper interface. Since there are numerous DoF at the interface, the rotations are implicitly included in the coupling process [66].

By consecutively including one, two, three and four number of nodes per side of the interface (i.e. there are two sides of the interface and 3 DoFs per node), the FRFs reconstructed for the coupled system using the LMFBS method are shown in Fig.6.6. The interface nodes are also shown to the left of each sub-figure. The comparison is made with the reference FRF which is calculated by coupling all the interface DoF, as it was done in Fig 6.5.

The results improve by successively increasing the number of nodes or DoF. Clearly, 1 interface node per side (6 DoF for the total interface) are not enough in Fig. 6.6(a). By considering 2 interface nodes per side (12 DoF – Fig. 6.6(b)), the coupling has improved up to 1200 Hz. Since the damping is not included, differences in the amplitude peaks at resonances are ignored. The first high modal density region between 600 Hz to 760 Hz is very well approximated even with just two interface nodes per side. It is further seen quantitatively in Table 6.1 that mode 3, 4 and 5 have a small error of less than 2% with just 2 nodes per side. This implies that the choice of nodes gives nearly rigid behaviour of the interface for these frequencies. The high frequency region, of course, would need more DoF for a better reconstruction. The choice of number of interface nodes depends on the modes of interest.

For the case of 2-node interface of Fig. 6.6(b), a further sensitivity is done against the distance between the two nodes which is presented in Fig. 6.7. The relative error is high if the two nodes are closely spaced. It starts decreasing as the distance increases, however, an increasing error can be noticed if the nodes are placed at the edges especially for the first mode. The FRF shown earlier in Fig. 6.6(b) corresponded to the location that had the lowest error.

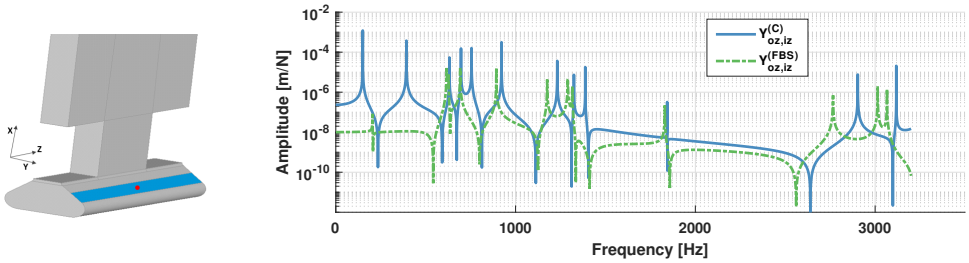

(a) 1 interface node per side

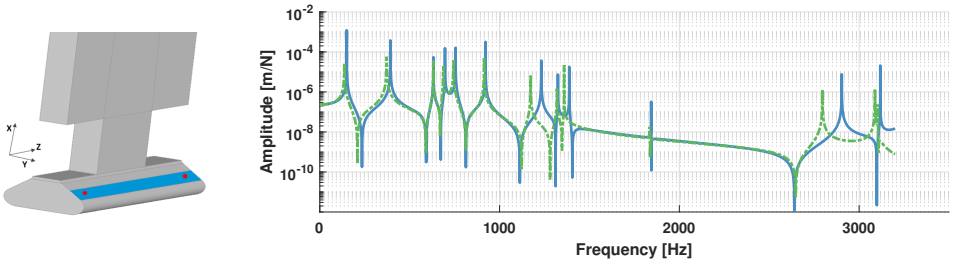

(b) 2 interface node per side

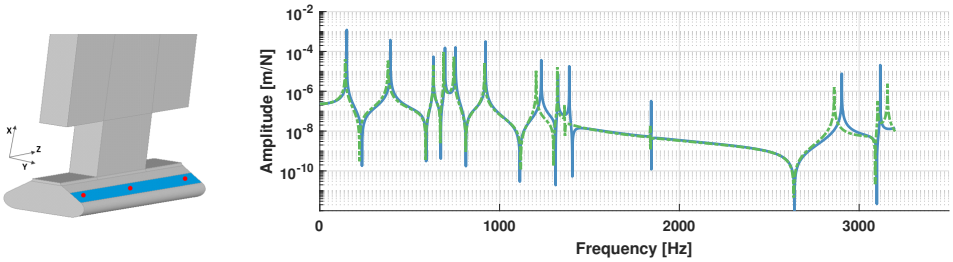

(c) 3 interface node per side

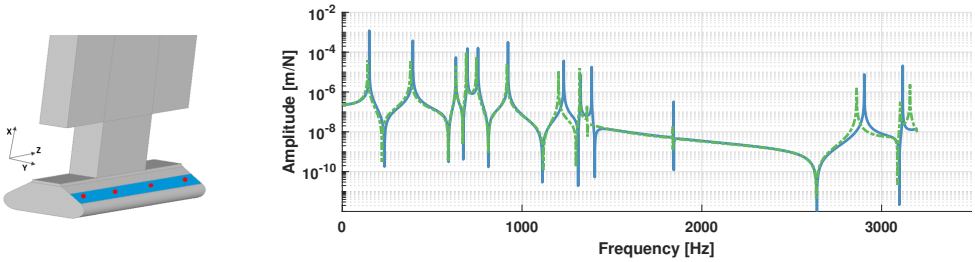

(d) 4 interface node per side

Fig. 6.6 FRFs obtained by the LMFBS method on the bladed-disk by considering different nodes per side. Each node is described by 3 DoFs.

6.1.1 Remarks on the numerical sensitivity analysis

From this analysis on a numerical test system, it is evident that the final coupled response (without a joint model in between) is highly sensitive to the location and

Table 6.1 Relative error in natural frequencies of the coupled blade and disk by the LMFBS method.

Nodes per side	Mode1	Mode2	Mode3	Mode4	Mode5
1	15.9%	55.4%	-2.4%	-3.7%	17.7%
2	-8.8%	-5.2%	-0.2%	-1.4%	-1.5%
3	-6.1%	-3.4%	-0.2%	-1.1%	-1.2%
4	-4.5%	-2.7%	-0.2%	-0.8%	1.1%
5	-4.1%	-2.2%	-0.2%	-0.6%	-0.8%

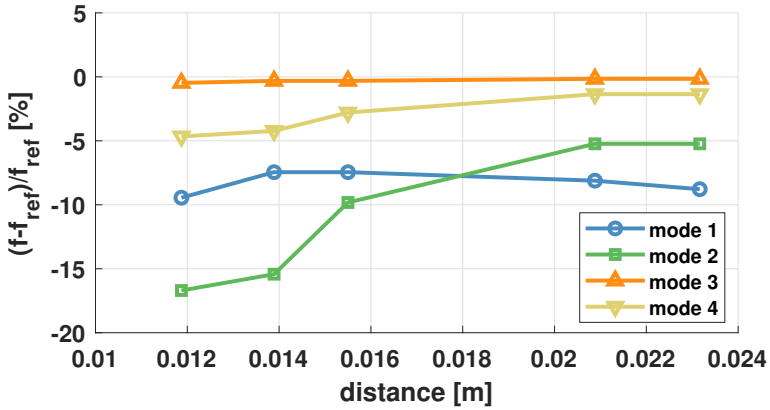

Fig. 6.7 Relative error in modal frequencies for 2-interface nodes per side as a function of distance between the nodes. f_{ref} is the reference frequency of the reference system.

number of DoF. Since these DoF are selected in a non-collinear way (no three DoF fall on a line for more than 1 node-per-side cases), the rotational effect is implicitly included in the interface [66]. Hence, a better coupling system response is observed for two or more nodes-per-side cases. This means that this type of interface in which only two sides are considered, at least two nodes-per-side (or 12 translations) must be measured for a reasonably representative coupled system. On an actual system, a 12×12 FRF matrix should be constructed for each substructure. For this case, the nodes should neither be right at the edge nor in the middle of the interface. This study thus gives a great insight on how to approach this type of interface experimentally. It should also be remarked that only two sides of this interface are considered in the numerical tests. The actual interface has also the third side for fastening purpose, as will be seen later. One can thus anticipate a bit more complex interface behaviour in an experimental setting to be discussed in the next section.

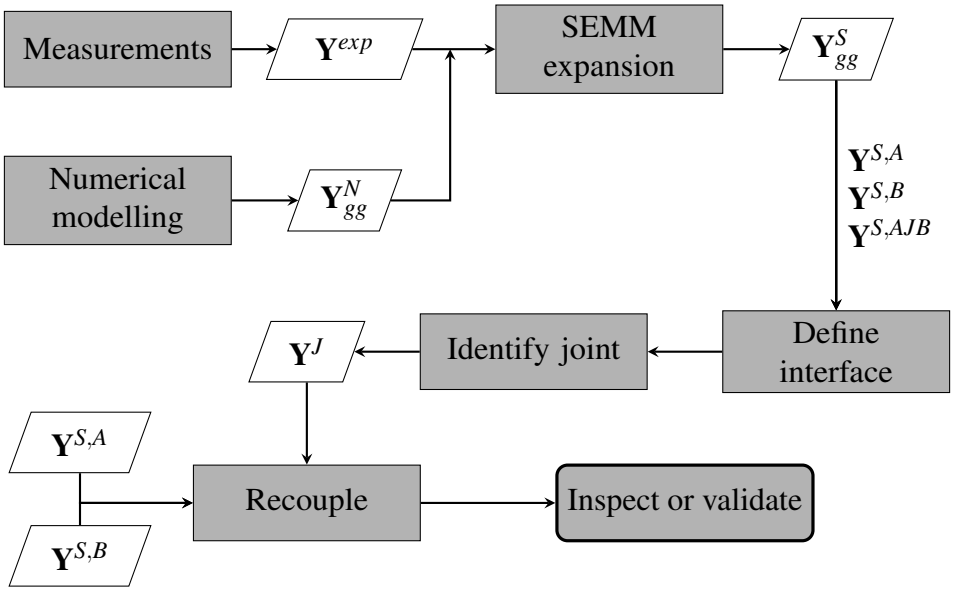

Fig. 6.8 The process for inspecting and validating an interface through the SEMM decoupling method

6.2 An experimental investigation of the blade-disk interface

An interface provides the links or paths through which the dynamic coupling between substructures is established. The more accurately they are measured or expanded, the more accurate will be the coupled system's predicted dynamics (also for the decoupling or joint identification). Therefore, it is essential that the interface is described appropriately.

In this section, different cases of interface coupling of the actual blade and disk are studied. Since there is some compliance at the interfaces in the actual blade-disk, a rigid coupling of the blade and disk cannot produce the response of the reference assembled system (measured). A joint model has to be inserted in between the two substructures. The SEMM based decoupling method, as presented in Section 5.5 is then used to identify the joint. A detailed discussion on the method and its convergence is done in Section 7. Furthermore, to make the comparison of interfaces fair, the identified joint dynamics are not compared with each other as the joint system and size, depending on the interface type, would be different. Instead, the identified joint (converged) for each interface type is recoupled to the blade and

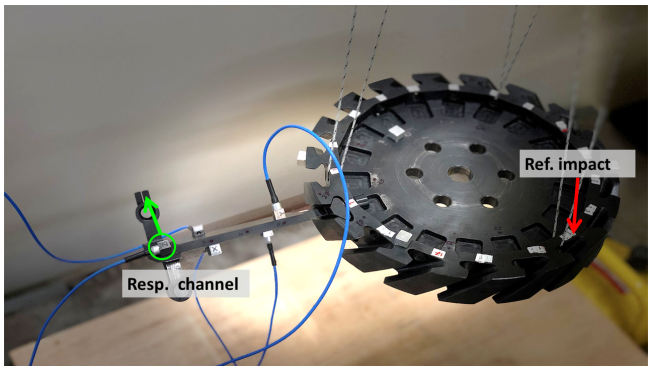

Fig. 6.9 Assembly of the blade and disk. Due to limited data acquisition system channels availability, the assembly measurements were carried out in two steps. The picture of the assembly shown is one of those steps in which the sensors are mounted on the blade. The arrows represent the locations of reference FRF measurements for validation. The measurement locations of sensors and impacts are identical to those on the single blade and disk.

disk and compared with the reference FRF measurements which were not used in the identification process. This process is depicted schematically in Fig. 6.8.

6.2.1 Measurements on the assembly

Since this process requires a set of measurements on the assembly, in addition to the individual substructures (already shown in Chapters 3 and 4), an actual measurement campaign had to be conducted. The measurements on the assembly presented here were a part of campaign-2 discussed in Section 3.5 and 3.6. In order to identify the joint using the SEMM decoupling method, the assembly AB should have the same measurement locations as on the substructures A and B. Therefore, all the sensor and impact locations of Fig 3.8 are retained whilst performing measurements on the assembled blade and disk.

Figure 6.9 shows the sensors (triaxial accelerometers) and impacts positions for reference (validation) measurements. The key details regarding the experimental setup and the different models are consolidated in Table 6.2.

Table 6.2 Measurement channels and models details for the joint identification

Description	**Blade** A	**Disk** B	**Assembly** AB
Number of response channels (α)	15	15	30
Number of impacts (β)	18	19	37
Experimental validation channels	–		Figure 6.9
Total internal DoF ($\gamma = \alpha + \beta$)	33	34	67
Size of experimental FRF matrix $\mathbf{Y}^{ov}$	14×18	14×19	27×36 [2]
Number of Boundary DoF [3]	27	27	–
Size of numerical FRF matrix	60×60	61×61	– [4]
Size of hybrid FRF matrix (before VP transformation)	60×60	61×61	–

6.2.2 Translational DoF interface

In the numerical models of the blade and disk, some translational DoF on the mating surfaces are selected as representative boundary DoF (Figure 6.10b and 6.10c) which are then expanded over in their respective hybrid models. Since the expansion is done by virtue of measurements on the internal DoF, it is assumed that these DoF can properly represent the interface DoF. However, it is not true for any arbitrary set of interface DoF, because different interface DoF combinations will produce different effects (as discussed in Section 6.1 and to be discussed next).

It is seen in Figure 6.10 that the blade-root joint has three mating sides. A total of 27 translational DoF (9 nodes) are selected on these sides, indicated in Figure 6.10b and 6.10c. The nodes are shown only on the blade. Of course, a corresponding set is also selected on the disk interface. Among these nodes, multiple combinations can be tried. We examine only two cases of 12 DoF per substructure (24×24 joint model) here:

Case 1: Coupling of the DoF at nodes $\{1,3,4,6\}$ – two physical nodes on the left and two on the right side, as shown in Figure 6.11a.

[2] One sensor channel had unusually high noise and it had to be discarded, therefore, the experimental FRF matrices are one channel short for the blade and disk and two channels short for the assembly. However, one response channel and one input channel was additionally left out for the validation in the assembly.

[3] These DoF are inaccessible and expanded over. Some or all of the boundary DoF are then used to represent the interface.

[4] The size of the coupled system depends on the interface type and the formulation in FBS (primal or dual).

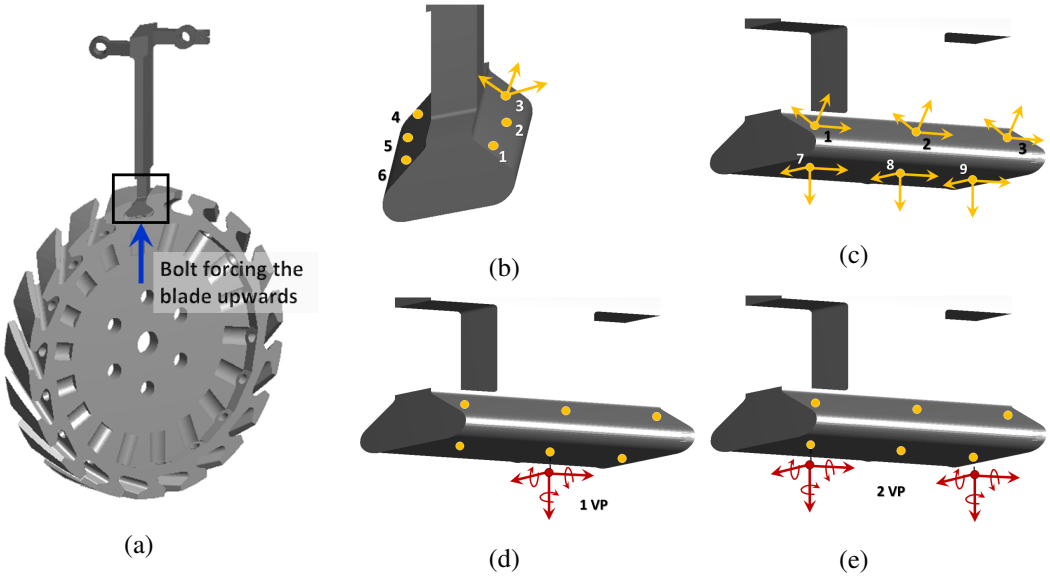

Fig. 6.10 Different representations of interface DoF on the blade. (a) Assembled blade and disk depicting the connection (b) Left and right surfaces on the blade interface with three translational DoF per node. (c) Another view of the blade interface indicating additional three nodes on the bottom surface. (d) One virtual point interface formed by transforming all the translational DoF on nodes 1 through 9. There are six DoF per virtual point. (e) Two virtual point interface.

Case 2: Coupling of the DoF at nodes $\{1,4,7,9\}$ – one physical node on the left, one on the right and two on the bottom, as shown in Figure 6.11b.

Remark 2. ***Identification Rank:*** *Since measurements on the assembled system have a rank of 27 (see Table 6.2), one can identify a joint with the same maximum rank. However, one or more channels are kept for validation and we allow for some over-fitting, the maximum rank of the joint system is set to be 24. That is, a* 24×24 *joint FRF matrix is identified.*

The reconstructed FRFs in blue in Figure 6.11 are obtained by recoupling the identified joint $\mathbf{Y}^J$ with the hybrid model of the blade $\mathbf{Y}^{S,A}$ and disk $\mathbf{Y}^{S,B}$. Note $\mathbf{Y}^J$ is retrieved after the convergence criterion has been met, as outlined in Section 5.5. Clearly, the interface of Case 1 has a lot of spurious effect even though it follows the shape of the reference FRF (orange colour in Figure 6.11a), even though this interface configuration resembled the one in Fig. 6.6. This means that by considering only two sides of the interface, the joint is not properly identified. Note that the

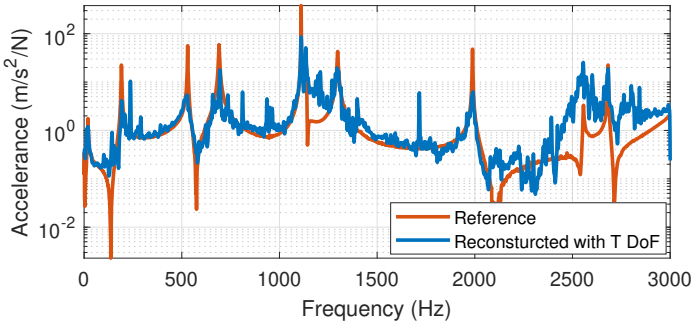

(a) Interface nodes set {1,3,4,6}

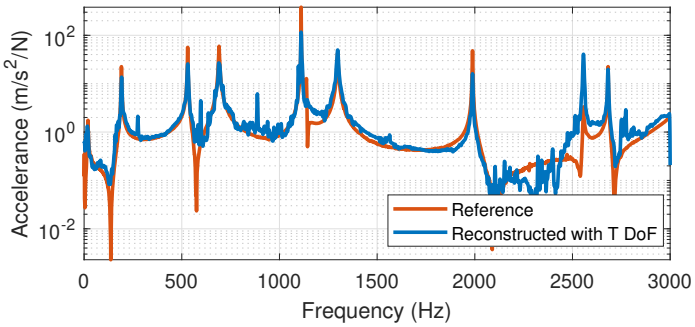

(b) Interface nodes set {1,4,7,9}

Fig. 6.11 FRFs on the coupled blade-disk by considering only translational DoF at the interface. The reference FRF is measured at the locations shown in Figure 6.9.

reference FRF corresponds to the DoF not included in the identification procedure, also discussed in the footnotes of Table 6.2.

In Case 2, the third (bottom) side of the interface is taken into account through nodes 7 and 9. The reconstructed FRF (Fig. 6.11b) overlaps the reference FRF well until 2000 Hz with the exceptional spurious peaks around 250, 600 and 800–1000 Hz. The response near anti-resonance of 600 Hz is also not accurately predicted. The reconstructed FRF of Case 2 is certainly better than that of Case 1 because the bottom side is thought to be a key location where the bolts are connected and push the blade to fit the other two surfaces of the disk. The interface seems to be better described by these locations and it gives an idea to consider these locations for further analysis. However, an interface defined by only the translational DoF of the two bottom nodes (7 and 9) would not be sufficient i.e. the other sides should also be considered.

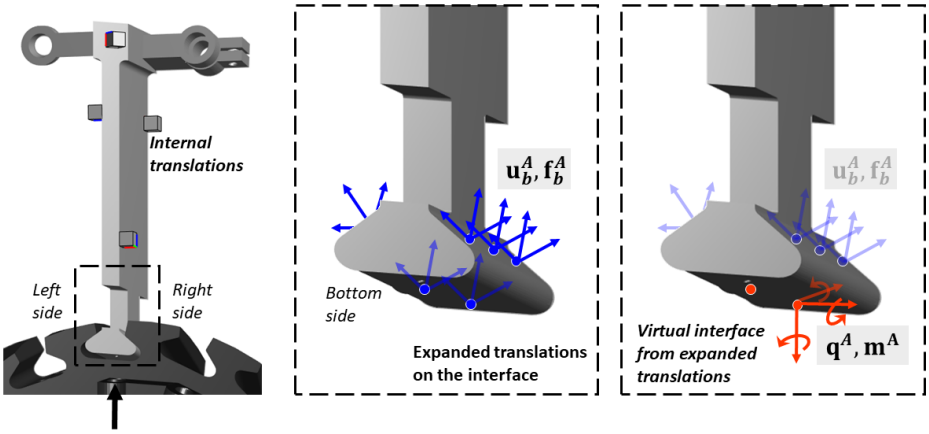

Fig. 6.12 The measured internal translations are expanded as translations on the interface (blue) which are further transformed to virtual translations and rotations (orange).

6.2.3 Virtual point interface

In an interface defined only by the translational DoF, the selection of the corresponding nodes is an arbitrary choice of the user in terms of location (and numbers of nodes) involved in the identification. Therefore, many combinations are possible and it is not easy to understand what is the most promising combination. This problem can be overcome by creating a virtual interface characterized by both translations and rotations. All the measured or expanded translational DoF can then be used and projected to the virtual interface by least-squares [153]. Consider the hybrid model, for example, of the blade $\mathbf{Y}^{S,A}$ with the expanded dynamics on all the translational DoF $\mathbf{u}_b^A$ in Fig. 6.12. The boundary translations $\mathbf{u}_b^A$ relate to the virtual displacements (translational and angular) $\mathbf{q}^A$ by:

$$\begin{Bmatrix} \mathbf{u}_i^A \\ \mathbf{u}_b^A \end{Bmatrix} = \underbrace{\begin{bmatrix} \mathbf{I} & \mathbf{0} \\ \mathbf{0} & \mathbf{R}_u^A \end{bmatrix}}_{\mathbf{R}^A} \begin{Bmatrix} \mathbf{u}_i^A \\ \mathbf{q}^A \end{Bmatrix} \tag{6.1}$$

where $\mathbf{R}_u^A$ is called the interface displacement modes (IDM) matrix and contains the position vectors and orientations of the translational DoF $\mathbf{u}_b^A$ (sensors in general or expanded translations in our case) with respect to the virtual point(s). For the sake of completeness, let us construct the IDM matrix. Consider that there are p nodes corresponding to the expanded translations $\mathbf{u}_b^{A,p}$ and they are to be transformed to

v number of virtual coordinates $\mathbf{q}^{A,v}$. Each p-th node consists of three translations $\{u_{b,x}^{A,p},\, u_{b,y}^{A,p},\, u_{b,z}^{A,p}\}$ in the local coordinates $\{x,y,z\}$ and each v-th coordinate consists of six DoF – three translations $\{q_X^{A,v},\, q_Y^{A,v},\, q_Z^{A,v}\}$ and three rotations $\{q_{\theta_X}^{A,v},\, q_{\theta_Y}^{A,v},\, q_{\theta_Z}^{A,v}\}$ – with respect to the global coordinates $\{X,Y,Z\}$. Then the following kinematic relationship can be established:

$$\begin{Bmatrix} u_{b,x}^{A,p} \\ u_{b,y}^{A,p} \\ u_{b,z}^{A,p} \end{Bmatrix} = \begin{bmatrix} e_{x,X}^{p} & e_{x,Y}^{p} & e_{x,Z}^{p} \\ e_{y,X}^{p} & e_{y,Y}^{p} & e_{y,Z}^{p} \\ e_{z,X}^{p} & e_{z,Y}^{p} & e_{z,Z}^{p} \end{bmatrix} \begin{bmatrix} 1 & 0 & 0 & 0 & r_Z^p & -r_Y^p \\ 0 & 1 & 0 & -r_Z^p & 0 & r_X^p \\ 0 & 0 & 1 & r_Y^p & -r_X^p & 0 \end{bmatrix} \begin{Bmatrix} q_X^{A,v} \\ q_Y^{A,v} \\ q_Z^{A,v} \\ q_{\theta_X}^{A,v} \\ q_{\theta_Y}^{A,v} \\ q_{\theta_Z}^{A,v} \end{Bmatrix} + \begin{Bmatrix} \mu_x^{A,p} \\ \mu_y^{A,p} \\ \mu_z^{A,p} \end{Bmatrix} \tag{6.2}$$

where the matrices above can be expressed in a compact form, in the order of appearance:

$$\begin{aligned} \mathbf{u}_b^{A,p} &= \mathbf{E}^{pT}\, \bar{\mathbf{R}}_u^{A,pv}\, \mathbf{q}^{A,v} + \mu^{A,p} \\ \mathbf{u}_b^{A,p} &= \mathbf{R}_u^{A,pv}\, \mathbf{q}^{A,v} + \mu^{A,p} \end{aligned} \tag{6.3}$$

The orientation of the local node belonging to the expanded translations is contained in $\mathbf{E}^p = \{e_x^p,\, e_y^p; e_z^p\}$, whilst $r_\star^p$ are the distances among the local coordinates of the sensor (or the expanded translations) and the virtual point coordinate. As a result of the transformation, any residual (the non-rigid motion about the virtual point or other inconsistencies) ends up in the residual vector $\mu^{A,p}$.

The IDM matrix $\mathbf{R}_u^{A,pv}$ can then be extended to include other interface translations and virtual coordinates:

$$\mathbf{R}_u^A = \begin{bmatrix} \mathbf{R}_u^{1,1} & & & \\ \mathbf{R}_u^{2,1} & & & \\ \mathbf{R}_u^{3,1} & & & \\ & \mathbf{R}_u^{4,2} & & \\ & \mathbf{R}_u^{5,2} & & \\ & \mathbf{R}_u^{6,2} & & \\ & & \ddots & \\ & & & \mathbf{R_u}^{N_p,N_v} \end{bmatrix}^A \tag{6.4}$$

Eq. (6.3) can now be written to include the IDMs of substructure A as:

$$\mathbf{u}_b^A = \mathbf{R}_u^A \mathbf{q}^A + \mu^A \tag{6.5}$$

The residual μ^A is shown in [8, 188] to be minimized in a least quadratic sense if the right hand side of Eq. (6.1) is calculated as follows:

$$\begin{Bmatrix} \mathbf{u}_i^A \\ \mathbf{q}^A \end{Bmatrix} = \underbrace{\left((\mathbf{R}^A)^T \mathbf{R}^A\right)^{-1} (\mathbf{R}^A)^T}_{\mathbf{T}_u^A} \begin{Bmatrix} \mathbf{u}_i^A \\ \mathbf{u}_b^A \end{Bmatrix} \tag{6.6}$$

and ensuring that $N_p > N_v$ i.e., there are more channels than the VP coordinates. The matrix $\mathbf{T}_u^A$ is the desired transformation matrix for obtaining in the least square way an interface which is spatially described by translations and rotations.

In order to obtain the virtual forces and moments $\mathbf{m}^A$ from the applied translational forces $\mathbf{f}^A$, a similar transformation $\mathbf{T}_f^A$ can be derived. This force transformation matrix is the result of a constrained minimization problem [188]. If the DoF are collocated, as obtained by the hybrid models and Fig. 6.12 then

$$\mathbf{T}_u^A = \mathbf{T}_f^A = \mathbf{T}^A \tag{6.7}$$

The new hybrid FRF matrix $\bar{\mathbf{Y}}^{S,A}$ with the virtual interface is calculated by

$$\bar{\mathbf{Y}}^{S,A} = \mathbf{T}^A \, \mathbf{Y}^{S,A} \, (\mathbf{T}^A)^T. \tag{6.8}$$

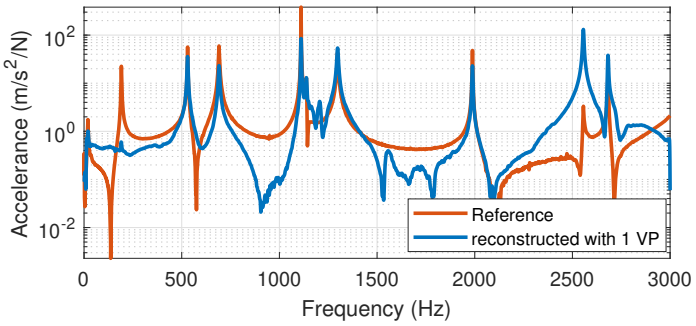

(a) One virtual point

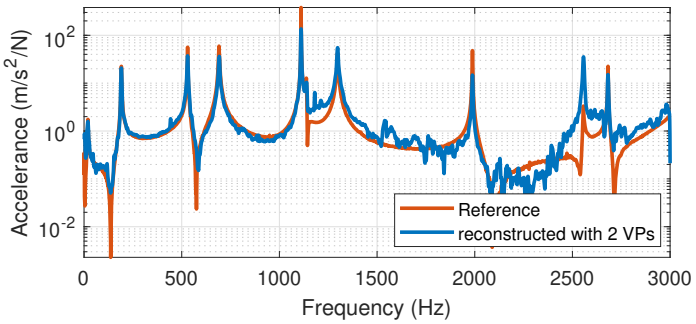

(b) Two virtual points

Fig. 6.13 FRF of the blade-disk assembly coupled by the virtual interface descriptions. The reference FRF is measured at the locations shown in Figure 6.9.

In continuation of the previous two cases of translational interface in Section 6.2.2, we again consider two different configurations of virtual interface in which the expanded translational DoF are transformed to the VP(s) shown in Figure 6.10d and 6.10e, respectively. Note that the VP position can be defined even outside the structure, as long as the condition of rigid transformation holds. The following two new cases are presented for the virtual interface:

Case 3: One virtual point (3 translations and 3 rotations per substructure). The joint is characterized by a 12×12 system, unlike Case 1 and Case 2.

Case 4: Two virtual points (6 translations and 6 rotations per substructure). The joint is characterized by a 24×24 system.

The respective reconstructed FRFs are plotted in Figure 6.13. In the FRFs of Case 3 (Figure 6.13a), not a good agreement is observed between the reconstructed and reference FRFs. This shows that an interface with 6 virtual DoF despite a least

squares contribution from all the translational FRFs is not sufficient to capture the coupled system dynamics accurately.

The FRF obtained for Case 4 (two VPs) is shown in Figure 6.13b. The reconstructed FRF has certainly better agreement than that of Case 3. It is of more interest to compare this reconstructed FRF with that of Case 2 with translational DoF (Figure 6.11b). With the two VP interface (Case 4), the identification resulted in

i. a significantly reduced spurious effect up to 1100 Hz,

ii. a better amplitude estimation on the resonances,

iii. a good approach on the two anti-resonances around 150 and 600 Hz, and

iv. slightly increased spurious effects between 1300 to 2000 Hz.

The prediction beyond 2000 Hz is poor for both the cases. For practical purposes of low to medium frequency range, the two VP interface (Case 4) is considered to be a good choice and will be used in the subsequent joint identifications in Chapter 7.

6.3 Summary

This chapter elaborates part of the detailed working before being able to identify a joint in dynamic substructuring. The task is to find the right set of DoF on each substructure which would predict the assembled structure's response, when coupled on those DoF. Due to the variability of the contact – especially that of a blade-root shown in the beginning of the chapter – the task becomes a bit more challenging. In order to understand how such an interface would behave, firstly, a numerical study is performed on the blade and disk assembly in which only translational DoF are considered on the condensed numerical models. The coupling on limited number of DoF is performed to simulate a measurement. It was found out that at least 12 DoF per substructure are required for a reasonable accuracy.

Secondly, an experimental sensitivity analysis of the interface is performed on the actual blade and disk. Since this involves measuring on an assembly wherein some compliance exists on the interface yet to be calculated (the so-called joint), the joint identification has to be performed. However, due to different joint sizes and

models, the validation is done by recoupling the identified joint with its substructures and comparing with the reference measurements on the assembly. In this test-based validation, two translations-only interfaces and two virtual interfaces are created. The mathematical approach to construct the virtual interface is also discussed in detail. The interface on the dove-tail root with coupling on three sides is shown not to be well-represented with only translational DoF. A single virtual interface is also not found suitable. The two-point virtual interface effectively predicts the validation FRF, thereby, presenting itself as the representative interface. The same will be used in further joint identification in Chapter 7.

Chapter 7

Identifying the Blade-root Joint

Part of the work described in this chapter was previously published in [69, 71, 189].

This chapter presents and evaluates the joint identification strategy based on substructure decoupling and SEMM methods (see Section 5.5). The blade and disk test-case of Chapter 3 and Chapter 4 are assembled and tested. We recall that in the previous chapters, the following were discussed:

1. How to generate substructure models and expand the experimental measurements to inaccessible boundary DoF in Chapter 3.

2. How to reduce some effect of noise and unavoidable measurement and modelling errors by using singular value truncation in the substructure models in Chapter 3.

3. How to identify any uncorrelated measurements with the expanded models and thus further improve the substructure quality in Chapter 4.

4. What method, out of many, would be suitable for joint identification, specifically, for the blade and disk connection. Due to the complexity of the substructures and the interface, the substructure decoupling method using SEMM expansion is a suitable method, as outlined in Chapter 5. Although the method by Tol and Özgüven [3] was applied on a test-geometry of two beams in [62] as part of this research, the challenges of that method were discussed therein from a practical point of view.

5. What form of the interface one should use for the blade-root connection in Chapter 6. Out of many possibilities, the 2-virtual point interface including translational and rotational DoF was found the most appropriate.

To this end, the method and the substructure models are available. The coupled sub-models will now be used to identify the joint. This chapter is organized as: Section 7.1 creates a dummy assembly by inserting simulated joint values to test the SEMM based substructure decoupling method, referred as *SEMM decoupling*, hereafter. Section 7.2 discusses the actual joint identification between the blade and disk when the disk was fixed at its centre. In Section 7.3, the constraint is removed from the assembly to discuss important aspects that had a noticeable influence on the joint identification such as the disk constraint itself, the correlated SEMM, the curve-fitting challenges and the singular value filtering in substructures.

7.1 A dummy coupled system

In this section, the SEMM decoupling method is verified by using the blade and disk expanded models ($\mathbf{Y}^{S,A}$ and $\mathbf{Y}^{S,B}$) and coupling them with a joint system to create a dummy or simulated assembly denoted by $\mathbf{Y}^{AJB,d}$. The so-created dummy assembly is shown in Fig. 7.1 and the joint parameters are given in Table 7.1. Since the joint parameters are input by the user and so known in advance (Table 7.1), it is relatively easy to check if the method is able to identify the joint.

Table 7.1 Parameters of the dummy joint

	Translational	Rotational
Stiffness	1×10^7 N/m	1×10^4 Nm/rad
Damping	1×10^3 Ns/m	1×10^2 Nms/rad
Mass	5 g	5 gm^2/rad

As shown in Fig. 7.1, between the two components' expanded models $\mathbf{Y}^{S,A}$ and $\mathbf{Y}^{S,B}$, the dummy-joint FRF model $\mathbf{Y}^{J,d}$ is introduced to create a *dummy-coupled* model that we then used to generate simulated measurements instead of the actual experimental measurements of the full-system. This ensures that measurement and expansion errors are the same for both the coupled and uncoupled models. If the

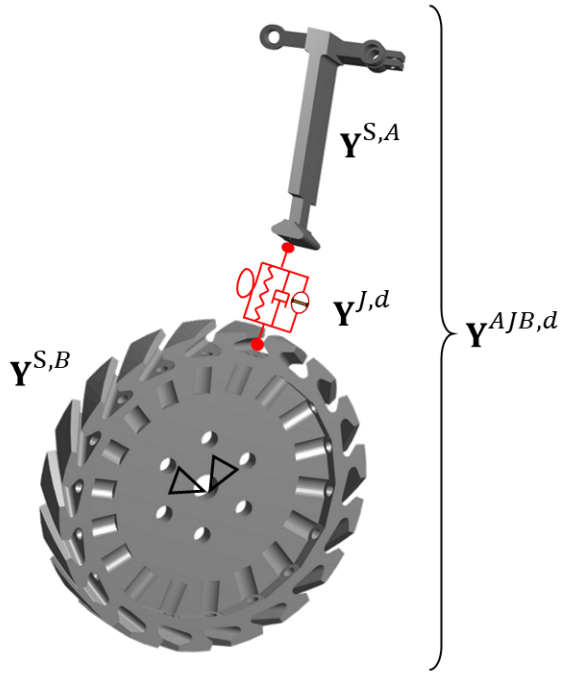

Fig. 7.1 A simulated assembly model by using dummy joint values of stiffness, damping and mass. Rotational spring (left of the translational spring) and rotational damper (right of the dashpot) are also sketched. The red dots indicate the joint mass. The joint size is 24×24 in order to couple with 2 VP interface (12×12) on either side. Since the disk expanded model $\mathbf{Y}^{S,B}$ is from campaign-1 in which the disk was fixed at the center, the constraint is shown by triangles.

internal DoF can observe the dynamics at the boundary – a minimum requirement for the SEMM decoupling approach – then our proposed iterative strategy should be able to identify the interface dynamics. The reverse formulation is also true: if the joint is properly identified, then the internal DoF fully observe and control the boundary DoF and the decoupling step itself is validated. The dummy joint is a simple one-to-one mass-spring-damper system with the parameters[1] in Table 7.1.

Fig. 7.2 shows the identified dummy dynamic stiffnesses along the frequency axis for translational and rotational DoF. The actual dynamic stiffness of the dummy joint is calculated from the parameters in Table 7.1, whilst the identified stiffness is calculated by inverting the identified FRF matrix. In each figure, there are two

[1]The mass in the joint parameters of Table 7.1 exists to easily create a non-singular system. In order to obtain the accelerance matrix, the dynamic stiffness is to be inverted which is singular without the mass. The mass may be considered to be present in the true joint if there are un-modelled fasteners in the substructures.

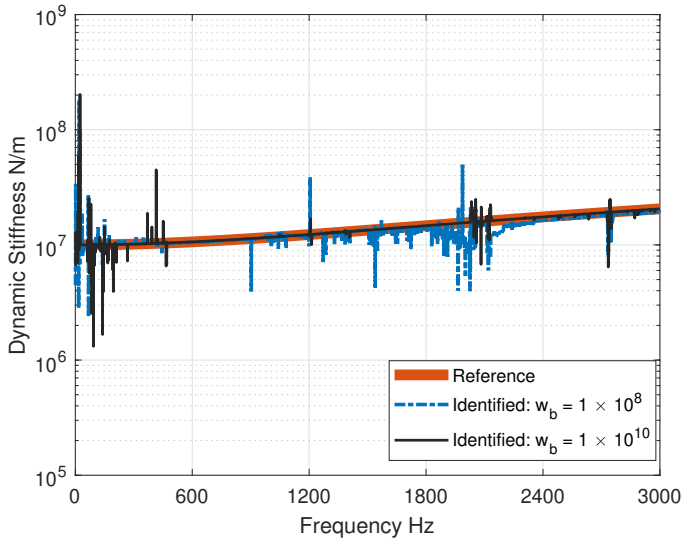

(a)

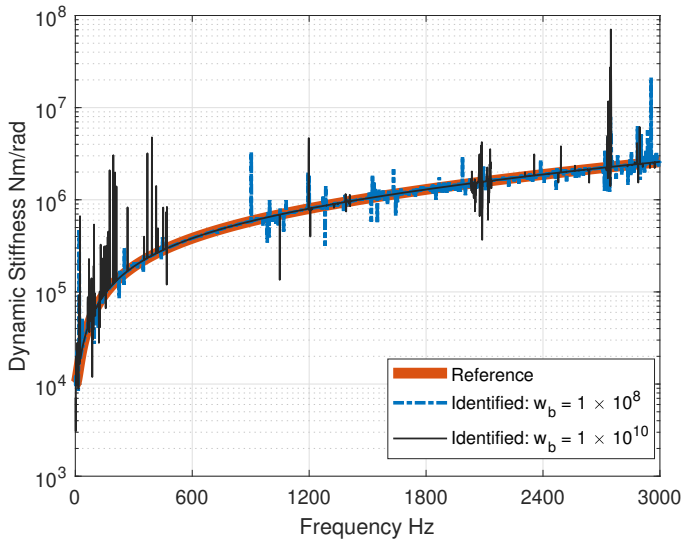

(b)

Fig. 7.2 The reference and identified dynamic stiffness of the dummy joint for: (a) Translational DoF (b) Rotational DoF on one of the two virtual points depicted on the blade in Fig. 7.3a. The identified stiffness plots are obtained after three iterations. In the first iteration, no initial guess was used i.e. the substructures were left uncoupled.

joint identification plots for different weights of weighted pseudo-inverses discussed in Section 5.5.6. The effect of the weights on convergence will also be discussed in the coming Section 7.2.1. Focusing on the identified stiffness for the case of $w_b = 1 \times 10^8$ (with all the other DoF assigned $w_i = 1$), the figure shows that, with

the exception of spurious effects, the dynamic stiffness of the dummy joint can be identified. The spurious effects are spread across the whole frequency band but pronounced in the region between 0 to 500 Hz in which the disk expanded model has some discrepancies. In this region, it is assumed that the boundary dynamics are not uniquely observed. The same is true for frequency regions near 1200 and 2100 Hz where sub-system resonances of the blade are observed in the FRF of Fig. 3.10. Recall that the disk was fixed at its centre and it largely affected the expansion. In these resonance regions, the identification can be influenced by the internal subsystems. Its reason and a way to mitigate it are discussed below.

In fact, by the method outlined in Section 5.5, the *dummy-coupled* system's dynamics are to be expanded on its coupled parent model and subsequently, the joint is to be identified. The expansion occurs uniformly (if no weightings are assigned to $\mathbf{u}_b$) all over the DoF through the SEMM interface (Fig. 3.4 in Chapter 3). When talking about the SEMM interface, the pseudo-inverses that pre- and post-multiply in the SEMM equation (3.29) should be kept in mind, since their role is pivotal in the expansion. This is where the subsystem's internal influence comes into play, including resonances[2] and noise in the hybrid models i.e. through the pseudo-inverses in Eq. (3.29). If one of the subsystem is near resonance, the expansion would occur through the ill-conditioned matrices and hence the errors propagate also to the interface which are later identified and dubbed as the joint. Forcing the SEMM method to observe only the interface could easily rectify this problem, e.g. by inclusion of a stronger weight towards interface DoF $\mathbf{u}_b$, or by ignoring internal DoF altogether through the weighted pseudo-inverses. By doing so, the internal subsystem's resonances or errors are not expanded to the interface or the joint.

The dummy joint of Fig. 7.2 with $w_b = 1 \times 10^8$ has identified some of the characteristics that belong to the internal subsystem, as discussed above. By further suppressing the weight of internal DoF would reduce the influence of those errors. This is evident by the identified joint with $w_b = 1 \times 10^{10}$ shown as the black stiffness line. The spurious errors throughout the frequency band have decreased and localized. Further increasing w_b would suppress more the internal subsystem influence but could also significantly deteriorate the numerical conditioning of the pseudo inverses in Eq. (3.29). The spurious errors are, nevertheless, easily recognizable in this test.

[2]Note that the internal subsystem influence does not apply to a single substructure being expanded by SEMM because it is not composed of subsystems. This is also why the weightings were not discussed before in Chapter 3. However, there is no restriction on using them on a single substructure.

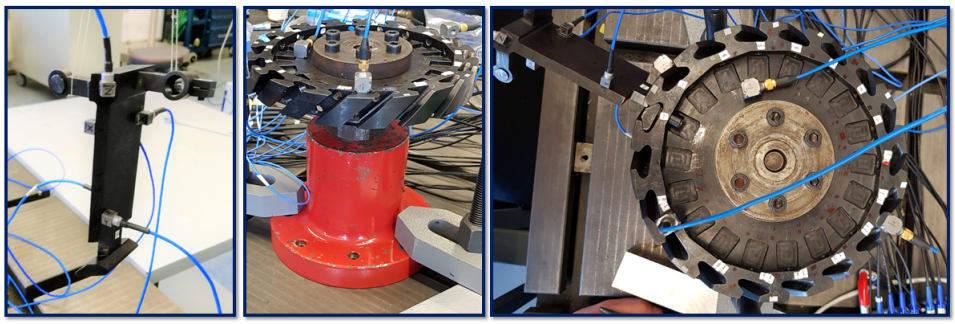

Fig. 7.3 The measurements setup for the assembly impact test campaign: (a) the blade hanged by wires (b) the disk fixed at its centre (c) the coupled blade and disk with the same constraint conditions as the disk. This is campaign-1, as discussed in Chapter 3. The blade and disk are reprinted here.

7.2 Experiments on the assembly: the fixed disk

In the previous section, the assembled system was created from a numerical joint. This section discusses the actual assembly obtained by joining the blade in its root in the disk. The blade is attached with the disk using two bolts. One of the bolts has a pin which also aligns the blade to its correct position. The bolts are tightened to a torque of 10 Nm. The assembly is shown in Fig. 7.3. On the assembled system, five tri-axial accelerometers are positioned on the blade and five on the disk. The impact positions were indicated in Fig. 3.8. The individual blade and disk, as tested, are also reprinted alongside in Fig. 7.3 from campaign-1 in Section 3.5. It was briefed in Section 5.5 that the sensor and impact positions should remain unchanged in the assembly as well as the single components. A side advantage of this is that the sensor mass effect, if significant enough to cause changes in the dynamic behaviour of the components and the assembly, can be removed in the decoupling process.

It is assumed that the coupled system behaves linearly since the energy of the impacts is not so high to introduce slip in the interface. Therefore, the SEMM approach for assembling and decoupling as proposed here is thus licit. The interface between the blade and disk is modelled by using virtual points (VPs). For this test-case, two VPs are considered on each substructure [62] where each VP consists of three translations and three rotations. The two VPs are depicted on the blade-root in Fig. 6.10e. Thus, the joint is represented by a 24×24 DoF system.

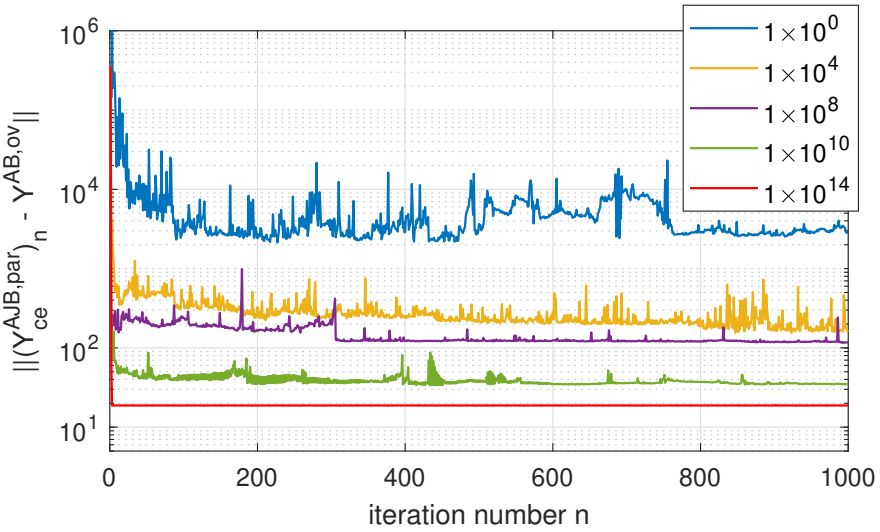

Fig. 7.4 Effect of weights on the convergence of Euclidean norm of the expansion error between the coupled parent model and the measured overlay model. The physical boundary DoF $\mathbf{u}_b$ are weighted whilst computing the pseudo inverses, as per Eq. (5.65) and Eq. (5.66).

7.2.1 Convergence

Before investigating the joint, the convergence of the method is discussed in this section. The convergence plot (Fig. 7.4) is obtained from the assembly measurements from which the coupled SEMM model is created. We recall from Section 5.5.6 that the assembled system's SEMM model can be computed by the weighted pseudo inverses in Eq. (5.65) and (5.66). This helps in faster convergence of the joint properties by assigning higher weights to the physical boundary DoF $\mathbf{u}_b$ and expanding the measured dynamics in a weighted least squares sense.

Fig. 7.4 shows Euclidean norm of the expansion error at each iteration step n for different weights w_b assigned to the physical boundary DoF $\mathbf{u}_b$. The weights of the remaining DoF set are, by default, set to 1. When no weighting value is used for $\mathbf{u}_b$, the convergence is not ensured even after 1000 iterations. This means that the measured dynamics are being expanded equally in all DoF. Thus, the joint or boundary DoF updating and the identification takes more iterations. If SEMM is forced to expand or observe only the boundary DoF, a higher weight is assigned to them. Evidently, the method converges faster when a high weighting value is used for $\mathbf{u}_b$ in Fig. 7.4. To test the method's convergence, the weights as high as $w_b = 1 \times 10^{14}$ are used. It took only 3 iterations to convergence at this weight. This

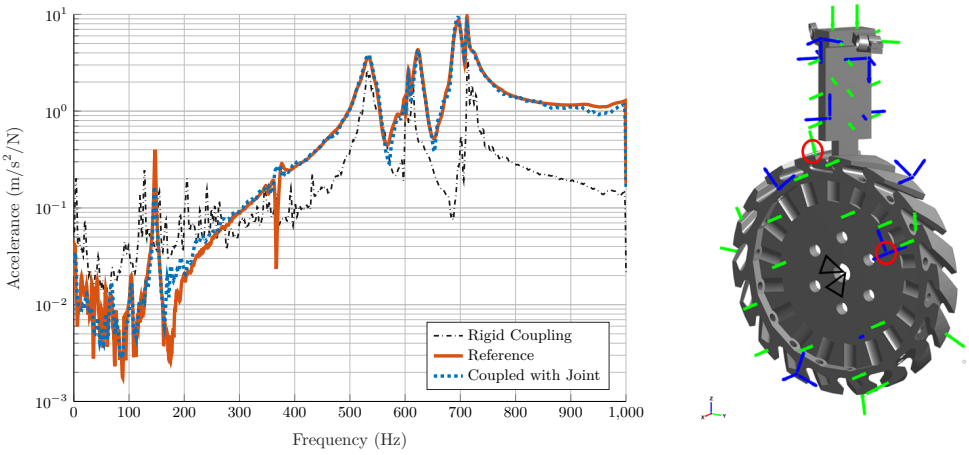

Fig. 7.5 The agreement of the FRF before and after identification. The solid validation line is a measured FRF of the full-system labelled 'Reference' (on the circle marked DoF in the right figure, where the triads of blue markers indicate an accelerometer and green markers indicate impacts). The blue dotted line indicates the coupled results (with the joint identified by the SEMM procedure). The dash-dotted black line is the would-be rigid coupling (without joint).

implies that SEMM has ignored the internal DoF almost entirely and focused the expansion to the boundary and thus it converged to a hybrid model with minimum expansion error. Such high weightings, though guarantee the method's convergence, were avoided in the joint identification presented so far and hereafter due to possible numerical issues.

The choice of weights was $w_b = 1 \times 10^8$ for the presented results, unless otherwise stated, due to the fact that the order of stiffness is between $10^7 - 10^8$.

7.2.2 Identification of the actual joint

Using the assembly measurements, the method is applied to the identification of the actual joint in this section. In the following discussion on the actual joint identification, the presented results are, obviously, extracted from a converged system. The identification process was validated in two different steps.

In the first step, here called *self-validation*, all the measured FRFs are included in the overlay model of the assembled disk and blade $\mathbf{Y}^{\mathrm{ov},AB}$. It is called *self-validation* because the recoupled system after the identified joint $\mathbf{Y}^{J}$ is compared with the same measurements from which it was originally identified. The resulting agreement

check between the measured and the recoupled FRFs ($\mathbf{Y}^{S,A}, \mathbf{Y}^{J}$ and $\mathbf{Y}^{S,B}$) should be a trivial comparison which is shown in Fig. 7.5. Ideally, the FRF of the recoupled system labelled as 'Coupled with Joint' should overlap the reference measurement at all frequencies which is however not the case. Note that the FRF labelled 'Reference' was measured on the circle marked DoF in the same figure and was included in the identification procedure. This shows that, in the joint identification process, the self-validation step is not so trivial. Indeed, it is assumed that the only difference between the coupled and uncoupled models was the existence of joint dynamics. Theoretically this may be true, but practically other differences exist between the coupled and uncoupled measurements, and the method can not discriminate between them. This is the reason why the joints are generally noisy, and sensitive to measurement and expansion bias errors [2, 170].

In Fig. 7.5, the dotted curve named as 'Rigid Coupling' is the FRF obtained by rigidly coupling the blade and the disk models ($\mathbf{Y}^{S,A}$ and $\mathbf{Y}^{S,B}$), without any joint between them. From the comparison of the 'Rigid Coupling" and the 'Reference' FRFs, it can be noted that they are poorly overlapping. This confirms that there is a significant contribution of the joint flexibility $\mathbf{Y}^{J}$ to the dynamics of the assembled system, which cannot be modelled just with a rigid connection between the blade and disk.

In the second step of the validation, here called *on-board validation*, we kept out some FRFs from the measured FRFs of the assembled system (disk plus blade) in order to use them only as reference for validation. This approach is the same as for SEMM validation on the single component blade or disk in Chapters 3 and 4. This is more restrictive than the *self-validation* step since the measured FRFs considered as 'Reference' are not included in the procedure of the joint identification, but they are kept only for validation purposes. In the actual systems, this is the only check to test the veracity of the identification [37].

In Fig. 7.6, the FRF obtained after recoupling $\mathbf{Y}^{S,A}, \mathbf{Y}^{J}$ and $\mathbf{Y}^{S,B}$, is labelled as 'Coupled with Joint' and compared with the reference measurement performed at the circled marked DoF. The comparison of these two FRFs is acceptable but, as expected, not so good as in Fig. 7.5. The recoupled FRF is more noisy than the 'Reference' one and its amplitude is higher throughout the frequency band. However, the resonance frequencies are well captured and it can be noted that the FRF of the first mode is also well identified.

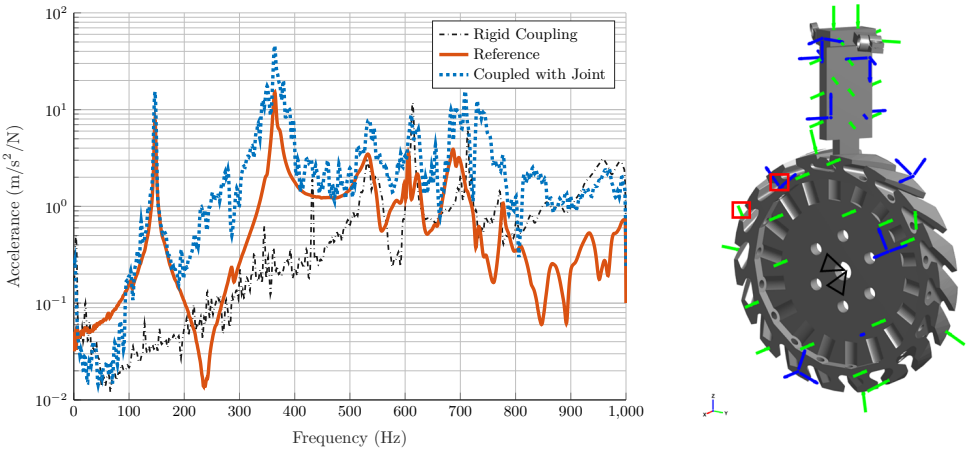

Fig. 7.6 The on-board validation of the joint. The solid validation line is a measured FRF of the full-system. This FRF (on the square marked DoF in the right figure, where the triads of blue markers indicate an accelerometer and green markers indicate impacts) has not been used to identify the joint. The blue dotted line indicates the coupled results (with the joint identified by the SEMM procedure). The dash-dotted black line is the would-be rigid coupling (without joint).

The dotted curve named as 'Rigid Coupling' is completely different from the 'Reference' even for the first mode. This validation process, therefore, leads to two main conclusions:

1. inserting a joint, after identifying it, between the blade and the disk models is better than rigidly coupling them, since the obtained FRFs are more similar to the measured FRFs of the assembled system,

2. the set of chosen measurements are suitable to identify the joint in the frequency range around the first mode, whilst they do not lead to an accurate reconstruction of the FRFs of the jointed system, both in amplitude and in frequency, for a wider frequency range.

7.2.3 The identified joint

The identified joint is a 24×24 DoF system, as mentioned before. Fig. 7.7 shows the plots of dynamic stiffness of one of the translational and rotational DoF versus the frequency. As expected, there are spurious effects which are typical of the

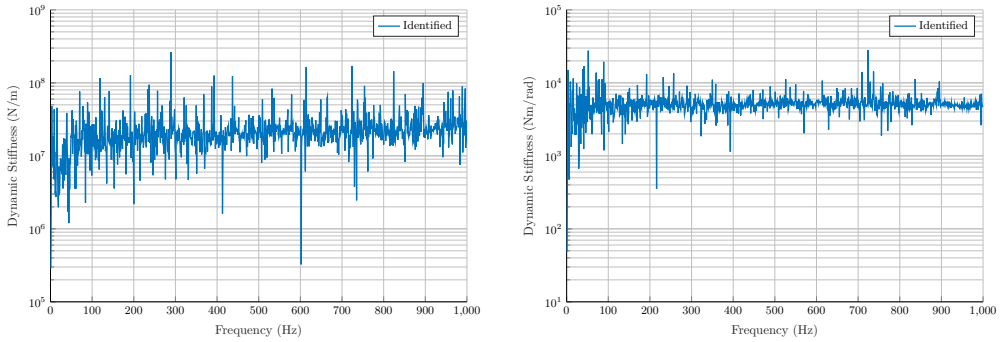

(a) (b)

Fig. 7.7 The identified dynamic stiffness of the actual joint for: (a) translational DoF (b) rotational DoF

identification process [3]. Their presence indicates that some measurement or expansion errors have propagated in the identified joint.

If the only contribution of the joint was the spring stiffness, then the dynamic stiffness of Fig. 7.7 would be a frequency independent line - known as a 0th order line. The identified joint dynamic stiffness does not have a straight horizontal line (constant spring stiffness), however, it can be easily seen that a curve can be fit on it. This applies to the dynamic stiffness of both the translational and of the rotational DoF.

The damping effects should be visible at higher frequencies. If the interface exhibits a viscous damping, a frequency dependent contribution is expected which becomes dominant at higher frequencies. In the case of structural damping, this relation is not as straightforward. Regardless of the type of damping in the joint, its effects should be derivable from the imaginary part of the complex FRF. Unfortunately, due to the limited damping contributions these effects are under the noise floor of the identification procedure, which makes fitting the damping parameters inappropriate.

7.3 Experiments on the assembly: the free disk

In the previous section, the identified joint had marginal success in predicting the reference measurements. The main reason of this is the disk constraint which seemed to corrupt not only the disk substructure but also the blade-disk assembly. It was

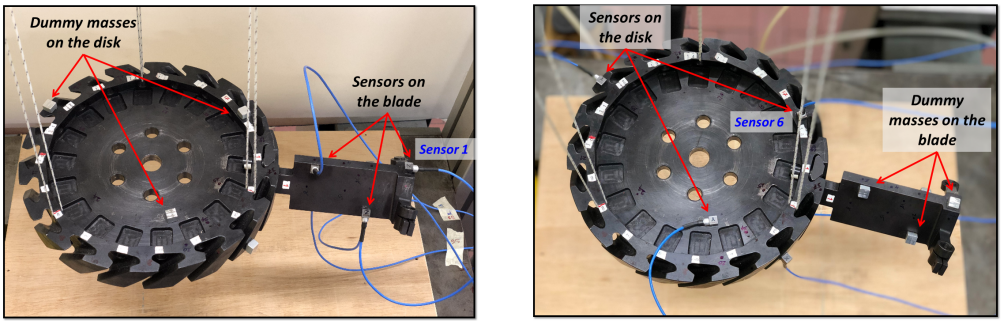

(a) (b)

Fig. 7.8 Experimental setup of the blade coupled to the disk. Due to limited number of sensors and channels in the data acquisition system, the campaign was conducted first by (a) mounting the sensors on the blade and the dummy masses on the disk and then by (b) mounting sensors on the disk and the dummy masses on the blade. Each dummy mass value is equivalent to the sensor's nominal mass. The sensor and impact positions were preserved exactly as Fig. 3.8.

then decided to get rid of this constraint since it posed serious modelling challenges as well as expansion errors.

In this section, the same blade and disk assembly are retested without the central constraint on the disk, as shown in Fig. 7.8. The free constraint is realized by flexible strings on which the coupled system is suspended. Note that the disk-alone also had be tested in the free condition. Since this new test-campaign was performed at the AERMEC lab of Politecnico di Torino (in contrast to the previous one at Applied Mechanics chair of Technical University of Munich), the setup and the acquisition systems were different. Therefore, this was referred to as campaign-2 in Section 3.5 and will so be done here.

Due to limited sensors and measurement channels availability, the tests on the assembly had to be done in two steps to cancel the sensor mass effect. In the first measurement step, the sensors were mounted on the blade while dummy masses equivalent to sensor mass were placed on the disk. In the second step, the sensors and the masses were swapped.

The impact tests were carried out on the new assembly with the same sensor and impact positions as in campaign-1. The set of FRF measurements on the assembly is denoted by $\mathbf{Y}^{\text{exp},AB}$. Similar to the approach of on-board validation, one row and column of this measured matrix was not used in the identification. So, the size of the

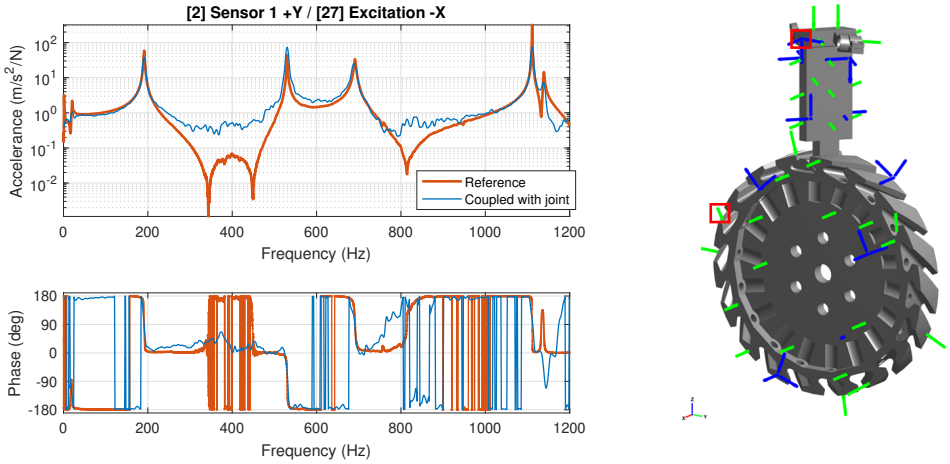

Fig. 7.9 FRF on the coupled blade and assembly. The reference measured FRF is $\mathbf{Y}^{\text{exp},AB}_{2,27}$ indicated also on the right with square markers. The FRFs have been smoothed for clarity.

overlay model $\mathbf{Y}^{\text{ov},AB}$ is 27×36 (see Table 6.2). Particularly, the experimental FRF used for validation is $\mathbf{Y}^{\text{exp},AB}_{2,27}$.

7.3.1 Effect of constraint removal on joint identification

After identifying the joint from the new assembly measurements in campaign-2, and recoupling it with the substructure models, the plot of Fig. 7.9 is obtained together with the reference FRF. A significant improvement is clearly evident from the recoupled FRF when compared with those in Fig. 7.6. By looking just at the FRF of Fig. 7.9, it can be noticed that both the recoupled FRFs (standard and correlated) are almost overlapped to the reference curve in the regions close to the peak resonances. This proves our hypothesis that the constraint influenced the identification adversely. In fact, constraint modelling has remained a huge research challenge, even after decades of research on model updating methods [186, 160]. The removal of constraint and the resulting improvement provides certain confidence that one can identify the joint and predict other measurements by using the SEMM decoupling method. It should be noted from Fig. 7.9 that the non-resonance regions are poorly predicted, thus, necessitating further investigation.

7.3.2 Effect of correlated SEMM models on joint identification

In Chapter 4, we developed a new method of filtering those measurements or DoF do not correlate well with the corresponding numerical models. Their effect on a substructure level was also examined by the experimental results. The correlation analysis revealed on the free blade and free disk components (see Table 4.2) that

- channel 4 and input channels 4 and 17 had low correlation on the blade;
- channel 27 and input channels 30 and 31 had the lowest correlations on the free disk.

These channels were then removed from the experimental FRF matrices and new expanded models were generated, called as correlated SEMM models. The previous expanded models are referred as standard SEMM models. The joint identification is then performed with the correlated models and then recoupled back to predict the validation FRF. The accelerance FRFs so-obtained with both correlated and standard SEMM (Fig. 7.9) are shown in Fig. 7.10 together with the reference. By looking just at the FRF of Fig. 7.10, it can be noticed that the correlated SEMM is almost overlapped to the reference curve in the regions close to the peak resonances. It outperforms the prediction of the standard SEMM. By close observation, using the correlated SEMM, gives a general improvement in the regions of small amplitudes (ranges 220–740 Hz, 300–500 Hz, 800–900 Hz) where the FRF estimated by correlated SEMM is closer (than the one obtained by standard SEMM) to the reference FRF. Even though the results have been shown for the frequency up to 1200 Hz, a better agreement was achieved even beyond 1200 Hz and up to 3000 Hz.

By looking in detail at the values of the peaks' amplitude in Table 7.2, one may observe that the values predicted by the correlated SEMM at resonance are in general better than the standard SEMM (except for mode 4 where the difference is negligible). In particular, the amplitude values predicted by correlated SEMM are much better for the first two peaks i.e. below 600 Hz. This improvement is given by the correlated SEMM, instead of standard, in the model of the disk, and this was particularly effective for the disk in 0-600 Hz range (see Fig. 4.7). From Table 7.2, it can be seen that, using the correlated SEMM, it is still advantageous in high frequency modes (3 to 5) even if the difference with standard SEMM is not always as evident as for modes 1 and 2. In these high frequency regions, other factors

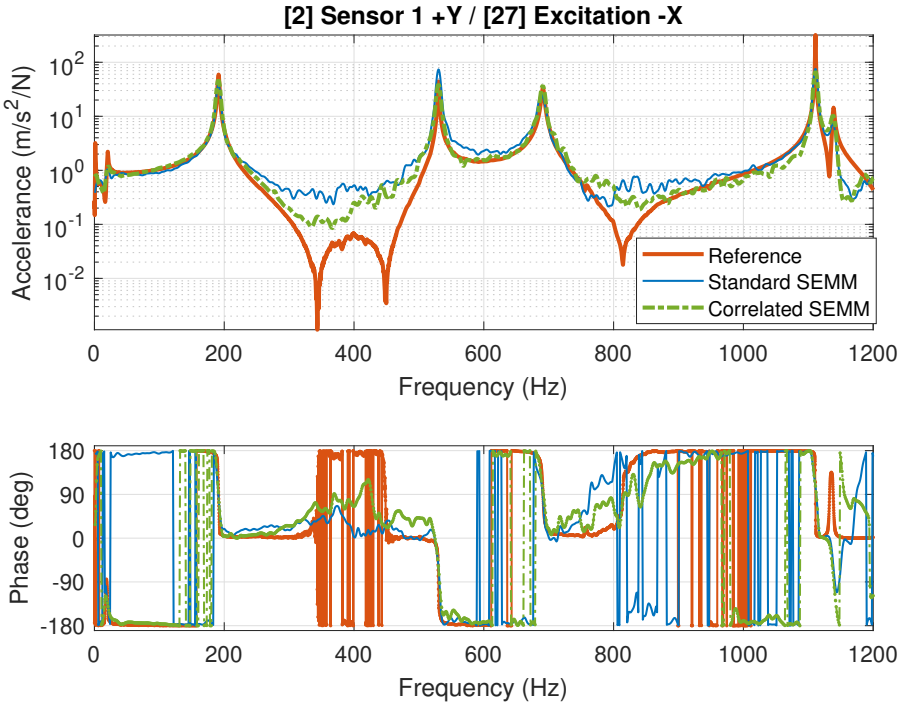

Fig. 7.10 FRF on the coupled blade and assembly. The reference measured FRF is $\mathbf{Y}_{2,27}^{\text{exp},AB}$ indicated also on the right with square markers. The FRFs have been smoothed for clarity.

such as interface definition and singular value filtering can also play an important role in better predicting the coupled system's dynamics.

7.3.3 The joint and fitting

So far, we have examined the on-board validation by recoupling the identified joint to its substructures. For actual systems, this is the only viable check as argued by D'Ambrogio and Fregolent in [37] during identification of their known mass by substructure decoupling method. They noted that it was quite straightforward to detect errors in case of the known mass; however, it would not be the case if the system to be identified is unknown. They went on to assert that the only check that can be performed is to couple the predicted FRFs of the unknown subsystem with those of the known subsystem (to form the mathematically coupled system) and to compare it with the reference measured FRF on the assembly.

Table 7.2 Peak value comparison for the FRFs reconstructed by the standard SEMM and correlated SEMM methods. All amplitudes are in m/s^2/N.

Mode	**Frequency**	**Experiment**	**Standard SEMM**		**Correlated SEMM**	
	(Hz)	Amplitude	Amplitude	% Difference	Amplitude	% Difference
1	191.3	59.3	48.6	-18.0%	60.3	1.7%
2	530.0	44.7	91.4	104.6%	48.5	8.5%
3	691.1	33.6	25.5	-24.2%	41.5	23.3%
4	1111.1	298.3	99.0	-66.8%	89.7	-69.9%
5	1138.9	14.4	8.3	-42.7%	12.2	-15.5%

It is, however, important to see also the joint obtained from the above tests for its behaviour and physical interpretation. The identified joint accelerance FRFs are shown in Fig. 7.11 belonging to selected few DoF, both bad and good in relative terms. Recall that these are only four of the 24×24 system. The first two plots are for the translational DoF (Fig. 7.11a and Fig. 7.11b), and the other two are for the rotational DoF (Fig. 7.11c and Fig. 7.11d). It is seen in the figures that despite some noisy behaviour, which is typical after a decoupling procedure (see Chapter 5), the joint seems to follow a trend.

This behaviour is representative of a system with high stiffness, low damping and low mass i.e. a stiffness dominant line on a logarithmic scale [51]. The fluctuations are due to the measurement and modelling errors, which propagate in the hybrid models. It can be observed that the accelerances obtained by the correlated SEMM exhibit slightly less fluctuations than the ones obtained by standard SEMM. Correlated SEMM in fact removes the channels that introduce more variability in the identification. However, the fluctuations still remain because the measurement noise cannot be completely removed.

It can be noticed in the translational accelerance (Fig. 7.11b) and in the rotational one (Fig. 7.11c) that around 100 Hz, the accelerances from standard SEMM have a kind of a hump. This could be interpreted as an internal resonance of the joint. However, the hump disappears in the corresponding accelerance identified by the correlated SEMM, confirming that it was due to some spurious, non-physical effects which were eliminated by the correlated SEMM.

At this point, the accelerance FRF with irregular pattern in Fig. 7.11a and Fig. 7.11c are discussed further by examining their imaginary part plotted in Fig. 7.12b

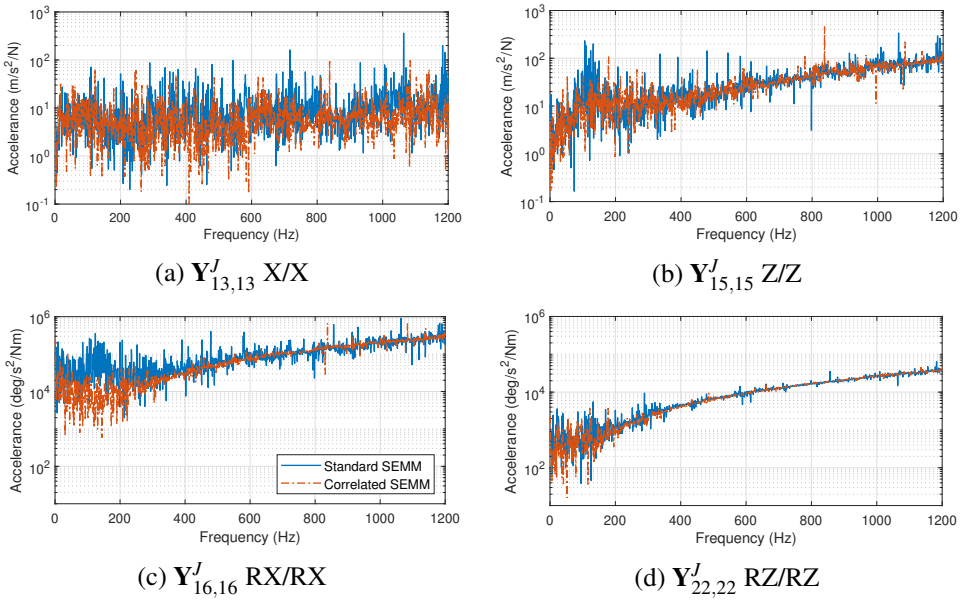

(a) $\mathbf{Y}^J_{13,13}$ X/X (b) $\mathbf{Y}^J_{15,15}$ Z/Z

(c) $\mathbf{Y}^J_{16,16}$ RX/RX (d) $\mathbf{Y}^J_{22,22}$ RZ/RZ

Fig. 7.11 The decoupled joint accelerance on two translational DoF (a) and (b) and two rotational DoF (c) and (d) for both standard SEMM and correlated SEMM.

and Fig. 7.12d, respectively, on a linear scale. The objective of this exercise is to see if it is possible to curve-fit the highly fluctuating accelerance and if correlated SEMM provides better insights than standard SEMM. Before that, one of the accelerance FRF of a 2-DoF oscillator is briefly recapitulated through its both real and imaginary parts in Fig. 7.12a. Even though the blade-root joint system is defined by multiple DoF, each DoF on blade is coupled only to the corresponding DoF on the disk interface. Therefore, the 2-DoF oscillator is considered a suitable demonstration for the purpose. Additionally, the frequency range shown in Fig. 7.12a is such that the system is far from its resonance. As seen in the figure, the real part is negative and grows in amplitude with frequency. It would change its sign at the resonances (at 2251 Hz and 3899 Hz). The imaginary part remains positive and would grow gradually depending on the damping coefficient and the model. Here, only the proportional damping is used for the demonstration.

The imaginary part of the identified joint in Fig. 7.12b and Fig. 7.12d has fluctuations about the horizontal axis. The sign changes are non-physical, but they are to be expected in the identification process due to errors [3]. By careful examination, it can be seen that correlated SEMM has produced relatively less fluctuations compared to standard SEMM both in the real and imaginary parts. After performing a curve-fitting procedure based on rational fractional polynomials (RFP)

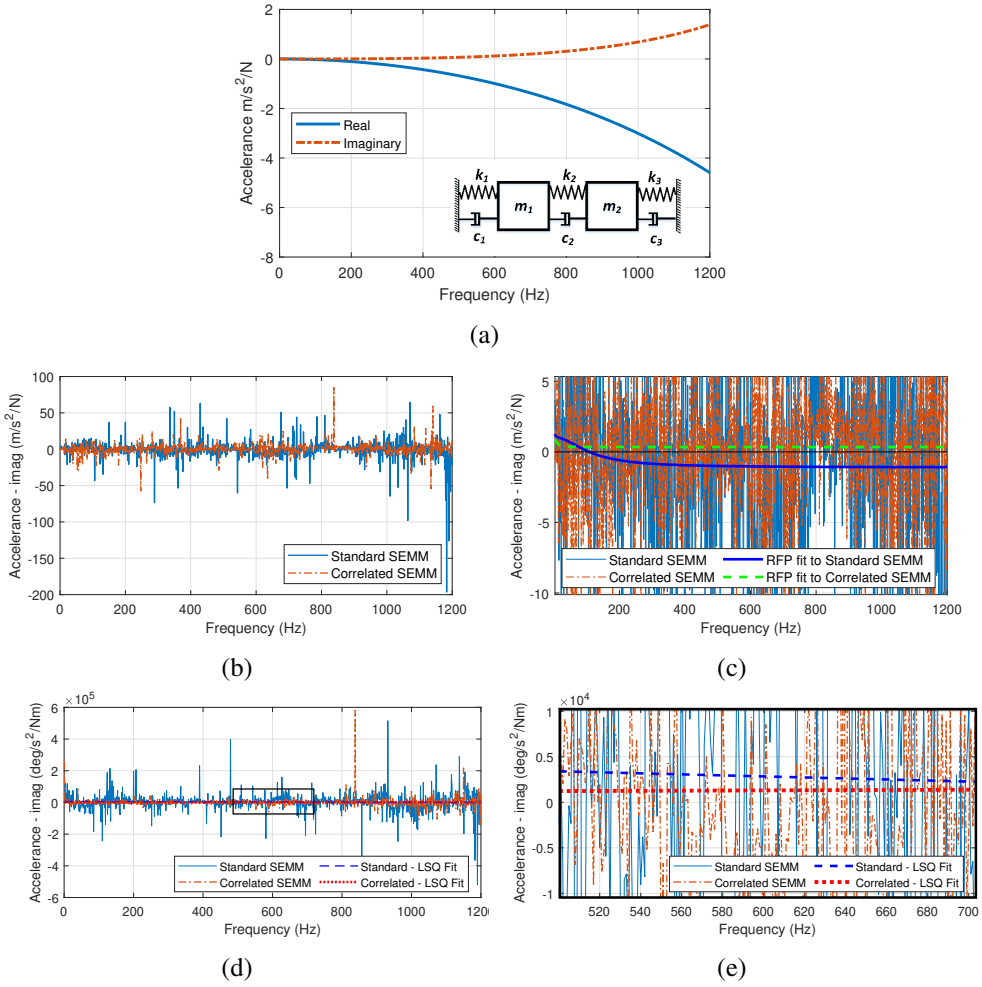

Fig. 7.12 (a) Real and imaginary parts of a two DoF oscillator's accelerance ($\mathbf{Y}_{11}$). The mass, stiffness and damping parameters are $m_1 = m_2 = 0.05$ kg, $k_1 = k_2 = k_3 = 1 \times 10^7$ N/m and $c_1 = c_2 = c_3 = 3 \times 10^{-5} k_1$ N.s/m, respectively. The undamped natural frequencies are: 2251 Hz and 3899 Hz. The shown frequency range is far from the resonance. (b) Imaginary part of the identified joint accelerance of the translational DoF in Fig. 7.11a. (c) Fitting results with a readjusted vertical scale. (d) Imaginary part of the rotational joint accelerance Fig. 7.11a. (e) The close-up view for the curves fitted to both the standard and correlated SEMM.

[190] to the entire joint system, the RFP fitted-curves are plotted in Fig. 7.12b both for standard and correlated SEMM. The figure's vertical scale has been adjusted. The fitted curve to the standard SEMM is estimating mostly the negative imaginary values which is non-physical. On the other hand, the curve fitted to the correlated SEMM is positive in the entire range implying that some errors have been removed by the correlated hybrid models.

On the rotational FRF's imaginary part in Fig. 7.12d, the same RFP fitting method provided the similar results. However, other fitting procedures could also be tried. The linear least squared (LSQ) fit [191] to the joint accelerance data is shown in the same figure. The region in the rectangle is zoomed-in and replotted in Fig. 7.12e. Again, a good fit is obtained for the correlated SEMM. Whereas the correlated SEMM seems to have decreasing imaginary part – again not physical.

In spite of the fact that the correlated SEMM produced better fits, as observed on the two FRFs of Fig. 7.11a and Fig. 7.11c, one needs to bear in mind that this joint system is large and has high fluctuations. Whereas in the past, the identified joints were limited to small systems under simplified motion and assumptions. To note a few examples of stiff joints, a 2×2 spring-damper system was identified quite recently in [3], and a 4×4 spring-mass-damper system in [170]. This was also discussed at length in Chapter 5.

More importantly, the fitted joint must be able to predict the assembly response. For our more realistic joint system compared to the others in the cited literature, it would require curve-fitting to every FRF (a total of 576×2 curves including real and imaginary parts) in the joint accelerance whilst maintaining good matrix conditioning and symmetry. With such a large system, it is in itself a challenging task. Also, due to the used SEMM formulation which allows to avoid the drive-point FRFs, the expanded models become non-reciprocal [117]. As a result, the joint system does not essentially remain symmetric adding another hurdle to the curve-fitting. In fact, in our experience, various curve-fitting procedures could not predict the assembled response.

Note that the joint accelerance of Fig. 7.11 is coupled as such without any fitting to the respective substructures due to the above-cited difficulties. This type of on-board validation, as already discussed, predicts the reference FRFs (not included in the identification) in the same measurement campaign by recoupling the identified joint with the respective substructures.

7.3.4 Effect of singular value truncation on joint identification

In Section 3.6.2, the substructure SEMM models were inspected for their condition number by truncating the smallest singular values (SV) while computing the pseudo-inverses of the substructure numerical models. Of course, by doing so, the condition

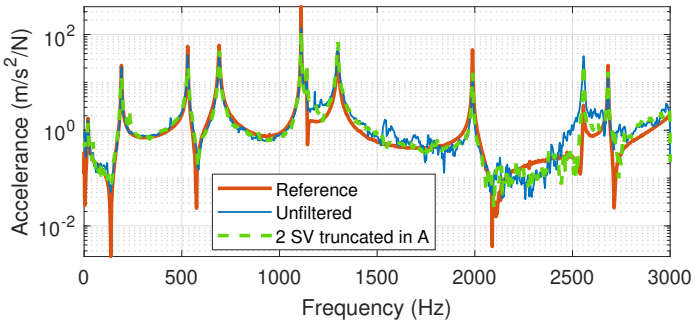

(a) SV filter in the blade

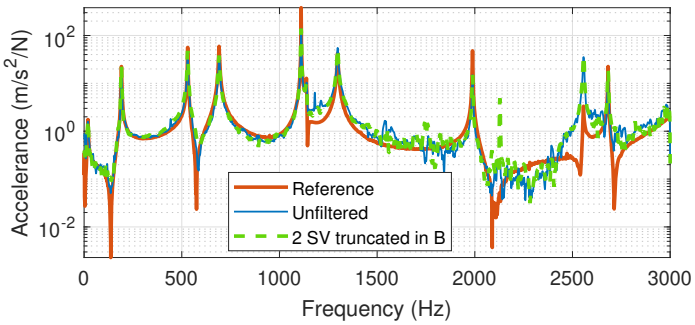

(b) SV filtering in the disk

Fig. 7.13 Effect of singular value filters on the recoupled system after joint identification. The filters are applied separately to the blade and disk. The reference FRF is measured at the locations shown in Fig. 6.9.

number decreases but can one reap any benefit from it in the joint identification context? This is what we investigate in this subsection.

The SV filtered hybrid models of the blade and disk are used to identify the joint with the two VP interface. To see a significant effect, two SVs are filtered in each hybrid sub-model at a time i.e. if the SVs are filtered in the blade, the disk model is kept as such and vice versa. The corresponding validation FRFs are shown in Fig. 7.13a and Fig. 7.13b. The unfiltered FRF is also shown for comparison. The predictions are much better here because an FRF between two different DoF is being considered now compared to the previous subsection. This can happen because through the identified joint, a different set of internal DoF can be better observed (or controlled). Conversely, another DoF set may not be better observed.

Since a good agreement up to 1100 Hz was observed with the unfiltered models in Figs. 7.13, the attention is given to the frequency range greater than 1100 Hz. In the reconstructed FRF of Fig. 7.13a, the identification by filtering in the blade

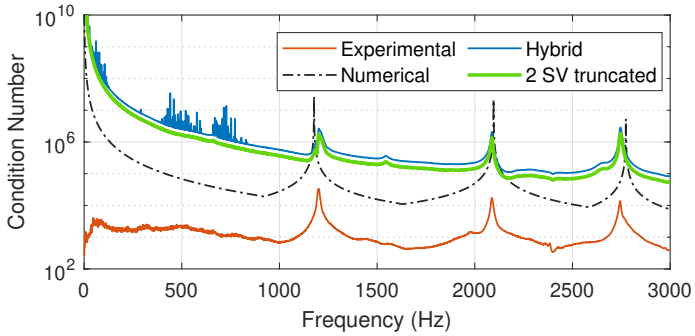

(a) Blade models

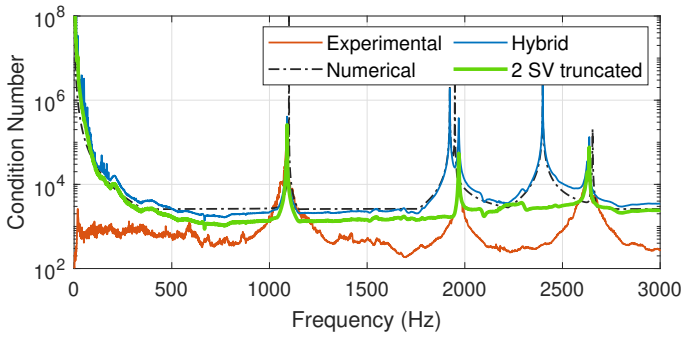

(b) Disk models

Fig. 7.14 The condition number of the experimental, numerical and hybrid FRF matrices of (a) the blade and (b) the disk. In each hybrid model, the condition number by truncating two singular values is also plotted.

has improved between 1500–2000 Hz. It overlaps well with the reference FRF. The resonances around 2700 Hz is also better estimated. The identification after the anti-resonance of 2100 Hz is also improved in comparison with the unfiltered FRF; however, it still has some spurious effect. The low amplitude regions like these are likely to get affected by the measurement errors. Despite this, it can be confidently said that the removal of the two lowest SVs in the blade hybrid model has appreciably improved the joint identification.

The SV filtering in the disk hybrid model has instead slightly degraded the identification in the high frequency range, as evident in the FRF of Fig. 7.13b. In order to understand the reasons, the condition number plots of the disk models are seen in Fig. 7.14b. The disk's hybrid model's condition number is nearly of the same order as that of the numerical model and it is not as high as in the case of the blade (Fig. 7.14a). By looking at the 2 SV truncated condition number of the disk, there is a considerable change in the condition number pattern from its unfiltered hybrid

model. This implies that the lowest filtered SVs are not very small and insignificant to be truncated. That is why, their filtration altered the disk hybrid dynamics.

From the above analysis, it is proposed that the SV filters should be deployed in the hybrid sub-models based on their condition number before and after filtering. If the condition number pattern of the filtered hybrid models is significantly different, the filtering may not affect positively on the joint identification.

Remark 3. *The SV filter is applied only to the substructures here i.e. whilst computing the hybrid FRF models of the blade and disk. One might consider to apply the same filter to the assembly's hybrid model in Eq. (3.29). If the SV filters are applied to the assembly, then recalling the iterative nature of the decoupling method, the assembled system's dynamics in the hybrid model are updated at each iteration due to two factors: the updated joint and the modified substructures (due to filtered SVs). As a result, convergence is not guaranteed for the joint identification. From another perspective, the system which we aim to identify is being modified at every iteration of the identification. This makes the filtration unwarranted on the assembled systems.*

7.4 Summary

This chapter concerns the results of the joint identification after all the theoretical basis was provided in the previous chapters including the identification methods and the individual substructure interface modelling. The substructure models were then used to identify the joints (prepared in previous chapters) from different assembled systems of the blade and disk system in this chapter. In order to test the SEMM decoupling method's ability to find the joint, a dummy coupled system was created by inserting a numerical joint between the blade and disk in Section 7.1. Despite measurement errors, the joint could be identified in a broad frequency range.

Then the actual assembly was used in which the disk was held fixed (Section 7.2). The method's convergence by varying weights of the pseudo-inverses was studied which showed a good convergence rate with higher weights assigned to the interface DoF. The self- and on-board validation after a joint identification were demonstrated. In the presence of large expansion errors, with the fixed disk both in the assembly and alone, the success seemed marginal. The joint had a lot of spurious effect.

Since the disk support seemed to hinder the joint identification, the disk was then left free of the support in Section 7.3. By doing so, the method did show great success in predicting the validation FRFs. The next test was to see whether the correlated SEMM models would augment the joint identification or not since they are thought to remove the erroneous or uncorrelated channels. A significant improvement was witnessed in the prediction including the non-resonance regions and amplitudes at resonances. Some of the joint accelerance plots were also discussed wherein a behaviour of low mass and high stiffness system was observed in the joint despite high fluctuations in values. Challenges related to fitting or parameter finding were also discussed even though correlated SEMM had more meaningful fitting curves. Finally, effect of singular value filtering in substructures was seen to improve further the results, especially filtering in the blade.

Chapter 8

Conclusions and Future Directions

8.1 Brief overview of the current work

One of the main challenges in predicting the dynamic response of the built-up systems is the presence of joints. Whilst they connect various components together, they introduce uncertainties and make the dynamic response prediction extremely challenging. The aim of this work is to investigate dynamic substructuring methods which can enable us to identify the blade-root interface (connection) dynamics by experimental measurements on a realistic blade and disk system.

Considering that in a typical dove-tail connection of a blade-root, it is not possible to measure directly on the interfaces, the dynamics at the interface have to be predicted by measurements at accessible points away from the joint. Dynamic expansion methods then become a necessity.

The thesis presents first dynamic substructuring methods and representations to express mechanical systems in a certain domain. The frequency based substructuring has since long been utilized in test-based analyses with a renewed interest after a generalized framework was developed by De Klerk et al. [40]. Thereafter, several dynamic expansion methods in general, and System Equivalent Model Mixing (SEMM) in particular, were discussed. SEMM, a recent method has the capability to expand measurements to inaccessible DoF on a substructure whilst possessing full rank, as opposed to its modal counterpart –SEREP.

The substructures – blade and disk – were tested and numerically modelled to undergo the SEMM expansion. The resulting expanded models could predict the interface dynamics better than the corresponding numerical models. As with any method, SEMM had some drawbacks. The noise and modelling errors propagate in the expanded models. In this research work, an upgrade has been proposed in SEMM that allows to identify the best and least correlated DoF. The newly developed method is called correlated SEMM. The procedure employs Frequency Response Assurance Criteria (FRAC). Its effectiveness on the measured blade and disk in different constraint conditions and from sensor-intrusiveness perspective was evaluated.

After generating reliable SEMM based expanded substructures, the joint identification has to be performed from the measured assembled system. For this purpose, several identification methods were first analysed and classified into i) inverse receptance coupling, ii) inverse substructuring, and iii) substructure decoupling methods. This provides an insight to a reader as to where a particular method belongs. The differences in the approaches are rooted in the treatment of rotations, usage of a set of coupling equations and joint parameter estimation. Most identification approaches reviewed herein have been limited to small joint systems. The substructure decoupling can be utilized to identify the joint under consideration, but it needed one more step. That is, even in the assembly, the joint DoF must be explicitly present in order to decouple the substructures and identify the joint. Again, SEMM was utilized for this purpose and the SEMM based iterative decoupling strategy was applied to the blade-disk joint system for the first time in this research.

For the blade-root interface, it was found through numerical and experimental studies that an interface consisting of minimum 12 DoF per substructure should be employed. A two virtual points interface, which includes both translations and rotations, was created.

The SEMM based decoupling strategy was then tested with a dummy-coupled system which was created by inserting a numerical joint between the blade and disk substructures. The method produced satisfactory results on the simulated joint. Later, the actual joint was also identified on the assembly of the same blade and disk (with the fixed disk). The on-board validation showed some limited success.

Since the fixed constraint posed modelling difficulties, it was then chosen to model both the structural components (blade and disk) in free conditions (as well

as their assembly). As a result, a very good agreement between experimental and identified FRFs was obtained.

The next step was to test the improved substructure models obtained by correlated SEMM in the joint identification. The validation procedure was then done and compared by using the standard SEMM and the correlated SEMM approaches. The recoupled FRF obtained by the correlated SEMM proved to be much more overlapped to the measured reference FRF than the FRF obtained by standard SEMM. In particular, the correlated SEMM showed to capture better the FRF plot in the non-resonance ranges.

Some of the joint accelerance plots were also discussed to inspect their behaviour. The joint accelerances were indicative of low mass and high stiffness system despite high fluctuations in values. Challenges related to fitting or parameter finding were also discussed. The correlated SEMM approach produced physically more meaningful fitting curves. Finally, the effect of singular value filtering in substructures was seen to improve further the results.

8.2 Contributions to knowledge

Contributions to the literature, based on the work presented in this thesis, can be summarized as following:

1. A simple experimental test-rig of two Aluminium beams (not discussed in the thesis) was used to identify the bolted joint by inverse receptance coupling approach. The challenges faced therein and preliminary blade-disk interface dynamics were studied in the context of frequency based substructuring [62].

2. An expansion (SEMM) based substructure decoupling method was applied for the first time to a blade-root connection experimentally which showed the possibility to identify the joint. Such an interface needed to be described by a large set of FRFs through rigorous measurement campaigns on the substructures and the assembly [189].

3. A correlation based strategy was developed and introduced in SEMM to filter the DoF which are least correlated with the corresponding numerical models.

Consequently, the quality of the expanded models and interface dynamics was improved [72, 119].

4. The correlation strategy was further refined and extended to the joint system of the blade and disk connection [71].

5. Further improvement of the joint identification strategy by incorporating singular value filtering in substructures and interface parametric studies [69].

6. A mathematical review of various linear joint identification methods in the literature is presented. Using the general framework of dynamic substructuring in frequency domain, the methods can be linked and categorized in three classes of linear joint identification.

8.3 Critical assessment of the approach

Based on the results presented in different chapters and especially in chapter 7, a real three dimensional and a complex structural system of a blade and disk has been tested and expanded with SEMM in order to identify the joint. As a general observation, the results are affected by various factors including the constraint modelling, choice of internal (measurements) and interface (identification) DoF and the measurement errors. During this research, some of those factors were heuristically taken in consideration to reduce their detrimental effect. For instance:

- The presence of hub (constraint) in the disk was removed after its considerable effect on the identification.

- It was observed during the post-processing that some measurements and numerical FRFs had high discrepancies. Consequently, a correlation based strategy was developed. This method, in general, can be very useful in other applications to identify high or low correlated DoF.

- Even still the substructure models can have noise coming from the measurements whose effect was considered to be reduced by filtering the lowest singular values.

Despite some instances given above, there is certainly much more that could be done. It seems natural that whenever we fix a problem, another one comes up. In this context and in particular to our approach, the following critical remarks are made:

1. The extended interface formulation of SEMM made it possible to avoid the drive-point FRFs to produce square FRF matrices suitable for substructure decoupling. This is a great advantage; however, the resulting hybrid models are not symmetric. This can pose additional problems in joint identification as well as in curve-fitting.

2. In the reviewed classifications of inverse methods in this thesis, the identification comes out to be frequency-dependent. Thus, the curve-fitting should be expected in this process. In an attempt to identify the blade-root type complex joint system, a curve-fitting that could predict a set of reference measurements was not successful.

3. In almost all the cited test-based identifications (inverse-approaches), no accounts of uncertainty or confidence intervals were provided. One part of this is due to the fact that the testing becomes cumbersome when many FRFs have to be measured. The other part is the absence of a robust framework of uncertainty propagation in the inverse FRF-based problems.

8.4 Future work

The critical assessment in the previous section brings us to suggests the following for further research.

1. In order to avoid the non-symmetric FRF system, as a result of the extended formulation of SEMM, a modal filter can be applied to measured FRFs to produce synthesized FRFs. Although it would introduce other limitations usually encountered in modal parameter estimation, the SEMM would produce a symmetric model whilst measuring only a few drive-point FRFs – a trade-off would have to be made. It can be shown that SEMM would still have sufficient rank. Furthermore, SEMM being a very useful tool, needs to be investigated for its optimal basis – both regarding the numerical and experimental models.

2. The identified joints in this work can be seen to provide a foundation to attempt more complex systems. Its results can be investigated further to perform curve-fitting using global optimization techniques.

3. There is a strong need to develop a robust yet practical error (uncertainty) quantification framework for handling of large FRF-based systems. At the root of such a framework should be the frequently encountered yet a very valid question of repeatability in measured built-up systems.

It is thought that in the joint modelling and (linear) identification problems, the last two recommendations are a pre-requisite for a multi-joint system identification, such as multiple blade-roots in bladed-disks.

References

[1] B. A. Cowles. High cycle fatigue in aircraft gas turbines—an industry perspective. *International Journal of Fracture*, 80(2-3):147–163, apr 1996.

[2] J.-S. Tsai and Y.-F. Chou. The identification of dynamic characteristics of a single bolt joint. *Journal of Sound and Vibration*, 125(3):487–502, sep 1988.

[3] Şerife Tol and H. Nevzat Özgüven. Dynamic characterization of bolted joints using FRF decoupling and optimization. *Mechanical Systems and Signal Processing*, 54:124–138, mar 2015.

[4] Matthew R W Brake. *The Mechanics of Jointed Structures*. Springer International Publishing, Cham, 2018.

[5] Maria Angelica Mayorca. *Numerical methods for turbomachinery aeromechanical predictions*. PhD thesis, KTH Royal Institute of Technology, Stockholm, 2011.

[6] Richard Budynas and Keith Nisbett. *Shigley's Mechanical Engineering Design, Ninth Edition*. McGraw-Hill, New York, NY, USA, 2009.

[7] Laurent Keersmaekers, Luc Mertens, Rudi Penne, Patrick Guillaume, and Gunther Steenackers. Decoupling of mechanical systems based on in-situ frequency response functions: The link-preserving, decoupling method. *Mechanical Systems and Signal Processing*, 58-59:340–354, jun 2015.

[8] Maarten V. van der Seijs. *Experimental Dynamic Substructuring Analysis and Design Strategies for Vehicle Development*. PhD thesis, TU Delft, Delft, The Netherlands, 2016.

[9] Michael Haeussler, Eric A Pasma, T Mueller, Eric A Pasma, J Freund, O Westphal, and T Voehringer. Component TPA: benefit of including rotational degrees of freedom and over-determination. In *ISMA 2020 - International Conference on Noise and Vibration Engineering*, number September, pages 1135–1148, 2020.

[10] JWR Meggitt, AS Elliott, AT Moorhouse, and H. Kevin Lai. In situ determination of dynamic stiffness for resilient elements. *Proceedings of the Institution of Mechanical Engineers, Part C: Journal of Mechanical Engineering Science*, 230(6):986–993, apr 2016.

[11] M. Haeussler, S.W.B. Klaassen, and D.J. Rixen. Experimental twelve degree of freedom rubber isolator models for use in substructuring assemblies. *Journal of Sound and Vibration*, 474:115253, may 2020.

[12] Walter C Hurty. Vibrations of structural systems by component mode synthesis. *Journal of the Engineering Mechanics Division*, 86(4):51–69, 1960.

[13] Roy R. Craig and Mervyn C.C. Bampton. Coupling of substructures for dynamic analyses. *AIAA Journal*, 6(7):1313–1319, jul 1968.

[14] G. M.L. Gladwell. Branch mode analysis of vibrating systems. *Journal of Sound and Vibration*, 1(1):41–59, jan 1964.

[15] Robert J. Guyan. Reduction of stiffness and mass matrices. *AIAA Journal*, 3(2):380, feb 1965.

[16] Richard H. MacNeal. A hybrid method of component mode synthesis. *Computers and Structures*, 1(4):581–601, dec 1971.

[17] S. Rubin. Improved Component-Mode Representation for Structural Dynamic Analysis. *AIAA Journal*, 13(8):995–1006, aug 1975.

[18] Daniel J. Rixen. A dual Craig-Bampton method for dynamic substructuring. *Journal of Computational and Applied Mathematics*, 168(1-2):383–391, jul 2004.

[19] Stefano Zucca. On the dual Craig–Bampton method for the forced response of structures with contact interfaces. *Nonlinear Dynamics*, 87(4):2445–2455, 2017.

[20] Sang-Ho Lim, Ronnie Bladh, Matthew P. Castanier, and Christophe Pierre. Compact, Generalized Component Mode Mistuning Representation for Modeling Bladed Disk Vibration. *AIAA Journal*, 45(9):2285–2298, sep 2007.

[21] Jan Ronnie Bladh. Efficient predictions of the vibratory response of mistuned bladed disks by reduced order modeling. Technical report, The University of Michigan,, 2001.

[22] P. Vargiu, C. M. Firrone, S. Zucca, and M. M. Gola. A reduced order model based on sector mistuning for the dynamic analysis of mistuned bladed disks. *International Journal of Mechanical Sciences*, 53(8):639–646, aug 2011.

[23] G. Battiato, C. M. Firrone, T. M. Berruti, and B. I. Epureanu. Reduction and coupling of substructures via Gram–Schmidt Interface modes. *Computer Methods in Applied Mechanics and Engineering*, 336:187–212, jul 2018.

[24] S. Mehrdad Pourkiaee and Stefano Zucca. A Reduced Order Model for Nonlinear Dynamics of Mistuned Bladed Disks With Shroud Friction Contacts. *Journal of Engineering for Gas Turbines and Power*, 141(1), jan 2019.

[25] S. Mehrdad Pourkiaee and Stefano Zucca. Mixed-Boundary Component Mode Substitution for Nonlinear Dynamics of Mistuned Shrouded Bladed Disks. *AIAA Journal*, 58(1):402–414, jan 2020.

[26] Fabian M. Gruber and Daniel J. Rixen. Evaluation of substructure reduction techniques with fixed and free interfaces. *Strojniski Vestnik/Journal of Mechanical Engineering*, 62(7-8):452–462, 2016.

[27] Raul Rodriguez Sanchez, Martin Buchschmid, and Gerhard Müller. Model order reduction in structural dynamics. *ECCOMAS Congress 2016 - Proceedings of the 7th European Congress on Computational Methods in Applied Sciences and Engineering*, 2(June):4221–4247, 2016.

[28] Dimitri Krattiger, Long Wu, Martin Zacharczuk, Martin Buck, Robert J. Kuether, Matthew S. Allen, Paolo Tiso, and Matthew R.W. Brake. Interface reduction for Hurty/Craig-Bampton substructured models: Review and improvements. *Mechanical Systems and Signal Processing*, 114:579–603, jan 2019.

[29] W.J. Duncan. XXXV. The admittance method for obtaining the natural frequencies of systems. *The London, Edinburgh, and Dublin Philosophical Magazine and Journal of Science*, 32(214):401–409, nov 1941.

[30] Thomas G. Sofrin. The Combination of Dynamical Systems. *Journal of the Aeronautical Sciences*, 13(6):281–288, 1946.

[31] Bjorn Jetmundsen, Richard L. Bielawa, and William G. Flannelly. Generalized Frequency Domain Substructure Synthesis. *Journal of the American Helicopter Society*, 33(1):55–64, jan 1988.

[32] Walter D'Ambrogio and Aldo Sestieri. A Unified Approach to Substructuring and Structural Modification Problems. *Shock and Vibration*, 11(3-4):295–309, 2004.

[33] J.H. Gordis, R.L. Bielawa, and W.G. Flannelly. A general theory for frequency domain structural synthesis. *Journal of Sound and Vibration*, 150(1):139–158, oct 1991.

[34] Dennis De Klerk, Daniel J. Rixen, and Jasper De Jong. The Frequency Based Substructuring (FBS) method reformulated according to the dual Domain Decomposition method. In *Modal analysis conference; IMAC XXIV*, pages 2166–2179, St. Louis, MO, 2006.

[35] Walter D'Ambrogio and Annalisa Fregolent. Promises and pitfalls of decoupling procedures. In *Proceeding of the Twenty-Sixth International Modal Analysis Conference*, number February 2008, Orlando, Florida, 2008.

[36] Walter D'Ambrogio and Annalisa Fregolent. The role of interface DoFs in decoupling of substructures based on the dual domain decomposition. *Mechanical Systems and Signal Processing*, 24(7):2035–2048, oct 2010.

[37] Walter D'Ambrogio and Annalisa Fregolent. Inverse dynamic substructuring using the direct hybrid assembly in the frequency domain. *Mechanical Systems and Signal Processing*, 45(2):360–377, apr 2014.

[38] S. N. Voormeeren. *Dynamic substructuring methodologies for integrated dynamic analysis of wind turbines*. PhD thesis, TU Delft, Delft, The Netherlands, 2012.

[39] Matthew S Allen, Daniel Rixen, Maarten van der Seijs, Paolo Tiso, Thomas Abrahamsson, and Randall L Mayes. *Substructuring in Engineering Dynamics*, volume 594 of *CISM International Centre for Mechanical Sciences*. Springer International Publishing, Cham, 2020.

[40] D. de Klerk, D. J. Rixen, and S. N. Voormeeren. General Framework for Dynamic Substructuring: History, Review and Classification of Techniques. *AIAA Journal*, 46(5):1169–1181, may 2008.

[41] Daniel J. Rixen and Paul L.C. Van Der Valk. An impulse based substructuring approach for impact analysis and load case simulations. *Journal of Sound and Vibration*, 332(26):7174–7190, dec 2013.

[42] Paul L.C. Van der Valk and Daniel J. Rixen. An Impulse Based Substructuring method for coupling impulse response functions and finite element models. *Computer Methods in Applied Mechanics and Engineering*, 275:113–137, jun 2014.

[43] Per Sjövall, Tomas McKelvey, and Thomas Abrahamsson. Constrained state-space system identification with application to structural dynamics. *Automatica*, 2006.

[44] Per Sjövall and Thomas Abrahamsson. Component system identification and state-space model synthesis. *Mechanical Systems and Signal Processing*, 2007.

[45] Per Sjövall and Thomas Abrahamsson. Substructure system identification from coupled system test data. *Mechanical Systems and Signal Processing*, 22(1):15–33, jan 2008.

[46] Matthew S Allen and Randall L Mayes. Comparison of FRF and Modal Methods for Combining Experimental and Analytical Substructures. Technical report.

[47] Matthew S. Allen, Randall L. Mayes, and Elizabeth J. Bergman. Experimental modal substructuring to couple and uncouple substructures with flexible fixtures and multi-point connections. *Journal of Sound and Vibration*, 329(23):4891–4906, nov 2010.

[48] Daniel J. Rixen. How measurement inaccuracies induce spurious peaks in Frequency Based Substructuring. In *Conference Proceedings of the Society for Experimental Mechanics Series*, pages 1–15, Bethel, CT, 2008.

[49] S.N. Voormeeren, D. de Klerk, and D.J. Rixen. Uncertainty quantification in experimental frequency based substructuring. *Mechanical Systems and Signal Processing*, 24(1):106–118, jan 2010.

[50] S.N. Voormeeren and D.J. Rixen. A family of substructure decoupling techniques based on a dual assembly approach. *Mechanical Systems and Signal Processing*, 27(1):379–396, feb 2012.

[51] D J Ewins. *Modal testing : theory, practice and application*. Baldock : Research Studies, Baldock, 2nd ed edition, 2000.

[52] Miha Pogačar, Tomaž Bregar, Gregor Čepon, and Miha Boltežar. Near-to-node modal identification using multiple related response models. *Measurement*, 171:108793, 2021.

[53] Eric J Ruggiero and Daniel J Inman. A Comparison between SISO and MIMO Modal Analysis Techniques on a Membrane Mirror Satellite. *Journal of Intelligent Material Systems and Structures*, 16(3):273–282, mar 2005.

[54] M A Peres, C Kallmeyer, M C Witter, R Carneiro, F D Marques, and L P R de Oliveira. Advantages of Multiple-Input Multiple-Output (MIMO) testing using low level excitation systems. In *International Conference on Noise and Vibration Engineering*, 2014.

[55] Peter Avitabile. *Modal Testing: A Practitioner's Guide*. John Wiley and Sons Ltd, Chichester, UK, nov 2017.

[56] Walter D'Ambrogio and Annalisa Fregolent. Direct decoupling of substructures using primal and dual formulation. In *Conference Proceedings of the Society for Experimental Mechanics Series*, volume 2, pages 47–76. 2011.

[57] H. Nevzat Özgüven. Structural modifications using frequency response functions. *Mechanical Systems and Signal Processing*, 4(1):53–63, jan 1990.

[58] Y. Ren and C. F. Beards. Identification of 'Effective' Linear Joints Using Coupling and Joint Identification Techniques. *Journal of Vibration and Acoustics*, 120(2):331–338, apr 1998.

[59] Jiantie Zhen, Teik C Lim, and Guangqing Lu. Determination of system vibratory response characteristics applying a spectral-based inverse sub-structuring approach. Part I: analytical formulation. *International Journal of Vehicle Noise and Vibration*, 1(1/2):1, 2004.

[60] Walter D'Ambrogio and Annalisa Fregolent. Are Rotational DoFs Essential in Substructure Decoupling? In *Conference Proceedings of the Society for Experimental Mechanics Series*, volume 1, pages 27–36. Springer New York LLC, 2014.

[61] Armin Drozg, Gregor Čepon, and Miha Boltežar. Full-degrees-of-freedom frequency based substructuring. *Mechanical Systems and Signal Processing*, 98:570–579, jan 2018.

[62] Z. Saeed, C. M. Firrone, and T. M. Berruti. Substructuring for Contact Parameters Identification in Bladed-disks. *Journal of Physics: Conference Series*, 1264(1):012037, jul 2019.

[63] M L M Duarte and D J Ewins. Some Insights into the Importance of Rotational Degrees-of-freedom and Residual Terms in Coupled Structure Analysis. In *Proceedings of the 13th International Modal Analysis Conference*, volume 2460, pages 164–170, 1995.

[64] Tomaž Bregar, Nikola Holeček, Gregor Čepon, Daniel J. Rixen, and Miha Boltežar. Including directly measured rotations in the virtual point transformation. *Mechanical Systems and Signal Processing*, 141:106440, jul 2020.

[65] Maria Lúcia M. Duarte and David J. Ewins. Rotational degrees of freedom for structural coupling analysis via finite-difference technique with residual compensation. *Mechanical Systems and Signal Processing*, 14(2):205–227, mar 2000.

[66] D. De Klerk, D. J. Rixen, S. N. Voormeeren, and F. Pasteuning. Solving the RDoF problem in experimental dynamic substructuring. Technical report, 2008.

[67] M. V. van der Seijs, D. de Klerk, D. J. Rixen, and S. Rahimi. Validation of Current State Frequency Based Substructuring Technology for the Characterisation of Steering Gear–Vehicle Interaction. In *Topics in Experimental Dynamic Substructuring - Proceedings of the 31st IMAC, A Conference on Structural Dynamics, 2013*, volume 2, pages 253–266. 2014.

[68] T. C. Lim and J. Li. A theoretical and computational study of the FRF-based substructuring technique applying enhanced least square and TSVD approaches. *Journal of Sound and Vibration*, 231(4):1135–1157, apr 2000.

[69] Z Saeed, M Kazeminasab, C M Firrone, and T M Berruti. Improved identification of a blade-disk coupling through a parametric study of the dynamic hybrid models. *ISMA 2020 - International Conference on Noise and Vibration Engineering*, pages 1323–1336, 2020.

[70] Zeeshan Saeed, Steven W.B. Klaassen, Christian M. Firrone, Teresa M. Berruti, and Daniel J. Rixen. Experimental joint identification using system equivalent model mixing in a bladed disk. *Journal of Vibration and Acoustics, Transactions of the ASME*, 142(5):051001, oct 2020.

[71] Zeeshan Saeed, Christian M. Firrone, and Teresa M. Berruti. Joint identification through hybrid models improved by correlations. *Journal of Sound and Vibration*, 494:115889, mar 2021.

[72] Zeeshan Saeed, Christian Maria Firrone, and Teresa Maria Berruti. Hybrid Numerical-Experimental Model Update Based on Correlation Approach for Turbine Components. In *Volume 11: Structures and Dynamics: Structural*

Mechanics, Vibration, and Damping; Supercritical CO2. American Society of Mechanical Engineers, sep 2020.

[73] Julie Harvie and Peter Avitabile. Effects of precise FRF measurements for frequency based substructuring. *Sound and Vibration Magazine*, 52(1):3–7, feb 2018.

[74] Alex Berman. Mass Matrix Correction Using an Incomplete Set of Measured Modes. *AIAA Journal*, 17(10):1147–1148, oct 1979.

[75] Jay C. Chen and John A. Garba. Analytical Model Improvement Using Modal Test Results. *AIAA Journal*, 18(6):684–690, jun 1980.

[76] Menahem Baruch. Optimal correction of mass and stiffness matrices using measured modes. *AIAA Journal*, 20(11):1623–1626, nov 1982.

[77] John E. Mottershead, Michael Link, and Michael I. Friswell. The sensitivity method in finite element model updating: A tutorial. *Mechanical Systems and Signal Processing*, 2011.

[78] J.E. Mottershead and M.I. Friswell. Model Updating In Structural Dynamics: A Survey. *Journal of Sound and Vibration*, 167(2):347–375, oct 1993.

[79] Melissa Arras. *On the use of Frequency Response Functions in the finite element model updating*. PhD thesis, Sapienza University of Rome, Rome, 2016.

[80] E. Dascotte. Applications of finite element model tuning using experimental modal data. *Sound and Vibration Magazine*, 25(6):22–26, 1991.

[81] N. Cottin, H. P. Felgenhauer, and H. G. Natke. On the parameter identification of elastomechanical systems using input and output residuals. *Ingenieur-Archiv*, 54(5):378–387, 1984.

[82] A. Sestieri and Walter D'Ambrogio. Why be Modal: How to Avoid the Use of Modes in the Modification of Vibrating Systems. In *Proceedings of the 7th International Modal Analysis Conference*, pages 25–30, 1989.

[83] H. G. Natke. Updating computational models in the frequency domain based on measured data: a survey. *Probabilistic Engineering Mechanics*, 1988.

[84] R.M. Lin and J. Zhu. Model updating of damped structures using FRF data. *Mechanical Systems and Signal Processing*, 20(8):2200–2218, nov 2006.

[85] J.W.R. Meggitt and A.T. Moorhouse. Finite element model updating using in-situ experimental data. *Journal of Sound and Vibration*, 489:115675, dec 2020.

[86] D. Martinez, T. Carne, D. Gregory, and A. Miller. Combined experimental/analytical modeling using component mode synthesis. In *25th Structures, Structural Dynamics and Materials Conference*, Reston, Virigina, may 1984. American Institute of Aeronautics and Astronautics.

[87] M. L. M. Duarte and D. J. Ewins. Improved experimental component mode synthesis (IECMS) with residual compensation based purely on experimental results. In *Proceedings of the 14th IMAC*, pages 641–647, Dearborn, MI, 1996.

[88] S. A. Hosseini Kordkheili, S. H. Momeni Massouleh, M. J. Kokabi, and H. Bahai. A modal coupling procedure to improve residual modal effects based on experimentally generated data. *Journal of Sound and Vibration*, 331(1):66–80, jan 2012.

[89] T. N. Shiau and J. L. Hwang. Generalized Polynomial Expansion Method for the Dynamic Analysis of Rotor-Bearing Systems. *Journal of Engineering for Gas Turbines and Power*, 115(2):209–217, apr 1993.

[90] A. Czekanski and V. V. Zozulya. Dynamics of vibrating beams using first-order theory based on Legendre polynomial expansion. *Archive of Applied Mechanics*, 90(4):789–814, apr 2020.

[91] Yuanchang Chen, Peter Avitabile, Christopher Page, and Jacob Dodson. A polynomial based dynamic expansion and data consistency assessment and modification for cylindrical shell structures. *Mechanical Systems and Signal Processing*, 154:107574, jun 2021.

[92] Andy Moorhouse and Andy Elliott. The "round trip" theory for reconstruction of Green's functions at passive locations. *The Journal of the Acoustical Society of America*, 134(5):3605–3612, nov 2013.

[93] John C. O'Callahan, Peter Avitable, and Robert Riemer. System equivalent reduction expansion process (SEREP). In *7th International Modal Analysis Conference*, pages 29–37, Boston, MA, 1989. Society for Experimental Mechanics, Bethel, CT.

[94] Steven W.B. Klaassen, Maarten V. van der Seijs, and Dennis de Klerk. System equivalent model mixing. *Mechanical Systems and Signal Processing*, 105(December):90–112, may 2018.

[95] Dana Nicgorski and Peter Avitabile. Conditioning of FRF measurements for use with frequency based substructuring. *Mechanical Systems and Signal Processing*, 24(2):340–351, feb 2010.

[96] Hasan G. Pasha, Randall J. Allemang, and Allyn W. Phillips. Techniques for Synthesizing FRFs from Analytical Models. In G. Foss and C. Niezrecki, editors, *Special Topics in Structural Dynamics, Volume 6. Conference Proceedings of the Society for Experimental Mechanics Series*, pages 73–79. Springer, Cham, 2014.

[97] Julie Harvie and Peter Avitabile. An Improved Expansion Process for Guyan Reduced Models: Technique for Improved Guyan Expansion Reconstruction (TIGER). In G. Foss and C. Niezrecki, editors, *Special Topics in Structural*

Dynamics, Volume 6. Conference Proceedings of the Society for Experimental Mechanics Series, pages 109–120. Springer, Cham, 2014.

[98] Gregor Čepon, Armin Drozg, and Miha Boltežar. Introduction of line contact in frequency-based substructuring process using measured rotational degrees of freedom. *Journal of Physics: Conference Series*, 1264(1):012025, jul 2019.

[99] Marius Tarpø, Bruna Nabuco, Christos Georgakis, and Rune Brincker. Expansion of experimental mode shape from operational modal analysis and virtual sensing for fatigue analysis using the modal expansion method. *International Journal of Fatigue*, 130:105280, jan 2020.

[100] Mahesh Murugan Jaya, Rosario Ceravolo, Luca Zanotti Fragonara, and Emiliano Matta. An optimal sensor placement strategy for reliable expansion of mode shapes under measurement noise and modelling error. *Journal of Sound and Vibration*, 487:115511, nov 2020.

[101] Anders T. Johansson and Thomas J.S. S. Abrahamsson. Selecting Appropriate Analytical Mode Basis for SEREP-Expansion of Experimental Modes. In T. Proulx, editor, *Modal Analysis Topics, Volume 3. Conference Proceedings of the Society for Experimental Mechanics Series*, volume 3, pages 1–15. Springer, New York, NY, 2011.

[102] Louis Thibault, Adam Butland, and Peter Avitabile. Variability improvement of key inaccurate node groups - VIKING. In *Conference Proceedings of the Society for Experimental Mechanics Series*, volume 6, pages 603–624. Springer, New York, NY, 2012.

[103] A.M. Steenhoek, M.W. van der Kooij, M.L.J. Verhees, D.D. van den Bosch, and J.M. Harvie. Test-Based Modeling, Source Characterization and Dynamic Substructuring Techniques Applied on a Modular Industrial Demonstrator. In *Conference Proceedings of the Society for Experimental Mechanics Series*, pages 73–76, 2020.

[104] S. Krügel and D.J. Rixen. Frequency based model mixing for machine condition monitoring. In *Conference Proceedings of the Society for Experimental Mechanics Series*, pages 157–161, 2021.

[105] Miha Kodrič, Gregor Čepon, and Miha Boltežar. Experimental framework for identifying inconsistent measurements in frequency-based substructuring. *Mechanical Systems and Signal Processing*, 154:107562, jun 2021.

[106] T. Bregar, K. Zaletelj, G. Čepon, J. Slavič, and M. Boltežar. Improved frf estimation from noisy high-speed camera data using semm. In *Conference Proceedings of the Society for Experimental Mechanics Series*, pages 115–118, 2020.

[107] Tomaž Bregar, Klemen Zaletelj, Gregor Čepon, Janko Slavič, and Miha Boltežar. Full-field FRF estimation from noisy high-speed-camera data using a

dynamic substructuring approach. *Mechanical Systems and Signal Processing*, 150:107263, mar 2021.

[108] Domen Ocepek, Miha Kodrič, Gregor Čepon, and Miha Boltežar. On the estimation of structural admittances from acoustic measurement using a dynamic substructuring approach. *Applied Acoustics*, 180:108115, sep 2021.

[109] H. A. van der Vorst. Bi-CGSTAB: A Fast and Smoothly Converging Variant of Bi-CG for the Solution of Nonsymmetric Linear Systems. *SIAM Journal on Scientific and Statistical Computing*, 13(2):631–644, mar 1992.

[110] Yousef Saad and Henk A van der Vorst. Iterative solution of linear systems in the 20th century. *Journal of Computational and Applied Mathematics*, 123(1-2):1–33, nov 2000.

[111] Weiwei Xiao, Li Li, and Sheng Lei. Accurate modal superposition method for harmonic frequency response sensitivity of non-classically damped systems with lower-higher-modal truncation. *Mechanical Systems and Signal Processing*, 85:204–217, feb 2017.

[112] U. Hetmaniuk, R. Tezaur, and C. Farhat. Review and assessment of interpolatory model order reduction methods for frequency response structural dynamics and acoustics problems, jun 2012.

[113] Michele Benzi. Preconditioning techniques for large linear systems: A survey. *Journal of Computational Physics*, 182(2):418–477, nov 2002.

[114] Navneet Pratap Singh and Kapil Ahuja. Reusing Preconditioners in Projection Based Model Order Reduction Algorithms. *IEEE Access*, 8:133233–133247, mar 2020.

[115] Navneet Pratap Singh and Kapil Ahuja. Preconditioned linear solves for parametric model order reduction. *International Journal of Computer Mathematics*, 97(7):1484–1502, jul 2020.

[116] James R. Bunch and John E. Hopcroft. Triangular Factorization and Inversion by Fast Matrix Multiplication. *Mathematics of Computation*, 28(125):231, jan 1974.

[117] Steven W.B. Klaassen and Daniel J. Rixen. The inclusion of a singular-value based filter in SEMM. In *International Modal Analysis Conference*, pages 1—-15, Houston, Texas, 2020.

[118] D.J. Ewins. On predicting point mobility plots from measurements of other mobility parameters. *Journal of Sound and Vibration*, 70(1):69–75, may 1980.

[119] Zeeshan Saeed, Christian Maria Firrone, and Teresa Maria Berruti. Hybrid Numerical-Experimental Model Update Based on Correlation Approach for Turbine Components. *Journal of Engineering for Gas Turbines and Power*, 143(4):041009, apr 2021.

[120] Henning Grafe. *Model Updating of Large Structural Dynamics Models Using Measured Response Functions*. PhD thesis, Imperial College of Science, Technology and Medicine, University of London, 1998.

[121] R. J. Allemang and D. L. Brown. Correlation Coefficient for Modal Vector Analysis. In *Proceedings of the International Modal Analysis Conference and Exhibit*, pages 110–116, 1982.

[122] N. A. J. Lieven and D. J. Ewins. Spatial correlation of mode shapes: the coordinate modal assurance criterion (COMAC). In *Proceedings of the 6th International Modal Analysis Conference (IMAC)*, 1988.

[123] P. Avitabile and F. Pechinsky. THE COORDINATE ORTHOGONALITY CHECK (CORTHOG). *Mechanical Systems and Signal Processing*, 12(3):395–414, may 1998.

[124] D. J. Ewins. Model validation: correlation for updating. In *Sadhana - Academy Proceedings in Engineering Sciences*, volume 25, pages 221–234, 2000.

[125] D. J. Nefske and H. Sung. Correlation of a Coarse-Mesh Finite Element Model Using Structural System Identification and a Frequency Response Assurance Criterion. In *14th International Modal Analysis Conference (IMAC)*, pages 597–602, Dearborn, USA, 1996.

[126] W Heylen and S Lammens. FRAC: A Consistent way of Comparing Frequency Response Functions. In *Proceedings, International Conference on Identification in Engineering, Swansea*, pages 48–57, 1996.

[127] C. Zang, H. Grafe, and M. Imregun. Frequency-domain criteria for correlating and updating dynamic finite element models. *Mechanical Systems and Signal Processing*, 15(1):139–155, jan 2001.

[128] R. Pascual, J. C. Golinval, and M. Razeto. A frequency domain correlation technique for model correlation and updating. In *International Modal Analysis Conference (IMAC)*, pages 587–592, 1996.

[129] M. Arras and G. Coppotelli. Finite-Element Structural Updating Using Frequency Response Functions. *Journal of Aircraft*, 52(5):1454–1468, sep 2015.

[130] Yuanchang Chen, Peter Avitabile, and Jacob Dodson. Data Consistency Assessment Function (DCAF). *Mechanical Systems and Signal Processing*, 141:106688, jul 2020.

[131] Alessandro Zanarini. Full field optical measurements in experimental modal analysis and model updating. *Journal of Sound and Vibration*, 442(July 2013):817–842, mar 2019.

[132] Navid Hasheminejad, Cedric Vuye, Wim Van den bergh, Joris Dirckx, and Steve Vanlanduit. A Comparative Study of Laser Doppler Vibrometers for Vibration Measurements on Pavement Materials. *Infrastructures*, 3(4):47, nov 2018.

[133] A.B. Stanbridge, D.J. Ewins, and A.Z. Khan. Modal Testing Using Impact Excitation and a Scanning LDV. *Shock and Vibration*, 7(2):91–100, 2000.

[134] O. Cakar and K.Y Sanliturk. Elimination of transducer mass loading effects from frequency response functions. *Mechanical Systems and Signal Processing*, 19(1):87–104, jan 2005.

[135] Shusheng Bi, Jun Ren, Wei Wang, and Guanghua Zong. Elimination of transducer mass loading effects in shaker modal testing. *Mechanical Systems and Signal Processing*, 38(2):265–275, jul 2013.

[136] Jun Ren, Jun Wang, Xiaodong Zhou, and Kwun-Lon Ting. Correction of Multiple Transducers Masses Effects From the Measured FRFS. In *Volume 8: 29th Conference on Mechanical Vibration and Noise*, volume 8. American Society of Mechanical Engineers, aug 2017.

[137] M I Friswell. Inverse problems in structural dynamics. In *Proceedings of the 2th International Conference on Multidisciplinary Design Optimization and Applications", Gijon, Spain*, 2008.

[138] Charles W Groetsch. *Inverse problems in the mathematical sciences*, volume 52. Springer, 1993.

[139] Stefano Zucca and Christian Maria Firrone. Nonlinear dynamics of mechanical systems with friction contacts: Coupled static and dynamic Multi-Harmonic Balance Method and multiple solutions. *Journal of Sound and Vibration*, 333(3):916–926, 2014.

[140] Jerry H. Griffin. A Review of Friction Damping of Turbine Blade Vibration. *International Journal of Turbo and Jet Engines*, 7(3-4):297–308, jan 1990.

[141] R.A. Ibrahim and C.L. Pettit. Uncertainties and dynamic problems of bolted joints and other fasteners. *Journal of Sound and Vibration*, 279(3-5):857–936, jan 2005.

[142] Loic Salles, Laurent Blanc, Fabrice Thouverez, Aleksander M. Gouskov, and Pierrick Jean. Dynamic Analysis of a Bladed Disk With Friction and Fretting-Wear in Blade Attachments. *Volume 6: Structures and Dynamics, Parts A and B*, pages 465–476, 2009.

[143] Cagri Tepe and Ender Cigeroglu. Structural coupling of two-nonlinear structures. In *Conference Proceedings of the Society for Experimental Mechanics Series*, volume 4, pages 163–173. 2015.

[144] Malte Krack, Loic Salles, and Fabrice Thouverez. Vibration Prediction of Bladed Disks Coupled by Friction Joints. *Archives of Computational Methods in Engineering*, 24(3):589–636, jul 2017.

[145] Erhan Ferhatoglu, Ender Cigeroglu, and H. Nevzat Özgüven. A new modal superposition method for nonlinear vibration analysis of structures using hybrid mode shapes. *Mechanical Systems and Signal Processing*, 107:317–342, jul 2018.

[146] G. Kerschen, M. Peeters, J. C. Golinval, and A. F. Vakakis. Nonlinear normal modes, Part I: A useful framework for the structural dynamicist. *Mechanical Systems and Signal Processing*, 23(1):170–194, jan 2009.

[147] S. Ponsioen, T. Pedergnana, and G. Haller. Analytic prediction of isolated forced response curves from spectral submanifolds. *Nonlinear Dynamics*, 98(4):2755–2773, dec 2019.

[148] Jie Yuan, Fadi El-Haddad, Loic Salles, and Chian Wong. Numerical Assessment of Reduced Order Modeling Techniques for Dynamic Analysis of Jointed Structures With Contact Nonlinearities. *Journal of Engineering for Gas Turbines and Power*, 141(3), mar 2019.

[149] Martin Jahn, Sebastian Tatzko, Lars Panning-von Scheidt, and Jörg Wallaschek. Comparison of different harmonic balance based methodologies for computation of nonlinear modes of non-conservative mechanical systems. *Mechanical Systems and Signal Processing*, 127:159–171, jul 2019.

[150] Simon S. Park, Yusuf Altintas, and Mohammad Movahhedy. Receptance coupling for end mills. *International Journal of Machine Tools and Manufacture*, 43(9):889–896, jul 2003.

[151] Tony L. Schmitz, Matthew A. Davies, and Michael D. Kennedy. Tool Point Frequency Response Prediction for High-Speed Machining by RCSA. *Journal of Manufacturing Science and Engineering*, 123(4):700–707, nov 2001.

[152] Majid Mehrpouya, Eldon Graham, and Simon S. Park. FRF based joint dynamics modeling and identification. *Mechanical Systems and Signal Processing*, 39(1-2):265–279, aug 2013.

[153] Maarten V. Van Der Seijs, Daniël D. Van Den Bosch, Daniel J. Rixen, and Dennis De Klerk. An improved methodology for the virtual point transformation of measured frequency response functions in Dynamic Substructuring. In *ECCOMAS Thematic Conference - COMPDYN 2013: 4th International Conference on Computational Methods in Structural Dynamics and Earthquake Engineering, Proceedings - An IACM Special Interest Conference*, pages 4334–4347, Athens, apr 2013. Institute of Structural Analysis and Antiseismic Research School of Civil Engineering National Technical University of Athens (NTUA) Greece.

[154] M. Sturm, M. Yankonis, R. Bosch, C. Marchand, S. Sherman, J. Hirscher, M. Priebe, P. Parikh, and A.T. Moorhouse. Robust NVH Development of Steering Systems Using In-Situ Blocked Forces from Measurements with Low-Noise Driver Simulators. *INTER-NOISE and NOISE-CON Congress and Conference Proceedings*, 254(2):687–694, 2017.

[155] Dongwoo Hong and Byeongil Kim. Quantification of Active Structural Path for Vibration Reduction Control of Plate Structure under Sinusoidal Excitation. 2019.

[156] Christoph W. Schwingshackl. Measurement of Friction Contact Parameters for Nonlinear Dynamic Analysis. pages 167–177. 2012.

[157] A. Fantetti, C. Pennisi, D. Botto, S. Zucca, and C. Schwingshackl. Comparison of contact parameters measured with two different friction rigs for nonlinear dynamic analysis. *Proceedings of ISMA 2020 - International Conference on Noise and Vibration Engineering and USD 2020 - International Conference on Uncertainty in Structural Dynamics*, pages 2165–2174, 2020.

[158] Muhammad Umer, Chiara Gastaldi, and Daniele Botto. Friction damping and forced-response of vibrating structures: An insight into model validation. *International Journal of Solids and Structures*, 202:521–531, oct 2020.

[159] Jacopo Brunetti, Walter D'Ambrogio, and Annalisa Fregolent. Analysis of the Vibrations of Operators' Seats in Agricultural Machinery Using Dynamic Substructuring. *Applied Sciences*, 11(11):4749, may 2021.

[160] S. Smith, J. C. Bilbao-Ludena, S. Catalfamo, M. R. W. Brake, P. Reuß, and C. W. Schwingshackl. The Effects of Boundary Conditions, Measurement Techniques, and Excitation Type on Measurements of the Properties of Mechanical Joints. In G. Kerschen, editor, *Nonlinear Dynamics, Conference Proceedings of the Society for Experimental Mechanics Series*, volume 1, pages 415–431. Springer, Cham, 2016.

[161] Y Ren and C F Beards. An Iterative FRF Joint Identification Technique. In *Proceedings of the 11th International Modal Analysis Conference*, volume 2, pages 1133–1139. SPIE INTERNATIONAL SOCIETY FOR OPTICAL, 1993.

[162] F. C. Batista and N. M.M. Maia. An iterative uncoupling technique for the identification of the dynamic properties of joints. *International Conference on Noise and Vibration Engineering 2012, ISMA 2012, including USD 2012: International Conference on Uncertainty in Structure Dynamics*, 5(May):3403–3415, 2012.

[163] S. W.B. Klaassen and D. J. Rixen. Using SEMM to Identify the Joint Dynamics in Multiple Degrees of Freedom Without Measuring Interfaces. In *Conference Proceedings of the Society for Experimental Mechanics Series*, pages 87–99. 2020.

[164] Ahmed El Mahmoudi, Daniel J. Rixen, and Christian H. Meyer. Comparison of Different Approaches to Include Connection Elements into Frequency-Based Substructuring. *Experimental Techniques*, 44(4):425–433, aug 2020.

[165] Mohammad Mahdi Rezaei, Mohammad R. Movahhedy, Hamed Moradi, and Mohammad T. Ahmadian. Extending the inverse receptance coupling method for prediction of tool-holder joint dynamics in milling. *Journal of Manufacturing Processes*, 14(3):199–207, aug 2012.

[166] Tony L. Schmitz and G. Scott Duncan. Three-Component Receptance Coupling Substructure Analysis for Tool Point Dynamics Prediction. *Journal of Manufacturing Science and Engineering*, 127(4):781–790, nov 2005.

[167] A. Ertürk, H. N. Özgüven, and E. Budak. Analytical modeling of spindle-tool dynamics on machine tools using Timoshenko beam model and receptance coupling for the prediction of tool point FRF. *International Journal of Machine Tools and Manufacture*, 46(15):1901–1912, dec 2006.

[168] Burcu Sayin and Ender Cigeroglu. A new structural modification method with additional degrees of freedom for dynamic analysis of large systems. In *Topics in Experimental Dynamic Substructuring - Proceedings of the 31st IMAC, A Conference on Structural Dynamics, 2013*, volume 2, pages 137–144. 2014.

[169] O. Özşahin, A. Ertürk, H. N. Özgüven, and E. Budak. A closed-form approach for identification of dynamical contact parameters in spindle-holder-tool assemblies. *International Journal of Machine Tools and Manufacture*, 49(1):25–35, jan 2009.

[170] Y. Ren and C.F. Beards. Identification of joint properties of a structure using frf data. *Journal of Sound and Vibration*, 186(4):567–587, oct 1995.

[171] Y. Ren and C. F. Beards. On substructure synthesis with FRF data. *Journal of Sound and Vibration*, 185(5):845–866, sep 1995.

[172] Uttara V. Kumar and Tony L. Schmitz. Spindle dynamics identification for Receptance Coupling Substructure Analysis. *Precision Engineering*, 36(3):435–443, jul 2012.

[173] C-H Cheng, Tony L Schmitz, and G Scott Duncan. Rotating tool point frequency response prediction using RCSA. *Machining Science and Technology*, 11(3):433–446, 2007.

[174] J.W.R. Meggitt. *On In-situ Methodologies for the Characterisation and Simulation of Vibro-Acoustic Assemblies*. PhD thesis, University of Salford, Greater Manchester, 2017.

[175] Jiantie Zhen, Teik C. Lim, and Guangqing Lu. Determination of system vibratory response characteristics applying a spectral-based inverse sub-structuring approach. Part II: motor vehicle structures. *International Journal of Vehicle Noise and Vibration*, 1(1/2):31, 2004.

[176] Andy Moorhouse, Andrew S. Elliot, and YongHwa Heo. Intrinsic characterisation of structure-borne sound sources and isolators from in-situ measurements. In *Proceedings of Meetings on Acoustics*, page 065053, Montreal, Canada, 2013.

[177] Jun Wang, Xiang Hong, Yi Qian, Zhi-wei Wang, and Li-xin Lu. Inverse Sub-Structuring Method for Multi-Coordinate Coupled Product Transport System. *Packaging Technology and Science*, 27(5):385–408, may 2014.

[178] Jun Wang, Qi-li Wang, Zhong-zhen Sun, Li-xin Lu, and Zhi-wei Wang. Inverse Sub-structuring Method for Rigidly Coupled Product Transport System based on Frequency Response Function Testing Probe Technique. *Packaging Technology and Science*, 30(8):373–386, aug 2017.

[179] Pengtao Wang, Jun Wang, Teik C Lim, Lixin Lu, and Liao Pan. A strategy for decoupling of nonlinear systems using the inverse sub-structuring method and the parametric modal identification technique. *Mechanical Systems and Signal Processing*, 140:106695, jun 2020.

[180] Walter D'Ambrogio and Annalisa Fregolent. Replacement of unobservable coupling DoFs in substructure decoupling. *Mechanical Systems and Signal Processing*, 95:380–396, oct 2017.

[181] Michael Hanss, Stefan Oexl, and Lothar Gaul. Identification of a bolted-joint model with fuzzy parameters loaded normal to the contact interface. *Mechanics Research Communications*, 29(2-3):177–187, mar 2002.

[182] J.W.R. Meggitt and A.T. Moorhouse. A covariance based framework for the propagation of correlated uncertainty in frequency based dynamic substructuring. *Mechanical Systems and Signal Processing*, 136:106505, feb 2020.

[183] F. Trainotti, M. Haeussler, and D.J. Rixen. A practical handling of measurement uncertainties in frequency based substructuring. *Mechanical Systems and Signal Processing*, 144:106846, oct 2020.

[184] Hamid Ahmadian and Hassan Jalali. Identification of bolted lap joints parameters in assembled structures. *Mechanical Systems and Signal Processing*, 21(2):1041–1050, feb 2007.

[185] L. Gaul and R. Nitsche. The Role of Friction in Mechanical Joints. *Applied Mechanics Reviews*, 54(2):93–106, mar 2001.

[186] J.P. Noël and G. Kerschen. Nonlinear system identification in structural dynamics: 10 more years of progress. *Mechanical Systems and Signal Processing*, 83:2–35, jan 2017.

[187] Giuseppe Vitrani. Caratterizzazione Preliminare di un Simulacro di Disco Palettato in Presenza di Contatti per Attrito. Technical report, Politecnico di Torino, Torino, 2018.

[188] Michael Haeussler and Daniel Jean Rixen. Optimal transformation of frequency response functions on interface deformation modes. In M. Allen, R. Mayes, and D. Rixen, editors, *Conference Proceedings of the Society for Experimental Mechanics Series*, number January, pages 225–237. Springer, Cham, 2017.

[189] Z. Saeed, G. Jenovencio, S. Arul, J. Blahoš, A. Sudhakar, L. Pesaresi, J. Yuan, F. El Haddad, H. Hetzler, and L. Salles. A Test-Case on Continuation Methods for Bladed-Disk Vibration with Contact and Friction. In G. Kerschen, M. Brake, and L. Renson, editors, *Nonlinear Structures and Systems, Volume 1. Conference Proceedings of the Society for Experimental Mechanics Series*, pages 209–212. Springer, Cham, 2020.

[190] Mark H Richardson and David L Formenti. Global curve fitting of frequency response measurements using the rational fraction polynomial method. *Proceeding of 3rd IMAC*, pages 390–397, 1985.

[191] Gilbert Strang. *Computational Science and Engineering*. Wellesley-Cambridge Press, 2016.

Appendix A

Dynamic stiffness of the internal system

Let $\mathbf{Z}$ be the dynamic stiffness with the following partitions and the displacement field on boundary be $\mathbf{u}_2 = 0$.

$$\begin{bmatrix} \mathbf{Z}_{11} & \mathbf{Z}_{12} \\ \mathbf{Z}_{21} & \mathbf{Z}_{22} \end{bmatrix} \begin{Bmatrix} \mathbf{u}_1 \\ \mathbf{u}_2 = 0 \end{Bmatrix} = \begin{Bmatrix} \mathbf{f}_1 \\ \mathbf{f}_2 \end{Bmatrix} \tag{A.1}$$

The subscripts 1 and 2 denote internal and boundary DoF, respectively. This leads to the following identity:

$$\mathbf{f}_1 = \mathbf{Z}_{11}\mathbf{u}_1 \tag{A.2}$$

In order to obtain $\mathbf{f}_1$ from measurements, we express the following relation with FRFs $\mathbf{Y}$.

$$\begin{Bmatrix} \mathbf{u}_1 \\ \mathbf{u}_2 = 0 \end{Bmatrix} = \begin{bmatrix} \mathbf{Y}_{11} & \mathbf{Y}_{12} \\ \mathbf{Y}_{21} & \mathbf{Y}_{22} \end{bmatrix} \begin{Bmatrix} \mathbf{f}_1 \\ \mathbf{f}_2 \end{Bmatrix} \tag{A.3}$$

From the second equation of the above, we get

$$\mathbf{Y}_{21}\mathbf{f}_1 + \mathbf{Y}_{22}\mathbf{f}_2 = 0 \quad \Longrightarrow \quad \mathbf{f}_2 = -\mathbf{Y}_{22}^{-1}\mathbf{Y}_{21}\mathbf{f}_1 \tag{A.4}$$

Substituting $\mathbf{f}_2$ in the first of Eq. (A.3) and solving for $\mathbf{f}_1$, we have

$$\begin{aligned} \mathbf{Y}_{11}\mathbf{f}_1 - \mathbf{Y}_{12}\mathbf{Y}_{22}^{-1}\mathbf{Y}_{21}\mathbf{f}_1 &= \mathbf{u}_1 \\ \mathbf{f}_1 = \underbrace{(\mathbf{Y}_{11} - \mathbf{Y}_{12}\mathbf{Y}_{22}^{-1}\mathbf{Y}_{21})^{-1}}_{\mathbf{Z}_{11}}\mathbf{u}_1 &. \end{aligned} \tag{A.5}$$

Comparing it with Eq. (A.2), one can see that $\mathbf{Z}_{11}$ is obtained by condensing the FRF matrix on the boundary DoF. In other words, $\mathbf{Z}_{11}$ is obtained by constraining the boundary DoF i.e. $\mathbf{u}_2 = 0$. The above equation has a similar structure to the numerical residual ρ^{N} in Eq. (3.21) for the standard interface formulation. So the modes contained in $\mathbf{Z}_{11}$ or the modes of the internal system with the boundary DoF fixed may appear in the hybrid model depending on the frequency range and the choice of boundary DoF.

Appendix B

Constraint Matrix for Frequency-independent Joint Parameters

In Section 5.2.2, we discussed the method of Ren and Beards [170] in relation to the constraints introduced to make the joint parameters frequency independent. In this appendix, we use slightly different constraint matrix but the approach is similar to theirs. Let us consider a two mass system of Fig. B.1 connected by a spring with stiffness k and a dashpot with damping coefficient c. The two masses are denoted by m_1 and m_2.

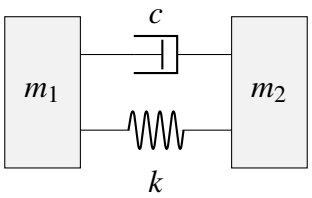

Fig. B.1 A simple spring mass system representing an inertial joint

The dynamic stiffness $\mathbf{Z}$ of this system is expressed as

$$\mathbf{Z}(\omega) = \begin{bmatrix} Z_{11}(\omega) & Z_{12}(\omega) \\ Z_{21}(\omega) & Z_{22}(\omega) \end{bmatrix} = \begin{bmatrix} k + i\omega c - \omega^2 m_1 & -k - i\omega c \\ -k - i\omega c & k + i\omega c - \omega^2 m_2 \end{bmatrix} \tag{B.1}$$

Given that there are four unknown parameters namely $\mathbf{x} = \{k, c, m_1, m_2\}^T$, one can use four equations given by $Z_{11}, Z_{12}, Z_{21}, Z_{22}$, respectively. Although Z_{pq} depends on frequency ω, one could uniquely determine the same joint parameters $\mathbf{x}$ irrespective of the frequency value. Since dynamic stiffness identified through inverse receptance coupling or substructure decoupling methods can have fluctuating values of dynamic stiffness, it is desired to identify a unique set (best fit) of joint parameters $\mathbf{x}$ from $\mathbf{Z}(\omega_1), \mathbf{Z}(\omega_2), \ldots, \mathbf{Z}(\omega_N)$. Here we shall consider only two frequencies ω_1 and ω_2 to derive the constraint matrix which can nonetheless be extended to N frequencies.

Similar to Ren and Beards [170], a simple and easy transformation can be obtained if we first define a vector of dynamic stiffness elements $\mathbf{z}$ and a vector of joint parameters $\mathbf{x}$

$$\mathbf{z} = \begin{Bmatrix} Z_{11}(\omega_1) \\ Z_{12}(\omega_1) \\ Z_{21}(\omega_1) \\ Z_{22}(\omega_1) \\ \hline Z_{11}(\omega_2) \\ Z_{12}(\omega_2) \\ Z_{21}(\omega_2) \\ Z_{22}(\omega_2) \end{Bmatrix} \quad \text{and} \quad \mathbf{x} = \begin{Bmatrix} k \\ c \\ m_1 \\ m_2 \end{Bmatrix}. \tag{B.2}$$

The constraint $\mathbf{T}$ between $\mathbf{x}$ and $\mathbf{z}$ can thus be defined as follows:

$$\mathbf{T} = \left[\begin{array}{cccc} 1 & i\omega_1 & -\omega_1^2 & 0 \\ -1 & -i\omega_1 & 0 & 0 \\ -1 & -i\omega_1 & 0 & 0 \\ 1 & i\omega_1 & 0 & -\omega_1^2 \\ \hline 1 & i\omega_2 & -\omega_2^2 & 0 \\ -1 & -i\omega_2 & 0 & 0 \\ -1 & -i\omega_2 & 0 & 0 \\ 1 & i\omega_2 & 0 & -\omega_2^2 \end{array}\right] \tag{B.3}$$

The system $\mathbf{z} = \mathbf{T}\mathbf{x}$ is over-determined and so one can continue to append more frequency blocks to obtain the joint parameters

$$\mathbf{x} = \mathbf{T}^{+}\mathbf{z}\,. \tag{B.4}$$

where $\mathbf{T}^{+}$ is the generalized inverse of $\mathbf{T}$. The modelling parameters and the size of the final joint system are left to the user's choice which would result in a different matrix $\mathbf{T}$.